FULLY COUPLED THERMO-HYDRO-MECHANICAL MODELING OF DISCONTINUITIES IN POROUS MEDIA INCORPORATING HIGH ASPECT RATIO INTERFACE ELEMENTS

A Dissertation

by

MICHAEL ANDRADE MAEDO

Submitted to the Office of Graduate and Professional Studies of
Texas A&M University
in partial fulfillment of the requirements for the degree of

DOCTOR OF PHILOSOPHY

Chair of Committee,	Marcelo Sánchez
Committee Members,	Charles Aubeny
	Minsu Cha
	Robert Lytton
	Alan Needleman
Head of Department,	Robin Autenrieth

August 2019

Major Subject: Civil Engineering

ABSTRACT

The process of evolving discontinuities (in the form of fractures, cracks or fissures) in porous media is a very complex problem and possesses several challenges. This research proposal aims to progress the current understanding in this area by developing a fully coupled thermo-hydro-mechanical (THM) approach. The discontinuity will be modeled by using the mesh fragmentation technique (MFT), which consists of introducing finite elements with high aspect ratio between the standard (bulk) elements of the mesh. This new methodology has been successfully employed in concrete structures and soils, but by only assuming the mechanical problem. In this dissertation, the mass and heat flows are also incorporated in the formulation by considering THM processes. The MFT has been implemented in the in house CODE_BRIGHT finite element program, which was originally developed to solve coupled THM problems in continuous porous media. In this context, numerical simulations were performed in order to achieve a better understanding of discontinuities under complex conditions, mimicking desiccation tests in soils and energy production in rock reservoirs. The results have shown that the technique is very promising to model the formation and propagation of discontinuities in geo-engineering problems.

DEDICATION

To my wife, Ana Paula

ACKNOWLEDGMENTS

First, I would like to thank my committee chair, mentor and supervisor Marcelo Sánchez for his guidance, friendship and dedication. He has helped me through my academic career by teaching me, not only scientific and technological concepts, but also methods to improve my writing and speaking skills. Work with him has been a great experience. His "Transport Phenomena in Porous Media" course inspired me to pursue a research related to Thermo-Hydro-Mechanical processes in porous materials. In addition, Dr. Sanchez's course contributed significantly for the development of my Ph.D.

Thanks also to my former supervisor Osvaldo Manzoli, Professor of Structural Engineering at the São Paulo State University (UNESP) in Bauru – Brazil, for his assistance and support. Dr. Manzoli was the first one who showed me the capabilities of finite elements with high aspect ratio. His "Continuum Mechanics" course instigated me to keep working with numerical modeling and pursue a Ph.D.

I am indebted to Leonardo Guimarães, Professor of Geotechnical Engineering at the Federal University of Pernambuco (UFPE) in Recife – Brazil, who gave me full access to his version of CODE_BRIGHT. I had the opportunity to work with him a couple of times and he was always available to help me with anything.

Special thanks go to my friend Pedro Cleto for his invaluable collaboration in the investigation of some cases associated with the hydraulic fracturing process. I would also like to thank my friends Chen Yue, Du YiChi, Luo Xi, Gai Xuerui, Son JungRak, Lee Junho, Husham Al Janabi, Anahita Goudarzi, Pavan Akula and Alfredo Saab for making my time at the United States a great adventure. Those nights we spent together working, discussing, laughing or celebrating were unforgettable.

This work would not have been possible without the financial support provided by the CNPq (Conselho Nacional de Desenvolvimento Científico e Tecnológico, Brazil) through the process n^{o}: 234003/2014-6.

Special thanks also to my wife Ana Paula for her patience and encouragement. She kept me company in so many nights I had to work and study. Finally, I wish to express my thanks to my family, specially my father, mother, brother and mother-in-law for their support and understanding during these last four years.

CONTRIBUTORS AND FUNDING SOURCES

Contributors

This work was supported by a dissertation committee consisting of Professors Marcelo Sánchez (Advisor), Charles Aubeny, Minsu Cha and Robert Lytton of the Department of Civil Engineering and Professor Alan Needleman of the Department of Materials Science & Engineering.

All other work conducted for the dissertation was completed by the student independently.

Funding Sources

Graduate study was supported by a fellowship from CNPq (Conselho Nacional de Desenvolvimento Científico e Tecnológico, Brazil) and a research fellowship from Texas A&M Energy Institute.

TABLE OF CONTENTS

Page

ABSTRACT ii

DEDICATION iii

ACKNOWLEDGMENTS iv

CONTRIBUTORS AND FUNDING SOURCES vi

TABLE OF CONTENTS vii

LIST OF FIGURES x

LIST OF TABLES xv

1. INTRODUCTION 1
  - 1.1 Motivation 1
  - 1.2 Smeared Crack Models 4
  - 1.3 Cohesive Models with Adaptive Remeshing 5
  - 1.4 Cohesive Interface Elements 6
  - 1.5 Elements with Embedded Discontinuity 7
  - 1.6 Extended Finite Element Method 9
  - 1.7 Elements with High Aspect Ratio 10
  - 1.8 Objectives 11
  - 1.9 Dissertation layout 12

2. COUPLED THERMO-HYDRO-MECHANICAL FORMULATION FOR CONTINUOUS POROUS MEDIA 14
  - 2.1 Introduction 14
  - 2.2 Balance Equations 15
    - 2.2.1 Solid Mass Balance Equation 15
    - 2.2.2 Water Mass Balance Equation 17
    - 2.2.3 Internal Energy Balance Equation 19
    - 2.2.4 Equilibrium equation 20
  - 2.3 Initial and Boundary Conditions 21
  - 2.4 Constitutive Equations 22
    - 2.4.1 Hydraulic Constitutive Equations 22
    - 2.4.2 Phase properties 24
    - 2.4.3 Thermal Constitutive Equations 25

2.4.4 Mechanical Constitutive Model 26
2.4.4.1 Mechanical Model for Unsaturated Soils 26
2.4.4.2 Mechanical Model for Rock 28
2.5 Equilibrium Restrictions 28
2.5.1 Henry's Law 29
2.5.2 Psychrometric Law (Kelvin's Equation) 29
2.5.3 Mass Fractions of Water in the Liquid Phase and Air in the Gaseous Phases . 31

3. MODELING DESICCATION PROCESSES IN SOILS INVOLVING DISCONTINUITIES 32

3.1 Introduction 32
3.2 Numerical Framework 34
3.3 Modeling the Fracture Behavior 36
3.4 Effects of the Fracture in a Narrow Band 38
3.5 Finite Element Equations 39
3.5.1 Weak Form of the Governing Equations 39
3.5.2 Fluid Mass Balance Equation in the Fracture 40
3.5.3 FEM Approximations 42
3.6 Modeling Discontinuities with High Aspect Ratio Finite Elements 44
3.6.1 Solid Finite Element with High Aspect Ratio 44
3.6.2 Damage Models for HAR-FE 45
3.6.3 Mesh Fragmentation Technique (MFT) 47
3.7 Applications 49
3.7.1 Desiccation Cracks in Circular Plate Tests under Laboratory Atmospheric Conditions 49
3.7.2 Crack Patterns Observed in a Flood Embankment 57
3.8 Conclusion 61

4. MODELING EMERGING PHENOMENA IN DRYING SOILS 63

4.1 Introduction 63
4.2 Mesh Fragmentation Technique (MFT) 65
4.3 Orthotropic Interface Model 68
4.3.1 Tension Damage Model 71
4.3.2 Implicit-Explicit Integration Scheme (IMPL-EX) 72
4.4 Applications 72
4.4.1 Synthetic Benchmarks 74
4.4.2 Experimental Validation of the Orthotropic Model 76
4.4.3 Modeling a Slab Desiccation Tests with Orthotropic Characteristics 81
4.4.3.1 Modeling the Contact Between Materials with an Isotropic Mechanical Model 83
4.4.3.2 Modeling a Slab Desiccation Test using the Orthotropic Interface Model 84
4.5 Experimental and Numerical Studies of Soil Curling 86
4.6 Materials and Experimental Methods 89

        4.6.1 Samples Description 89
        4.6.2 Experimental Investigation 90
    4.7 Test Results 92
    4.8 Modeling Soil Shrinkage Behavior 96
        4.8.1 Damage Model to Simulate the Soil-Plate Interface Behavior 96
    4.9 Computational Aspects 101
    4.10 Numerical Modeling of the Soil Surface Curling 102
    4.11 Discussion 112
    4.12 Conclusions 114

5. MODELING COUPLED MULTIPHYSICS PHENOMENA IN ROCKS INVOLVING DISCONTINUITIES 116

    5.1 Introduction 116
    5.2 The Mesh Fragmentation Technique (MFT) 119
    5.3 Governing Equations 123
        5.3.1 Mechanical Model 123
        5.3.2 Hydraulic Model 125
        5.3.3 Thermal Model 126
    5.4 Finite Element Equations 127
        5.4.1 Weak Form of the Governing Equations 127
        5.4.2 Fluid Mass Balance Equation in the Fracture 128
        5.4.3 Internal Energy Balance Equation in the Fracture 129
        5.4.4 FEM Approximations 130
    5.5 Applications 133
        5.5.1 Benchmarks 133
            5.5.1.1 2D Hot Dry Rock Benchmark 133
            5.5.1.2 2D Hot Sedimentary Aquifer Benchmark 134
        5.5.2 Hydraulic Fracturing Propagation 136
            5.5.2.1 Storage-Toughness Dominated Regime 139
            5.5.2.2 Storage-Viscosity Dominated Regime 142
        5.5.3 Thermal Fracking in Transparent Sample 142
            5.5.3.1 Specimen 1 144
            5.5.3.2 Specimen 2 146
    5.6 Conclusions 147

6. CONCLUSIONS AND FUTURE WORK 151

    6.1 Conclusions 151
    6.2 Future Work 152

REFERENCES 154

LIST OF FIGURES

FIGURE Page

2.1 Porous medium (adapted from [182]) 15

3.1 Schematic representation of a body containing a subdomain Ω^h, which converges to a discontinuity surface S when $h \rightarrow 0$ (modified from[126]) 36

3.2 Solid interface finite elements: (a) three-node triangular element; (b) four-node tetrahedral element 45

3.3 Main steps related to the mesh fragmentation process: (a) original mesh composed by two different materials, called materials 1 and 2; (b) the elements associated with material 1 are separated, which leads to the formation of gaps of thickness h; (c) elements with high aspect ratio are inserted in these gaps, which are a result of the previous step; (d) zoom showing in detail all the new elements that are generated by the mesh fragmentation process (modified from[123, 184]) 48

3.4 Soil-water retention curve adopted for the drying test 51

3.5 Variation of permeability with porosity [179] 52

3.6 Variation of tensile strength with degree of saturation according to the experimental results [179] 52

3.7 Relationship between tensile strength and degree of saturation: (a) proposed expression; (b) curve adopted to model the behavior of the waste 53

3.8 Drying test results for the specimen with thickness of 40 mm and diameter of 250 mm: (a) vertical strain; (b) water loss 54

3.9 Mesh, geometry, and boundary conditions used to replicate the drying test 55

3.10 Crack patterns for different thickness: (a-c) photos of the final state of the samples (reprinted from [179]); (d-f) top views of the models with thickness equals to 4 mm, 8mm, and 16 mm, respectively; (g-i) contour of the major principal (tensile) stress at the end of the analysis 56

3.11 Photo of the landward face of the embankment (reprinted from [74]) 57

3.12 Photos of the crack patterns of the Thorngumbald embankment flood during: (a) the first visit in 2003 and (b) the third visit in 2006 (reprinted from [60]) 58

3.13 Finite element mesh, geometry, mechanical and flux boundary conditions adopted to study the Thorngumbald embankment flood 58

3.14 Soil-water retention curve assumed to study the Thorngumbald embankment flood .. 59

3.15 Desiccation cracks obtained via the MFT 60

3.16 Evolution of the Thorngumbald embankment flood's results obtained via the MFT: (a) crack pattern; (b) contours of vertical displacements; (c) contours of major (tensile) principal stress; (d) contours of liquid saturation 62

4.1 Mesh fragmentation process (modified from [121, 123]): (a) original finite element mesh; (b) soil finite elements are disconnected from each other, resulting in a fragmented mesh with spaces among elements; (c) the spaces are filled with two different types of finite elements with high aspect ratio, one that will represent the crack process (soil-soil interface elements), and other that will simulate the soil-plate interface 66

4.2 Four-node tetrahedral finite element (reprinted from [125]) 68

4.3 Reprinted from [125]: (a) schematic representation of the orthotropic model with the option to define different strengths in two orthogonal directions; (b) plot showing the sliding at the interface between materials, with the corresponding displacement jumps in two orthogonal directions 71

4.4 Geometry and boundary conditions related to the proposed synthetic benchmark (reprinted from [125]) 74

4.5 Failure envelopes related to the direct shear tests (reprinted from [125]): (a) experimental, and (b) numerical results [125] 76

4.6 Modified direct shear box for testing soil–plate interface strength: (a) front photograph; (b) top photograph (reprinted from [125]) 76

4.7 Different types of plate surfaces: (a) spiral grooves, (b) grooves oriented orthogonal respect to the shear direction, (c) grooves oriented parallel to the shear direction, and (d) smooth surface (reprinted from [125]) 77

4.8 Modeling of direct shear tests, main components (reprinted from [125]): (a) interfaces formed formed with HAR FEs, (b) interfaces, shear box, plates and soil; and (c) final FE mesh with all the components to simulate the test 79

4.9 Modeling of the direct shear test of soil-plate interfaces (reprinted from [125]): (a) before testing, (b) deformed specimen after applying the vertical load $\mathbf{F}_n$ at the top, and (c) deformed specimen after shearing 79

4.10 Reprinted from [125]: shear force against horizontal displacements when load is applied perpendicular to the grooves (*i.e.*, Figure 4.7b): (a) experimental results; (b) numerical outputs 80

4.11 Failure envelopes related to the direct shear tests (reprinted from [125]): (a) experimental, and (b) numerical results 81

4.12 Drying tests on saturated clay samples prepared in slab plates (reprinted from [166]): a detail of the soil slap contact showing the 2-mm notches, b typical examples of crack formation in 3 different soil samples (2009 Canadian Science Publishing or its licensors. Reproduced with permission) 82

4.13 3D modeling of the drying tests on saturated clay samples prepared in slab plates discretizing the indentation at the soil–plate interface (reprinted from [125]) 84

4.14 Modeling the slab specimen using an isotropic interface model for the soil–plate contact surface, (a) 3D and (b) top views, respectively (reprinted from [125]) 84

4.15 Modeling the slab specimen using an orthotropic interface model for the soil–plate contact surface – structured mesh (reprinted from [125]) 85

4.16 Modeling the slab specimen using an orthotropic interface model for the soil–plate contact surface – unstructured mesh (reprinted from [125]) 87

4.17 Soil-water retention curve of the mixture 85% kaolinite and 15% silica-sand 90

4.18 Photo of the adopted set-up 91

4.19 Evolution of suction with time 92

4.20 Sample of pure silica-sand prepared at $w = 65\%$ and subjected to drying, pictures at the end of the drying process from: (a) size view, and (b) top views. Curling deformation of the pure kaolin soil sample at the end of the test: (c) side view; (d) top view. 93

4.21 Stages of the curling development in the mixture 85/15 kaolinite/sand subjected to drying 94

4.22 Pictures of the 80/20 kaolinite/sand mixture at the end of the drying test: (a) lateral photo showing the curled and broken sample; (b) front image of the broken section sample showing the soil segregation, with the larger sand grains settle at the bottom of the sample; (c) image of the bottom of the sample showing the deposition of the sand particles. 95

4.23 Crack pattern of the soil sample, 85% kaolinite with 15% silica sand at the end of the test: (a) side view; (b) top view 95

4.24 Scheme representation of new interface damage model: (a) and (c) lateral and top views, respectively, of a soil experiencing shrinkage only, (b) and (d) lateral and top view, respectively, of a specimen exhibiting shear displacement at the soil-plate contact and curling with soil detachment from the plate 98

4.25 Geometry and boundary conditions of the model adopted for the drying test 106

4.26 Photo of the adopted set-up 106

4.27 Contours of stress field of the model reproducing the behavior of the 85/15 kaolinite/silica sand 107

4.28 Contours of stress field of the model reproducing the behavior of the sample prepared with 80% kaolinite and 20% silica sand 108

4.29 (a) Geometry and boundary conditions of the model adopted for the drying test; (b) 3D finite element mesh adopted for the drying test 109

4.30 Deformation of the model reproducing the behavior of pure kaolinite at the end of the analysis: (a) side view; (b) isometric view; (c) top view; (d) front view 110

4.31 Stages of the curling development in a thin soil layer of 85% kaolinite and 15% silica sand 112

4.32 Curling deformation of the soil sample prepared with 80% kaolinite and 20% silica sand at the end of the simulations: (a) side view; (b) isometric view; (c) top view; (d) front view 113

4.33 Crack pattern of the soil sample prepared with 85/15 kaolinite/silica sand at the end of the analysis: (a) side view; (b) isometric view; (c) top view; (d) front view 113

5.1 Main stages associated with the mesh fragmentation technique: (a) original finite element mesh;(b) size of the bulk elements are reduced, creating gaps between them; (c) such gaps are filled with elements with high aspect ratio, which can reproduce the discontinuity behavior (adapted from [123]) 120

5.2 Fracture propagation with HAR finite elements 121

5.3 Three-node triangular finite element (adapted from [121, 123]) 122

5.4 Hot dry rock benchmark: (a) geometry and boundary conditions;(b) finite element mesh (reprinted from [210]) 134

5.5 Results from the numerical modeling of the 2D hot dry rock reservoir: (a) temperature distribution after 30 years; (b) steady-state pressure distribution after 30 years 135

5.6 Temporal evolution of production temperature of the 2D hot dry rock reservoir 135

5.7 Hot dry rock benchmark: (a) geometry and boundary conditions;(b) finite element mesh (reprinted from [210]) 136

5.8 Results from the numerical modeling of the 2D hot sedimentary aquifer: (a) temperature distribution after 30 years; (b) pressure distribution after 30 years; (c) fluid velocity distribution; (d) temporal evolution of the production temperature 137

5.9 Mesh, geometry and boundary conditions of the hydraulic fracturing 138

5.10 HAR finite element solution of the fracture aperture for the storage-toughness dominated regime with the analytical and the numerical results [39] found in the literature: (a) fracture profile at $t = 10$ s; (b) time history of fracture aperture 141

5.11 Comparison of the storage-toughness dominated regime results obtained via HAR elements with the numerical ones reported by Carrier and Granet [39] in terms of: (a) injection pressure or $k = 1 \times 10^{-16}$ m^2; (b) fracture length 141

5.12 Numerical and analytical curves for the storage-viscosity dominated regime: (a) fracture aperture; (b) injection pressure; (c) fracture length 143

5.13 Acrylic specimen 1: (a) experimental sample [41]; (b) mesh, geometry and boundary conditions........ 145

5.14 Temperature evolution of the numerical model and thermal shock experiment........ 146

5.15 Acrylic specimen 1: (a-d) experimental crack pattern (reprinted from [41]); (e-h) numerical cracks; (i-l) contours of temperature versus time 148

5.16 Acrylic specimen 2: (a) experimental sample [41]; (b) mesh, geometry and boundary conditions........ 149

5.17 Acrylic specimen 2: (a-d) experimental crack pattern (reprinted from [41]); (e-h) numerical cracks; (i-l) contours of temperature versus time 150

LIST OF TABLES

TABLE Page

3.1 Continuum damage models 46

3.2 Hydraulic properties of the model [179] 51

3.3 Mechanical properties of the bulk elements used to study the drying test of circular soil plates 55

3.4 Mechanical properties of the interface elements used to study the drying test of circular soil plates 55

3.5 Mechanical properties of the bulk elements adopted to model the Thorngumbald embankment flood 60

3.6 Mechanical properties of the HAR finite elements adopted to model the Thorngumbald embankment flood 60

4.1 IMPL-EX integration scheme for the orthotropic damage model 73

4.2 Properties of the blocks and interface used to study the synthetic benchmarks 75

4.3 Material properties of soil, pate, shear box and interfaces used in the numerical analysis of the interface shear test 81

4.4 Material properties of soil and plate used in the simulations of desiccation cracks 86

4.5 Parameters of the soil water retention curve used in the model 90

4.6 IMPL-EX integration scheme for the interface damage model 103

4.7 Mechanical properties adopted for the 2D model 105

4.8 Mechanical properties of the interface elements 105

4.9 Mechanical properties adopted for the kaolin and upper layer 3D model 110

4.10 Mechanical properties adopted for the lower layer 3D model 111

5.1 Main rock properties 139

5.2 First five terms of the asymptotic solution [33] 140

5.3 Mechanical properties adopted for the thermal shock test 144

5.4 Thermal properties adopted for the thermal shock test 144

1. INTRODUCTION

1.1 Motivation

The formation and propagation of discontinuities in porous media (*i.e.*, in the form of fractures, cracks or fissures) correspond to a relevant and complex phenomena of interest for different engineering applications. For example, the potential migration of gas and/or pollutants flow through discontinuities can seriously jeopardize the performance of repositories for high-level nuclear waste and other type of barrier systems. The mechanical integrity of the geomaterials (*i.e.*, rocks and soils) comprising a geological system is a key component in several problems involving energy production. For instance, in unconventional fields oil and/or gas are trapped in very low porosity/permeability rocks (*e.g.*, gas/oil shales) and special recovery operations (outside the conventional techniques) are required to produce hydrocarbons for this type of system. Hydraulic fracturing is the most common enhanced recovery technique used in shale gas fields and consists in injecting engineered fluids (*e.g.*, CO_2, H_2O) at very-high pressures into a reservoir via injection wells. The high pressurized fluid breaks the rocks, forming the fractures and allowing the release of the trapped oil and gas. Similar techniques are required to assist oil production from recently found very-deep oil reservoirs.

The crack formation in soils is also a subject of practical interest. Drying cracks strongly affect the permeability and strength of soil and may lead to compromise the integrity of civil infrastructure. The analysis of desiccation cracks in soils involves coupled Hydro-Mechanical (HM) phenomena and interactions. To design and build more economical and safer geostructures, such as levees and road embankments, it is essential to better understand and properly model the processes behind the formation and propagation of drying cracks in soils. Despite the ongoing efforts in this area, it is still difficult to simulate the actual 3D crack networks observed in desiccated soils.

The numerical modeling of developing discontinuities, as the ones in the engineering problems discussed above, it is a quite challenging problem that involves the coupling of several physical processes. One of the first theoretical/analytical approaches dealing with the formation of fractures was developed by Inglis [90], who mathematically described the elastic solution for stress at an elliptic hole in an infinite plate subjected to tensile stresses. He noticed that, in the limit situation where the smallest dimension of the hole tends to zero, the ellipse collapses to a straight crack line, and the stress at the sharp end of the hole (*i.e.*, at the crack tip) tends to infinity no matter how small the applied tensile stresses are, which is unrealistic. In order to tackle this discrepancy, Griffith [77] proposed an energy criterion of rupture which states that the sum of the potential and strain energies of a solid body deformed due to the application of external forces are reduced by the formation of a crack with traction-free surfaces. In other words, the crack only propagates when the amount of energy available in the system is equal to the energy required for the crack formation per surface area.

In 1957, Irwin [92] suggested an alternative physical treatment to study the fracture process. According to him, in the case of a brittle isotropic linear elastic material, the concentration of stresses near the crack tip can be determined by means of the stress intensity factors K_I, K_{II} and K_{III}, so that K_I is associated with the crack opening mode, and the two factors K_{II} and K_{III} correspond to the in-plane and out-of-plane shear sliding modes, respectively. Expressions for stress intensity factors can be difficult to obtain depending on the geometry and boundary conditions of the problem. Over the years several equations for stress intensity factors have been provided for different shapes, sizes and applied loads in order to simplify and facilitate the calculation process. It is worthwhile to comment that this approach is only valid for linear fracture mechanics, while the theory of rupture based on energy concepts developed by Griffith is also capable of treating general fracture mechanics problems. In the context of the energy approach, Rice [176, 177] introduced the J-integral concept to find the flux of energy through a curve enclosing the crack tip of an elastic material, linear or not. In addition, he realized that J-integral is equal to the energy release rate when the crack surfaces are traction-free, the solid is free of body forces and the material enclosed by the curve is homogeneous [29]. The author also has shown that the integral is path-independent and its use is not restricted to linear fracture mechanics, but it can be extended to elastoplastic fracture mechanics. The theory formulated by Griffith [77], Irwin [92, 93] and Rice [176, 177] is known as the Linear Engineering Fracture Mechanics (LEFM) and it has been widely used to ensure the safety of general engineering systems.

However, the LEFM is only valid for very brittle materials such as glass and brittle ceramics, so that the solid must remain elastic up to the crack formation [20], which is not the case for most materials. Therefore, non-linear fracture mechanics theories were developed in order to address the non-linear phenomena involved in the fracking process. In this context, Barenblatt [16, 17] proposed a theory to eliminate the annoying stress singularity at the crack tip. He postulated that cohesive forces act on opposite faces of the crack at a fixed terminal region close to the end of the crack, which leads to a high, but limited, concentration of stress. Dugdale [58] also developed a framework able to reproduce limited cohesive stress (yield stress) in a narrow band near the crack tip. Although his model did not consider the crack propagation, it provided insights into the fracture mechanisms related to ductile materials.

The advent of powerful digital computer machines led to the development of numerical tools, such as the finite difference method (FDM) and finite element method (FEM), in which the domain described by continuous functions is discretized by a set of subdomains mathematically expressed by algebraic equations. Although these traditional computational methods can properly handle real-life problems consisting of complicated geometries and boundary conditions, they are not suitable for discontinuity modeling. Over the years, several techniques have been proposed to include the effects of discontinuity in the finite element formulation. These approaches can be classified into two main groups: (i) the smeared crack models and (ii) the discrete crack concepts. The former converts the displacement jump into inelastic strains, while the latter considers a traction-separation law to associate the cohesive traction on the crack faces with the displacement jump. Moreover, the discrete approach can be categorized into intraelement crack models, in which the discontinuity propagates through the element (*e.g.*, X-FEM and strong discontinuity approach), and interelement crack models, in which the crack develops along the boundaries of adjacent elements (*e.g.*, cohesive models with adaptive remeshing, cohesive special/interface elements and solid finite elements with high aspect ratio). The understanding of the advantages and disadvantages of each method is essential to select the appropriate strategy. Hence, the main aspects of each approach are covered in the next sections to clarify their limitations.

1.2 Smeared Crack Models

The smeared crack approach, proposed by Rashid [173], relies on continuum mechanics concepts and it uses stress-strain relations to represent the constitutive behavior of the cracked material. The crack initiation occurs when a failure criterion is satisfied (*e.g.*, the major principal stress of the finite element reaches the tensile strength of the material). The degradation process is characterized by a gradual decline of stress with increasing strain, and therefore, the constitutive model must be able to accommodate the softening behavior of the material. Consequently, the strength and stiffness of the element must be modified to take into account the effect of cracks [40]. In general, damage or plasticity constitutive models are used to tackle the crack process [50]. The direction of crack propagation, at least initially, depends on the failure criterion adopted (*i.e.*, Rankine, von Mises, etc) and the post-peak region of the stress-strain curve is controlled by means of softening parameters.

In this context, two different approaches were proposed: the fixed and rotating smeared crack models. The former keeps the crack orientation fixed throughout the analysis, while the latter allows the crack to rotate according to the direction normal to the orientation of the major principal strain.

In order to overcome the stress locking resulting from the rotation of the principal strain direction along the analysis, Jirásek and Zimmermann [97] proposed a constitutive law in which the rotating crack model (RCM) is used at the early stage of the crack and the damage model describes the late stage of the degradation process. In this case, the damage variable ensures that the anisotropic stiffness due to the RCM gradually drops to zero as the crack evolves. This method is called rotating crack model with transition to scalar damage (RC-SD).

The smeared crack model became very popular and it was widely implemented in finite element programs because the implementation only requires the addition of a new constitutive model into the code. Although these models are able to reproduce the effect of multiple cracks closely spaced in large regions, they cannot suitably represent the formation of macro-localized cracks. In addition, it was discovered that the energy dissipated during the crack process is proportional to the size of the finite element. Hence, as the mesh of a problem is refined, and the size of the elements decreases, the dissipated energy also decreases, which shows that the results are unobjective and mesh dependent [20].

To solve the mesh dependency problem, Bazant and Oh [18] proposed the crack band model in which the crack is represented by a localized band with fixed width and the displacement discontinuity is converted into inelastic strains smeared over the band. In this case, a traction-separation law expresses the relationship between the traction acting on the crack faces and the displacement discontinuity, which represents the crack opening. These models revealed that the strain softening is associated with the fracture energy and the size of the finite element with cracks.

1.3 Cohesive Models with Adaptive Remeshing

Early models of discrete cracks relied on the separation of nodal points at the edges of adjacent elements [143, 144]. Therefore, as the crack grows, the mesh topology needs to be updated to accommodate the discontinuity. Based on the cohesive crack models, Hillerborg *et al.* [87] incorporated the principles of cohesive zone, tensile strength and fracture energy into a finite element code and successfully simulated the cracking process for concrete structures. Furthermore, LEFM or cohesive crack models can only be applied to initially cracked materials, but the fictitious crack model of Hillerborg is able to capture the crack formation for intact materials.

In the geo-mechanics community, this approach has been adopted to study cohesive fractures in 2-D multi-phase porous media [194] and to simulate 3-D hydraulic fracturing in fully saturated geo-materials [187]. In this case, the finite element framework corresponds to a fully coupled model that incorporates Biot's theory, the small displacement hypothesis, quasi-static and non-isothermal conditions [195].

The cohesive surface model treats the cracking process by means of a discrete constitutive relation between traction and relative displacements in the discontinuities, which are represented by the faces of adjacent finite elements. The constitutive model establishes the interaction between these faces [91]. Since the crack position is unknown before the analysis, this method requires a remeshing procedure to adapt the discontinuity into the finite element mesh [186], which can be expensive in terms of computation time. Moreover, 3-D analyses requires complex remeshing algorithms and a solution for problems involving multiple cracks may not be possible.

1.4 Cohesive Interface Elements

To avoid the necessity of successive re-meshing strategies, cohesive interface elements, which are inserted between the regular finite elements (bulk elements) of the initial mesh, have been developed to model discontinuities in solids subjected to dynamic effects [213, 215, 214, 37, 159]. The behavior of such interface elements are described by cohesive models between traction and relative displacements. In this case, the crack path advances by contouring the boundaries of the bulk elements of the mesh. Since this technique does not need algorithms for remeshing, it seems to be very appealing for problems with multiple dynamic cracks. The analyses conducted by Xu and Needleman [213] showed that these special elements can qualitatively reproduce the experimental observations of fast crack growth in brittle materials. Camacho and Ortiz [37] proposed an algorithm to introduce the cohesive interface elements at the faces of regular elements when a combination of stresses reaches the tensile strength of the material. In their work, they used 6-node triangular elements to avoid volumetric and shear locking. To tackle the dynamic cracks growth of 3-D problems, Ortiz and Pandolfi [156] designed a 12-node triangular cohesive element that is able to simulate mixed-mode fracture. They also admitted two crack growth criteria to account for both brittle and ductile mechanics.

This technique has been extensively used to study the formation of fluid-driven fracture in a rock mass. In this context, Papanastasiou [161] investigated the impact of plastic mechanisms in hydraulic fracture analyses. In his work, the rock was modeled by means of the Mohr-Coulomb plastic model to account for frictional dilatancy and 6-node isoparametric quadratic interface elements with zero-thickness were used to mimic the cohesive fracture behavior. Segura and

Carol [188, 189] developed a zero-thickness interface elements with double nodes for fluid flow and explore the performance and effect of both fully coupled and iteratively coupled formulations. Chen *et al.* [44] were able to reproduce the analytical responses of the toughness-dominated hydraulic regime for an impermeable medium with the aid of cohesive interface elements. The mentioned approach was also employed by Sarris and Papanastasious [185] to verify the influence of the cohesive zone in the hydro-fracking process. Carrier and Granet [39] also adopted zero-thickness elements to simulate the four asymptotic regimes (*i.e.*, storage-toughness; storage-viscosity, leak-off-toughness, leak-off-viscosity) associated with the two dissipation and two storage mechanisms. Their numerical results agree very well with the analytical ones in terms of crack opening displacement, injection pressure and crack length.

According to Needleman [141], there are two categories of cohesive interface formulations: (i) the intrinsic cohesive formulation and (ii) the extrinsic cohesive formulation. In the intrinsic formulation, interface elements are introduced between the regular elements of the mesh before the analysis, in the preprocess phase, which leads to an increase in the number of degrees of freedom. In addition, a large value must be assigned to the initial stiffness of the interface elements to ensure a rigid connection at the nodes. On the other hand, in the extrinsic formulation the cohesive elements are added when a certain damage criterion is satisfied [159]. This formulation requires complex schemes to change the topology of the mesh and insert adaptively the interface elements during the analysis. Both strategies require a significant computational effort, which is the main drawback associated with this approach. More details about the cohesive interface elements can be found elsewhere [141].

1.5 Elements with Embedded Discontinuity

Another possibility of reproducing cracks without the need of re-meshing techniques consists of enriching the finite elements with interpolate functions able to incorporate the strain or displacement discontinuities. This approach was pioneered by Ortiz *et al.* [155]. The geometry of the localized deformation (*i.e.*, shear band) and the onset of localization are determined by means of a bifurcation analysis based on the acoustic tensor and the combination of a pair of unit vectors that defines the discontinuity modes. From this information, shape functions that can capture the strain localization are added in the finite element formulation. Belytschko *et al.* [23] extended this idea by enriching the finite element with a band of localized strain, which reduces the element-size sensitivity.

These works influenced the development of elements embedded with strong displacement discontinuity [59, 106, 193, 152]. According to Simo *et al.* [193], strong discontinuities are associated with jumps in the displacement field, while weak discontinuities correspond to jumps in the strain field. In the strong discontinuity approach (SDA) introduced by Simo *et al.* [193] and further explored by Oliver [150] and by Armero and Garikipati [10], the displacement field is described by a continuous and discontinuous part, as well as the strain field. The Heaviside function and the dirac-delta dictate the strong discontinuity measure of the displacement and strain fields, respectively. In this case, bounded stresses are evaluated from unbounded strains by means of traditional plastic or continuum damage models exhibiting strain softening with a distributional character. In this context, Oliver *et al.* [151, 152] proposed a smooth transition from weak to strong discontinuity.

Armero *et al.* [9] applied the SDA to investigate discontinuities in saturated poro materials. The authors carried out 1-D analyses with the Mohr-Coulomb model to reproduce the dilatancy related to the discontinuity. In their formulation, the poro-pressure field remains continuous with discontinuous fluid flow across the discontinuity and the dilatancy is responsible for the localized fluid content. Foster *et al.* [64] incorporated two physical mechanisms, the slip weakening and frictional response, in the SDA framework to properly model discontinuities in rocks. The SDA has also been used to predict strong discontinuities in partially saturated poro-plastic materials *et al.* [36].

Although the crack can randomly progress over a fixed mesh in the SDA, the method still depends on tracking algorithms to determine the discontinuity path during the analysis. Elements with embedded discontinuity are one of the most common approaches in fracture mechanics nowadays. A literature review of this technique can be found in [95, 138].

1.6 Extended Finite Element Method

The extended finite element method (X-FEM) [22, 134, 133, 31], or generalized finite element method (G-FEM) [128, 53, 55], is another technique in which the discontinuity progresses through the finite element, and therefore, is mesh-independent. Inspired by the advance of meshless (or meshfree) methods [56, 57, 25], Belytschko and Black [22] proposed the use of the partition of unity method to enrich the interpolation functions. In this case, extra degrees of freedom were added at the nodes surrounding the discontinuity. Moes *et al.* [134] and Dolbow *et al.* [51] incorporated a general Heaviside enrichment for nodes away from the crack tip and introduced simple rules to enrich the nodes near the tip. Daux *et al.* [49] enhanced the technique in order to reproduce cracks with arbitrary branches. X-FEM has also been able to deal with three dimensional cracks [200], dynamic cracks [54], cohesive cracks [133, 135] and multiple crack growth [31].

This approach was extended to handle the hydraulic fracturing process in [112, 135, 208, 175]. Lecampion [112] compared the numerical results obtained via X-FEM with the analytical solutions and showed that it is essential to correct the loss of partition of unity in the transitional region between the enriched and regular parts of the mesh. Mohammadnejad and Khoei [135] used X-FEM with cohesive crack model to investigate the influence of viscosity, injection rate and permeability in the crack opening, injection pressure and fracture length. Wang [208] considered a mathematical framework based on X-FEM, cohesive zone model and Mohr-Coulomb plasticity theory to study the propagation of fluid-driven fractures in both brittle and ductile rocks. Remij *et al.* [175] introduced a X-FEM capable of capturing several phenomena, such as formation and propagation of fractures triggered by fluid pressure, natural fractures and the interaction between them.

Jirásek [96] reported the differences between the X-FEM and the SDA. Oliver [154] compared these two techniques in terms of computational performance and concluded that the X-FEM is in general more expensive than the SDA for both single crack and multiple cracks analyses. The literature review related to the X-FEM can be found in [100, 1, 24, 171].

1.7 Elements with High Aspect Ratio

Based on the continuum strong discontinuity approach, Manzoli *et al.* [127] showed that cohesive interfaces can be treated with solid finite elements with high aspect ratio (HAR) whose mechanical behavior is expressed by conventional continuum constitutive relations (between stress and strain) based on plasticity or damage theories.

Sánchez *et al.* [184] extended the applicability of HAR elements to model the 3-D crack network in drying soils. In their work, solid tetrahedral elements with high aspect ratio were introduced between the bulk elements of the original mesh (fragmentation process). Therefore, the crack evolves along the faces of the bulk elements. This method is called mesh fragmentation technique (MFT) and relies on the energy and continuum mechanics concepts to model the cohesive crack behavior. Maedo [121] and Manzoli *et al.* [124, 123] conducted a series of mesh sensitivity analyses to verify the MFT-objectivity. The comparison of their numerical results with the experimental ones indicates that the technique is mesh independent. They also studied the influence of the HAR element thickness in the load-displacement curve. They concluded that HAR elements with aspect ratio smaller than 1% does not affect the response. In his work, Maedo [121] also obtained preliminary results for hydraulic fracturing analyses. A complete study of this subject was carried out by Cleto [45]. This approach also has been used in biomedical sciences to analyze the behavior of dentin crack growth under various loading conditions [172].

This form of reproducing discontinuity does not require the use of any special element or tracking algorithm scheme. The traditional three-node triangular element available in any finite element code can be used to tackle the 2-D discontinuity, so that the failure process is described by constitutive models based on different fracture modes, such as sliding, opening or mixed modes. However, the softening law must take into account the thickness (*i.e.*, smaller dimension) of the HAR element to ensure the correct energy dissipation. For 3-D analyses, the discontinuity can be modeled by four-node tetrahedral elements with the same damage constitutive models previously mentioned for the 2-D cases. Therefore, the MFT only requires the implementation of a suitable constitutive model in a finite element program and a preprocess code to fragment the mesh. An obvious drawback of this technique is that the fragmentation process increases significantly the number of degrees of freedom and elements of the problem. One way to overcome this is to use adaptive coupling finite elements as in Rodrigues *et al.* [178].

1.8 Objectives

In the present dissertation we intend to model fractures in porous media by using the mesh fragmentation technique (MFT). The technique is very promising for THM modeling of problems involving discontinuities and it has been able to reproduce the behavior of crack formation in concrete structures. In the MFT, the phenomena of fracturing occurs entirely in the continuum mechanics context and it can be easily implemented in any commercial code.

The potential applications of the technique is countless. For example, we can model the behavior of hydraulic fracturing, which is a very common process in petroleum engineering to enhance gas and oil production. We can also use it to represent desiccation cracks in soils, which strongly affect the key properties and strength of soils. This may lead to compromise the integrity of civil infrastructure and building. As a last example, we can cite fractures that are induced in Enhanced Geothermal Systems. In this case, cold water is injected through a well in a hot dry reservoir with low permeability and hot/steam water is recovered from another well. The thermal shock due to the cold water leads to development of a crack network, which facilitates the heat extraction. Thus, based on the previous cited applications, the primary objectives of this work are:

- to gain a better understanding of the key properties and phenomena that control the formation and propagation of discontinuities in geo-materials;
- to develop and enhance constitutive models that captures these processes;
- to investigate the potential of the MFT for coupled multi-physics problems and its implementation in a finite element code.
- to validate and verify the proposed formulation;
- to apply the MFT to solve problems of practical interest.

It is worthwhile to mention that the use of solid finite elements with high aspect ratio to model the behavior of fractures and interfaces in porous media is a novel and remarkable technique, which can improve and transform our current understanding of fracture's behavior in geo-engineering.

1.9 Dissertation layout

This work is organized in 6 chapters, which are briefly described in the following paragraphs. Chapter 1 discusses the importance of studying discontinuities in geo-materials and presents the literature review related to the subject. It also introduces the objectives of this research.

Chapter 2 is devoted to the mathematical framework associated with the continuous formulation of transport phenomena in porous media. Thus, Chapter 2 describes the governing equations (*i.e.*, balance equations, constitutive relations, equilibrium restrictions, initial and boundary conditions) used to study THM processes in porous materials.

Chapter 3 focuses on an orthotropic damage model capable of emulate the orthotropic behavior between distinct materials. The main ingredients required to develop the constitutive models are presented. A drying test of a soil sample prepared in slab plates is modeled by using the presented technique and the crack patterns obtained from the numerical analyses are compared with the experimental ones. Afterwards, the orthotropic damage model is extended to model the soil curling behavior, which occurs due to the differential shrinkage. A set of numerical tests are performed to study the effect of the heterogeneity in the soil curling by using the MFT to capture the behavior of the soil samples during drying in both horizontal and vertical directions. An addition test with a bottom grooved surface is also carried out to show that the soil cracks when there is some restriction at the bottom interface between the soil and the container. All numerical results are compared with experimental ones and it is proved that the model is able to properly capture the curling phenomena when the soil is free to move, and it can reproduce the crack formation when the soil is restricted at the bottom.

In Chapter 4, the proposed technique is employed to model the formation and propagation of cracks in drying soils. The main components of the fully coupled hydro-mechanical formulation of the HAR finite elements are presented with special emphasis on the constitutive models and finite element equations. Three drying tests are simulated considering circular plates with different heights in order to study the development of desiccation cracks. Thus, the drying process is reproduced by imposing a suction gradient at the top of the soil specimen. The obtained crack patterns are compared against experimental tests to validate the proposed method. The soil crack network of an embankment flood is also explored by means of the MFT. The distance and depth of the cracks obtained via the MFT are compared with those observed in the field.

In Chapter 5, the modeling of the formation and propagation of discontinuities in rocks is investigated by using HAR finite elements. A critical component of the formulation is a mechanical model based on the damage theory that is able to properly reproduce the rock degradation observed during loading. The proposed approach is fully coupled and has been implemented in the finite element program CODE_BRIGHT, which was especially developed to tackle coupled thermo-hydro-mechanical problems in geological media. The chapter provides the main aspects related to THM processes and its implementations in the finite element code. It also discusses the main advantages and some shortcomings associated with it. Benchmarks found in the literature are used to verify the MFT capabilities of replicate thermo-hydro processes. The technique is also validated using available analytical solutions associated with the problem of hydraulic fracturing in rocks and it is also applied to solve engineering problems involving the formation and propagation of discontinuities in geomaterials. Finally, the cracks network observed in transparent samples due to temperature gradients are simulated via HAR finite elements and the numerical and experimental crack patters are compared with each other.

Chapter 6 summarizes the main conclusions achieved and presents suggestions for future work related to discontinuities in porous media.

2. COUPLED THERMO-HYDRO-MECHANICAL FORMULATION FOR CONTINUOUS POROUS MEDIA

2.1 Introduction

According to Bear [21], a porous medium is a heterogeneous or multiphase matter in which at least one of the phases is not solid. The non-solid phases are referred as void spaces (also called porous space) and they may be liquid and/or gas, while the skeleton (*i.e.*, solid particles) is usually called matrix. Soil, rocks, concrete, bones and even the human heart are some examples.

The applicability of fluid mechanics in porous medium is countless. In Geotechnical Engineering, the water flow must be considered in the design of earth structures such as embankment floods, retaining walls, tunnels and foundations in soils expansive and collapse soils. In Petroleum Engineering, the injection of fluids (*e.g.*, CO_2 and H_2O) at very high pressure is generally necessary to assist oil production from mature (conventional) reservoirs (porous medium). In Groundwater Hydrology and Agricultural Sciences, the movement of subsurface water is also usually dictated by porous medium concepts.

To study the transport phenomena in porous media, this work adopts the mathematical framework proposed by Olivella *et al.* [148], in which the governing equations are defined by assuming a three phase porous medium, as shown in Figure 2.1. As can be seen, the material is composed of three phases: solid (s), liquid (l) and gas (g); and three species: solid particles (s), water (w) and air (a). The liquid phase contains water and dissolved air, while the gas phase consists of dry air and water vapor. The porous medium is treated as a continuum material, and therefore, the discontinuities and void spaces due to the molecular structure of matter are ignored. Hence, all physical laws governing the problem are described by continuous equations, which can be classified into four main groups: (i) balance equations, (ii) constitutive relations, (iii) the equilibrium restrictions, and (iv) initial and boundary conditions. Such expressions are essential to consider coupled Thermo-Hydro-Mechanical processes in porous medium and they will be explained in detail in the next sessions.

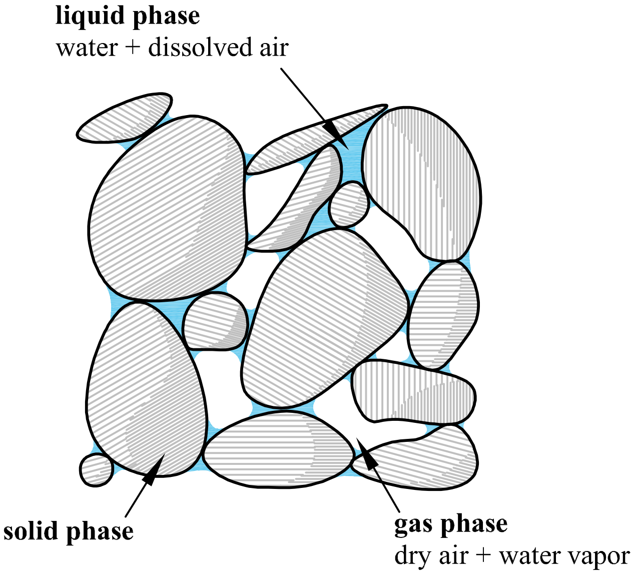

Figure 2.1: Porous medium (adapted from [182])

2.2 Balance Equations

The following theory adopts the compositional approach [158], in which the balance equations are expressed in terms of the species rather than the phase. Based on this approach, following four balance equations are admitted: (i) solid mass balance equation, (ii) water mass balance equation, (iii) internal energy balance equation and (iv) the balance of momentum (*i.e.*, equilibrium equation). The original work from Olivella [148] also assumed the air mass balance equation and the saline concentration in the medium. However, since in this work the gas pressure remains constant and the salt solution is not taken into account, these last two phenomena are neglected.

2.2.1 Solid Mass Balance Equation

Throughout the loading process, the medium may deform and assume a more compact configuration, which leads to a porosity reduction. On the other hand, porosity tends to increase when the body experiences expansion. Such porosity variations are computed by means of the solid mass balance equation given by:

$$\frac{\partial}{\partial t}[\rho_s(1-\phi)] + \boldsymbol{\nabla}\cdot\mathbf{j}_s = 0 \tag{2.1}$$

where ρ_s is the solid density, ϕ is the porosity of the medium, $\boldsymbol{\nabla}\cdot(\bullet)$ is the divergent operator of $(\bullet)$ and $\mathbf{j}_s$ is the flux of solid expressed as

$$\mathbf{j}_s = \rho_s(1-\phi)\dot{\mathbf{u}} \tag{2.2}$$

Substituting Eq. (2.2) into (2.1) gives

$$\frac{\partial}{\partial t}[\rho_s(1-\phi)] + \boldsymbol{\nabla}\cdot[\rho_s(1-\phi)\dot{\mathbf{u}}] = 0 \tag{2.3}$$

in which $\dot{\mathbf{u}}$ represents the velocity of the solid grains. Expanding the above yields:

$$(1-\phi)\frac{\partial\rho_s}{\partial t} - \rho_s\frac{\partial\phi}{\partial t} + \dot{\mathbf{u}}\cdot\boldsymbol{\nabla}(\rho_s)(1-\phi) - \dot{\mathbf{u}}\cdot\boldsymbol{\nabla}(\phi)\rho_s + [\rho_s(1-\phi)]\,\boldsymbol{\nabla}\cdot\dot{\mathbf{u}} = 0 \tag{2.4}$$

with $\boldsymbol{\nabla}(\bullet)$ denoting the gradient of $(\bullet)$.

The previous mass balance equation is given in terms of the spatial coordinates (*i.e.*, following the spatial description or Eulerian description). It is possible to determine the time rate of change of a property expressed in spatial description for a specific particle by means of the called material time derivative in spatial coordinates. Thus,

$$\frac{D}{Dt}(\bullet) = \frac{\partial}{\partial t}(\bullet) + \dot{\mathbf{u}}\cdot\boldsymbol{\nabla}(\bullet) \tag{2.5}$$

where the first term in the right hand side (RHS) is the local derivative (or spatial time derivative) and the second term is the convective derivative. Taking the material time derivative of Eq. (2.4) gives

$$(1-\phi)\underbrace{\left[\frac{\partial \rho_s}{\partial t}+\dot{\mathbf{u}}\cdot\boldsymbol{\nabla}(\rho_s)\right]}_{\frac{D\rho_s}{Dt}}-\rho_s\underbrace{\left[\frac{\partial \phi}{\partial t}+\dot{\mathbf{u}}\cdot\boldsymbol{\nabla}(\phi)\right]}_{\frac{D\phi}{Dt}}+\left[\rho_s(1-\phi)\right]\boldsymbol{\nabla}\cdot\mathbf{u}=0$$

$$\therefore\ \frac{D\phi}{Dt}=\frac{(1-\phi)}{\rho_s}\frac{D\rho_s}{Dt}+(1-\phi)\boldsymbol{\nabla}\cdot\mathbf{u} \tag{2.6}$$

The main variable associated with Eq. (2.6) is porosity. For the particular case of incompressible solid particles (*i.e.*, solid density remains constant), the previous equation reduces to: $(1-\phi)\boldsymbol{\nabla}\cdot\mathbf{u}$, which expresses the variation of porosity due to the volumetric deformation.

2.2.2 Water Mass Balance Equation

Water is found in both liquid and gaseous phases and its balance equation in the Eulerian description is expressed by three terms:

$$\underbrace{\frac{\partial}{\partial t}(\theta_l^w S_l\phi+\theta_g^w S_g\,\phi)}_{\text{storage variation of the mass of water}} \quad + \quad \underbrace{\boldsymbol{\nabla}\cdot(\mathbf{j}_l^w+\mathbf{j}_g^w)}_{\text{flows entering/leaving the body}} \quad = \quad \underbrace{f^w}_{\text{external supply of water}} \tag{2.7}$$

where S_l and S_g are the volumetric fraction of pore volume occupied by the liquid and gaseous phase, respectively. The notation follows the one adopted by Olivella [148], where superscript denotes specie and subscript the phase. Therefore, the volumetric mass of water in the liquid phase θ_l^w is the product of mass fraction of water, ω_l^w, and the liquid density, ρ_l, *i.e.* $\theta_l^w = \omega_l^w\ \rho_l$. Analogously, θ_g^w is the volumetric mass of water vapor. The total flows of mass of water in the liquid ($\mathbf{j}_l^w$) and gaseous ($\mathbf{j}_g^w$) phase can be decomposed into another three terms, as follows:

$$\mathbf{j}_l^w=\underbrace{\mathbf{i}_l^w+\omega_l^w\rho_l\mathbf{q}_l}_{\mathbf{j}_l'^w}+\theta_l^w S_l\phi\dot{\mathbf{u}}=\mathbf{j}_l'^w+\theta_l^w S_l\phi\dot{\mathbf{u}} \tag{2.8a}$$

$$\mathbf{j}_g^w=\underbrace{\mathbf{i}_g^w+\omega_g^w\rho_g\mathbf{q}_g}_{\mathbf{j}_g'^w}+\theta_g^w S_l\phi\dot{\mathbf{u}}=\mathbf{j}_g'^w+\theta_g^w S_g\phi\dot{\mathbf{u}} \tag{2.8b}$$

in which the first term on RHS represents the non-advective flux, the second one corresponds to the advective flux induced by fluid motion (governed by Darcy's law), and the third one is the advective flux due to the solid motion. After applying the material time derivative operator Eq. (2.5) to Eq. (2.7), the mass balance equation becomes:

$$\left[\frac{D}{Dt}(\theta_l^w S_l \phi + \theta_g^w S_g\, \phi) - \dot{\mathbf{u}} \cdot \boldsymbol{\nabla}(\theta_l^w S_l \phi + \theta_g^w S_g\, \phi)\right] + \boldsymbol{\nabla} \cdot (\mathbf{j}_l^w + \mathbf{j}_g^w) = f^w \tag{2.9}$$

Applying the divergence operator to Eq. (2.8) gives

$$\begin{aligned}\boldsymbol{\nabla} \cdot (\mathbf{j}_l^w + \mathbf{j}_g^w) &= \boldsymbol{\nabla} \cdot \left[(\mathbf{j}_l'^w + \theta_l^w S_l \phi \dot{\mathbf{u}}) + \left(\mathbf{j}_g'^w + \theta_g^w S_g \phi \dot{\mathbf{u}}\right)\right] \\ &= \boldsymbol{\nabla} \cdot (\mathbf{j}_l'^w + \mathbf{j}_g'^w) + \dot{\mathbf{u}} \cdot \boldsymbol{\nabla}(\theta_l^w S_l \phi + \theta_g^w S_g \phi) + (\theta_l^w S_l \phi + \theta_g^w S_g \phi)\, \boldsymbol{\nabla} \cdot \dot{\mathbf{u}}\end{aligned} \tag{2.10}$$

Substituting Eq. (2.10) into Eq. (2.9) gives, after rearranging the terms

$$\begin{aligned}\phi \frac{D}{Dt}(\theta_l^w S_l + \theta_g^w S_g) + \frac{D\phi}{Dt}(\theta_l^w S_l + \theta_g^w S_g) - \dot{\mathbf{u}} \cdot \boldsymbol{\nabla}(\theta_l^w S_l \phi + \theta_g^w S_g \phi) + \boldsymbol{\nabla} \cdot (\mathbf{j}_l'^w + \mathbf{j}_g'^w) \\ + \dot{\mathbf{u}} \cdot \boldsymbol{\nabla}(\theta_l^w S_l \phi + \theta_g^w S_g \phi) + (\theta_l^w S_l \phi + \theta_g^w S_g \phi) \boldsymbol{\nabla} \cdot \dot{\mathbf{u}} = f^w\end{aligned}$$

$$\begin{aligned}\therefore \phi \frac{D}{Dt}(\theta_l^w S_l + \theta_g^w S_g) + \frac{D\phi}{Dt}(\theta_l^w S_l + \theta_g^w S_g) + \boldsymbol{\nabla} \cdot (\mathbf{j}_l'^w + \mathbf{j}_g'^w) \\ + (\theta_l^w S_l \phi + \theta_g^w S_g \phi) \boldsymbol{\nabla} \cdot \dot{\mathbf{u}} = f^w\end{aligned} \tag{2.11}$$

Finally, substituting the solid mass balance equation Eq. (2.6) into Eq. (2.11) yields:

$$\begin{aligned}\phi \frac{D}{Dt}(\theta_l^w S_l + \theta_g^w S_g) + \frac{(1-\phi)}{\rho_s}\frac{D\rho_s}{Dt}(\theta_l^w S_l + \theta_g^w S_g) + (1-\phi) \boldsymbol{\nabla} \cdot \dot{\mathbf{u}}(\theta_l^w S_l + \theta_g^w S_g) \\ + \boldsymbol{\nabla} \cdot (\mathbf{j}_l'^w + \mathbf{j}_g'^w) + (\theta_l^w S_l \phi + \theta_g^w S_g \phi) \boldsymbol{\nabla} \cdot \dot{\mathbf{u}} = f^w\end{aligned} \tag{2.12}$$

and rearranging the terms

$$\phi \frac{D}{Dt}(\theta_l^w S_l + \theta_g^w S_g) + \left[\frac{(1-\phi)}{\rho_s}\frac{D\rho_s}{Dt} + \boldsymbol{\nabla} \cdot \dot{\mathbf{u}}\right](\theta_l^w S_l + \theta_g^w S_g) + \boldsymbol{\nabla} \cdot (\mathbf{j}_l'^w + \mathbf{j}_g'^w) = f^w \tag{2.13}$$

In Eq. (2.13), $\phi \frac{D}{Dt}(\theta_l^w S_l + \theta_g^w S_g)$ represents the variation in water storage due to variation in partial saturation; $\left[\frac{(1-\phi)}{\rho_s}\frac{D\rho_s}{Dt} + \boldsymbol{\nabla} \cdot \dot{\mathbf{u}}\right](\theta_l^w S_l + \theta_g^w S_g)$ gives the variation in water storage due to solid compressibility $\left(\frac{D\rho_s}{Dt}\right)$ and volume change of the porous medium skeleton $(\boldsymbol{\nabla}\cdot\dot{\mathbf{u}})$; the term $\boldsymbol{\nabla}\cdot(\mathbf{j}_l'^w+\mathbf{j}_g'^w)$ is associated with the fluxes of water (respect to the solid particles) in the liquid and gas phases entering/leaving the volume; the last term is related to the sink/source of water, as previously mentioned.

2.2.3 Internal Energy Balance Equation

The total energy of a medium, neglecting gravitational effects and electric current flowing through the body, is usually expressed by the sum of two terms: the mechanical work input and heat input. Heat is the energy transferred from a thermodynamic system to another by any mechanisms other than mechanical work. In engineering, energy transfer is usually categorized as follows: (i) thermal conduction, when the energy is conducted by the direct contact of particles of matter; (ii) fluid advection (and convection), which occurs due to mass motion; (iii) thermal radiation, when electromagnetic waves transfer the energy from one body to another.

When the liquid phase (l) and the composing species (*i.e.*, water and air) move, the energy attached to each of them is also transported. The advective fluxes of energy associated with the liquid phase ($\mathbf{j}_{El}$) can be calculated by multiplying the internal energy of the species times the total flux of the species in the liquid phase:

$$\mathbf{j}_{El}=E_l^w\,\mathbf{j}_l^w+E_l^a\,\mathbf{j}_l^a=\underbrace{E_l^w\,\mathbf{i}_l^w+E_l^a\,\mathbf{i}_l^a+E_l\,\rho_l\,\mathbf{q}_l}_{\mathbf{j}'_{El}}+E_l\,\rho_l\,S_l\,\phi\dot{\mathbf{u}}=\mathbf{j}'_{El}+E_l\,\rho_l\,S_l\,\phi\dot{\mathbf{u}} \tag{2.14}$$

with E_l^w and E_l^a representing the internal energies of water and air in the liquid phase, respectively. Similar expression can be obtained for the gas phase:

$$\mathbf{j}_{Eg}=E_g^w\,\mathbf{j}_g^w+E_g^a\,\mathbf{j}_g^a=\underbrace{E_g^w\,\mathbf{i}_g^w+E_g^a\,\mathbf{i}_g^a+E_g\,\rho_g\,\mathbf{q}_g}_{\mathbf{j}'_{Eg}}+E_g\,\rho_g\,S_g\,\phi\dot{\mathbf{u}}=\mathbf{j}'_{Eg}+E_g\,\rho_g\,S_g\,\phi\dot{\mathbf{u}} \tag{2.15}$$

where E_g^w and E_g^a are the internal energies of water and air in the gaseous phase. For the solid phase, the advective flux of energy can be obtained by pre-multiplying the solid mass $(\rho_s\,(1-\phi))$

by its velocity ($\dot{\mathbf{u}}$) and by post-multiplying by the internal energy (E_s):

$$\mathbf{j}_{Es} = E_s\,\rho_s\,(1-\phi)\dot{\mathbf{u}} \tag{2.16}$$

Assuming thermal equilibrium between the phases in the porous medium (*i.e.*, at a given material point in the porous medium the solid, liquid and gas phases are at the same temperature), and neglecting any contribution associated with the mechanical work input (which is common in non-isothermal systems), the internal energy balance equation is established taking into account the internal energy of each phase (E_s, E_l and E_g):

$$\frac{\partial}{\partial t}\left[E_s\,\rho_s(1-\phi) + E_l\,\rho_l\,S_l\,\phi + E_g\,\rho_g\,S_g\,\phi\right] + \boldsymbol{\nabla}\cdot(\mathbf{i}_c + \mathbf{j}_{Es} + \mathbf{j}_{El} + \mathbf{j}_{Eg}) = f^Q \tag{2.17}$$

where $\mathbf{i}_c$ is the heat conduction computed by using Fourier's law and f^E is an internal/external energy supply. Similarly to the water mass balance equation, the internal energy balance equation can be rewritten by applying the material time derivative operator and substituting Eqs. (2.14), (2.15) and (2.16) into Eq. (2.17), which yields

$$\begin{aligned}\phi\frac{D}{Dt}\left(E_l\,\rho_l\,S_l\; + E_g\,\rho_g\,S_g\right) + \left(E_l\,\rho_l\,S_l + E_g\,\rho_g\,S_g\right)\left[\frac{(1-\phi)}{\rho_s}\frac{D\rho_s}{Dt} + \boldsymbol{\nabla}\cdot\dot{\mathbf{u}}\right]&\\ + (1-\phi)\rho_s\frac{DE_s}{Dt} + \boldsymbol{\nabla}\cdot\left(\mathbf{i}_c + \mathbf{j}'_{El} + \mathbf{j}'_{Eg}\right) = f^Q&\end{aligned} \tag{2.18}$$

2.2.4 Equilibrium equation

In a rigid body, the deformation of the solid is so small that they are usually neglected and the problem can be modeled by assuming only the internal energy and the mass balance equations. However, for most problems, the deformation cannot be ignored. In this case, the mechanical behavior of the medium must be taken into account by means of the kinematics of deformable bodies and the momentum equation, which states that the sum of the forces acting in a medium is equal to the temporal rate of change of the total momentum [122]. However, since only quasi-static analyses were performed, the inertial terms are neglected, and consequently, the momentum equation becomes the following equilibrium equation:

$$\boldsymbol{\nabla} \cdot \boldsymbol{\sigma} + \mathbf{b} = \mathbf{0} \tag{2.19}$$

in which $\boldsymbol{\sigma}$ is the total stress tensor and $\mathbf{b}$ is the vector of body forces.

2.3 Initial and Boundary Conditions

For thermo-hydro-mechanical processes, the displacement ($\bar{\mathbf{u}}$), liquid pressure ($\bar{p}_l$) and temperature ($\bar{T}$) fields prescribed at the boundary Γ_u, Γ_{p_l} and Γ_T, respectively, define the essential boundary conditions, while the prescribed traction ($\bar{\mathbf{t}}$), water flow ($\bar{j}'^w$) and heat flow ($\bar{j}'_E$) prescribed at Γ_σ, Γ_{j^w}, and Γ_{j_E}, respectively, comprises the natural boundary conditions. In other words,

$$\begin{aligned}
&\mathbf{u}(\mathbf{X},t) = \bar{\mathbf{u}}(t) && \forall \mathbf{X} \in \Gamma_u,\\
&p_l(\mathbf{X},t) = \bar{p}_l(t) && \forall \mathbf{X} \in \Gamma_{p_l},\\
&T(\mathbf{X},t) = \bar{T}(t) && \forall \mathbf{X} \in \Gamma_T,\\
&\boldsymbol{\sigma}(\mathbf{X},t) \cdot \mathbf{n}_\Gamma = \bar{\mathbf{t}}(t) && \forall \mathbf{X} \in \Gamma_\sigma,\\
&\mathbf{j}'^w(\mathbf{X},t) \cdot \mathbf{n}_\Gamma = \bar{j}'^w(t) && \forall \mathbf{X} \in \Gamma_{j^w},\\
&\mathbf{j}'_E(\mathbf{X},t) \cdot \mathbf{n}_\Gamma = \bar{j}'_E(t) && \forall \mathbf{X} \in \Gamma_{j_E},
\end{aligned} \tag{2.20}$$

where $\mathbf{j}'^w = (\mathbf{j}'^w_l + \mathbf{j}'^w_g)$ is the total flow of water mass and $\mathbf{j}'_E = (\mathbf{i}_c + \mathbf{j}'_{El} + \mathbf{j}'_{Eg})$ is the total heat flux. The initial conditions are written in terms of displacement field, liquid pressure and temperature as

$$\mathbf{u}(\mathbf{X}, t=0) = \mathbf{u}_0, \;\; p_l(\mathbf{X}, t=0) = (p_l)_0, \;\; T(\mathbf{X}, t=0) = T_0 \tag{2.21}$$

In Eqs. (2.20) and (2.21), $\mathbf{X}$ stands for the material point, t is the time and $\mathbf{n}_\Gamma$ is the unit outward vector normal to the boundary Γ

2.4 Constitutive Equations

Following, the constitutive equations adopted to reproduce the thermo-hydro-mechanical behavior of geo-materials (*bulk elements*) are presented. Note that the constitutive relations describing the discontinuity behavior is explained in the other parts of this dissertation, since this chapter only gives an overview of the main phenomena associated with the modeling of continuous geo-materials.

2.4.1 Hydraulic Constitutive Equations

Fluid flow in saturated porous media is mathematically modeled by means of the mass balance equations and Darcy's law, which establishes the relation between the fluid flow and the pressure field for a Newtonian viscous fluid in a laminar flow as follows:

$$\mathbf{q}_\alpha = -\mathbf{K}_\alpha \cdot \boldsymbol{\nabla} h \tag{2.22}$$

where $\mathbf{K}_\alpha$ is the hydraulic conductivity tensor and h is the total head described by the Bernoulli's theorem as:

$$h = \frac{p_\alpha}{\rho_\alpha\, g} + z = \frac{1}{\rho_\alpha\, g}(p_\alpha + \rho_\alpha\, g\, z) \tag{2.23}$$

with g denoting the acceleration due to gravity. Note that the kinetic term is neglected, since the seepage velocities are usually small in porous media. The hydraulic gradient is defined by:

$$\boldsymbol{\nabla} h = \boldsymbol{\nabla}\left[\frac{1}{\rho_\alpha\, g}(p_\alpha + \rho_\alpha\, g\, z)\right] = \frac{1}{\rho_\alpha\, g}\left[\boldsymbol{\nabla} p_\alpha + \boldsymbol{\nabla}(\rho_\alpha\, g\, z)\right] = \frac{1}{\rho_\alpha\, g}(\boldsymbol{\nabla} p_\alpha - \rho_\alpha\, \mathbf{g}) \tag{2.24}$$

in which $\boldsymbol{\nabla} p_\alpha$ is the gradient the fluid pressure of the phase α. The hydraulic conductivity tensor in Eq. (2.22) is:

$$\mathbf{K}_\alpha = \mathbf{k}\frac{k_{r\alpha}}{\mu_\alpha}\rho_\alpha\, g \tag{2.25}$$

where μ_α is the dynamic viscosity of the fluid α, $\mathbf{k}$ is the intrinsic permeability tensor and $k_{r\alpha}$ is the relative permeability. The intrinsic permeability depends only on the properties of the solid skeleton and it is expressed by a tensor, in which the components vary with the direction (*i.e.*, if the material is isotropic or anisotropic) and uniformity (*i.e.*, if the medium is homogeneous or heterogeneous) of the material.

Substituting Eqs. (2.25) and (2.24) into Eq. (2.22) gives

$$\mathbf{q}_\alpha = -\mathbf{k}\frac{k_{r\alpha}}{\mu_\alpha}\left[\boldsymbol{\nabla} p_\alpha - \rho_\alpha \mathbf{g}\right] \tag{2.26}$$

Note that the previous equation can be used for both the gaseous and the liquid phases.

However, in unsaturated materials, as the case of drying soils, the gaseous phase also must be considered in the process and the analysis becomes much more complex. Since the inner gas remains in equilibrium with the outer atmosphere during the analysis, the gas pressure (p_g) is maintained constant and equals to the atmospheric pressure [47]. Note that the constitutive equations involving the gaseous phase are needed for the computation of the variables associated with the water vapor. Thus, the molecular diffusion of the vapor in the gaseous phase and dissolved air in the liquid phase are modeled by Fick's law, which states:

$$\mathbf{i}^i_\alpha = -\mathbf{D}^i_\alpha \, \boldsymbol{\nabla}\omega^i_\alpha \tag{2.27}$$

in which $\alpha = l, g$ and $i = a, w$ depends on if diffusion occurs in the liquid (dissolved air) or in the gaseous phase (water vapor); $\mathbf{D}^i_\alpha$ is the dispersion tensor expressed by:

$$\mathbf{D}^i_\alpha = \underbrace{\rho_\alpha S_\alpha \phi \tau D^i_{\mathrm{m}} \mathbf{I}}_{\text{Molecular diffusion}} + \underbrace{\rho_\alpha \mathbf{D}'_\alpha}_{\text{Mechanical dispersion}} \tag{2.28}$$

where τ is a tortuosity parameter, D^i_{m} is the coefficient associated with the molecular diffusion of the specie i, $\mathbf{D}'_\alpha$ is the mechanical dispersion tensor of the phase α. The term that corresponds to the mechanical dispersion dominates at high velocities, while the molecular diffusion dominates in the case at low velocities.

Finally, the retention curve proposed by van Genuchten [205] was employed to relate degree of saturation (S_l) with suction (ψ):

$$S_l = \left[1 + \left(\frac{\psi}{P_o}\right)^{\frac{1}{1-\lambda_l}}\right]^{-\lambda_l} \tag{2.29}$$

where P_o is the pore air entry value and λ_l is the pore size distribution parameter

2.4.2 Phase properties

As reported by Lewis and Schrefler [114], the material time derivative of the solid density can be written as a function of the pressure, temperature and mean effective stresses, as follows:

$$\frac{1}{\rho_s}\frac{D\rho_s}{Dt} = \frac{\dot{p}_s}{K_s} - \alpha_T\dot{T} - \frac{\dot{\sigma}'_m}{K_s(1-\phi)} \tag{2.30}$$

where K_s is the intrinsic modulus of the solid particles, α_T is the linear thermal expansion coefficient for the grains and $\dot{\sigma}'_m$ is the derivative of the effective means stress with respect to time expressed as

$$\dot{\sigma}'_m = K\left(\boldsymbol{\nabla}\cdot\dot{\mathbf{u}} + \frac{\dot{p}_s}{K_s} - \alpha_T\dot{T}\right) \tag{2.31}$$

in which K is the bulk modulus of the dry porous material and p_s is the pressure in the solid phase defined as:

$$p_s = S_l\, p_l + S_g\, p_g \tag{2.32}$$

Substituting Eq. (2.31) into (2.30) and rearranging the terms gives

$$\frac{1}{\rho_s}\frac{D\rho_s}{Dt} = \frac{1}{(1-\phi)}\left[\frac{(b-\phi)}{K_s}\dot{p}_s - (b-\phi)\alpha_T\dot{T} - (1-b)\boldsymbol{\nabla}\cdot\dot{\mathbf{u}}\right] \tag{2.33}$$

where b is the Biot's parameter [27] defined by

$$b = 1 - \frac{K}{K_s} \tag{2.34}$$

For incompressible solid particles $K_s \to \infty$, and consequently, $b = 1$. It is worthwhile to mention that the porous material in this case cannot be treated as a rigid body because the medium may deform due to porosity changes.

2.4.3 Thermal Constitutive Equations

The thermal conduction concept was first introduced by Joseph Fourier, who established the following relation between the heat flux and the temperature gradient:

$$\mathbf{i}_c = -\lambda\, \boldsymbol{\nabla} T \tag{2.35}$$

where λ is the thermal conductivity of the material. In general, the thermal properties of the geomaterials are the same in all directions, which means that the medium exhibits a thermal isotropic behavior.

The heat capacity, on the other hand, is a physical entity that characterizes the heat required to change the temperature of a body and is defined by the following differential expression:

$$C = \frac{\mathrm{d}Q}{\mathrm{d}T} \tag{2.36}$$

where T is the temperature and Q is the heat added to the system.

Note that the heat capacity is an extensive property, and therefore, its value is proportional to the mass of the body. However, it is convenient to express this phenomenon as a property that does not depend on the amount of matter in the system (*i.e.*, as an intensive property). The specific heat capacity (c), which is an intensive quantity, is obtained by dividing the heat capacity of the body by its mass and it is usually defined at constant pressure or constant volume, since it is path dependent. In the International System of Units, the heat capacity is expressed in Joules (J) per Kelvin (K), while the unit of specific heat is Joules per Kelvin per kilogram ($\mathrm{J}/(\mathrm{kg\,K})$).

Although the specific heat capacity should be specified at constant volume because Eq. 2.18 is described in terms of internal energy, this work assumes heat capacity at constant pressure, which it is easier to measure for solids and liquids [68]. The difference is usually negligible for these two phases. For gases, the following relation is used:

$$c_{g,p} - c_{g,v} = R \tag{2.37}$$

in which c_p and c_v are the heat capacities of the gas at constant pressure and constant volume, respectively, and R is the universal gas constant.

Finally, the specific internal energy 'E' for a given specie is computed based on the specific heat 'c' at constant pressure. Thus, the specific heat of the solid, liquid and gases phase are given by

$$E_s = c_s T \tag{2.38a}$$

$$E_l = (c_l^w \omega_l^w + c_l^a \omega_l^a) T \tag{2.38b}$$

$$E_g = (c_g^w T + l)\omega_g^w + c_g^a \omega_g^a T \tag{2.38c}$$

with l denoting the specific latent heat of the evaporation/condensation.

2.4.4 Mechanical Constitutive Model

2.4.4.1 Mechanical Model for Unsaturated Soils

In unsaturated soils, the mechanical behavior of the material can be described by following the concepts of (i) effective stress or (ii) two state variables. The former was originally proposed by Bishop [28] and it expresses the effective stress in terms of suction and total stress. Some authors have also considered the presence of degree of saturation in the formulation [76, 111, 47] . The use of two state variables was presented by Fredlund and Morgenstern [65]. In their work, they concluded that the stress state in an unsaturated soil can be represented by the combinations of two state variables involving liquid pressure (p_l), total stress (σ) and gas pressure (p_g). In this work, the net stress:

$$\sigma' = \sigma - \mathbf{I} p_g \tag{2.39}$$

and the matric suction (also known as capillary pressure):

$$\psi = p_g - p_l \tag{2.40}$$

were used to model the soil behavior, in which **I** is the second order unit tensor.

The relationship between stress and strain can be described by constitutive models that have been developed to tackle the soil mechanical behavior. Mohr-Coulomb, modified von Mises, and Cam Clay model are some examples. However, to simulate the behavior of unsaturated soils, it is necessary to choose a model that is capable of taking into account the effect of the matric suction, ψ, and mean stress, σ'_m, in the volumetric deformation. In this work, the elastic part of the Barcelona Basic Model presented by Allonso *et al.* [6] was used to mimic the shrinkage process of the soil. According to this model, the elastic volumetric deformation of the porous medium is given by:

$$\mathrm{d}\epsilon_v^e = \frac{\mathrm{d}\sigma'_m}{K} + \frac{\mathrm{d}\psi}{K_\psi} - \frac{\mathrm{d}T}{K_T} \tag{2.41}$$

where K, K_ψ and K_T are

$$K = \frac{(1+e)\,\sigma'_m}{\kappa_i}; \qquad K_\psi = \frac{(1+e)(\psi + p_{\text{atm}})}{\kappa_\psi}; \qquad K_T = \frac{1}{\alpha_0 + 2\alpha_2 \Delta T} \tag{2.42}$$

in which α_0 and α_2 are thermo-mechanical properties, e denotes void ratio, p_{atm} is the atmospheric pressure, κ_i and κ_ψ are the slopes of the unloading-reloading and wetting-drying curves, respectively, defined by

$$\begin{aligned} \kappa_i(\psi) &= \kappa_{io}(1 + \alpha_i \psi) \\ \kappa_\psi(p', \psi) &= \kappa_{\psi o}\left[1 + \alpha_{\psi p} \ln\left(\frac{\sigma'_m}{p_{\text{ref}}}\right)\right] \exp(\alpha_\psi \psi) \end{aligned} \tag{2.43}$$

where κ_{io} is the virgin elastic slope of the $e - \ln(\sigma'_m)$ line, $\kappa_{\psi o}$ is the initial elastic slope of the $e - \ln(\psi)$ diagram, α_ψ and $\alpha_{\psi p}$ are material properties controlling the evolution of κ_ψ, and α_i governs the change of κ_i with matric suction.

2.4.4.2 Mechanical Model for Rock

According to the Bishop [28], in a partially saturated deformable porous material, the effective stress tensor can be expressed as follows:

$$\boldsymbol{\sigma}' = \boldsymbol{\sigma} - \mathbf{I}\,[p_g - \chi\,\psi] \tag{2.44}$$

in which χ is a weighting parameter related to the area fractions between solid and fluids. Bishop suggested the use of $\chi = S_l$ and Lewis and Schrefler [114] incorporated the Biot's coefficient into the previous equation. Hence, a more general equation can be written as [114]

$$\boldsymbol{\sigma}' = \boldsymbol{\sigma} - \mathbf{I}\,b\,\underbrace{(S_l\,p_l + S_g\,p_g)}_{p_s} \tag{2.45}$$

In this work, all analyses were carried out in the context of small strain theory, and therefore, the deformations are defined by the infinitesimal strain tensor $\boldsymbol{\epsilon}$ expressed by

$$\dot{\boldsymbol{\epsilon}} = \dot{\boldsymbol{\epsilon}}^e + \dot{\boldsymbol{\epsilon}}^o = \mathbb{C}^{-1}\dot{\boldsymbol{\sigma}}' - \frac{\dot{p}_s}{K_s}\mathbf{I} + \dot{T}\,\beta\,\mathbf{I} \tag{2.46}$$

where $\dot{\boldsymbol{\epsilon}}^e$ is the elastic strain rate, $\dot{\boldsymbol{\epsilon}}^o$ is deformation caused by temperature and pore-pressure changes and $\mathbb{C}$ is the elastic tensor. Rearranging the above equation yields:

$$\dot{\boldsymbol{\sigma}}' = \mathbb{C} : \underbrace{(\dot{\boldsymbol{\epsilon}} - \dot{\boldsymbol{\epsilon}}^o)}_{\dot{\boldsymbol{\epsilon}}^e} = \mathbb{C} : \dot{\boldsymbol{\epsilon}} + \left[\mathbb{C} : \mathbf{I}\left(\frac{\dot{p}_s}{K_s}\right) - \mathbb{C} : \mathbf{I}\,(\dot{T}\,\beta)\right] \tag{2.47}$$

2.5 Equilibrium Restrictions

The term equilibrium restriction in general corresponds to the relation between the species concentration in the phases and the state variables. In this work, phase changes are treated as instantaneous processes, since the time associated with phase changes is much smaller than the time of typical problems in porous media. Following, the necessary laws to determine the volumetric masses and mass fractions are described.

2.5.1 Henry's Law

According to Henry's law, the quantity of dissolved air in the liquid is:

$$H = \frac{p_a}{x} \tag{2.48}$$

in which H is Henry's constant, p_a is the partial pressure of the air and x is the molar fraction given by:

$$x = c_a \frac{M_w}{\rho_l} \tag{2.49}$$

where M_w is the molar mass of water and c_a is the concentration of the dissolved air in the liquid phase defined by:

$$\omega_l^a = c_a \frac{M_a}{\rho_l} \Rightarrow c_a = \frac{\omega_l^a \, \rho_l}{M_a} \tag{2.50}$$

with M_a denoting the molar mass of air. Substituting Eqs. (2.50) and (2.49) into (2.48) and rearranging the terms gives:

$$\omega_l^a = \frac{p_a}{H} \frac{M_a}{M_w} \tag{2.51}$$

Therefore, the volumetric mass of air in the liquid phase can be computed as follows:

$$\theta_l^a = \omega_l^a \, \rho_l = \frac{p_a}{H} \frac{M_a}{M_w} \rho_l \tag{2.52}$$

2.5.2 Psychrometric Law (Kelvin's Equation)

Kelvin's law dictates the variation of vapor pressure due to the meniscus (*i.e.*, a curved vapor-liquid interface) and it is deduced by admitting a recipe where air and water are in equilibrium. A tube of radius r is inserted in the recipe, leading the fluid in the tube to move up to a height h, called capillary rise and defined as:

$$h = \frac{\psi}{\rho_l\, g} \tag{2.53}$$

In the system previously described, the variation of vapor pressure, $\mathrm{d}p_v$, in a differential height, $\mathrm{d}y$, can be expressed by:

$$\mathrm{d}p_v = -\rho_v\, g\, \mathrm{d}y \tag{2.54}$$

However, ρ_v depends on the pressure in accordance with the ideal gas law:

$$\rho_v = p_v \frac{M_w}{R\,T} \tag{2.55}$$

Substituting Eq. (2.55) into (2.54), one can write:

$$\mathrm{d}y = -\frac{1}{\rho_v\, g}\mathrm{d}p_v = -\frac{R\,T}{p_v\, M_w\, g}\mathrm{d}p_v \tag{2.56}$$

Integrating over the domain (o, h) or (p_v^o, p_v^A):

$$h = \int_0^h \mathrm{d}y = -\frac{R\,T}{M_w\, g}\int_{p_v^o}^{p_v^A} \frac{\mathrm{d}p_v}{p_v} = -\frac{R\,T}{M_w\, g} \ln\left(\frac{p_v^A}{p_v^o}\right) \tag{2.57}$$

Equating Eqs. (2.57) and (2.53):

$$p_v^A = p_v^o \exp\left(-\frac{\psi\, M_w}{R\,T\,\rho_l}\right) \tag{2.58}$$

The ratio (p_v^A/p_v^o) is called relative humidity and the equation

$$\mathrm{RH} = \frac{p_v^A}{p_v^o} = \frac{\theta_g^w}{(\theta_g^w)^o} = \exp\left(-\frac{\psi\, M_w}{R\,T\,\rho_l}\right) \tag{2.59}$$

expresses the ratio of water vapor in the gas phase in a given moment and the maximum amount of water that the air could contain. For a temperature in ^{o}C:

$$\theta_g^w = (\theta_g^w)^o \exp\left[-\frac{p_c M_w}{R(273.15+T)\rho_l}\right] \tag{2.60}$$

Note that volumetric mass fraction of water vapor changes with both suction and temperature.

2.5.3 Mass Fractions of Water in the Liquid Phase and Air in the Gaseous Phases

The density of humid air can be approximated by assuming a mixture of ideal gases. In this case, the gas density is computed as the sum of densities of dry air and water vapor:

$$\rho_g = \rho_v + \rho_a \tag{2.61}$$

where ρ_v and ρ_a are the densities of water vapor and dry air, respectively. The mass fractions of these two entities are:

$$\omega_g^w = \frac{m_v}{m_g} = \frac{\rho_v}{\rho_g} \tag{2.62a}$$

$$\omega_g^a = \frac{m_a}{m_g} = \frac{\rho_a}{\rho_g} \tag{2.62b}$$

Dividing both sides of Eq. (2.61) by ρ_g, and then inserting Eqs. (2.62a) and (2.62b) into (2.61) yields:

$$\omega_g^a + \omega_g^w = 1 \tag{2.63}$$

Consequently, it is possible to evaluate the mass fraction of air in the gaseous phase once the water vapor is known (see Psychrometric law)

Similar expression can be obtained for the liquid phase by considering the fractions of both species in the liquid phase, *i.e.*:

$$\omega_l^a + \omega_l^w = 1 \tag{2.64}$$

Analogously, once dissolved air have been obtained by means of Henry's equation, the mass fraction of liquid water can be determined by the above equation.

3. MODELING DESICCATION PROCESSES IN SOILS INVOLVING DISCONTINUITIES

3.1 Introduction

The formation and propagation of desiccation cracks of soils is a very complex phenomenon that involves hydro-mechanical processes. The soil desaturates from the fully saturated condition to close to fully dried as the matric suction overcomes the pore-air entry value and breaks the continuum air-liquid interface. Water is evaporated from the soil in order to find the equilibrium between the liquid and gaseous phases. The desaturation process leads the soil to shrink and induces the development of desiccation cracks, which impacts negatively on the soil properties. Drying cracks affect clay liners by creating preferential path for contaminant transport that pollutes the surrounding soils and groundwater. In addition, cracks alter the irrigation system in the case of agricultural applications and facilitate the transport of fertilizers and pesticides to the roots [129]. In drought periods, deep vertical cracks increase the hydraulic conductivity of the soil and jeopardize infrastructures, such as the foundations. Erosion also contributes to the development of drying cracks. In the case of embankments, the increase in infiltration caused by the presence of cracks may trigger failures and landslides. Moreover, the climate changes may exacerbate the problem and increase the risk of structural collapse.

Since the pioneering work of Kindle [103], who studied the influence of the soil composition, desiccation velocity, and degree of salinity in the mud-cracks, many experimental researches have been conducted to address the crack formation and propagation in soils. The main focus of these works is to study the effect of different factors (*e.g.*, initial conditions, soil-container interface, geometry, boundary conditions, sample thickness and soil texture) on the crack pattern in a controlled environment [179, 166]. Corte and Higashi's work [46] is particularly noteworthy because it showed that the morphology of the crack network depends more on the thickness of the soil sample and soil-container interface than on temperature or humidity. It is worthwhile to mention that field test experiments have also been performed to monitor the evolution of cracks under natural conditions [109, 60].

In the last few years, experimental studies have investigated the influence of geotextile and salt concentration in the crack path. Safari *et al.* [180] conducted two sets of tests in which three compacted clay liners were exposed to atmospheric conditions for one year. In the first one, the sample was exposed to open air and the second covered with white geotextile. The authors monitored the cracks by using a digital image technique. Their results indicated the geotextile reduced the crack intensity factor by 37.4 – 45.9%. He *et al.* [86] reported that desiccation cracks have more impact on hydraulic conductivity of compacted clays than leachates. Shokri *et al.* [191] evaluated the impact of salt concentration in the crack pattern of mixtures of bentonite and NaCl solutions. According to the authors, higher salt concentrations led to larger crack lengths caused by the effects of NaCl on colloidal interactions among particles. Song *et al.* [198] conducted an evaporation test on compacted clay in a large-scale environmental chamber under controlled atmospheric conditions and desiccation cracks were monitored along other soil responses. Varsei *et al.* [206] developed an apparatus to determine the soil tensile strength under drying conditions. In order to improve the crack resistance of expansive clays, Chaduvula *et al.* [42] studied the effect of polyester fiber reinforcement on desiccation cracking. The techniques used to monitor the crack development have also been enhanced. Ground-penetration-radar (GPR) system [113], X-ray computed tomography (XCT) scanning device [98] and the electric resistivity method [201] have been employed to characterize the crack morphology.

In the context of numerical modeling, the first efforts conducted to model the problem of desiccation cracks in soils were based on concepts of Linear Elastic Fracture Mechanics (LEFM) theory [137, 108]. In this case, the nonlinear zone associated with the fracture must be small compared to the body [20]. In practice, the applicability of LEFM is limited to very brittle materials and can be treated as a special case of quasi-brittle solids. Recently, different techniques have been proposed to tackle the problem from the continuum mechanics perspective, such as the discrete element method [192], distinct lattice spring model (DLSM) with two-phase bond mode (*i.e.*, spring and water bonds [78]), and hybrid continuum-discrete element model (*i.e.*, Unified Distinct

Element Code (UDEC)) [80]. The UDEC was also used with Voronoi tessellation to analyze the field soil desiccation behavior. Another approaches consist of using finite elements with zero thickness [207] or the finite difference method with two-phase flow [199] to mimic the hydro-mechanical behavior of cracks in drying soils.

In this work, the mesh fragmentation technique (MFT), in which solid finite elements with high aspect ratio (FE-HAR) are inserted between the regular (bulk) elements of the mesh, is used. This technique was successfully employed in quasi-brittle materials [123], such as concrete, and it has shown promising results. The MFT was initially proposed by Sanchez *et al.* [184] to study the mechanics of discontinuities in drying soils. They imposed volumetric strains by means of the constitutive model and analyzed the crack morphology. However, they did not consider the processes associated with the hydraulic properties of the material (*i.e.*, permeability, porosity, diffusion, dispersion, and retention curve), and therefore, their work was not able to capture the hydraulic responses, such as water loss, liquid saturation and matric suction. This work presents an extension of the research conducted by Sanchez *et al.* [184], so that FE-HAR are used to treat the problem of desiccation cracks in soils by assuming a fully coupled hydro-mechanical (HM) formulation. This paper is organized as follows: first, the complete hydro-mechanical mathematical framework is explained in detail; then, the MFT is presented; forward, the numerical results are compared with the experimental ones and finally, the conclusions obtained from the analyses are described.

3.2 Numerical Framework

The starting point of the proposed framework is the finite element program CODE_BRIGHT [149]. This computer code was developed to tackle coupled Themo-Hydro-Mechanical (THM) problems in porous media. The coupled formulation expresses mathematically the main THM phenomena and their mutual interactions in terms of: 1) momentum, mass and energy balance equations; 2) constitutive equations; and 3) equilibrium restrictions. The following main phenomena are considered: water flow (*e.g.*: liquid phase advection, water vapor diffusion, etc.), air flow (*e.g.*: gas phase, air solution in water, dissolved air diffusion, etc.), energy transfer (*e.g.*:

conduction, convection, etc.), elastoplastic mechanical behavior of soil including the influence of load history, suction, and temperature changes on stress-strain relationship. Equilibrium restrictions accounts for the amount of water vapor in gas phase in terms of pressure and temperature, as well as for the amount of dissolve air in water depending on the partial pressure of the air. This formulation has been widely validated and applied to solve different coupled THM problems in geological media [149, 163, 183]. The governing equations related to this approach are shown in the appendix.

CODE_BRIGHT was not developed originally to deal with the presence of discontinues in porous media. In this work, an extension of this code to deal with the formation and propagation of drying cracks is used to simulate two problems: (1) the shrinkage behavior of a soil specimen subjected to drying in a circular plate, and (2) fractures in geothermal reservoirs. The MFT was implemented in CODE_BRIGHT, following the ideas presented in Sanchez *et al.* [184]. By using this technique it is possible to include explicitly the formation and propagation of fractures and cracks in the numerical analysis. CODE_BRIGHT uses GiD (http://gid.cimne.upc.es), gmsh [71] or ParaView [14, 4] to generate the mesh and to prepare all the information required for a finite element simulation. The permeability of the joint elements can be computed in terms of the crack aperture (or width) by means of the well-known cubic law. As for the mechanical behavior, three different types of constitutive models have been adopted in the analysis, each one associated with a specific type of element. The behavior of the regular elements of the mesh (*i.e.*, the bulk elements) has been described by means of the Barcelona Basic Model (BBM), while the tensile damage model and the J2 damage model have been used to reproduce the behavior of the interface elements between the bulk elements and the interface elements at the soil-plate contact, in the case of the desiccation test, respectively. In the following sections, we will explain the mesh fragmentation technique and show that the kinematics of solid finite elements tends to the Continuum Strong Discontinuity Approach (CSDA), as the aspect ratio of the element increases. The constitutive models adopted to reproduce the behavior of interface elements and bulk elements are presented as well.

3.3 Modeling the Fracture Behavior

Consider a porous medium with a subdomain Ω^h as shown in Figure 3.1. The subdomain Ω^h consists of a narrow band of width h bounded by the surfaces S^+ and S^-. The displacement field for every material point in the domain can be expressed:

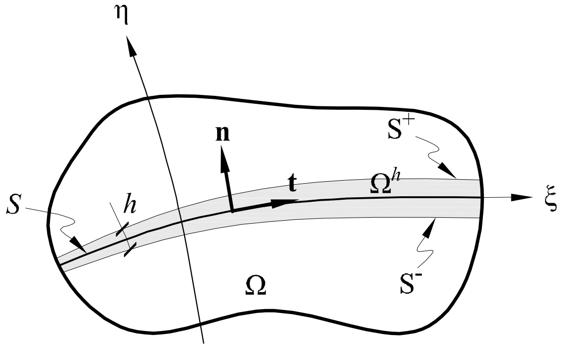

Figure 3.1: Schematic representation of a body containing a subdomain Ω^h, which converges to a discontinuity surface S when $h \to 0$ (modified from[126])

$$\mathbf{u} = \tilde{\mathbf{u}} + Z_S[\![\mathbf{u}]\!] \tag{3.1}$$

where $[\![\mathbf{u}]\!] = \mathbf{u}_{S^+} - \mathbf{u}_{S^-}$ and $Z_s(\eta)$ is a ramp function defined by:

$$Z_S(\eta) = \begin{cases} 0, & \text{if} \quad \eta < -\frac{h}{2} \\ 1, & \text{if} \quad \eta > \frac{h}{2} \\ \frac{\eta}{h} + \frac{1}{2}, & \text{if} \quad -\frac{h}{2} < \eta < \frac{h}{2} \end{cases} \tag{3.2}$$

In the limit situation where h tends to zero, the narrow band Ω^h becomes a discontinuity surface S. In this case, the displacement field can be written as

$$\mathbf{u} = \tilde{\mathbf{u}} + H_S[\![\mathbf{u}]\!] \tag{3.3}$$

where H_S is the Heaviside function localized at the surface S and $\llbracket \mathbf{u} \rrbracket$ becomes the measure of displacement discontinuity. Eq. (3.3) corresponds to the displacement field of the strong discontinuity regime, which can be interpreted as the limit situation of the weak discontinuity regime given by Eq. (3.1). Hence, in the weak discontinuity regime, the strain field is expressed as:

$$\boldsymbol{\epsilon} = \tilde{\boldsymbol{\epsilon}} + \frac{\zeta_S(\eta)}{h}(\mathbf{n} \otimes \llbracket \mathbf{u} \rrbracket)^S \tag{3.4}$$

in which $\mathbf{n}$ is the unit vector normal to S, $\tilde{\boldsymbol{\epsilon}}$ represents the continuous part of the strain field and ζ_S is the collocation function on the strain localization band given by:

$$\zeta(\eta) = \begin{cases} 1, & \text{if} \quad < -h/2\eta < h/2 \\ 0, & \text{if} \quad \eta < -h/2 \text{ or } \eta > h/2 \end{cases} \tag{3.5}$$

As shown by Manzoli *et al.* [126], the volumetric strain is determined by the following expression:

$$\boldsymbol{\nabla} \cdot \mathbf{u} = \boldsymbol{\nabla} \cdot \tilde{\mathbf{u}} + \frac{\llbracket u \rrbracket_n}{h} \tag{3.6}$$

where $\llbracket u \rrbracket_n$ is the normal component of the displacement jump along S.

In the case of the hydraulic process, the liquid pressure is continuous across the discontinuity surface S, *i.e.*

$$(p_l)_f = (p_l)_{S^+} = (p_l)_{S^-} \tag{3.7}$$

with $(p_l)_f$ denoting the pressure in S. The water flow field, on the other hand, is characterized by a jump across the discontinuity due to the transport of mass of water along the fracture, such that

$$\dot{M} = \dot{\tilde{M}} + H_S(\eta)\ (\llbracket\, \mathbf{j}'^{w} \,\rrbracket \cdot \mathbf{n}) \tag{3.8}$$

in which $\llbracket \mathbf{j}'^{w} \rrbracket = j'^{w}_{S^+} - j'^{w}_{S^-}$. The detailed description of the mathematical framework can be found elsewhere [126].

3.4 Effects of the Fracture in a Narrow Band

The constitutive equations previously mentioned must be enhanced in order take into account the effects of the fracture in the material of the FE-HAR. In the case of the mechanical behavior, the fracture process is described by a continuum damage model, in which the fracture energy, G_f, is associated with the energy consumed for the formation of fracture in mode I throughout the time interval $t \in [0, t_\infty]$, with t_∞ corresponding to the time at which complete degradation of the material has been achieved:

$$\int_0^{t_\infty} \sigma'_{nn}\,\mathrm{d}[\![u]\!]_n = \int_0^{t_\infty} \Big[\mathbf{n} \cdot \boldsymbol{\Sigma}_{\Omega^h}(\boldsymbol{\epsilon}) \cdot \mathbf{n}\Big] h\,\mathrm{d}\epsilon_{nn} = G_f \tag{3.9}$$

When $h \to 0$ the value of the discontinuous tensor $\hat{\boldsymbol{\epsilon}}$ is significantly higher than the continuous portion $\hat{\boldsymbol{\epsilon}}$ in the strain tensor, and consequently, $\mathrm{d}[\![u]\!]_n = h\,\hat{\epsilon}_{nn} \approx h\,\epsilon_{nn}$. Therefore, the energy required for the formation of the fracture depends only on the discontinuous part. In the above equation, the softening law of the constitutive equation, $\boldsymbol{\Sigma}_{\Omega^h}$, must depend on the height h to guarantee energy dissipation consistent with the fracture formation.

The hydraulic process also must incorporate the influence of the fracture in the constitutive equations. In the case of the intrinsic permeability tensor:

$$\mathbf{k}_{\Omega^h} = \mathbf{k} + \frac{[\![u]\!]_n^3}{R\,12\,h} \tag{3.10}$$

where $R \geq 1$ is a coefficient is a coefficient that considers the deviations from the ideal parallel plate conditions. The first term in the right hand side of the previous equation is the continuous part of the intrinsic permeability tensor and it is expressed as a function of porosity (*i.e.*, Kozeny's law or exponential law), while the second term is the enhancement in the s-direction due to fracture formation

According to Manzoli *et al.* [126], the fracture opening also leads to a porosity enhancement as follows:

$$\phi_{\Omega^h} = \phi + \frac{[\![u]\!]_n}{h} \tag{3.11}$$

Likewise to Eq. (3.10), the second term of Eq. (3.11) corresponds to the enrichment in the porosity field caused by the increase of void during the fracture process. The air entry value can be expressed in terms of the intrinsic permeability for a reference value (k_o) and its discontinuous part $(\hat{k})$, as suggested by Olivella and Alonso [147]:

$$(P_o)_{\Omega^h} = P_o \frac{\sqrt[3]{k_o}}{\sqrt[3]{k}} \tag{3.12}$$

3.5 Finite Element Equations

3.5.1 Weak Form of the Governing Equations

The weak forms of the governing equations can be obtained by multiplying both sides of the equation by a standard weight function, since the fracture is described by a model based on continuum mechanics concepts, and integrating in the domain:

$$\int_{\Omega} \delta\mathbf{u} : \big[\boldsymbol{\Sigma}_*(\boldsymbol{\epsilon}) + \mathbf{m}\, p_g\big] \mathrm{d}\Omega = \int_{\Gamma_\sigma} \delta\mathbf{u} \cdot \bar{\mathbf{t}}\, \mathrm{d}\Gamma + \int_{\Omega} \delta\mathbf{u} \cdot \mathbf{b}\, \mathrm{d}\Omega \qquad \forall \delta\mathbf{u} \in \mathbf{U}_0, \tag{3.13}$$

and

$$\begin{aligned}
&\int_{\Omega} \delta p_l \cdot \left\{ \phi_* \frac{D}{Dt} \Big[(S_l)_* \theta_l^w + (S_g)_* \theta_g^w \Big] \right\} \mathrm{d}\Omega \\
&\quad + \int_{\Omega} \delta p_l \cdot \left\{ \boldsymbol{\nabla} \cdot \dot{\mathbf{u}} \Big[(S_l)_* \theta_l^w + (S_g)_* \theta_g^w \Big] \right\} \mathrm{d}\Omega \\
&\quad + \int_{\Omega} \boldsymbol{\nabla} \delta p_l \cdot \left[\theta_l^w\, \mathbf{k}_* \frac{k_{rl}}{\mu_l} \left(\boldsymbol{\nabla} p_l - \rho_l \mathbf{g} \right) \right] \mathrm{d}\Omega \\
&\quad + \int_{\Omega} \boldsymbol{\nabla} \delta p_l \cdot \left[\theta_g^w\, \mathbf{k}_* \frac{k_{rg}}{\mu_g} \left(\boldsymbol{\nabla} p_g - \rho_g \mathbf{g} \right) \right] \mathrm{d}\Omega \qquad \forall \delta p_l \in \mathbf{P}_0 \\
&\quad + \int_{\Omega} \boldsymbol{\nabla} \delta p_l \cdot \Big[\rho_g (S_g)_* \phi_* \tau D_m^w \mathbf{I} + \mathbf{D}'_g \rho_g \Big] \boldsymbol{\nabla} \omega_g^w \mathrm{d}\Omega \\
&\quad - \int_{\Omega} \boldsymbol{\nabla} \delta p_l \cdot \Big[\rho_l (S_l)_* \phi_* \tau D_m^a \mathbf{I} + \mathbf{D}'_l \rho_l \Big] \boldsymbol{\nabla} \omega_l^a \mathrm{d}\Omega = \int_{\Gamma_{jw}} \delta p_l \, (\bar{j}'^w)\, \mathrm{d}\Gamma
\end{aligned} \tag{3.14}$$

where $\mathbf{U}_0 = \{\delta\mathbf{u} | \delta\mathbf{u} \in H^1, \delta\mathbf{u} = 0 \text{ on } \Gamma_u\}$ and $\mathbf{P}_0 = \{\delta p_l | \delta p_l \in H^1, \delta p_l = 0 \text{ on } \Gamma_{p_l}\}$ are the space of admissible displacement and pressure fields, respectively; H^1 is the space of functions with square integrable derivatives. Finally, the constitutive relations and set of material parameters are given by:

$$[\mathbf{\Sigma}_*(\bullet), \mathbf{k}_*, \phi_*, (P_o)_*, (S_l)_*] = \begin{cases} [\mathbf{\Sigma}_{\Omega^h}(\bullet), \mathbf{k}_{\Omega^h}, \phi_{\Omega^h}, (P_o)_{\Omega^h}, (S_l)_{\Omega^h}] \text{ in } \Omega^h \\ [\mathbf{\Sigma}(\bullet), \mathbf{k}, \phi, P_o, S_l] \text{ in } \Omega \backslash \Omega^h \end{cases} \tag{3.15}$$

Note that the constitutive equations were incorporated in the weak form (*i.e.*, Eqs. (3.13) and (3.14))

3.5.2 Fluid Mass Balance Equation in the Fracture

The weak form of the water mass balance equation for the subdomain Ω^h is expressed by:

$$\begin{aligned} &\int_\Omega \delta p_l \cdot \left\{ \phi_{\Omega^h} \frac{D}{Dt} \Big[(S_l)_{\Omega^h} \theta_l^w + (S_g)_{\Omega^h} \theta_g^w \Big] \right\} \mathrm{d}\Omega \\ &+ \int_\Omega \delta p_l \cdot \left\{ \mathbf{\nabla} \cdot \dot{\mathbf{u}} \Big[(S_l)_{\Omega^h} \theta_l^w + (S_g)_{\Omega^h} \theta_g^w \Big] \right\} \mathrm{d}\Omega \\ &+ \int_\Omega \mathbf{\nabla} \delta p_l \cdot \left[\theta_l^w \, \mathbf{k}_{\Omega^h} \frac{k_{rl}}{\mu_l} \left(\mathbf{\nabla} p_l - \rho_l \mathbf{g} \right) \right] \mathrm{d}\Omega \\ &+ \int_\Omega \mathbf{\nabla} \delta p_l \cdot \left[\theta_g^w \, \mathbf{k}_{\Omega^h} \frac{k_{rg}}{\mu_g} \left(\mathbf{\nabla} p_g - \rho_g \mathbf{g} \right) \right] \mathrm{d}\Omega \\ &+ \int_\Omega \mathbf{\nabla} \delta p_l \cdot \Big[\rho_g (S_g)_{\Omega^h} \phi_{\Omega^h} \tau D_m^w \mathbf{I} + \mathbf{D}'_g \rho_g \Big] \mathbf{\nabla} \omega_g^w \mathrm{d}\Omega \\ &- \int_\Omega \mathbf{\nabla} \delta p_l \cdot \Big[\rho_l (S_l)_{\Omega^h} \phi_{\Omega^h} \tau D_m^a \mathbf{I} + \mathbf{D}'_l \rho_l \Big] \mathbf{\nabla} \omega_l^a \mathrm{d}\Omega \\ &= - \left[\int_{S^+} \delta p_l \, j'^w_{S^+} \mathrm{d}S - \int_{S^-} \delta p_l \, j'^w_{S^-} \mathrm{d}S \right] \end{aligned} \tag{3.16}$$

in which $j'^w_{S^+} = \mathbf{j}'^w_{S^+} \cdot \mathbf{n}$ and $j'^w_{S^-} = \mathbf{j}'^w_{S^-} \cdot (-\mathbf{n})$ are the fluid flow from the subdomain towards the surrounding medium.

Substituting Eqs. (3.6), (3.10) and (3.11) into (3.14) yields

$$
\begin{aligned}
&\int_S \int_{-h/2}^{h/2} \delta p_l \cdot \left\{ \left(\phi + \frac{\llbracket u \rrbracket_n}{h} \right) \frac{D}{Dt} \Big[(S_l)_{\Omega^h} \theta_l^w + (S_g)_{\Omega^h} \theta_g^w \Big] \right\} \mathrm{d}\eta \, \mathrm{d}\xi \\
&\qquad + \int_S \int_{-h/2}^{h/2} \delta p_l \cdot \left\{ \frac{\llbracket \dot{u} \rrbracket_n}{h} \Big[(S_l)_{\Omega^h} \theta_l^w + (S_g)_{\Omega^h} \theta_g^w \Big] \right\} \mathrm{d}\eta \, \mathrm{d}\xi \\
&\qquad + \int_S \int_{-h/2}^{h/2} \boldsymbol{\nabla} \delta p_l \cdot \left[\theta_l^w \left(\mathbf{k} + \frac{\llbracket u \rrbracket_n^3}{R12h} \right) \frac{k_{rl}}{\mu_l} \left(\boldsymbol{\nabla} p_l - \rho_l \mathbf{g} \right) \right] \mathrm{d}\eta \, \mathrm{d}\xi \\
&\qquad + \int_S \int_{-h/2}^{h/2} \boldsymbol{\nabla} \delta p_l \cdot \left[\theta_g^w \left(\mathbf{k} + \frac{\llbracket u \rrbracket_n^3}{R12h} \right) \frac{k_{rg}}{\mu_g} \left(\boldsymbol{\nabla} p_g - \rho_g \mathbf{g} \right) \right] \mathrm{d}\eta \, \mathrm{d}\xi \\
&\qquad + \int_S \int_{-h/2}^{h/2} \boldsymbol{\nabla} \delta p_l \cdot \left[\rho_g (S_g)_{\Omega^h} \left(\phi + \frac{\llbracket u \rrbracket_n}{h} \right) \tau D_m^w \mathbf{I} + \mathbf{D}_g' \rho_g \right] \boldsymbol{\nabla} \omega_g^w \mathrm{d}\eta \, \mathrm{d}\xi \\
&\qquad - \int_S \int_{-h/2}^{h/2} \boldsymbol{\nabla} \delta p_l \cdot \left[\rho_l (S_l)_{\Omega^h} \left(\phi + \frac{\llbracket u \rrbracket_n}{h} \right) \tau D_m^a \mathbf{I} + \mathbf{D}_l' \rho_l \right] \boldsymbol{\nabla} \omega_l^a \mathrm{d}\eta \, \mathrm{d}\xi \\
&\qquad = - \left[\int_{S^+} \delta p_l \, j_{S^+}'^w \mathrm{d}S - \int_{S^-} \delta p_l \, j_{S^-}'^w \mathrm{d}S \right]
\end{aligned}
\tag{3.17}
$$

Neglecting the gravimetric terms, integrating over the width h and taking the limit as $h \to 0$ gives

$$
\begin{aligned}
&\int_S \delta p_l \llbracket u \rrbracket_n \frac{D}{Dt} \Big[(S_l)_{\Omega^h} \theta_l^w + (S_g)_{\Omega^h} \theta_g^w \Big] \mathrm{d}\xi + \int_S \delta p_l \llbracket \dot{u} \rrbracket \Big[(S_l)_{\Omega^h} \theta_l^w + (S_g)_{\Omega^h} \theta_g^w \Big] \mathrm{d}\xi \\
&\qquad + \int_S \frac{\partial \delta p_l}{\partial \xi} \theta_l^w \, \frac{\llbracket u \rrbracket_n^3}{R\,12} \frac{k_{rl}}{\mu_l} \frac{\partial p_l}{\partial \xi} \, \mathrm{d}\xi + \int_S \frac{\partial \delta p_l}{\partial \xi} \theta_g^w \, \frac{\llbracket u \rrbracket_n^3}{R\,12} \frac{k_{rg}}{\mu_g} \frac{\partial p_g}{\partial \xi} \, \mathrm{d}\xi \\
&\qquad + \int_S \frac{\partial \delta p_l}{\partial \xi} \rho_g (S_g)_{\Omega^h} \llbracket u \rrbracket_n \tau D_m^w \mathbf{I} \frac{\partial \omega_g^w}{\partial \xi} \, \mathrm{d}\xi - \int_S \frac{\partial \delta p_l}{\partial \xi} \rho_l (S_l)_{\Omega^h} \llbracket u \rrbracket_n \tau D_m^a \mathbf{I} \frac{\partial \omega_l^a}{\partial \xi} \, \mathrm{d}\xi \\
&\qquad = - \int_S \delta p_l \, \llbracket j'^w \rrbracket \mathrm{d}S
\end{aligned}
\tag{3.18}
$$

where $\llbracket j'^w \rrbracket$ is the jump in the water field caused by the discontinuity. Moreover, it follows from Eqs. (3.12) and (2.29) that $(S_l)_{\Omega^h}$ tends to zero when $h \to 0$, and therefore, $(S_g)_{\Omega^h} \to 1$. Hence, Eq. (3.18) can be rewritten as follows:

$$
\begin{aligned}
&\int_S \delta p_l \llbracket u \rrbracket_n \frac{D \theta_g^w}{Dt} \mathrm{d}\xi + \int_S \delta p_l \llbracket \dot{u} \rrbracket \theta_g^w \mathrm{d}\xi + \int_S \frac{\partial \delta p_l}{\partial \xi} \theta_l^w \, \frac{\llbracket u \rrbracket_n^3}{R12} \frac{k_{rl}}{\mu_l} \frac{\partial p_l}{\partial \xi} \, \mathrm{d}\xi \\
&\qquad + \int_S \frac{\partial \delta p_l}{\partial \xi} \theta_g^w \, \frac{\llbracket u \rrbracket_n^3}{R12} \frac{k_{rg}}{\mu_g} \frac{\partial p_g}{\partial \xi} \, \mathrm{d}\xi + \int_S \frac{\partial \delta p_l}{\partial \xi} \rho_g \llbracket u \rrbracket_n \tau D_m^w \mathbf{I} \frac{\partial \omega_g^w}{\partial \xi} \, \mathrm{d}\xi = - \int_S \delta p_l \llbracket j'^w \rrbracket \mathrm{d}S
\end{aligned}
\tag{3.19}
$$

The previous expression is the weak form of the following differential equation:

$$\begin{aligned}\llbracket u \rrbracket_n \frac{D\theta^w}{Dt} + \llbracket \dot{u} \rrbracket \theta_g^w + \frac{\partial}{\partial \xi}\left(\theta_l^w \frac{\llbracket u \rrbracket_n^3}{R12} \frac{k_{rl}}{\mu_l} \frac{\partial p_l}{\partial \xi}\right) + \frac{\partial}{\partial \xi}\left(\theta_g^w \frac{\llbracket u \rrbracket_n^3}{R12} \frac{k_{rg}}{\mu_g} \frac{\partial p_g}{\partial \xi}\right) \\ + \frac{\partial}{\partial \xi}\left(\rho_g \llbracket u \rrbracket_n \tau D_m^w \mathbf{I} \frac{\partial \omega_g^w}{\partial \xi}\right) + \llbracket j'^w \rrbracket = 0\end{aligned} \tag{3.20}$$

which is the strong form of the mass balance equation in the fracture.

3.5.3 FEM Approximations

The displacement and liquid pressure fields are approximated by:

$$\mathbf{u}(\mathbf{X}, t) \approx \mathbf{N}_u(\mathbf{X})\, \mathbf{U}(t) \tag{3.21}$$

$$p_l(\mathbf{X}, t) \approx \mathbf{N}_p(\mathbf{X})\, \mathbf{P}_l(t) \tag{3.22}$$

where $\mathbf{N}_u$ and $\mathbf{N}_p$ are matrices of the standard FE interpolation functions; $\mathbf{U}$ and $\mathbf{P}_l$ are the vectors of nodal displacements and nodal liquid pressure, respectively. Accordingly, the approximation of the strains and liquid pressure gradient are obtained as:

$$\boldsymbol{\epsilon}(\mathbf{X}, t) \approx \mathbf{B}(\mathbf{X})\, \mathbf{U}(t) \tag{3.23}$$

$$\boldsymbol{\nabla} p_l(\mathbf{X}, t) \approx \boldsymbol{\nabla}\mathbf{N}_p(\mathbf{X})\, \mathbf{P}_l(t) \tag{3.24}$$

with $\mathbf{B}$ and $\boldsymbol{\nabla}\mathbf{N}_p$ denoting the matrices of spatial derivatives of the interpolation functions.

In the classical approach, the chain rule is necessary to find the gradients of mass fractions in terms of temperature, liquid and gas pressures. In order to avoid second derivatives, as it is required by the classical approach, the diffusive terms are interpolated, and therefore, their gradients can be computed as:

$$\boldsymbol{\nabla} \omega_l^a(\mathbf{X}, t) \approx \boldsymbol{\nabla}\mathbf{N}_p(\mathbf{X})\, \boldsymbol{\omega}_l^a(t) \tag{3.25}$$

$$\boldsymbol{\nabla} \omega_g^w(\mathbf{X}, t) \approx \boldsymbol{\nabla}\mathbf{N}_p(\mathbf{X})\, \boldsymbol{\omega}_g^w(t) \tag{3.26}$$

The Galerkin finite element discretization of the governing equations (*i.e.*, Eqs. (3.13) and (3.20)) leads to the following set of algebraic equations:

$$\begin{aligned}
&\int_{\Omega} (\mathbf{B})^{\mathrm{T}}\, \Sigma_*(\boldsymbol{\epsilon})\, \mathrm{d}\Omega + \mathbf{Q}_{(u\,p_g)} \dot{\mathbf{P}}_g + \dot{\mathbf{F}}_{(u)} = \mathbf{R}_{(u)} \approx \mathbf{0} \\
&\mathbf{C}_{(p_l\,u)} \dot{\mathbf{U}} + \dot{\mathbf{S}}_{(p_l)} + \mathbf{A}_{(p_l\,p_l)} \mathbf{P}_l + \mathbf{A}_{(p_l\,p_g)} \mathbf{P}_g \\
&\qquad + \mathbf{A}_{(p_l\,\omega_g^w)} \boldsymbol{\omega}_g^w - \mathbf{A}_{(p_l\,\omega_l^a)} \boldsymbol{\omega}_l^a + \mathbf{F}_{(p_l)} = \mathbf{R}_{(p_l)} \approx \mathbf{0}
\end{aligned} \tag{3.27}$$

where the matrices of the mechanical and hydraulic problems are:

$$\mathbf{Q}_{(u\,p_g)} = \int_{\Omega} (\mathbf{B})^{\mathrm{T}}\, \mathbf{m}\, \mathbf{N}_p \,\mathrm{d}\Omega$$

$$\dot{\mathbf{F}}_u = \int_{\Gamma_\sigma} (\mathbf{N}_u)^{\mathrm{T}}\, \bar{\mathbf{t}} \,\mathrm{d}\Gamma + \int_{\Omega} (\mathbf{N}_u)^{\mathrm{T}}\, \mathbf{b} \,\mathrm{d}\Omega$$

$$\mathbf{C}_{(p_l\,u)} = \Big[(S_l)_* \theta_l^w + (S_g)_* \theta_g^w\Big] \int_{\Omega} (\mathbf{N}_p)^{\mathrm{T}}\, \mathbf{m}\, \mathbf{B} \,\mathrm{d}\Omega$$

$$\dot{\mathbf{S}}_{(p_l\,p_l)} = \phi_* \frac{\partial}{\partial t} \Big[(S_l)_* \theta_l^w + (S_g)_* \theta_g^w\Big] \int_{\Omega} (\mathbf{N}_p)^{\mathrm{T}} \,\mathrm{d}\Omega$$

$$\mathbf{A}_{(p_l\,p_l)} = \theta_l^w \frac{k_{rl}}{\mu_l} \int_{\Omega} (\boldsymbol{\nabla}\mathbf{N}_p)^{\mathrm{T}}\, \mathbf{k}_*\, \boldsymbol{\nabla}\mathbf{N}_p \,\mathrm{d}\Omega$$

$$\mathbf{A}_{(p_l\,p_g)} = \theta_g^w \frac{k_{rg}}{\mu_g} \int_{\Omega} (\boldsymbol{\nabla}\mathbf{N}_p)^{\mathrm{T}}\, \mathbf{k}_*\, \boldsymbol{\nabla}\mathbf{N}_p \,\mathrm{d}\Omega$$

$$\mathbf{A}_{(p_l\,\omega_g^w)} = \rho_g\, (S_g)_*\, \phi_*\, \tau\, D_g^w \int_{\Omega} (\boldsymbol{\nabla}\mathbf{N}_p)^{\mathrm{T}}\, \mathbf{I}\, \boldsymbol{\nabla}\mathbf{N}_p \,\mathrm{d}\Omega + \rho_g \int_{\Omega} (\boldsymbol{\nabla}\mathbf{N}_p)^{\mathrm{T}}\, \mathbf{D}'_g\, \boldsymbol{\nabla}\mathbf{N}_p \,\mathrm{d}\Omega$$

$$\mathbf{A}_{(p_l\,\omega_l^a)} = \rho_l\, (S_l)_*\, \phi_*\, \tau\, D_l^a \int_{\Omega} (\boldsymbol{\nabla}\mathbf{N}_p)^{\mathrm{T}}\, \mathbf{I}\, \boldsymbol{\nabla}\mathbf{N}_p \,\mathrm{d}\Omega + \rho_l \int_{\Omega} (\boldsymbol{\nabla}\mathbf{N}_p)^{\mathrm{T}}\, \mathbf{D}'_l\, \boldsymbol{\nabla}\mathbf{N}_p \,\mathrm{d}\Omega$$

$$\mathbf{F}_{p_l} = \int_{\Gamma_{j^w}} (\mathbf{N}_p)^{\mathrm{T}}\, j'^w \,\mathrm{d}\Gamma + \left(\theta_l^w \frac{k_{rl}}{\mu_l}\, \rho_l + \theta_g^w \frac{k_{rg}}{\mu_g}\, \rho_g\right) \int_{\Omega} (\boldsymbol{\nabla}\mathbf{N}_p)^{\mathrm{T}}\, \mathbf{k}_*\, \mathbf{g} \,\mathrm{d}\Omega$$

The time derivatives of the variables are discretized by using the finite difference method as follows:

$$\dot{\mathbf{U}} = \frac{\mathbf{U}_{(n+1)} - \mathbf{U}_{(n)}}{t_{(n+1)} - t_{(n)}} \tag{3.28}$$

Assuming the material time derivatives can be approximated as local derivatives because of the small strain rate assumption, one can write:

$$\frac{\partial}{\partial t}\Big[(S_l)_*\theta_l^w + (S_g)_*\theta_g^w\Big] = \frac{\Big[(S_l)_*\theta_l^w + (S_g)_*\theta_g^w\Big]_{(n+1)} - \Big[(S_l)_*\theta_l^w + (S_g)_*\theta_g^w\Big]_{(n)}}{t_{(n+1)} - t_{(n)}} \tag{3.29}$$

with $(\bullet)_{(n+1)}$ and $(\bullet)_{(n)}$ denoting the values of the variable $(\bullet)$ at the current time step $t_{(n+1)}$ and previous time-step $t_{(n)}$, respectively. Using the Newton-Raphson iteration method, the primary variables $\mathbf{U}$ and $\mathbf{P}_l$ at each time step are obtained by iteratively solving the fully-coupled non-linear system (*i.e.*, Eq. (3.27)).

3.6 Modeling Discontinuities with High Aspect Ratio Finite Elements

The next subsections aim to show that solid finite elements with high aspect ratio (HAR) can be used to reproduce the discontinuity behavior. In this sense, first is demonstrated that as the aspect ratio of standard finite element increases, the also increases, approaching the kinematics associated with the Continuum Strong Discontinuity Approach (CSDA). Afterwards, damage models capable of capturing the discontinuity behavior are presented. Finally, the main steps related to the process of inserting HAR elements in the original mesh are explained.

3.6.1 Solid Finite Element with High Aspect Ratio

Consider the three-node triangular finite element with base b and height h shown in Figure 3.2a. As shown by Manzoli *et al.* [127, 124, 123], the strain tensor of such element can be conveniently split into two parts as follows:

$$\boldsymbol{\epsilon} = \tilde{\boldsymbol{\epsilon}} + \frac{1}{h}\left(\mathbf{n} \otimes [\![\mathbf{u}]\!]\right)^S \tag{3.30}$$

where $\tilde{\boldsymbol{\epsilon}}$ contains the components of the strain tensor $\boldsymbol{\epsilon}$ that does not depend on h, $(\bullet)^S$ is the symmetric part of $(\bullet)$, $\mathbf{n}$ is the unit vector normal to the base of element, $\otimes$ is the dyadic product, and $[\![\mathbf{u}]\!]$ is the relative displacement between node 1 and its projection on the base of the element. The above expressions can also be obtained for the case of four-node tetrahedral element with height h and base of area A (Figure 3.2b).

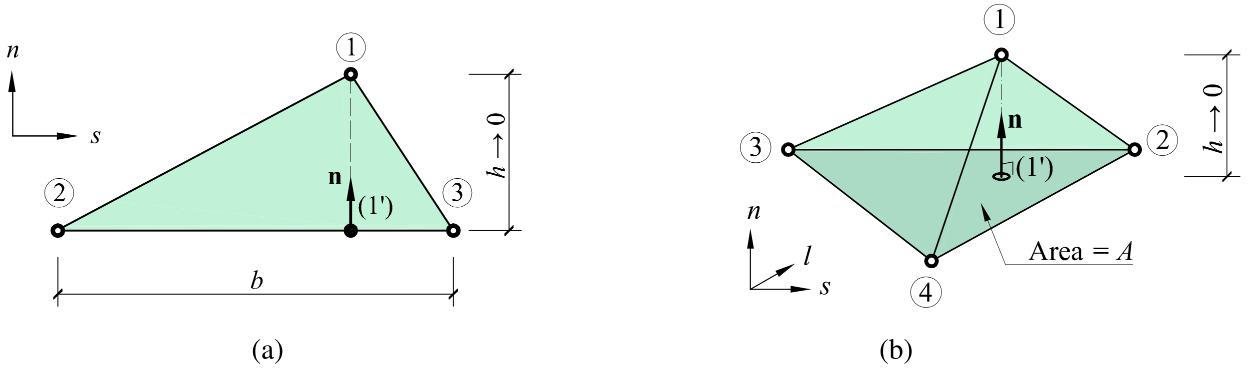

Figure 3.2: Solid interface finite elements: (a) three-node triangular element; (b) four-node tetrahedral element (adapted from [123])

In the limit situation where h tends to zero, node 1 and its projection converge to the same point and the discontinuity in the displacement field can be represented by the relative displacement $[\![\mathbf{u}]\!]$. Eq. (3.30) shows that the kinematics of HAR-FE is the same as the one corresponding to the CSDA. Therefore, all the problems that can be treated by CSDA can also be analyzed with HAR-FE.

3.6.2 Damage Models for HAR-FE

The behavior of the elements with high aspect ratio are described by the tensile damage models or the J2 damage model, depending on the type of element. As previously mentioned, the interface elements between the bulk elements are governed by the tensile damage model, while the elements that are used to mimic the interface between the soil and the plate are governed by the J2 damage model. Table 3.1 summarizes the main equations for the J2 damage models.

In the J2 damage model d acts only in the deviatoric part $(\bar{\boldsymbol{\sigma}}_d)$ of the elastic stress tensor $(\bar{\boldsymbol{\sigma}})$, and therefore, the volumetric part $(\bar{\boldsymbol{\sigma}}_v)$ remains unchanged. In the constitutive equation, $\mathbb{C}$ is the fourth-order elastic tensor, $\boldsymbol{\epsilon}$ is the strain tensor, $\mathbf{I}$ denotes the second order unit tensor, K is the bulk modulus and G is the shear modulus. In addition, the damage criterion of the J2 damage model considers the norm of the deviatoric stress J2 as the equivalent stress. According to the evolution law, maximum value that the strain-like internal variable, r, takes the reaches throughout the loading process, starting from the initial value of r_o. In the tensile damage model, this r_o is equal to the initial tensile strength of the material, f_t which is a function of the degree of saturation. In the J2 model, r_o is the cohesion (c) bond strength of the soil-plate interface. The damage variable evolution of the tensile model is related to a softening law (reduction of stresses with increasing strains), which is defined in terms of tensile strength, Young's modulus, E, and fracture energy of the material, G_f. In the case of the J2 damage model, it is assumed that the stress-liek internal variable is constant and equal to the cohesion.

Table 3.1: Continuum damage models

	Tensile damage model	J2 damage model
Constitutive equation	$\boldsymbol{\sigma} = \begin{cases}(1-d)\bar{\boldsymbol{\sigma}}, & \text{if } \bar{\tau} > 0 \\ \bar{\boldsymbol{\sigma}}, & \text{if } \bar{\tau} < 0\end{cases}$ $\bar{\boldsymbol{\sigma}} = \mathbb{C} : \boldsymbol{\epsilon}$	$\boldsymbol{\sigma} = (1-d)\bar{\boldsymbol{\sigma}}_d + \bar{\boldsymbol{\sigma}}_v$ $\bar{\boldsymbol{\sigma}}_d = 2G\boldsymbol{\epsilon}_d = 2G\left[\boldsymbol{\epsilon} - \frac{1}{3}\mathrm{tr}(\boldsymbol{\epsilon})\mathbf{I}\right]$ $\bar{\boldsymbol{\sigma}}_v = 3K\boldsymbol{\epsilon}_v = K[\mathrm{tr}(\boldsymbol{\epsilon})\mathbf{I}]$
Equivalent stress	$\bar{\tau} = \bar{\sigma}_{nn} = \frac{1}{h}E[\![u]\!]_n$	$\bar{\tau} = \frac{1}{\sqrt{2}}\Vert\bar{\sigma}_d\Vert$
Damage criterion	$\bar{\phi} = \bar{\tau} - r \leq 0$	$\bar{\phi} = \bar{\tau} - r \leq 0$
Evolution law	$r = \max_{S\in[0,t]}[f_t, \bar{\sigma}_{nn}]$	$r = \max_{S\in[0,t]}[\frac{1}{\sqrt{2}}\Vert\bar{\sigma}_d\Vert, r_o]$
Damage evolution	$d = 1 - q(r)/r$	$d = 1 - q(r)/r$
Softening law	$q(r) = f_t \exp\left[\frac{f_t^2}{G_f\,E}h\,(1 - r/f_t)\right]$	$q(r) = r_o = c$

It is a common sense in the study of concrete structure to insert the solid tetrahedral elements with high aspect ratio only in the region of interest in order to reduce computational effort. However, to capture the phenomena of desiccation cracks in soils these special elements were introduced between all bulk elements of the mesh. The plate at the bottom of the soil was removed to decrease the number of nodes and elements. But the soil-plate interface was kept it because such behavior is essential to properly address the desiccation phenomena.

3.6.3 Mesh Fragmentation Technique (MFT)

A MFT based on the inclusion of solid HAR interface elements was recently proposed to model the formation and propagation of fractures in rocks and soils [184]. The high aspect ratio elements [124, 123] are incorporated in-between the standard finite elements of a mesh. The main stages associated with the adaptation of a traditional FE mesh into a fragmented one are presented in Figure 3.3. The regular elements of a standard FE mesh (Figure 3.3a) are first separated by introducing gaps between them (Figure 3.3b). These gaps are relatively small (typically around 0.01mm). As demonstrated in Manzoli *et al.* [123], the size of the gaps does not affect the numerical results. In Figure 3.3b the spaces between elements are exaggerated to illustrate better the method. To complete the transformation of the standard FE mesh, HAR elements are placed to fill the gaps between regular FE (Figure 3.3c). These interface solid elements control the interaction between adjacent regular elements of the mesh. Different strategies can be adopted in relation to where and when to include the interface elements. For instance, interface elements can be introduced in the whole mesh (*i.e.*, at the contact between all the bulks elements of the model) at the beginning of the analysis. To reduce the number of interface elements, they could be included in some regions of the mesh or materials only, where the formation of cracks is anticipated. This strategy will lead to a reduction of the computational effort, but it is necessary to have reliable beforehand information about the zone(s) and/or material(s) where cracks may be formed. It can be also possible to start the analysis with a standard mesh of bulk element only, and, as the problem evolves, enhance the mesh with interface elements in those zones where the stress field indicates that are prone to form cracks. For this last option, techniques similar to the ones typically used in re-meshing strategies for the densification of meshes in critical zones can be adopted [67, 101, 168].

Sánchez *et al.* [184] discussed in detail the main advantages of the MFT respect to other methods based on the inclusion of special elements between standard FE, such as cohesive zone models and zero-thickness interface elements [34, 139, 159]. One key characteristic of the MFT is that the numerical analysis is entirely conducted in a continuum approach, with no need to define discrete mechanical models, or distinct integration rules and interpolation functions (as

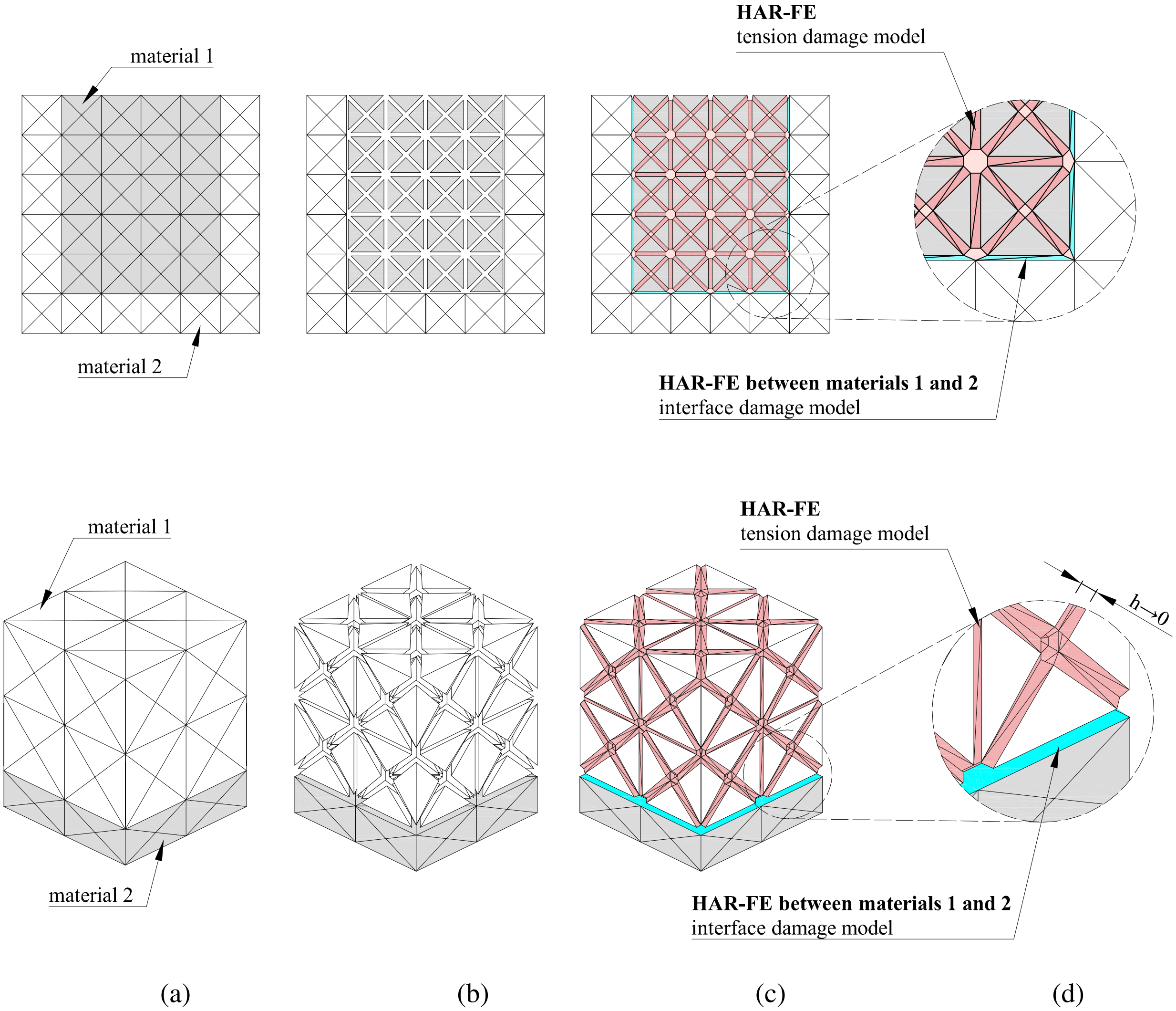

Figure 3.3: Main steps related to the mesh fragmentation process: (a) original mesh composed by two different materials, called materials 1 and 2; (b) the elements associated with material 1 are separated, which leads to the formation of gaps of thickness h; (c) elements with high aspect ratio are inserted in these gaps, which are a result of the previous step; (d) zoom showing in detail all the new elements that are generated by the mesh fragmentation process (modified from[123, 184])

it is necessary for zero-thickness elements). Manzoli *et al.* [127, 123] demonstrated that the implementation of HAR elements in conjunction with proper strain softening constitutive models allow simulating the kinematics associated with the formation of displacement discontinuities according to the continuous strong discontinuous approach [43, 151, 174, 193]. These elements can also be used to model discontinuities related to the degradation between distinct materials.

As interface elements, we adopted two non-linear constitutive models based on the damage theory. To represent the shear interfaces necessary to simulate the potential slip of the soil with respect to the boundary (*e.g.*soil-plate interphase in a drying test in the lab), we adopted a model defined in terms of the cohesion bond strength. To describe the interface between soil elements related to crack opening (*i.e.*, soil-soil interface), we selected a damage model which damage criterion and softening laws are defined in terms of both, soil tensile strength and soil fracture energy. Both models were introduced in detail in Section 3.6.2. As for the bulk elements, any appropriate constitutive model can be adopted when using this technique. In this work, we have chosen the Barcelona Basic Model for the analyses presented hereafter. We considered tensile stresses and strains as positive.

3.7 Applications

In this chapter the capabilities of the proposed technique to model desiccation cracks in soils using a fully coupled hydro-mechanical formulation is investigated by considering two different cases. In the first one, the experimental laboratory tests carried out by Rodriguez *et al.* [179] were simulated to explored the influence of soil thickness in the crack pattern. This test was previously replicated by Sanchez *et al.* [184] using the MFT. However, in their work the shrinkage phenomenon was modeled by imposing volumetric deformations in the elements and the hydraulic processes related to the problem were not taken into account. The second application corresponds to the field survey of crack pattern reported by Dyer *et al.* [60]. The crack depth and distance between cracks obtained with the proposed method were validated against the ones monitored in the field.

3.7.1 Desiccation Cracks in Circular Plate Tests under Laboratory Atmospheric Conditions

The experimental test conducted by Rodriguez *et al.* [179], in which a sample of mining waste with liquid limit of 43.9%, plasticity index of 4% and solid particle density equals to 3.97 Mg/m^3, is studied in this section by using the proposed approach. According to the authors [179], the soil was classified as ML (*i.e.*, low plasticity silt) according to the Unified Soil Classification

System. The retention curve of the waste is shown in Figure 3.4. The square symbols represents the experimental data obtained by Rodriguez *et al.* [179], while the continuous line refers to the modified van Genuchten law used to relate the degree of saturation with suction. To take into account the influence of porosity in the retention curve, the following modified van Genuchten law proposed by Rodriguez *et al.* [179] is adopted:

$$S_l = \left[1 + \left(\frac{\psi}{P_o\, f_n} \right)^{\frac{1}{1-\lambda_o}} \right]^{-\lambda_o} \quad ; \qquad f_n = \exp\left[-\eta(\phi - \phi_o)\right] \tag{3.31}$$

where P_o corresponds the air entry value at a reference porosity ϕ_o, λ_o is a material property that is associated with the pore size distribution and f_n is a function that defines the influence of porosity in the retention curve by means of the parameter η

The relationship between hydraulic conductivity (k_{sat}) and porosity is shown in Figure 3.5, in which the square symbols are the experimental data from [179] and the continuous line is a exponential fitting curve expressed by:

$$k_{\text{sat}} = k_o \, \exp\left[b(\phi - \phi_o)\right] \tag{3.32}$$

where b is a material property obtained from the experimental data and k_o denotes the intrinsic permeability at a reference porosity ϕ_o. Finally, a cubic law is used as a constitutive law between the relative permeability and the degree of saturation (*i.e.* $m = 3$). Table 3.2 contains the values of all hydraulic properties.

The variation of tensile strength with degree of saturation is also considered here. Based on the results published by Rodriguez *et al.* [179] and shown in Figure 3.6, a expression in which the tensile strength initially increases with decreasing drying, remains constant in a determined interval, decreases with decreasing drying and then remains constant again after reaching a certain value of degree of saturation, is proposed as follows:

Table 3.2: Hydraulic properties of the model [179]

Retention curve	
P_o (MPa)	1.05
λ	0.39
Hydraulic conductivity	
k_o (m/s)	2.5×10^{-9}
b	25
ϕ_o	0.60
m	3

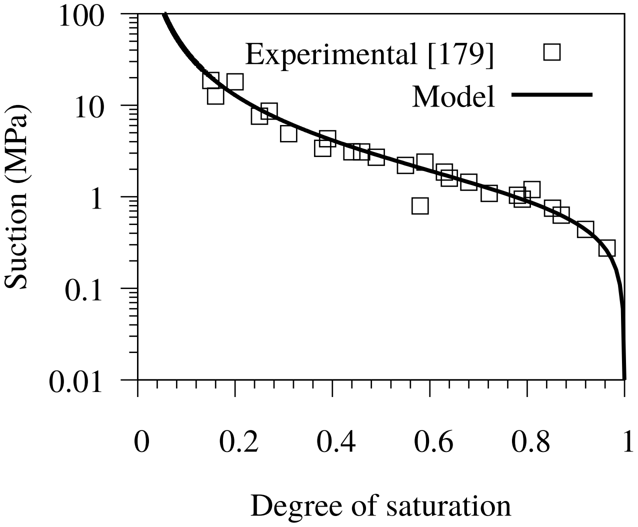

Figure 3.4: Soil-water retention curve adopted for the drying test

$$\sigma_u = \begin{cases} \dfrac{(\sigma_u)_{\max} - (\sigma_u)_o}{(S_l)_{\max 1} - (S_l)_o}\left[S_l - (S_l)_o\right] + (\sigma_u)_o & \text{if} \quad S_l \in [(S_l)_{\max 1}, (S_l)_o] \\ (\sigma_u)_{\max} & \text{if} \quad S_l \in [(S_l)_{\max 2}, (S_l)_{\max 1}] \\ \dfrac{(\sigma_u)_{\text{res}} - (\sigma_u)_{\max}}{(S_l)_{\text{res}} - (S_l)_{\max 2}}\left[S_l - (S_l)_{\max 2}\right] + (\sigma_u)_{\max} & \text{if} \quad S_l \in [(S_l)_{\text{res}}, (S_l)_{\max 2}] \\ (\sigma_u)_{\text{res}} & \text{if} \quad S_l \in [0, (S_l)_{\text{res}}] \end{cases} \tag{3.33}$$

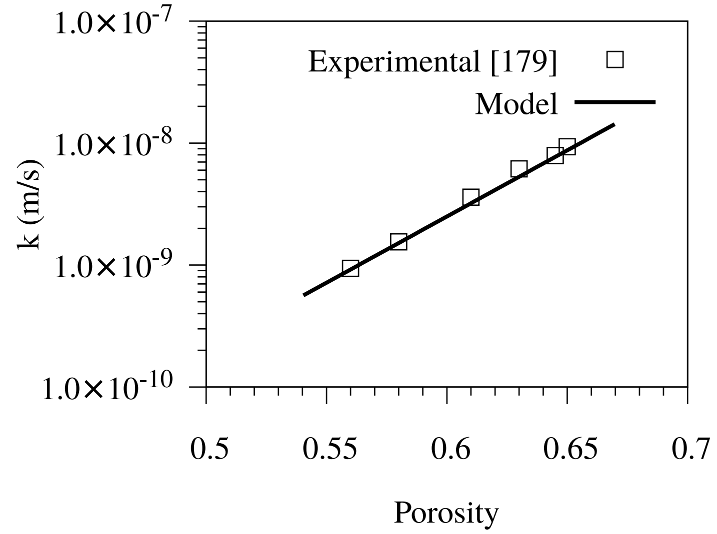

Figure 3.5: Variation of permeability with porosity [179]

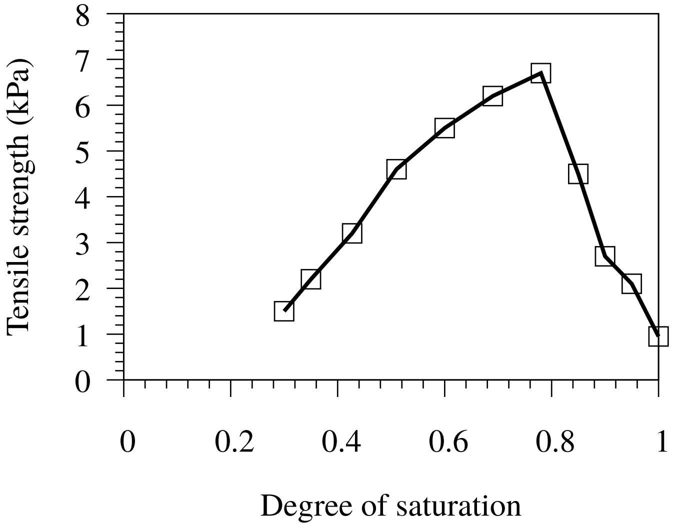

Figure 3.6: Variation of tensile strength with degree of saturation according to the experimental results [179]

Figure 3.7a is a sketch of the proposed tensile strength variation. Once the damage criterion of the HAR elements is reached the tensile strength is maintained constant to guarantee the correct energy dissipation. Figure 3.7b shows the curve used to mimic the experimental behavior of Figure 3.6.

Note that the tensile strength increases from an initial value of $(\sigma_u)_o = 1$ kPa to a peak value of $(\sigma_u)_{\max} = 7$ kPa at around 80% of saturation and then decreases as the soil dries until a saturation of 30% is reached, in which $(\sigma_u)_{\text{res}} = 1.5$ kPa.

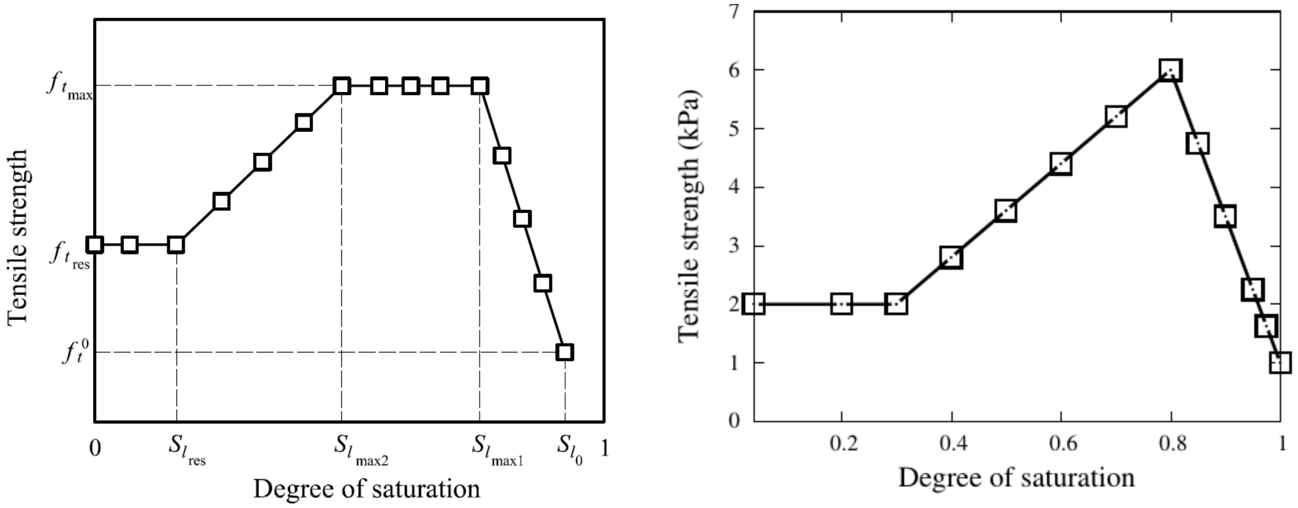

(a)

(b)

Figure 3.7: Relationship between tensile strength and degree of saturation: (a) proposed expression; (b) curve adopted to model the behavior of the waste

The hydraulic processes previously described and the variation of tensile strength with saturation are essential to calibrate the 3D finite element model adopted in this work. Based on these data, the drying tests of samples with diameter much higher than the height are numerically studied by using the MFT. Therefore, HAR elements are inserted between the bulk elements of the soil and in the soil-plate interface. Since the soil rests on a plate, HAR elements can capture the contact behavior between the soil and the plate. To ensure solution convergence the time is discretized in 2400 steps, so that the allowable maximum time increment is small. The waste is fully saturated at the beginning of the analysis with matric suction equals zero in every node of the mesh and no movement is allowed at the bottom of the plate. Maintaining the temperature constant and equals to 20^o C, a matric suction of 59 MPa (which is equivalent to a relative humidty of 65%) is imposed at the top surface of the model.

Tables 3.3 and 3.4 present the mechanical properties of the bulk and HAR interface elements, respectively. The parameters of the bulk elements were calibrated to match the time history of vertical strain (Figure 3.8a) and water loss (Figure 3.8b) of a specimen 40 mm high and 250 mm in diameter. In this case, a mesh containing 26094 elements, in which 14124 are HAR interface elements, and 10170 nodes is used to capture this results. The numerical results are compared against the experimental ones (Figure 3.8) and they show a good agreement for both, vertical strain and accumulated water loss. Note that in a first stage, the soil experiences shrinkage with water loss, but after 400 hours, the soil continues to lose water with no volume change.

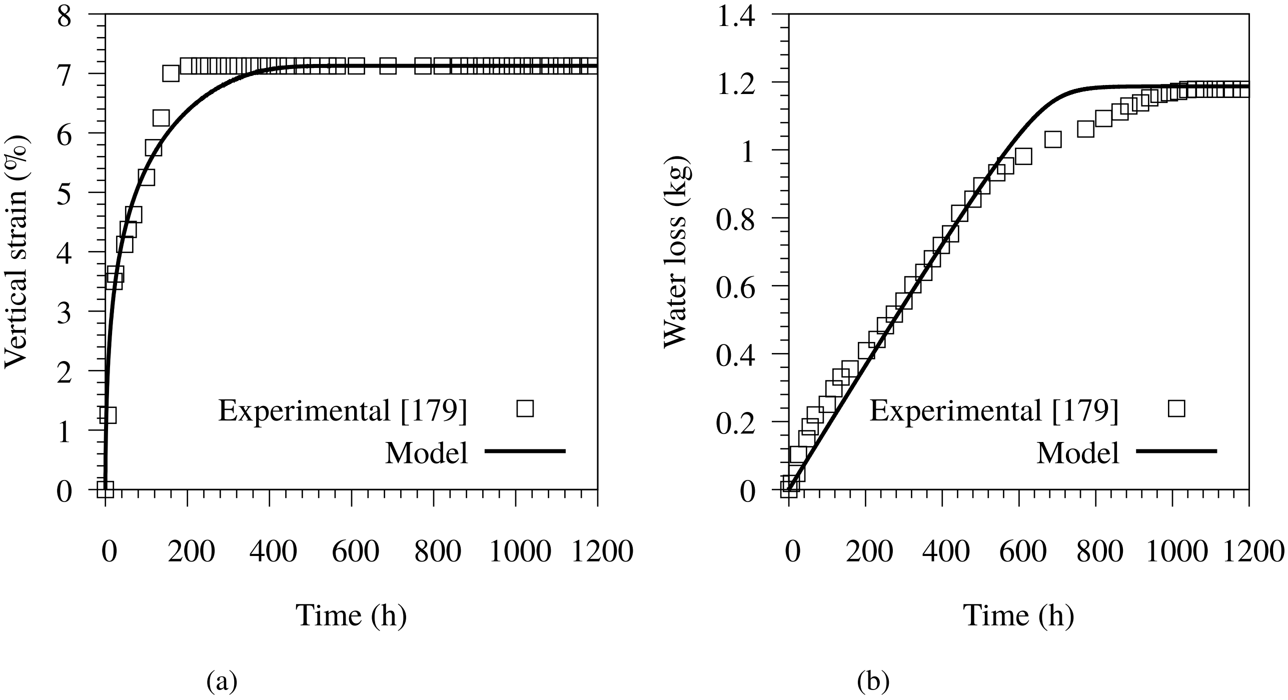

Figure 3.8: Drying test results for the specimen with thickness of 40 mm and diameter of 250 mm: (a) vertical strain; (b) water loss

To study the influence of sample thickness in the crack pattern, a specimen with diameter of 225 mm and subjected to a matric suction of 59 MPa, was numerically studied by considering a model with the geometry, boundary conditions and mesh shown in Figure 3.9. This mesh contains 26798

Table 3.3: Mechanical properties of the bulk elements used to study the drying test of circular soil plates

Elastic parameters of BBM						
κ_{i_o}	κ_{i_s}	α_i	α_{ss}	p_{ref}	ν	G (MPa)
0.043	0.076	0.016	-0.80	0.10	0.42	$\frac{3K(1-2\nu)}{3(1+\nu)}$

Table 3.4: Mechanical properties of the interface elements used to study the drying test of circular soil plates

Element	E (MPa)	ν	c (MPa)	G_f (N/m)	Constitutive model
Soil – soil interface	4	0.0	–	0.8	Tensile damage
Soil – plate interfaces	4	0.0	0.35	–	J2 damage

nodes, 6179 bulk elements and 55892 interface elements, where 31176 are elements with high aspect ratio inserted between the bulk elements and 24716 consist in soil-plate interface elements.

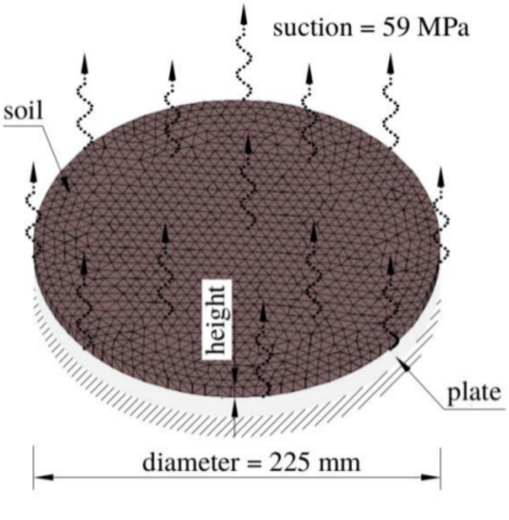

Figure 3.9: Mesh, geometry, and boundary conditions used to replicate the drying test

In this analysis, three simulations with the same material properties, mesh, and model, but different heights (4, 8, and 16 mm) were performed. The crack patterns resulting from the simulations were compared against those reported by Rodriguez *et al.* [179]. It is clear that the obtained results agree very well with the experimental ones. As can be seen, the crack pattern depends on the thickness of the soil sample. Moreover, as shown in Figure 3.10 and stated by Corte and Higashi [46], the total length of cracks decreases with increase in sample thickness.

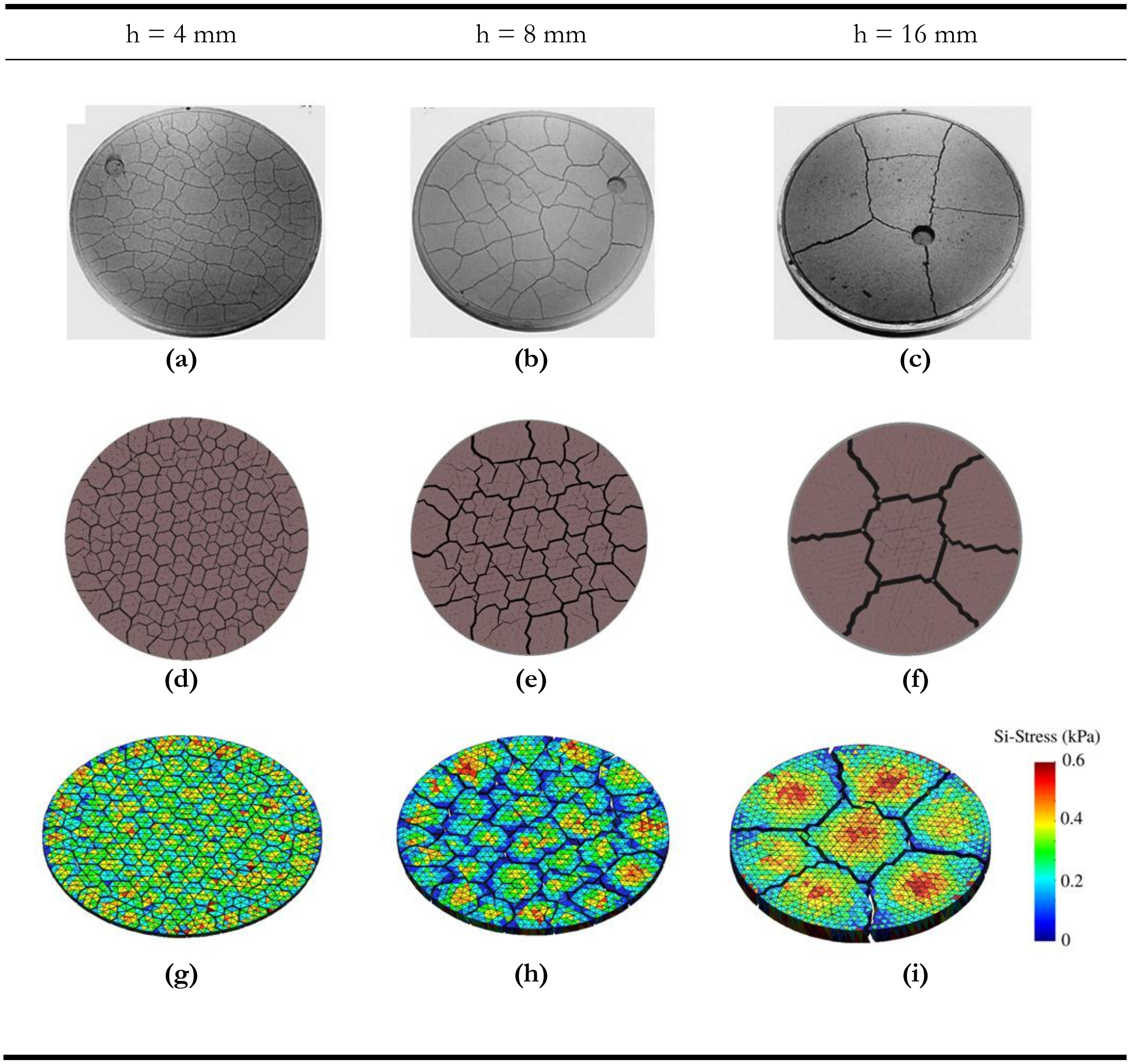

Figure 3.10: Crack patterns for different thickness: (a-c) photos of the final state of the samples (reprinted from [179]); (d-f) top views of the models with thickness equals to 4 mm, 8mm, and 16 mm, respectively; (g-i) contour of the major principal (tensile) stress at the end of the analysis

The crack process of the analysis is explained as follows. The suction, which is applied at the top surface of the soil, induces the bulk elements to shrink. This process is dictated by the nonlinear volumetric strains of the BBM. The tensile stresses increases as the elements shrink and the crack formation starts when the principal major (tensile) stress in the HAR element becomes larger than the tensile strength of the soil. Once the tensile strength has been exceeded, the degradation process of the HAR interface element is initiated according to the tensile damage model shown in Table 3.1 and the element is able to reproduce the crack behavior. Therefore, the crack process evolves as the stress field of the soil.

3.7.2 Crack Patterns Observed in a Flood Embankment

To show that the proposed technique can replicate the crack pattern observed in a field test, the field survey performed by Dyer *et al.* [60] in the flood embankment located at Thorngumbald near the city of Hull (England) is analyzed using HAR elements. In their work, the authors [60] monitored the evolution of desiccation cracks over the years in four trenches along the crest and landward slope of the embankment. In their first visit in 2003, cracks extended to a depth of 0.6 m, while in their last visit in 2006 they observed crack depth of 1 m. Figure 3.11 shows a photo of the embankment taken by Ghataora *et al.* [74], while Figures 3.12a and 3.12b contain photos taken by Dyer *et al.* [60] of the crack network in 2003 and 2006, respectively.

Figure 3.11: Photo of the landward face of the embankment (reprinted from [74])

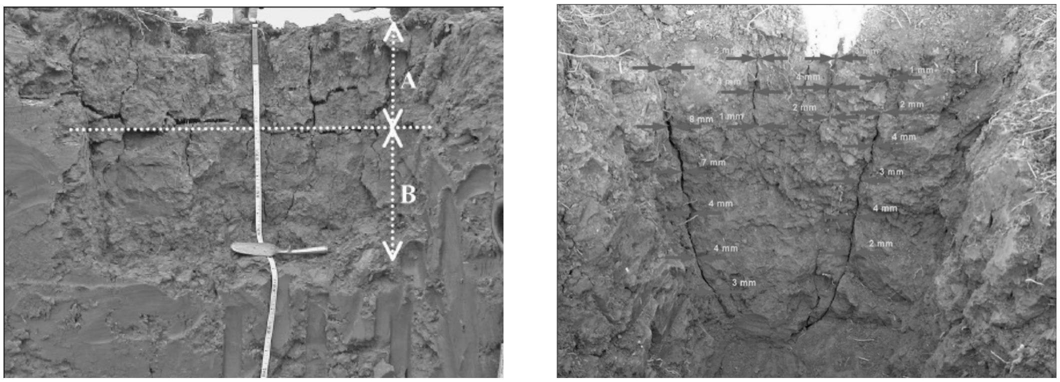

(a)

(b)

Figure 3.12: Photos of the crack patterns of the Thorngumbald embankment flood during: (a) the first visit in 2003 and (b) the third visit in 2006 (reprinted from [60])

The numerical study was conducted by considering an embankment subjected to 15 days of drying. The model assumes 2D plane strain conditions and a mesh with three-node triangular elements (9463 bulk elements, 28043 HAR elements, and 33295 nodes). Figure 3.13 illustrates the mesh, geometry and boundary conditions used to model the Thorngumbald embankment flood. The soil is assumed to be homogeneous, isotropic and initially fully saturated (*i.e.*, suction is defined as zero at $t_o = 0$). The bottom edge is fixed and the right edge present symmetry boundary

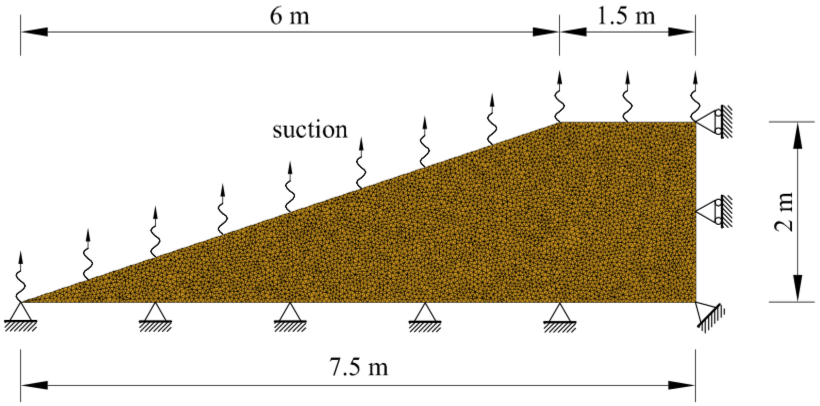

Figure 3.13: Finite element mesh, geometry, mechanical and flux boundary conditions adopted to study the Thorngumbald embankment flood

condition. In addition, suction of 17.8 MPa is imposed at the nodes lying on the top surface of the embankment. With respect to the hydraulic properties, the drying curve relating liquid saturation and suction is modeled by considering Eq. (3.31) with $P_o = 0.1$, $\lambda_o = 0.2$ and $\eta = 0$. In this case, the experimental soil-water retention curve reported by Zielinski *et al.* [218] is adopted as a reference curve. The liquid relative permeability is expressed by a cubic law and the relationship

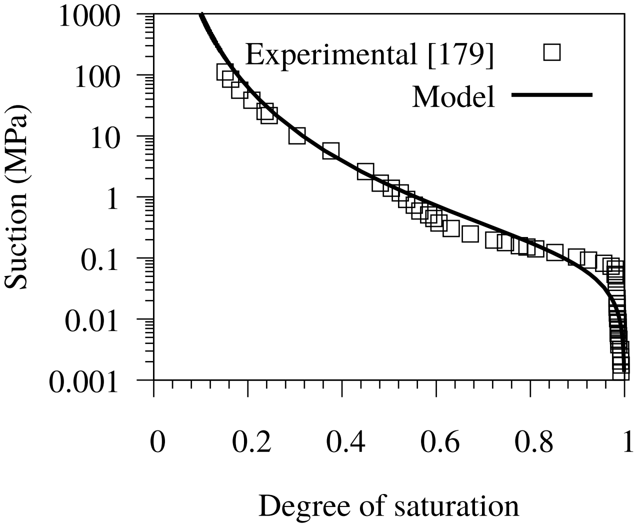

Figure 3.14: Soil-water retention curve assumed to study the Thorngumbald embankment flood

between intrinsic permeability and porosity is given by Kozeny's law:

$$\mathbf{k} = \mathbf{k}_o \frac{\phi^3}{(1-\phi)^2} \frac{(1-\phi_o)^2}{\phi_o^3} \tag{3.34}$$

where $\mathbf{k}_o = 2.0 \times 10^{-16}$ m^2 is the intrinsic permeability at a reference porosity $\phi_o = 0.3$. Finally, the mechanical properties adopted for the bulk and HAR elements are shown in Tables 3.5 and 3.6, respectively.

Figure 3.15 illustrate the crack pattern obtained via MFT at the end of the simulation. As can be seen, minimum and maximum spacing between cracks are 32 cm and 1 m, respectively, while the value of crack depth ranges from 43cm to 94 cm. In 2006, Dyer *et al.* [60] observed cracks

Table 3.5: Mechanical properties of the bulk elements adopted to model the Thorngumbald embankment flood

Elastic parameters of BBM						
κ_{i_o}	κ_{i_s}	α_i	α_{ss}	p_{ref}	ν	G (MPa)
0.011	0.005	0.0	0.0	0.1	0.42	$\frac{3K(1-2\nu)}{3(1+\nu)}$

Table 3.6: Mechanical properties of the HAR finite elements adopted to model the Thorngumbald embankment flood

Element	E (MPa)	ν	σ_u (kPa)	G_f (N/m)	Constitutive model
Soil – soil interface	4	0.0	4	2.5	Tensile damage

extending to a depth of 1 m and with spacing of 33 cm. Comparison between both results shows a reasonable agreement.

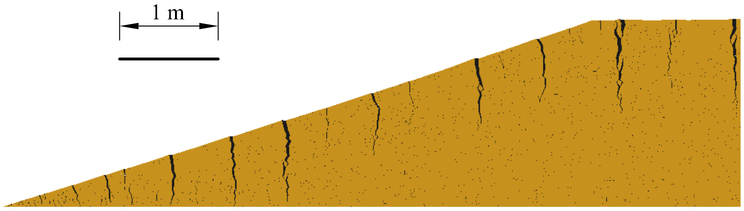

Figure 3.15: Desiccation cracks obtained via the MFT

Figure 3.16 presents the main results of the analysis. The cracks starts to develop at 22.6 h and the process is complete at 370h, which means that the humidity of the soil and in the air are in equilibrium. According to the vertical settlement in Figure 3.16b, the crack formation is initiated at early stages, when the vertical displacement is close to zero. In addition, the soil between cracks tends to curl up during the drying process. Figure 3.16c exhibits the contour of major (tensile

)principal stress and it indicates that the cracks propagate due to the concentration of tensile stresses associated to the shrinkage process. Note that the stress at HAR finite elements is zero because they are completely damaged. The compressive stresses at the lower part is related to the self weight of the soil. The liquid saturation in Figure 3.16d is characterized by fully dry HAR finite elements once the damage variable is close to 1. The P_o value of such elements decreases according to the cubic law that relates the intrinsic permeability with aperture, and consequently, they dry much faster after their degradation.

3.8 Conclusion

In this chapter, the drying crack in soils are numerically studied by using a technique that reproduces the discontinuity behavior by means of interface elements with high aspect ratio, which are introduced between the bulk elements of the finite element mesh. The proposed approach permits modeling discontinuities based on continuous concepts. Therefore, standard finite elements available in any finite element code can be adopted to treat evolving discontinuities in unsaturated soils. In addition, the HAR finite elements does not need to rely on large dummy values of stiffness to the uncracked state of the material (like the zero-thickness interface elements).

This chapter also explains the theoretical framework that describes the coupled hydro-mechanical processes involved in the study of unsaturated porous media with discontinuities. The weak form and the corresponding finite element equations are also presented.

The proposed approach is validated against two cases: (i) a laboratory experimental test and (ii) field observations. In the first study, a soil with three different thickness is modeled by using the proposed technique. The comparison of crack patterns has proved that the technique can be used to mimic the crack network and the main phenomena related to desiccation process of soils in the laboratory. The second case corresponds to a field survey of drying cracks in an embankment. The results have also shown that these special elements can also capture the crack depth and spacing observed in the field.

t = 22.6h t = 72.6h t = 370h

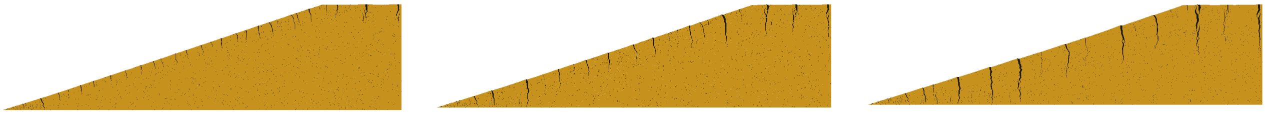

(a) Crack pattern

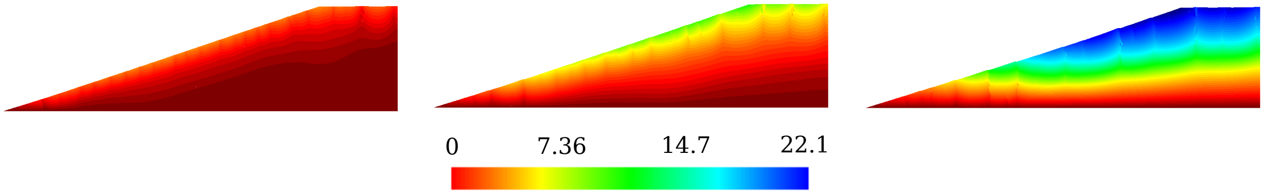

(b) Vertical settlement

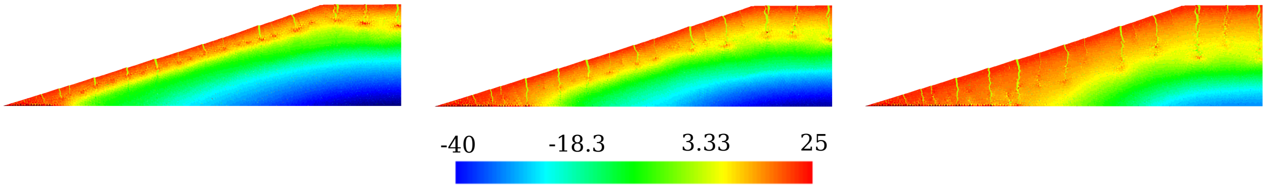

(c) Minimum stress distribution

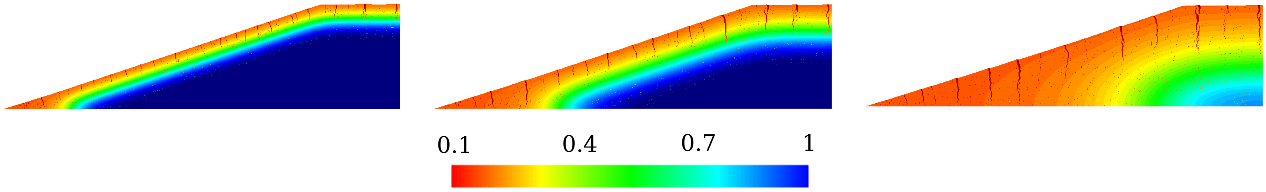

(d) Liquid Saturation

Figure 3.16: Evolution of the Thorngumbald embankment flood's results obtained via the MFT: (a) crack pattern; (b) contours of vertical displacements; (c) contours of major (tensile) principal stress; (d) contours of liquid saturation

4. MODELING EMERGING PHENOMENA IN DRYING SOILS

4.1 Introduction

The use of interface elements in the context of finite element (FE) simulations is based on the idea of introducing special elements in-between the standard (bulk) ones of a FE mesh [62, 127, 123, 124, 139, 159, 160, 184, 213]. For example, zero-thickness interface elements have been used to explicitly include the presence of discontinuities when modeling fractured rock masses [69]. This type of interface element has also been used in the meso-scale level modeling of cracks and fractures in concrete [35, 38, 61, 118, 119]. Approaches based on similar concepts, as *e.g.* cohesive zone models, have also been used in geo-engineering applications [136].

The formation and propagation of discontinuities in solids and porous media is a very challenging problem that is driving the development of both experimental [110, 117, 140, 166, 179, 181] and advanced numerical techniques [8, 11, 85, 157, 211]. In this context, the mesh fragmentation technique (MFT) in conjunction with high aspect ratio (HAR) elements have been used with success to model the problem of formation and grow of drying cracks in soils [184], as well as the problem of fracture generation and propagation in concrete structures [123, 124, 178]. Some advantages of this technique are discussed in Section 4.2.

The proper modeling of the contact between materials generally plays a critical role for a successful simulation of several problems, as for example, the shrinkage behavior of soils subjected to drying. Drying experiments show that the contact between the soil and the underlying (rigid) surface controls the formation of drying cracks, impacting in the spacing between them, their orientation and other characteristics of the crack network. For example, Peron *et al.* [166] reported that a clayey soil upon drying and under free shrinkage conditions did not crack. However, the same soil under identical environmental conditions, but with displacement restrictions at the soil-plate contact rigid-surface did develop desiccation cracks. To reproduce free shrinkage conditions the soil sample was prepared in a rectangular Teflon plate, whereas metallic rectangular notches were included at the contact between the soil and the plate to impose the restriction in the longitudinal direction. The numerical analysis of this experiment presented in Sánchez *et al.* [184] also shows that the adhesion between soil and the (no-deformable) surface controls the spacing between drying cracks. Furthermore, to properly simulate the shrinkage-restricted test discussed above, it was necessary to discretize every single notch presents at the soil-plate contact surface. An orthotropic interface mechanical model capable of distinguishing between strengths in different directions would highly facilitate the modeling of this type of problem. For example, it will minimize the time-consuming process of developing the meshes incorporating all the details of the contact surfaces that generally impact on directional adhesions and strengths. Furthermore, it will reduce the number of degree of freedoms of the problem (and therefore the associated CPU time), because the orthotropic characteristics of the contact surface(s) will be incorporated in the orthotropic mechanical model, and therefore the fine mesh generally necessary to explicitly represent textured contact surfaces will not be necessary when the directional properties are implicitly contemplated into the interface constitutive model. The benefits of an orthotropic constitutive model does not limit to the simulation of the laboratory tests discussed above, because several engineering problems are affected by the presence of orthotropic interfaces. For example, some authors suggested the term: unsaturated soil interface [83] to identify the contact surface between the more superficial and degraded soil (*i.e.* the one subjected directly to climate variations) and the underlying ground. A proper modeling of this type of interface would contribute to realistic predictions of relevant engineering problems involving this condition, such as, landslides, foundations, and slope stability. The application of the orthotropic interface model does not limit to soil mechanics only, because the presence of orthotropic surfaces have been reported in other engineering problems. For example, the study of orthotropic properties is very common in rock mechanics problems dealing with joints and discontinuities. The fracture roughness coefficient is based on an evaluation of the surface geometric properties, which generally varies with the direction of the analysis. In this context, Misra [132] proposed a micromechanical model for anisotropic discontinuities, and Li *et al.* [115] conducted an experimental research to study the anisotropic shear behavior of fractured rocks. Orthotropic models could also be useful for problems involving the analysis of indentation and micro-indentation in concrete [2].

A discrete anisotropic constitutive model was proposed by Ferrara and Pandolfi [62] and Pandolfi and Weinberg [160] to simulate the formation of cracks at inter-elemental surfaces of FE models dealing with anisotropic materials. The model was developed in the context of the zero-thickness finite element theory. Although this discrete model shares some characteristics with the orthotropic continuum damage model presented here, that one (*i.e.* [62, 157]) was designed to describe mixed-mode crack formation (with normal opening displacements), being not totally applicable to model contact and friction phenomena. Aspect that is required for describing the presence of interfaces between materials with orthotropic properties, as it occurs in the cases studied in this work.

This chapter focuses on the formulation and application of a damage orthotropic interface constitutive model developed in the framework of the MFT for dealing with problems involving contact surfaces with orthotropic strength properties and it is organized as follows. A brief review of the mesh fragmentation method is introduced first. Then, the complete mathematical formulation is presented together with the algorithm suggested for its numerical implementation. Some simple yet challenging synthetic benchmarks are analyzed to explore the model capabilities. Laboratory tests using different textures at the contact surface between materials were conducted to evaluate the strengths of the interface in different directions. These experiments were then used to validate the proposed model. Afterwards, we investigate the curling phenomenon that takes place when a thin layer of soil experiences desiccation. In all the application cases the performance of the model was very satisfactory.

4.2 Mesh Fragmentation Technique (MFT)

The MFT is a simple methodology that allows extending standard finite elements programs to deal with evolving discontinuities. After developing the FE mesh for the problem at stake, the elements are slightly reduced and thus separated from each other by a predefined (very) small distance leading to the generation of gaps between the regular elements the mesh. As a result of

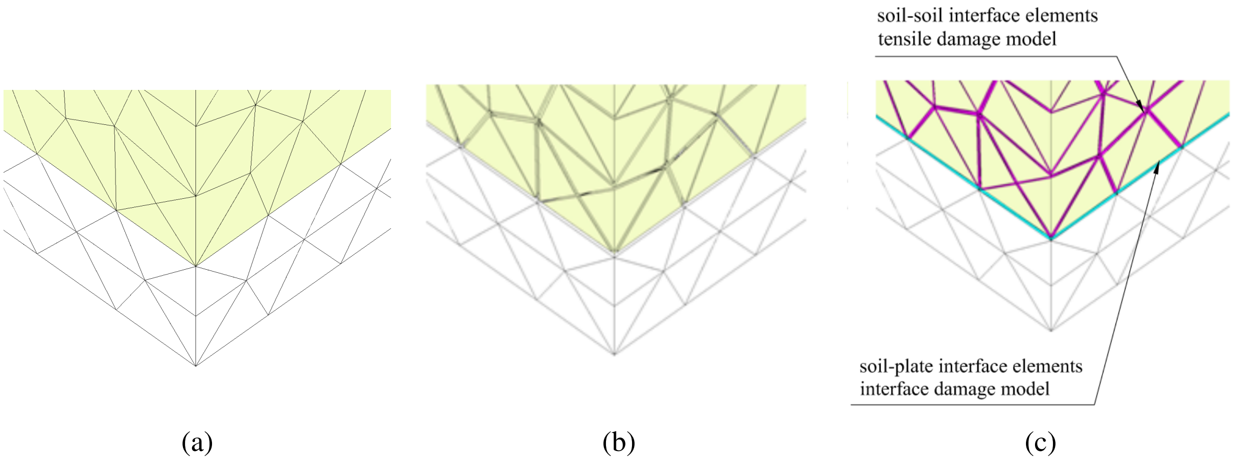

Figure 4.1: Mesh fragmentation process (modified from [121, 123]): (a) original finite element mesh; (b) soil finite elements are disconnected from each other, resulting in a fragmented mesh with spaces among elements; (c) the spaces are filled with two different types of finite elements with high aspect ratio, one that will represent the crack process (soil-soil interface elements), and other that will simulate the soil-plate interface

this process more nodes are added to the problem. These empty spaces are then filled with high aspect ratio (HAR) elements (which are introduced below). For example, Figure 4.1a corresponds to a (standard) FE mesh, while Figure 4.1b shows the mesh with the gaps between the standard FE elements and Figure 4.1c presents the final mesh with the two type HAR elements used in this research: interface element equipped with a new interface damage mechanical model (proposed in this wok) to describe the detachment of the soil from the plate; and interface elements placed in-between the standard soil elements based on a tension damage mechanical model able to simulate the formation and propagation of drying cracks.

The MFT is a very convenient that makes use of the standard FE technology, including typical interpolation functions and integration schemes [184, 125]. The HAR elements (also called interface elements in this work) were originally proposed by Manzoli *et al.* [127] to model the contact between the concrete and the reinforcement. They are basically solid triangular or tetrahedron elements, depending if dealing with 2D or 3D problems, respectively, where the high of the element is much smaller than its base. Recently, HAR elements have also been used to replicate the soil-structure interaction [125].

Figure 4.2 presents the four-node tetrahedral finite element shown, which is oriented according to the local coordinate system (n, s, l), so that the height h of the element is parallel to the $n-$axis and the area A is located in the plane (s, l). The strain tensor of such element can be split into two parts, as follows:

$$\boldsymbol{\epsilon} = \tilde{\boldsymbol{\epsilon}} + \hat{\boldsymbol{\epsilon}} \tag{4.1}$$

where $\tilde{\boldsymbol{\epsilon}}$ contains the components of the strain tensor that depends on h and the other components are grouped in $\hat{\boldsymbol{\epsilon}}$ such that:

$$\hat{\boldsymbol{\epsilon}} = \frac{1}{h} \left(\mathbf{n} \otimes [\![\mathbf{u}]\!]\right)^S \tag{4.2}$$

where $(\bullet)^S$ denotes the symmetric part of $(\bullet)$, $\mathbf{n}$ is the unit vector normal to the plane that contains the area A, $\otimes$ denotes the dyadic product, and $[\![\mathbf{u}]\!]$ is the relative displacement vector between the node 1 and its projection on the plane containing A. As shown in Manzoli, in the limit situation (*i.e.*, when h tends to zero) the components of $\hat{\boldsymbol{\epsilon}}$ become unbounded, and consequently, the measure of displacement discontinuity is given by the relative displacement vector $[\![\mathbf{u}]\!]$. The unbounded part of the strain tensor $(\hat{\boldsymbol{\epsilon}})$ can also be written in the matrix form as:

$$\hat{\boldsymbol{\epsilon}} = \begin{bmatrix} \hat{\epsilon}_{nn} & \hat{\epsilon}_{ns} & \hat{\epsilon}_{nl} \\ \hat{\epsilon}_{ns} & \hat{\epsilon}_{ss} & \hat{\epsilon}_{sl} \\ \hat{\epsilon}_{nl} & \hat{\epsilon}_{sl} & \hat{\epsilon}_{ll} \end{bmatrix} = \frac{1}{h} \begin{bmatrix} [\![u]\!]_n & \frac{1}{2}[\![u]\!]_s & \frac{1}{2}[\![u]\!]_l \\ \frac{1}{2}[\![u]\!]_s & 0 & 0 \\ \frac{1}{2}[\![u]\!]_l & 0 & 0 \end{bmatrix} \tag{4.3}$$

where $[\![u]\!]_n$, $[\![u]\!]_s$, and $[\![u]\!]_l$ are the components of the relative displacement vector according to the local coordinate system (n, s, l)

As demonstrated in Manzoli *et al.* [127], combining HAR elements with appropriate strain softening constitutive models, it is possible to describe the kinematics associated with the formation of displacement discontinuities according to the Continuous Strong Discontinuous Approach (CSDA). The mechanical constitutive models adopted in this wok are introduced next. The two damage constitutive laws associated with the HAR elements introduced at soil-plate interface and between bulk (soil) elements are described first. Then, the non-linear elastic model

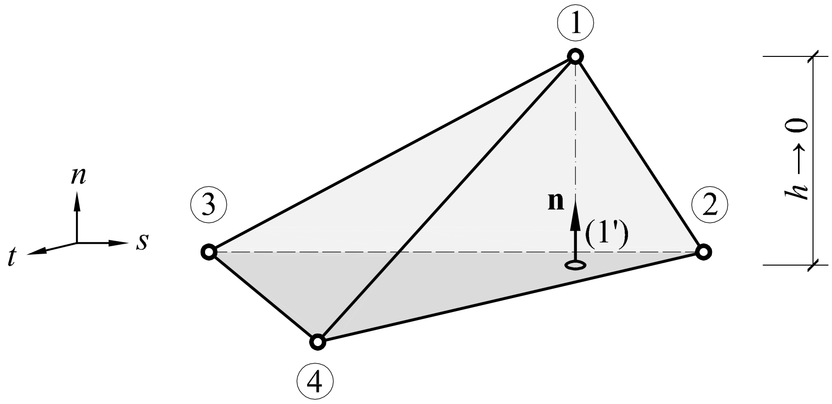

Figure 4.2: Four-node tetrahedral finite element (reprinted from [125])

adopted to simulate the soil behavior associated with the standard FE is discussed.

4.3 Orthotropic Interface Model

To reproduce the orthotropic character of interface surfaces, a model that considers two damage criteria is proposed hereafter in terms of the shear components of the stress tensor parallel to the base of the interface element, as follows:

$$f_s = ||\sigma_{ns}|| + \alpha_s \sigma_{nn} - q_s(r_s) \leq 0 \tag{4.4}$$

$$f_l = ||\sigma_{nl}|| + \alpha_l \sigma_{nn} - q_l(r_l) \leq 0 \tag{4.5}$$

where q_s and q_l are stress-like internal variables, r_s and r_l are strain-like internal variables, and α_s and α_l are the model parameters that control the influence of the component of the normal stress tensor $\sigma_{nn} \leq 0$

The model is expressed by the following constitutive equation relating the components of the stress tensor ($\boldsymbol{\sigma}$) and the strain tensor ($\boldsymbol{\epsilon}$) according to the local coordinate system $(n,\ s,\ l)$:

$$\underbrace{\begin{bmatrix} \sigma_{nn} & \sigma_{ns} & \sigma_{nl} \\ \sigma_{ns} & \sigma_{ss} & \sigma_{sl} \\ \sigma_{nl} & \sigma_{sl} & \sigma_{ll} \end{bmatrix}}_{\boldsymbol{\sigma}} = \underbrace{\begin{bmatrix} \bar{\sigma}_{nn} & 0 & 0 \\ 0 & \bar{\sigma}_{ss} & \bar{\sigma}_{sl} \\ 0 & \bar{\sigma}_{sl} & \bar{\sigma}_{ll} \end{bmatrix}}_{\bar{\boldsymbol{\sigma}}_{nsl}} + (1-d_s) \underbrace{\begin{bmatrix} 0 & \bar{\sigma}_{ns} & 0 \\ \bar{\sigma}_{ns} & 0 & 0 \\ 0 & 0 & 0 \end{bmatrix}}_{\bar{\boldsymbol{\tau}}_s} + (1-d_l) \underbrace{\begin{bmatrix} 0 & 0 & \bar{\sigma}_{nl} \\ 0 & 0 & 0 \\ \bar{\sigma}_{nl} & 0 & 0 \end{bmatrix}}_{\bar{\boldsymbol{\tau}}_l} \tag{4.6}$$

where $d_s \in [0, 1]$ and $d_l \in [0, 1]$ are the scalar damage variables,

$$\begin{bmatrix} \bar{\sigma}_{nn} & \bar{\sigma}_{ns} & \bar{\sigma}_{nl} \\ \bar{\sigma}_{ns} & \bar{\sigma}_{ss} & \bar{\sigma}_{sl} \\ \bar{\sigma}_{nl} & \bar{\sigma}_{sl} & \bar{\sigma}_{ll} \end{bmatrix} = \mathbb{C} : \begin{bmatrix} \varepsilon_{nn} & \varepsilon_{ns} & \varepsilon_{nl} \\ \varepsilon_{ns} & \varepsilon_{ss} & \varepsilon_{sl} \\ \varepsilon_{nl} & \varepsilon_{sl} & \varepsilon_{ll} \end{bmatrix} \tag{4.7}$$

where $\bar{\boldsymbol{\sigma}}$ is the elastic stress tensor (*i.e.*, the stresses related to the intact, undamaged, cross section, also known as effective stress in damage models) and $\mathbb{C}$ is the isotropic fourth-order elastic tensor.

Dividing Eqs. (4.4) and (4.5) by $(1 - d_s)$ and $(1 - d_l)$, respectively, the damage criteria can be expressed in terms of the elastic stresses, as:

$$\bar{f}_s = ||\sigma_{ns}|| + \alpha_s \bar{\sigma}_{nn} - r_s \leq 0 \tag{4.8}$$

$$\bar{f}_l = ||\sigma_{nl}|| + \alpha_l \bar{\sigma}_{nn} - r_l \leq 0 \tag{4.9}$$

where $r_s = (q_s - d_s \alpha_s \bar{\sigma}_{nn})/(1 - d_s)$ and $r_l = (q_l - d_l \alpha_l \bar{\sigma}_{nn})/(1 - d_l)$. $\bar{\sigma}_{ns}$ and $\bar{\sigma}_{nl}$ are the shear components of the elastic stress tensor, which is evaluated from the strains by linear elastic relationship (4.7). They are related to the stress components σ_{ns} and σ_{nl} by means of constitutive Eq. (4.6), so that $\sigma_{ns} = (1 - d_s)\bar{\sigma}_{ns}$ and $\sigma_{nl} = (1 - d_l)\bar{\sigma}_{nl}$. The corresponding strain-like internal variables, r_s and r_l, are obtained (after some algebra) from the following explicit evolution laws:

$$r_s = \max_{\tau \in [0,t]} [||\bar{\sigma}_{ns}(\tau)|| + \alpha_s \bar{\sigma}_{nn}(\tau), q_{s_o}] \tag{4.10}$$

$$r_l = \max_{\tau \in [0,t]} [||\bar{\sigma}_{nl}(\tau)|| + \alpha_l \bar{\sigma}_{nn}(\tau), q_{l_o}] \tag{4.11}$$

where t is the pseudo-time associated with the loading process. According to Eqs. (4.10) and (4.11), the variables r_s and r_l will adopt the maximum value associated with the corresponding elastic stresses (*i.e.*, $||\bar{\sigma}_{ns}|| + \alpha_s \bar{\sigma}_{nn}$ and $||\bar{\sigma}_{nl}|| + \alpha_l \bar{\sigma}_{nn}$, respectively) to be reached during the loading process, starting from the initial values (*i.e.*, q_{s_o} and q_{l_o}, respectively), which are regarded as material properties. Note that these variables are explicitly evaluated, since they depend on the components of the elastic components only, which are obtained explicitly from the strain components, via linear elastic relationship (4.7). Once these interval variables are obtained for each time step during the loading process, the damage variables can be evaluated from the following damage evolution rules in terms of the internal variables r_s and r_l:

$$d_s(r_s) = \frac{r_s - q_s}{r_s - \alpha_s \bar{\sigma}_{nn}} \tag{4.12}$$

$$d_l(r_l) = \frac{r_l - q_l}{r_l - \alpha_l \bar{\sigma}_{nn}} \tag{4.13}$$

The Kuhn-Tucker relations can be expressed as:

$$\bar{f}_{s,l} < 0, \quad \dot{r}_{r,l} > 0, \quad \dot{r}_{s,l} \bar{f}_{s,l} = 0 \tag{4.14}$$

The constitutive model is completed with the consistency condition, as follows:

$$\dot{r}_{s,l} \dot{\bar{f}}_{s,l} = 0 \quad \text{if} \quad \bar{f}_{s,l} = 0 \tag{4.15}$$

To represent the soil-plate interface, the stress-like variables are assumed to be constant:

$$q_s(r_s) = q_{s_o} = \beta_s \tag{4.16}$$

$$q_l(r_l) = q_{l_o} = \beta_l \tag{4.17}$$

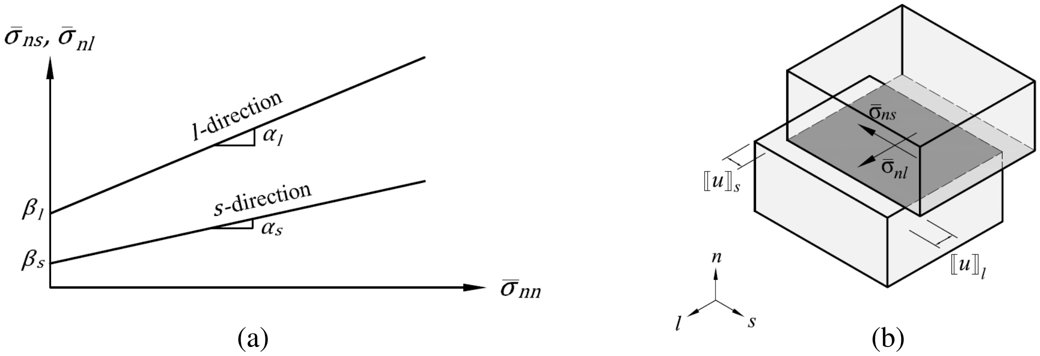

(a) (b)

Figure 4.3: Reprinted from [125]: (a) schematic representation of the orthotropic model with the option to define different strengths in two orthogonal directions; (b) plot showing the sliding at the interface between materials, with the corresponding displacement jumps in two orthogonal directions

where β_s and β_l are the cohesive bonding strengths of the soil-plate interface in directions s and l, respectively. Figure 4.3 presents a schematic representation of this model.

4.3.1 Tension Damage Model

The tension damage model used to describe cracks formation in the soil has the same structure as the previous model and other ones published before (*e.g.* [62, 159]). The constitutive equation in this case is given by:

$$\boldsymbol{\sigma} = (1 - d)\bar{\boldsymbol{\sigma}} \tag{4.18}$$

and the damage criterion is written in terms of the component of the stress normal to the element base:

$$f = \sigma_{nn} - q(r) \leq 0 \tag{4.19}$$

or in terms of the effective stress as:

$$\bar{f} = \bar{\sigma}_{nn} - r \leq 0 \tag{4.20}$$

The evolution of the stress-like variable is given by an exponential softening law of the form:

$$q(r) = \sigma_u \, \exp\left[\frac{\sigma_u^2}{G_f \, E}\left(1 - \frac{r}{\sigma_u}\right)\right] \tag{4.21}$$

where E is the Young's modulus, σ_u is the tensile strength and G_f is the mode I fracture energy of the soil. More details can be found elsewhere (*i.e.*, [123, 184]).

4.3.2 Implicit-Explicit Integration Scheme (IMPL-EX)

The implicit-explicit (IMPL-EX) integration algorithm proposed by Oliver *et al.* [153] was adopted in this work to update the stresses using the new orthotropic law. The IMPL-EX is a robust, efficient and stable numerical scheme to integrate mechanical models. A similar approach to the one suggested in Manzoli *et al.* [123] was followed in this chapter. Table 4.1 summarizes the main stages associated with the update of the stresses at a pseudo-time step $t_{(n+1)}$ using the orthotropic damage models with the IMPL-EX method. Note that any other algorithm (*i.e.*, implicit or explicit) could be adopted for the integration of the proposed constitutive model. However, based on our experience, the IMPL-EX method is very appropriate to deal with this type of problem.

4.4 Applications

This section is related to the application of the proposed model to different cases involving orthotropic interfaces. The first case consists of a series of synthetic benchmarks based on theoretical cases aimed at checking the capability of the proposed model to reproduce different possible orientations of the orthotropic interface respect to the loading direction. The second application focuses on the validation of the orthotropic mechanical model by using laboratory tests involving the shearing of soil specimens against plates especially grooved in different directions. Finally, the suggested model is applied to solve the slab test reported in Peron *et al.* [166].

All the examples were modeled using four-node tetrahedral finite elements. The Mohr-Coulomb type orthotropic damage model was used to describe the behavior of the interfaces between different materials. Following the MFT, interface elements with high aspect ratio were introduced between regular elements, which were modeled assuming a linear elastic behavior.

Table 4.1: IMPL-EX integration scheme for the orthotropic damage model

```
INPUT: $\boldsymbol{\epsilon}_{(n+1)}, \bar{\sigma}_{nn_{(n)}}, r_{s_{(n)}}, \Delta r_{s_{(n)}}, r_{l_{(n)}}, \Delta r_{l_{(n)}}$
  (i) Transform the current strain tensor obtaining its components according to the local coordinate system $(n, s, l)$
  (ii) Compute the elastic stress tensor
         $\bar{\boldsymbol{\sigma}}_{(n+1)} := \mathbb{C} : \boldsymbol{\epsilon}_{(n+1)}$
  (iii) Check the loading-unloading conditions.
      (a) in direction $s$
          IF $\left(||\bar{\sigma}_{ns_{(n+1)}}|| + \alpha_s\,\bar{\sigma}_{nn_{(n+1)}} - r_{s_{(n)}} \leq 0\right)$ THEN
              keep the threshold: $r_{s_{(n+1)}} := r_{s_{(n)}}$
          ELSE
              update the damage threshold: $r_{s_{(n+1)}} := ||\bar{\sigma}_{ns_{(n+1)}}|| + \alpha_s\,\bar{\sigma}_{nn_{(n+1)}}$
          END IF
      (b) in direction $l$
          IF $\left(||\bar{\sigma}_{nl_{(n+1)}}|| + \alpha_l\,\bar{\sigma}_{nn_{(n+1)}} - r_{l_{(n)}} \leq 0\right)$ THEN
              keep the threshold: $r_{l_{(n+1)}} := r_{l_{(n)}}$
          ELSE
              update the damage threshold: $r_{l_{(n+1)}} := ||\bar{\sigma}_{nl_{(n+1)}}|| + \alpha_l\,\bar{\sigma}_{nn_{(n+1)}}$
          END IF
  (iv) Compute the strain-like internal variable increments
         $\Delta r_{s_{(n+1)}} := r_{s_{(n+1)}} - r_{s_{(n)}}; \quad \Delta r_{l_{(n+1)}} := r_{l_{(n+1)}} - r_{l_{(n)}}$
  (v) Compute the explicit linear extrapolation of the strain-like internal variable
         $\tilde{r}_{s_{(n+1)}} := r_{s_{(n)}} + \frac{\Delta t_{(n+1)}}{\Delta t_{(n)}}\Delta r_{s_{(n)}}; \quad \tilde{r}_{l_{(n+1)}} := r_{l_{(n)}} + \frac{\Delta t_{(n+1)}}{\Delta t_{(n)}}\Delta r_{l_{(n)}}$
  (vi) Update the damage variables
         $\tilde{d}_{s_{(n+1)}} := \frac{\tilde{r}_{s_{(n+1)}} - \beta_s}{\tilde{r}_{s_{(n+1)}} - \alpha_s\,\bar{\sigma}_{nn_{(n)}}}; \quad \tilde{d}_{l_{(n+1)}} := \frac{\tilde{r}_{l_{(n+1)}} - \beta_l}{\tilde{r}_{l_{(n+1)}} - \alpha_l\,\bar{\sigma}_{nn_{(n)}}};$
  (vii) Compute the stress tensor according to Eq. (4.6)
         $\tilde{\boldsymbol{\sigma}}_{(n+1)} := \bar{\boldsymbol{\sigma}}_{nsl_{(n+1)}} + \left(1 - \tilde{d}_{s_{(n+1)}}\right)\bar{\boldsymbol{\tau}}_{s_{(n+1)}} + \left(1 - \tilde{d}_{l_{(n+1)}}\right)\bar{\boldsymbol{\tau}}_{l_{(n+1)}}$
  (viii) Rotate the stress tensor obtaining its components according to the global coordinate system $(x, y, z)$

OUTPUT: $\tilde{\boldsymbol{\sigma}}_{(n+1)}, \bar{\sigma}_{nn_{(n+1)}}, r_{s_{(n+1)}}, \Delta r_{s_{(n+1)}}, r_{l_{(n+1)}}, \Delta r_{l_{(n+1)}}$
```

4.4.1 Synthetic Benchmarks

The theoretical cases are based on two square blocks with an interface between them (Figure 4.4). One block (*i.e.* block A) is fixed to a wall with displacements restricted in all directions. In the other block (*i.e.* block B) a displacement field is imposed simultaneously on the four free nodes in the vertical plane with an inclination of 45^o, as shown in Figure 4.5a. It is assumed that the interface between blocks is grooved in one direction, restricting the relative movement between blocks in the orthogonal direction to the grooves. Four different cases are study to explore the capability of the proposed technique to reproduce the orthotropic behavior of the interfaces. The different cases are generated by placing the grooves in different orientations with respect to the direction of the imposed displacement field. The orthotropic model can simulate this type of problem by assigning different strengths to the two dominant directions existing in this problem. In all the cases considered below, it is assumed that the strength in the direction perpendicular to the grooves is much higher than the one related to the direction of the grooves. Table 4.2 lists the material properties of the blocks and interface. A total of 16 nodes and 30 elements were used to simulate this problem, 24 of them are 3D bulk elements (*i.e.* to model the 2 blocks) and 6 are HAR interface elements (they were placed at the interface between the 2 blocks only to simulate the contact behavior).

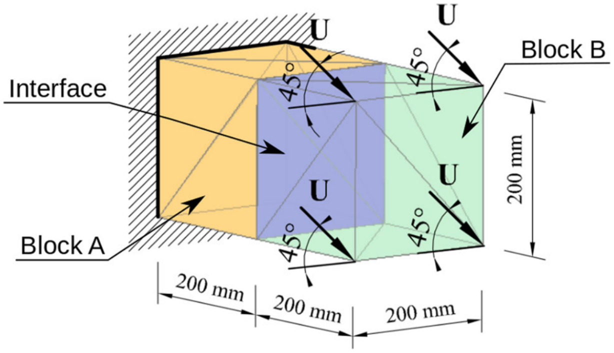

Figure 4.4: Geometry and boundary conditions related to the proposed synthetic benchmark (reprinted from [125])

Table 4.2: Properties of the blocks and interface used to study the synthetic benchmarks

Element	E (GPa)	ν	α_s	α_l	β_s (MPa)	β_l (MPa)	Constitutive model
Blocks (bulk)	30	0.0	-	-	-	-	Elastic
Block-block interfaces	30	0.0	0.00	0.00	90	300	Orthotropic damage

In the first case the grooves coincide with direction of the imposed displacement (Figure 4.5b). Under this condition, the relative movement between blocks is not restricted, this implies that block A does not deform, while block B freely slides along the grooves at 45^o (*i.e.* without deforming). In the second case the grooves are placed perpendicular to the direction of the imposed displacement field (Figure 4.5c). This implies that the relative movement between the two blocks is fully restricted and the two blocks deform as a monolithic body. The third case corresponds to the grooves oriented in the vertical direction (*i.e.* at 45^o respect to the imposed displacement field). In this case both blocks deform as a single piece in the x-direction, while sliding occurs in the y-direction (Figure 4.5d). In the last case the grooves are oriented in the x-direction (Figure 4.5e), therefore the blocks deform as a single body in the y-direction, and the adopted interface enables the sliding in the x-direction.

The top drawings in Figure 4.5 show the orientation of the grooves adopted in the different cases. The bottom ones show the deformed blocks after applying the displacement field (*i.e.* solid line), alongside their initial positions before loading (*i.e.* dashed line). It can be observed that the orthotropic model manages to reproduce very satisfactory the anticipated behavior under these different conditions, allowing sliding between blocks in the direction along the grooves only.

Once the capability of the orthotropic model to qualitatively reproduce the behavior of orthotropic interfaces through these challenging synthetic benchmarks was checked, the ability of the model to simulate the experimental behavior of this type of problem was investigated, as explained in the next section.

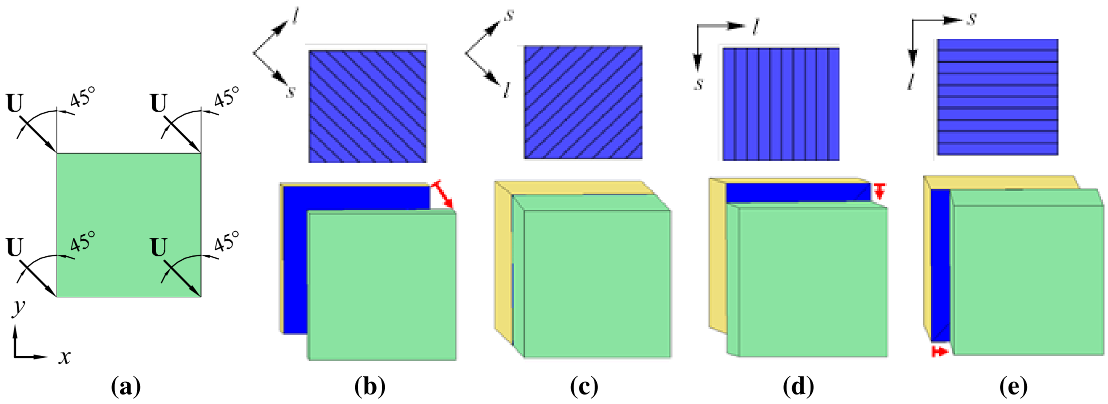

Figure 4.5: Failure envelopes related to the direct shear tests (reprinted from [125]): (a) experimental, and (b) numerical results [125]

4.4.2 Experimental Validation of the Orthotropic Model

A conventional direct shear apparatus was adapted to study the shear strength between soil-plate interfaces. The modification basically consisted of placing a square plate between the top and the bottom portions of the direct shear box device. Figure 4.6a shows a front view of the modified apparatus with the acrylic plate placed in-between the two portions of the shear box. Figure 4.6b corresponds to a top view of the adapted box. The study of soil interfaces of unsaturated soils was conducted before by Miller and Hamid [130] and Hamid and Miller [83] using a similar approach.

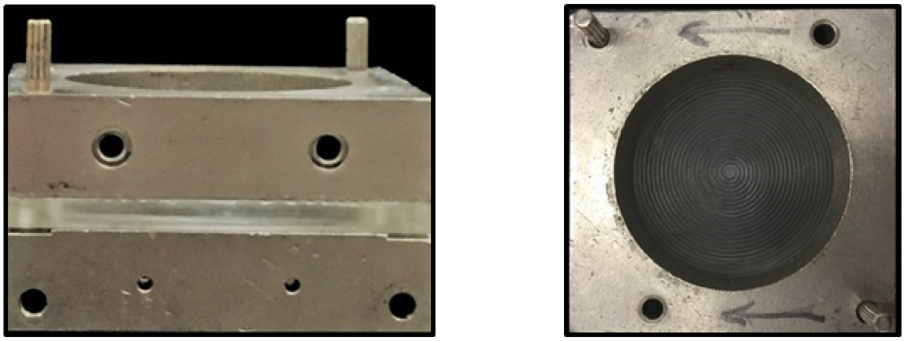
(a)
(b)

Figure 4.6: Modified direct shear box for testing soil–plate interface strength: (a) front photograph; (b) top photograph (reprinted from [125])

Acrylic square bases (88.9 mm side) and 6 mm high were grooved to study the effect of different interface textures on the shear strength. Triangular grooves 1 mm deep and spaced every 1.5 mm were machined following two main patterns: i) spiral, and ii) straight. Three sets of direct shear tests were conducted with these two plates: i) using the circular indentations (Figure 4.7a); ii) orienting the straight grooves perpendicular to the shearing direction (Figure 4.7b); and iii) placing the straight grooves parallel to the shearing direction (Figure 4.7c). The orientation of the local coordinate system (s, l) depends on the direction of the grooves, where s coincide with the direction of the grooves and l is perpendicular to them. Note that for the circular case, the coordinate system depends on the point under consideration and therefore l corresponds to the radial direction and s to the tangential one (Figure 4.7a). Two additional sets of direct shear tests were conducted, one of them using a smooth plate (Figure 4.7d); and another one to study the soil-soil shear strength, without interface (*i.e.* a standard direct shear test).

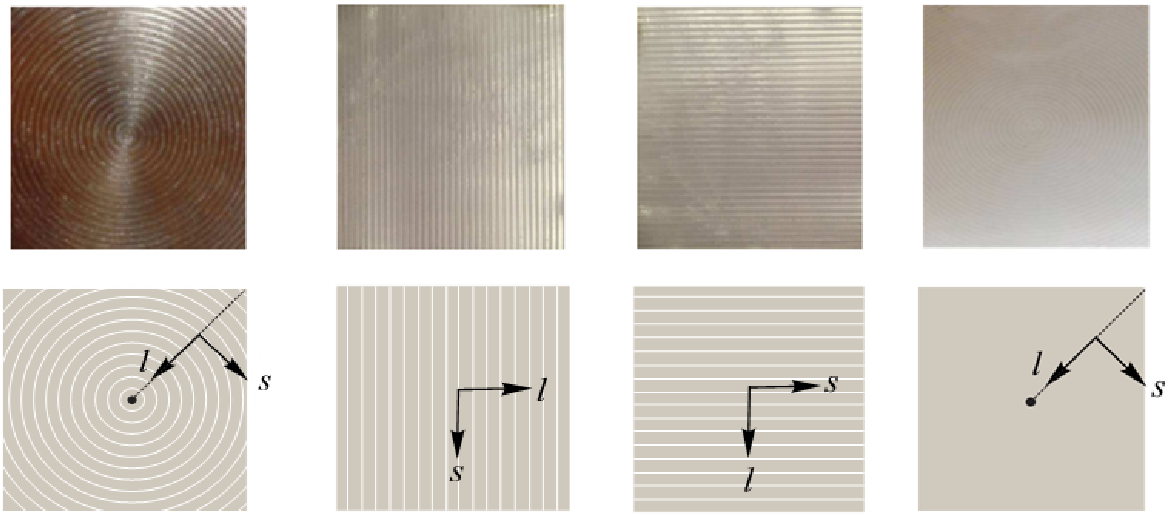

(a) **(b)** **(c)** **(d)**

Figure 4.7: Different types of plate surfaces: (a) spiral grooves, (b) grooves oriented orthogonal respect to the shear direction, (c) grooves oriented parallel to the shear direction, and (d) smooth surface (reprinted from [125])

The test protocol was the usual one for the direct shear test [13]. The shear tests were conducted for the four sets of experiments (*i.e.* circular indentations, straight grooves parallel and orthogonal to the shearing direction, smooth plates and soil-soil strength) at three different normal stresses: i) 0 kPa, ii) 6.2 kPa, and iii) 15.5 kPa. The specimens were sheared at a very low rate (*i.e.* 0.018 mm/min) to emulate drained conditions. Shearing was continued until the peak value of the shear force was clearly obtained or until it becomes almost constant. The tests were conducted up to a maximum displacement of around 9 mm. The tests were simulated using the MFT incorporating the orthotropic mechanical model to account for the different textures of the soil-plate interfaces discussed above. Figure 4.8 presents the main components incorporated in the modeling of these tests, *i.e.* interfaces (Figure 4.8a), shear-box, plates and soil (Figure 4.8b). Figure 4.8c shows all the model components together. The total number of nodes is 3928, with a total number of elements of 12154, where 8542 corresponds to bulk elements and 3612 to interface elements, which were placed at the plate-soil, and (shear) box-soil contacts only. A mesh convergence study was conducted to investigate the effect of the mesh size on the model outputs. It was observed that the adopted mesh yield results that are (almost) identical to the ones obtained with finer ones. Figure 4.9a shows the geometry of the problem and the adopted mesh before loading. Figure 4.9b presents the deformed mesh after applying the vertical load ($\mathbf{F}_n$), and Figure 4.9c shows the mesh after shearing the sample. Figure 4.10a presents the evolution of shear stress against the horizontal displacements for two experiments carried out under two different loading conditions, as follows: under a vertical stress of 15.5 kPa, and without a vertical load. In both cases the grooves were placed orthogonal to the shear direction. In both tests the shear stress increased (almost) monotonically until reaching the maximum value, and then remained (approximately) constant as the specimen continued deforming. As expected, the maximum shear depends on the applied vertical stress. Similar patterns of behavior were observed in the other experiments performed in the context of this study.

Figure 4.11 presents a summary in terms of failure envelopes of all the shear tests conducted under the different conditions discussed above. As it could be anticipated, the higher strength is obtained for the soil-soil experiments and the lower one for those tests involving the smooth plate.

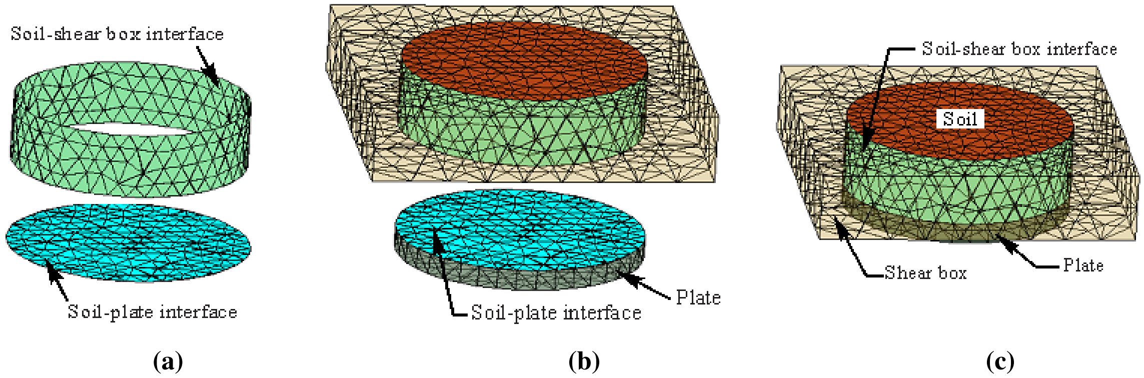

Figure 4.8: Modeling of direct shear tests, main components (reprinted from [125]): (a) interfaces formed formed with HAR FEs, (b) interfaces, shear box, plates and soil; and (c) final FE mesh with all the components to simulate the test

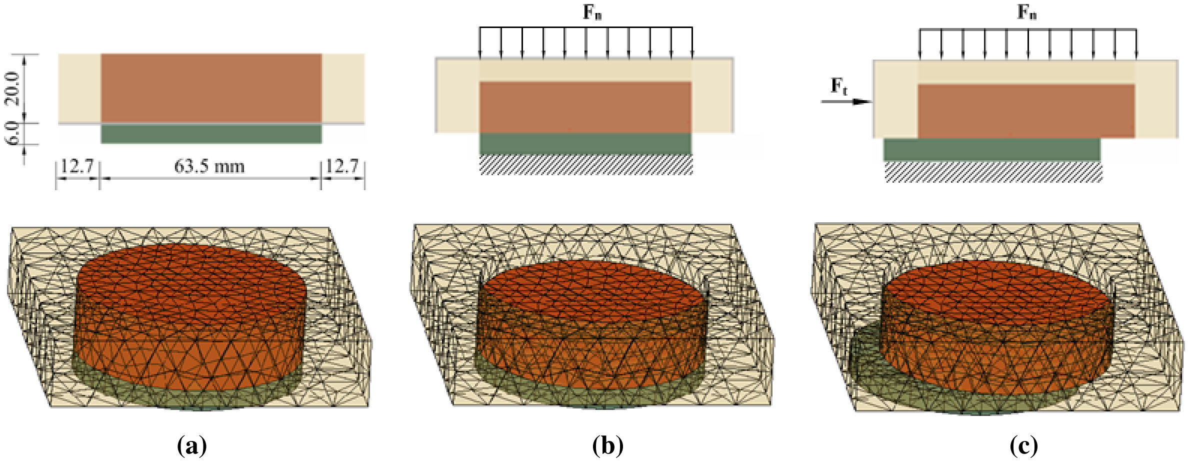

Figure 4.9: Modeling of the direct shear test of soil-plate interfaces (reprinted from [125]): (a) before testing, (b) deformed specimen after applying the vertical load $\mathbf{F}_n$ at the top, and (c) deformed specimen after shearing

The soil-plate strength for the base with the grooves oriented perpendicular to the direction of shearing is very high, similar to the soil-soil case, indicating that (under these conditions) the soil is strongly bonded to the plate and the shearing take places between soil-soil particles mainly. As it could be anticipated, the strength for the case of indentations oriented parallel to the shear direction is lower than the orthogonal one discussed above. As expected, the results involving the circular plate are in-between the ones obtained for the parallel and orthogonal cases. It is also observed that the different interfaces affect mainly the interception (*i.e.* b) of the linear envelope adopted to define shear strength, and the impact on the envelop inclination (*i.e.* a) is relatively minor.

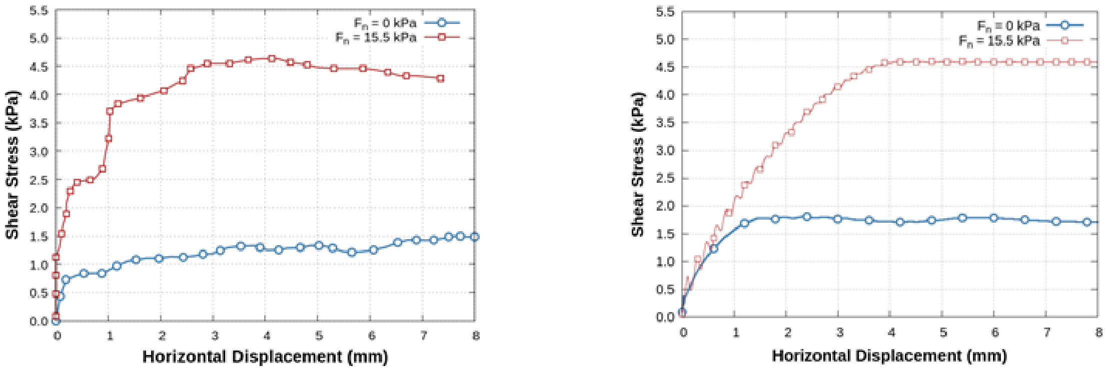

(a) (b)

Figure 4.10: Reprinted from [125]: shear force against horizontal displacements when load is applied perpendicular to the grooves (*i.e.*, Figure 4.7b): (a) experimental results; (b) numerical outputs

The following strategy was adopted to model the experiments involving grooves: two of them were used to obtain the model parameters and the third one was reserved for the model validation. The available experimental data (*i.e.* Figure 4.11a) was used to determine the strength parameters (*i.e.* b and a) for the case in which the shearing direction is perpendicular and parallel to the grooves. Afterwards, the circular case was used to validate the model using the same parameters adopted for the plates with straight grooves. As for the soil-soil and smooth cases, the parameters were adjusted based on the test results presented in Figure 4.11a. The material properties of the soil, plate, shear box and interfaces are listed in Table 4.3.

Figure 4.11b presents the results of the numerical simulations using the MFT together with the orthotropic mechanical model. It can be observed that the proposed orthotropic model is able to reproduce very satisfactorily the global experimental trends. In particular, the model manages to simulate that the strength of the case involving the circular grooves (acting as a benchmark case in this modeling) is in-between the strength obtained for the grooves parallel and orthogonal to the

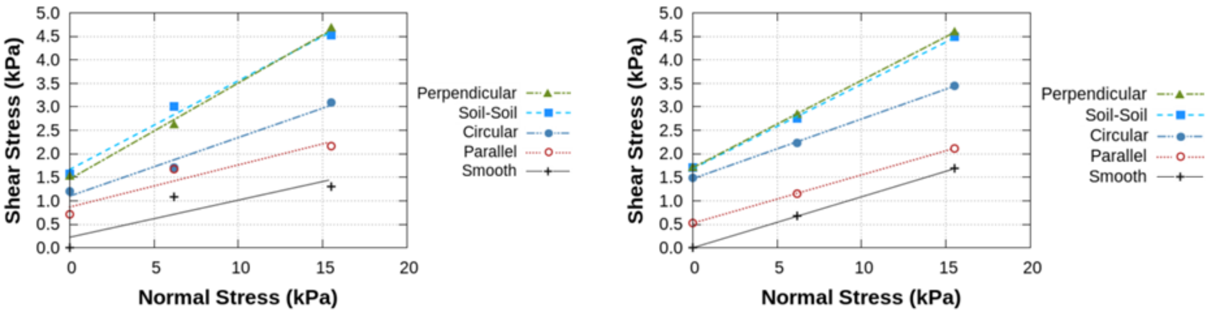

(a) **(b)**

Figure 4.11: Failure envelopes related to the direct shear tests (reprinted from [125]): (a) experimental, and (b) numerical results

Table 4.3: Material properties of soil, pate, shear box and interfaces used in the numerical analysis of the interface shear test

Element	E (kPa)	ν	α_s	α_l	β_s (kPa)	β_l (kPa)	Constitutive model
Soil (bulk)	40	0.2	-	-	-	-	Elastic
Plate	210×10^6	0.2	-	-	-	-	Elastic
Shear box	210×10^6	0.2	-	-	-	-	Elastic
Soil-shear box interfaces	40	0.0	0.00	0.00	0.00	0.00	Orthotropic damage
Soil-plate interfaces (soil-soil)	40	0.0	0.19	0.19	1.67	1.67	Orthotropic damage
Soil-plate interfaces (smooth)	40	0.0	0.11	0.11	0.00	0.00	Orthotropic damage
Soil-plate interfaces (perpendicular)	40	0.0	0.11	0.19	0.50	1.67	Orthotropic damage
Soil-plate interfaces (parallel)	40	0.0	0.11	0.19	0.50	1.67	Orthotropic damage
Soil-plate interfaces (circular)	40	0.0	0.11	0.19	0.50	1.67	Orthotropic damage

shearing directions.

4.4.3 Modeling a Slab Desiccation Tests with Orthotropic Characteristics

The desiccation tests conducted by Peron *et al.* [166] were selected to show the capabilities of the proposed approach to simulate the formation of cracks when orthotropic conditions at the soil-plate contact prevail. The experiments were based on slab samples prepared from clay slurries. Two types of contact surface were investigated:

(i) smooth contact between soil and plate;

(ii) longitudinal restricted displacement induced by the inclusion of notches at soil-plate the contact surface (Figure 4.12a).

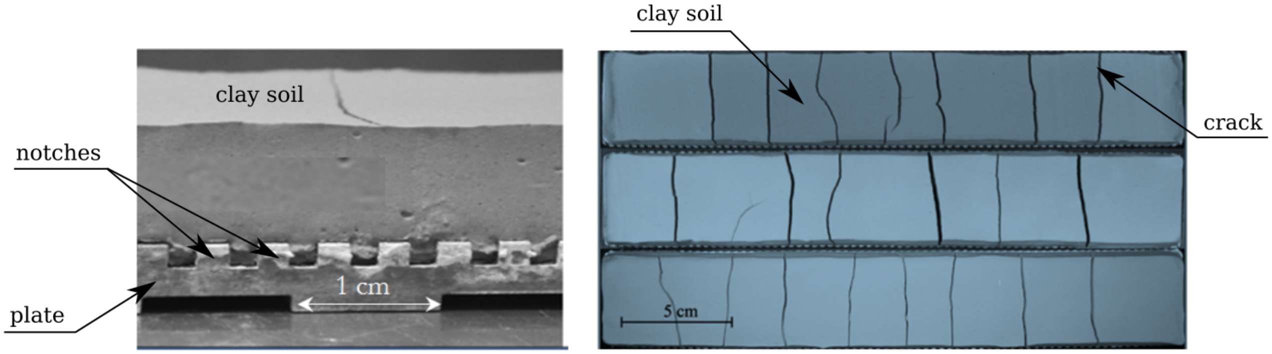

(a) (b)

Figure 4.12: Drying tests on saturated clay samples prepared in slab plates (reprinted from [166]): a detail of the soil slap contact showing the 2-mm notches, b typical examples of crack formation in 3 different soil samples (2009 Canadian Science Publishing or its licensors. Reproduced with permission)

As for the free shrinkage case (*i.e.* type i above), a base made of Teflon was used in combination with the application of a hydrophobic substance to prevent any displacement constrains at the soil-plate contact. Peron *et al.* [166] reported that all the specimens subjected to this drying condition did not crack. Sánchez *et al.* [184] modeled this experimental behavior using the MFT in conjunction with an isotropic constitutive model for the soil-plate interface that allows free displacements. As expected, tensile horizontal stresses in the soil did not developed and drying cracks did not formed. Similar behavior (*i.e.* shrinkage without cracking) has been observed in other investigations involving smooth contact soil-plate surface (*e.g.* [217]) In relation to the tests conducted under constrained desiccation conditions (*i.e.* case ii) above), the slurry samples were prepared in a similar manner as in the free drying tests, but the Teflon base was replaced by a metal surface with 2mm spaced parallel notches (Figure 4.12a). These notches created a constraint at the bottom surface, in the longitudinal direction only. Samples subjected to drying under these conditions experienced one-directional cracks only, and in the direction parallel to the constraint (Figure 4.12b). In the following sections this test is modeled using two different approaches: i) first the simulation of the experiment is conducted including the actual geometry of the notches in the mesh discretization, together with the adoption of an isotropic constitutive model for the soil-plate surface; ii) then a planar plate surface is assumed in conjunction with the proposed orthotropic mechanical model to account for the orthotropic characteristic of this problem.

In both cases the drying process is simulated by imposing an increasing uniform volumetric strain field to the bulk elements of the soil that is equivalent to the shrinkage induced during water evaporation in the soil mass. There is not an external load in addition to the self-weight. It is further assumed that the plate is fixed to the ground and therefore cannot move in any direction during the drying process, as indicated in Figure 4.13.

4.4.3.1 Modeling the Contact Between Materials with an Isotropic Mechanical Model

The MFT technique was successfully applied to model this test by exactly replicating the geometry of the base used in the experiments including the 2mm notches, as indicated in the zoom of Figure 4.13. No noticeable moisture gradients were measured in those experiments [166]. Therefore, an uniform deformation field was imposed to simulate the shrinkage process. As in the experiments, the model reproduce one-directional cracks only, which are parallel to the direction of the constraint with no longitudinal cracks (Figure 4.13).

To successfully model these experiments, it was necessary to explicitly include the indentations in the simulations. There are two main drawbacks associated with this type of solution: i) it is very laborious and time consuming to discretize the exact geometry of the interface (*i.e.* 2mm indentation in this case); and ii) a quite dense mesh is required to capture all the details associated with this particular soil-plate contact. Denser meshes are related to an increase in the degrees of freedom of the problem, resulting in more expensive numerical analysis in terms of CPU time. Note that the simulation of this problem without including the notches and using an isotropic mechanical model for the interface (as the one described in [184]) lead to unrealistic results with the formation of transversal and longitudinal cracks (Figure 4.14), which do not correspond to the observed behavior in this experiment, or in similar ones.

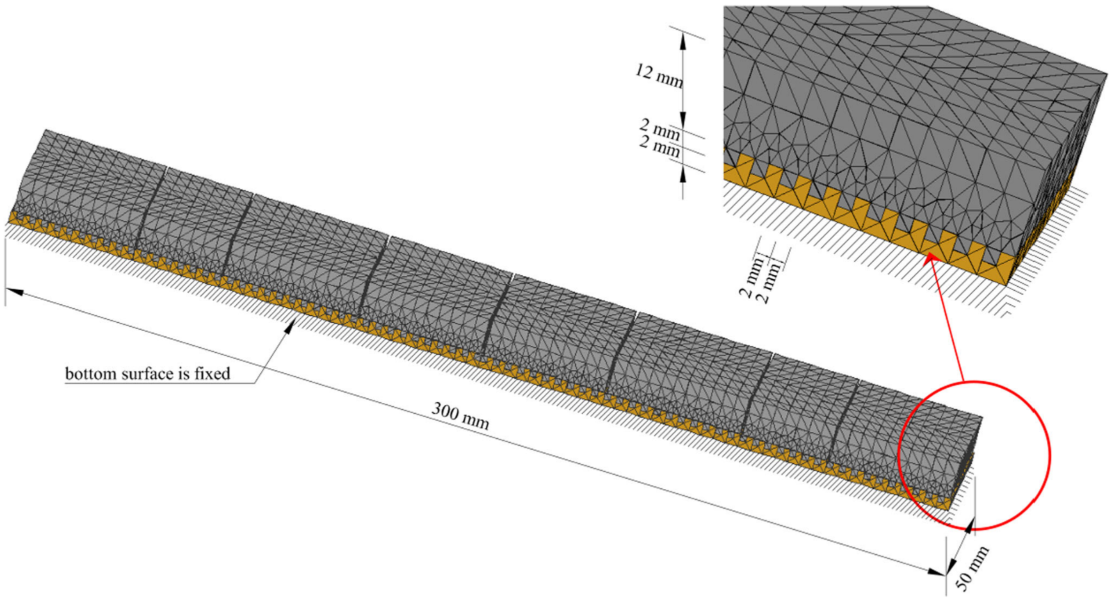

Figure 4.13: 3D modeling of the drying tests on saturated clay samples prepared in slab plates discretizing the indentation at the soil–plate interface (reprinted from [125])

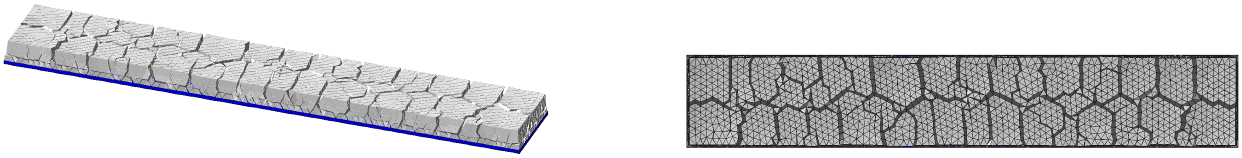

(a) (b)

Figure 4.14: Modeling the slab specimen using an isotropic interface model for the soil–plate contact surface, (a) 3D and (b) top views, respectively (reprinted from [125])

4.4.3.2 Modeling a Slab Desiccation Test using the Orthotropic Interface Model

The last application case is related to the modeling of the drying of the slab specimen discussed before, but now using the orthotropic mechanical model to implicitly consider the displacement restriction imposed by the notches present at the soil-plate interface. Therefore, a planar surface at this contact surface was assumed and the parameters of the orthotropic mechanical model are such that the longitudinal relative displacements are restricted and the soil can slide (almost freely) in the transversal direction only. This arrangement induces the formation of transversal cracks only as shown in Figure 4.15 and as it was observed in the experiments.

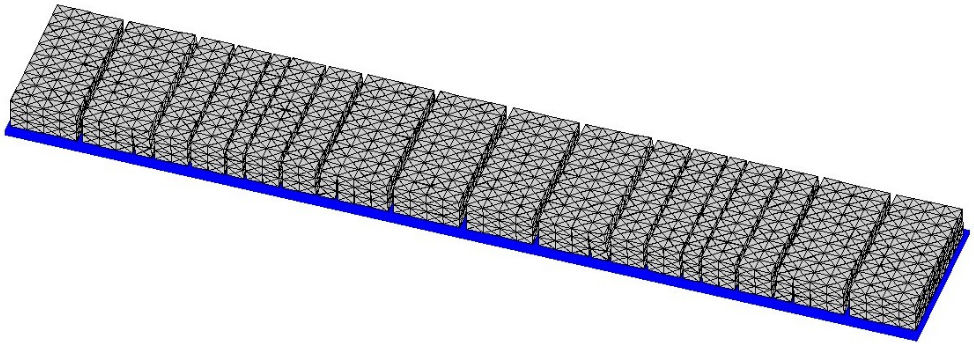

Figure 4.15: Modeling the slab specimen using an orthotropic interface model for the soil–plate contact surface – structured mesh (reprinted from [125])

After a quick inspection of Figures 4.13 and 4.15, it can be concluded that the results obtained with the mesh that includes a detailed geometrical representation of the orthotropic soil-plate contact surface (*i.e.* Figure 4.13) are (almost) identical to the ones obtained with a model that combines a (simple) planar plate-surface and the orthotropic mechanical law proposed in this work (*i.e.* Figure 4.15). The implicit discretization of the orthotropic characteristics of a contact surfaces between different materials through a mechanical model that includes the dependence of the materials strength in terms of the direction of the analysis has two main advantages: i) requires a simpler mesh (reducing therefore the time associated with its preparation), and ii) yields a mesh with less number of nodes with the associated reduction in the degree of freedom of the problem (saving therefore CPU time).

If we now compare the results obtained with these two different approaches (*i.e.* Figures 4.13 and 4.15) against the experimental observations (*i.e.* Figure 4.12b), it is evident that the perfectly straight vertical cracks simulated by these two models are not totally realistic. This outcome is related to the adoption of structured meshes to model this problem, which tend to induce the propagation of cracks through the well-defined, regular and straight (vertical) contacts between elements. A more realistic simulation of drying cracks can be achieved by using an unstructured mesh to model this problem. Figure 4.16 presents the 3D view of a model based on an unstructured mesh of 73048 nodes and 128853 elements, where 24741 corresponds to bulk elements and 104112 to interface elements (which were placed at the plate-soil contact and between standard bulk soil elements, *i.e.* all the domain but the plate). Table 4.4 lists the model parameters adopted in the simulation. This model output resembles quite accurately the actual cracked soil. As shown in Sánchez *et al.* [178], no noticeable dependence of the crack pattern on the adopted mesh size is observed when using the MFT. The difference in the aspect of the crack networks observed between the perfectly regular one, shown in Figure 4.15 (*i.e.* obtained with a structured mesh), and the apparently more realistic crack network presented in Figure 4.16 (*i.e.* obtained with an unstructured mesh) is because cracks tend to be aligned with the main orientations generally present in structured meshes; while in the case of an unstructured meshes, there is not a predominant direction for the crack to propagate.

Table 4.4: Material properties of soil and plate used in the simulations of desiccation cracks

Element	E (MPa)	ν	α_s	α_l	β_s (kPa)	β_l (kPa)	σ_u (kPa)	G_f (N/m)	Constitutive model
Soil (bulk)	4	0.2	-	-	-	-	-	-	Elastic
Plate	210×10^3	0.2	-	-	-	-	-	-	Elastic
Soil-soil interfaces	4	0.0	-	-	-	-	4.0	0.4	Tensile damage
Soil-plate interfaces	4	0.0	0.00	0.00	3.20	3.20	-	-	Isotropic damage
Soil-plate-interfaces	4	0.0	0.00	0.00	0.96	3.20	-	-	Orthotropic damage

4.5 Experimental and Numerical Studies of Soil Curling

Clayey soils usually experience volume shrinkage under drying. Shrinkage deformations can be associated with [217]: a) particle rearrangement (known as intra deformations), and b) volume changes (known as global deformation). Both phenomena are closely related, since intra-deformations lead to global changes in the soil structure, and vice-versa. Therefore, the drying process can be roughly described as the volumetric deformations induced the increase of capillary

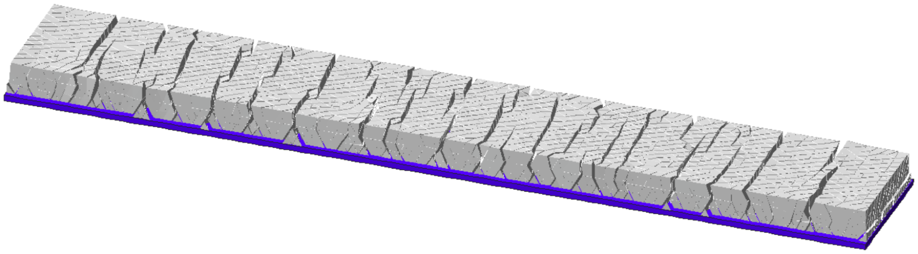

Figure 4.16: Modeling the slab specimen using an orthotropic interface model for the soil–plate contact surface – unstructured mesh (reprinted from [125])

pressure (*i.e.*, matric suction). There are several factors governing the curling deformation in soils, such as: initial and boundary mechanical and hydraulic boundary conditions; material properties and characteristics (soil grain size distribution, clay mineralogy and soil microstructure); geometry of the problem; soil water content and chemical interactions [217, 209, 104, 30, 52, 131]. Depending on these factors, soil shrinkage may lead to the development of drying cracks, or curling deformation, or a combinations of them.

The drying process of clayey soils has been a subject of interest over the years. Zielinski *et al.* [217] conducted an extensively review of the major researches since the pioneer work by Kindle [103], in which a series of laboratory experiments were carried out to examine how the velocity of desiccation, composition of the mixture and salinity of the porous medium influenced mud- cracks. In the last few years the study of the soil shrinkage has been emphasized on numerical simulations [5, 107] and physical modeling [52, 103, 105].

Allen [5] proposed a geometrical model to explain how the differential water loss (drying) and the differential contraction (shrinkage) due to a non-uniform texture interact to produce soil curling. Kodikara *et al.* [107] made use of nonlinear elasticity theory under large deformations to model curling deformations in thin homogenous soil layers upon drying. The uncoupled hydro-mechanical formulation mimics the evaporation process by introducing suction changes as stress increments. Most recently Hirobe and Oguni [88] used a finite element method (FE) to describe the desiccation process coupled with a particle discretization finite element scheme to model the fracture. Other approaches are based on cohesive fracture model with Voronoi tessellations [80, 79, 11] and finite element method [167] to reproduce the desiccation cracks during drying. However, the main focus of these works was on the study drying crack formation rather than modeling soil surface curling. Sánchez *et al.* [184] proposed a mesh fragmentation technique (MFT) based on high aspect ratio FE that was able to realistic capture typical crack patterns. The smoothed particle hydrodynamics method [32] and the finite difference method [7, 199] have been successfully applied to model curling behavior and crack formation.

The curling process has also been studied by means of laboratory desiccation tests, which usually considers a slurry paste placed in circular plates or rectangular molds. However, only few attempts have been made to capture and describe the entire phenomenon. A high precision 2D laser scanner has been used to construct a 3D image of the scanned surface of the soil [217]. Another approach consists of taking digital pictures of the sample. This technique has been widely employed in many soil science investigations over the last years. For instance, they are used to measure deformations in triaxial tests [26, 216], for soil erosion assessment [146], to determine soil surface roughness for agricultural applications [75] and to study the morphology of desiccation cracks [190]. Some of these works have adopted more than one camera to capture all the three-dimensional details involved in the tests. The use of two digital cameras appears to be very appealing to analyze the soil curling, since the soil tends to curl in both surface directions.

Although the soil curling behavior has been extensively studied over the years, several factors still need to be properly addressed. The phenomena of the reverse curling, in which the soil curls as a result of a differential drying between the top and bottom layers of the sample and then curls back due to the reduction of such differential, has not been investigated. Moreover, the influence of sedimentation in mixed soils with the presence of fine and granular material is also a subject that requires a more detailed analysis.

In this section, mixtures of kaolinite with silica sand (graded to pass through sieve No. 20 and retain on sieve No. 30) and pure kaolinite were studied by carrying out drying tests in the lab. The results of these experiments were compared with the numerical analyses, which considered a fully coupled hydro-mechanical formulation. This work aims to investigate the curling phenomenon that takes place when a thin layer of soil experiences desiccation.

4.6 Materials and Experimental Methods

Drying tests involving both pure kaolin and sand specimens, as well as mixtures of kaolinite with silica sand were carried out in the lab to study some key factors associated with the shrinkage process in soils. The study involved different types of soil-mold interfaces to investigate the influence of displacement restrictions on curling and cracking behavior during shrinkage. Furthermore, samples at different initial water contents were also studied. Since soils usually curls in both directions, two cameras were adopted to take side and front pictures at regular time intervals. The following sections briefly describe the selected soil specimens and the adopted experimental procedure.

4.6.1 Samples Description

Three different mixtures of artificial soils were used in this study: 85% of kaolin with 15% of silica sand, 80% of kaolin with 20% of silica sand, and a sample made up from pure kaolin. The kaolin contains 97% of kaolinite with a linear dry shrinkage of 5.8%. The median particle size of the clay is 1.36 m and its water of plasticity is 5.8%. The Ottawa silica sand is graded to pass through sieve No. 20 (850 m) and retain on sieve No. 30 (600 m), conforming to ASTM C778 [12]. The liquid limit of the mixture prepared with 85% of kaolinite and 15% of sand was found to be 39% and the initial dry density was around 0.637 Mg/m3. Figure 4.17 shows with triangles the experimental data obtained by measuring low-suction ranges with tensiometers and higher values of suction with the WP4-T chilled-mirror psychrometer device. The soil water retention curve (SWRC) has been modeled by considering the following equation, which is a modified expression of the one proposed by van Genuchten [205] but also takes into account high-suction range [68]:

$$S_l = \left[1 + \left(\frac{s}{P_o}\right)^{\frac{1}{1-\lambda_o}}\right]^{-\lambda_o} f_d \tag{4.22}$$

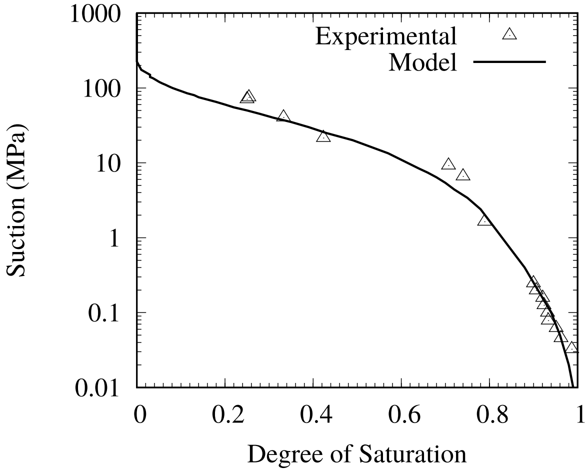

Figure 4.17: Soil-water retention curve of the mixture 85% kaolinite and 15% silica-sand

where P_o is the pore air-entry value, λ_o is a material parameter related to particle size distribution for low-suction range and f_d is a function that considers high-suction range and is given by:

$$f_d = \left(1 - \frac{s}{P_d}\right)^{\lambda_d} \tag{4.23}$$

where P_d is the oven-dry suction (1000 MPa) and λ_d is a model parameter. Table 4.5 contains the parameter values used to model the retention curve shown in Figure 4.17.

Table 4.5: Parameters of the soil water retention curve used in the model

P_o (MPa)	0.05
P_d (MPa)	1000
λ_o	0.05
λ_d	20

4.6.2 Experimental Investigation

The drying tests were conducted in samples prepared in Perspex molds 15.9 cm long, 2.9 cm width, and 1.429 cm height (with a volume ∼65.84 cm^3). All samples were dried under the lab atmosphere where the temperature and relative humidity were around 23.5 ± 0.5 ^{o}C and 45

± 5% respectively. Two Canon PowerShot G11 cameras with an optical sensor resolution of 10 megapixels were placed 90^o apart to capture the behavior of the soil samples during drying in both horizontal and vertical directions. This is a simple and efficient technique, suitable for the aims of this research. Figure 4.18 shows an image of the adopted setup in this research.

Figure 4.18: Photo of the adopted set-up

For the free shrinkage tests, silicone grease was applied on the inside surfaces of the molds (as a thin film) to reduce the soil-mold friction and facilitating in this manner a smooth shrinkage of the material. As for the restrained shrinkage experiments, silicone grease was applied on the lateral walls of a Perspex mold (as the one described above) only and acrylic rectangular notches were glued at the bottom of the container to achieve a strong soil-base adhesion to limit the displacements and restrict the soil movement at the bottom only.

The two components of the mixtures (*i.e.*, clay and sand) were weighted according to the target percentages and then were carefully mixed to ensure a uniform distribution of the sand particles in the specimens. The 85/15 and the 80/20 kaolin/sand mixtures were mixed with distilled water at water content 117% (*i.e.*, around 2.75 times the liquid limit, ∼42.5%) and 105%, respectively;

while the initial water contents of the pure kaolin and pure sand samples were 126% and 65%, respectively. All the specimens had the consistency of a slurry and after mixing them with water they were left inside a tightly sealed container for around 24 hours to ensure a homogenized moisture distribution in the samples. The specimens were then poured into the molds without applying any compaction effort. A light tamping was applied to remove any possible air bubbles from the material.

During drying, the total suction of these soil samples was measured every time with water content measurement by using tensiometers for lower values of suction and the WP4-T device for higher suction values. Figure 4.19 shows a representative drying curve obtained for a curling test of a thin soil layer of 85% kaolinite and 15% silica sand.

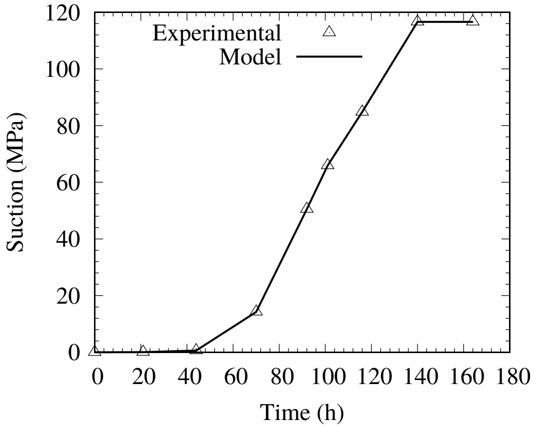

Figure 4.19: Evolution of suction with time

4.7 Test Results

Figures 4.20a and 4.20b present lateral and top pictures related to the pure-sand test obtained at the end of the drying process. As expected this sample exhibits limited shrinkage with no curling. Figures 4.20c and 4.20d present lateral and top pictures, respectively, related to the pure-kaolinite specimen after dying. As expected, this uniform kaolin shrinks without a noticeable curling. Some studies suggest that uniform soils first curl-up (*i.e.*, at the initial stages of evaporation); but then (at advanced stages of drying) the deformation reverses and the curled edges start to retreat downward, with no apparent final curling (*e.g.*, [217]). Nevertheless, the final outcome is that homogenous soils subjected to drying generally show a rather uniform shrinkage, as observed in Figure 4.20.

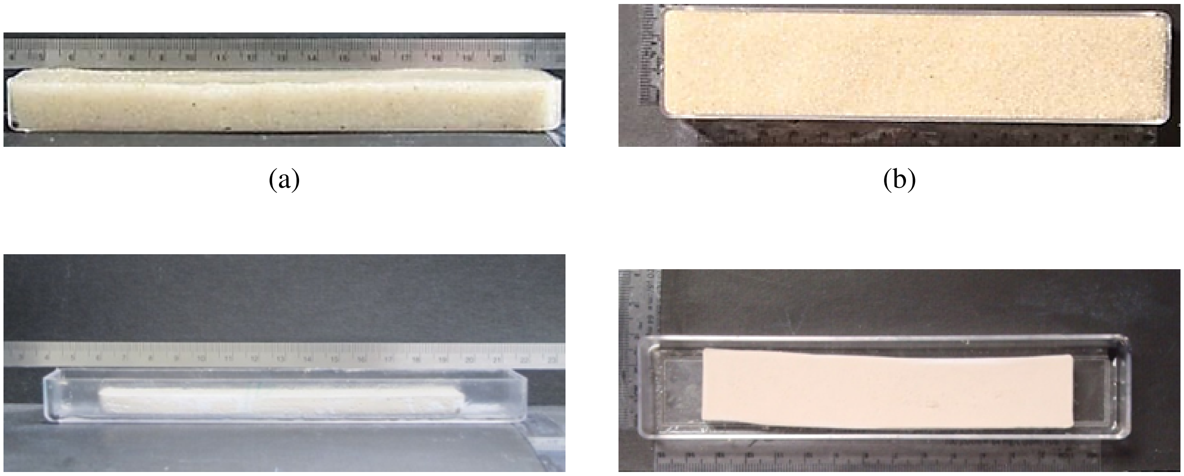

(a) (b)

(c) (d)

Figure 4.20: Sample of pure silica-sand prepared at $w = 65\%$ and subjected to drying, pictures at the end of the drying process from: (a) size view, and (b) top views. Curling deformation of the pure kaolin soil sample at the end of the test: (c) side view; (d) top view.

To study the effect of the particle sizes on curling behavior the two mixtures previously described (*i.e.*, 85/15 kaolin/sand and 80/20 kaolin/sand) were subjected to the dry process. Figure 4.21 presents the picture of the sample with 15% of sand experienced volumetric shrinkage and significant curling deformation (moving the edges of the sample upward during drying). Figure 4.21 shows the drying stages and curling development of this mixture under the laboratory atmosphere. As can be seen, expressive curling started to develop at 101 h from the start of the desiccation test and reached its maximum at 116 h. From this point, it was not possible to observe any additional curling deformation in the soil sample.

The second sample, which was prepared with 20% of silica sand, broke in the middle after experiencing high curling deformation (moving the edges of the sample upward during drying), as shown in Figure 4.22a. As shown in Figure 4.22c, sand particles were settled at the bottom of

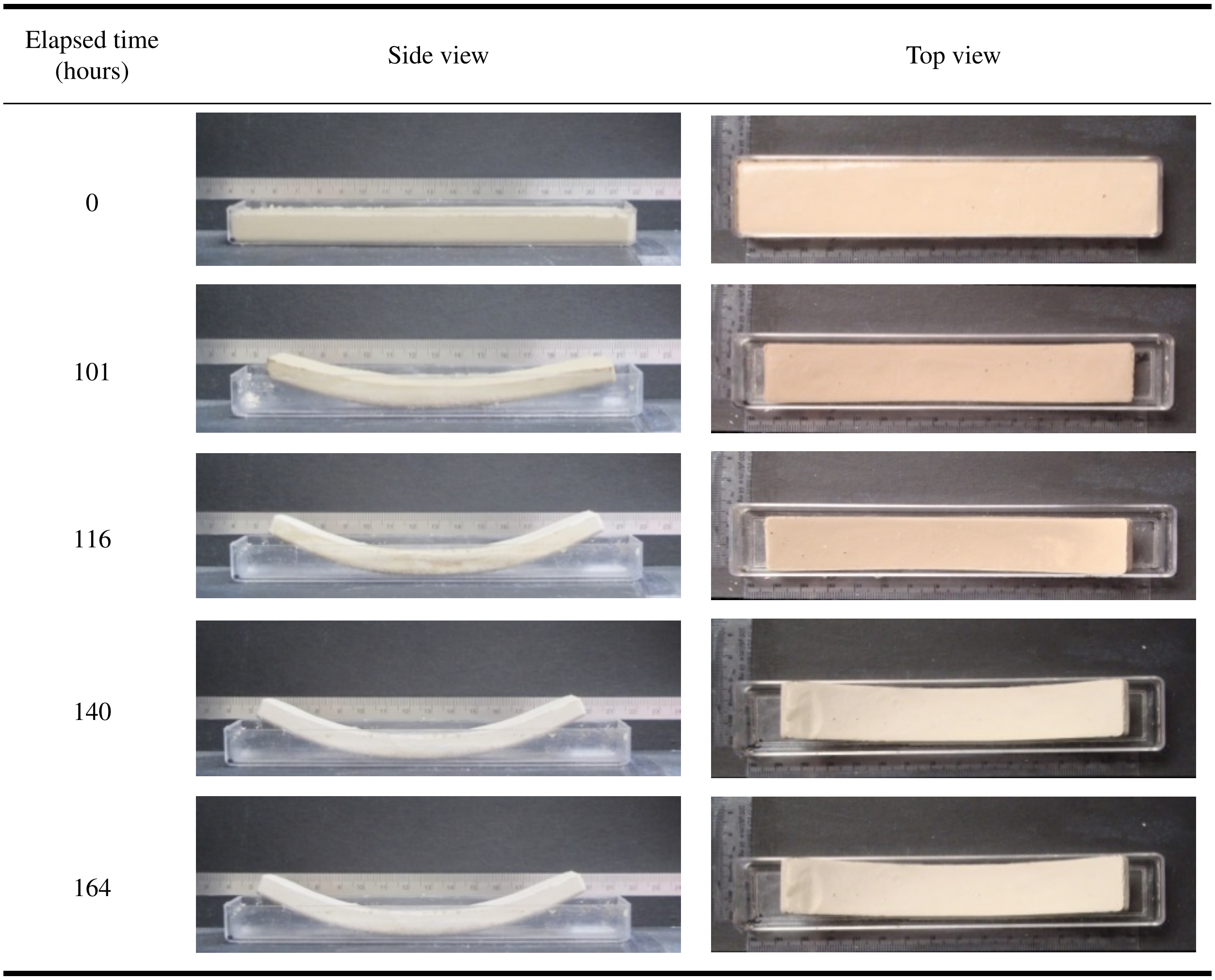

Figure 4.21: Stages of the curling development in the mixture 85/15 kaolinite/sand subjected to drying

the sample, and while the edges were moving up, these particles were moving toward the center. As time progressed, the middle part of the sample became weaker while the edges moved up. Therefore, the sample was broken from the middle and the particle size distribution was clearly shown in Figure 4.22b. Note that the top soil surface curled in both directions, which means that the soil experienced isotropic shrinkage.

The last case, in which the soil with 15% of sand was placed over a grooved surface, the soil exhibits cracks in the direction of the grooves and only small curling was observed, as shown in Figure 4.23. The grooves contribute with an additional restraining at the bottom and do not allow

(a) (b) (c)

Figure 4.22: Pictures of the 80/20 kaolinite/sand mixture at the end of the drying test: (a) lateral photo showing the curled and broken sample; (b) front image of the broken section sample showing the soil segregation, with the larger sand grains settle at the bottom of the sample; (c) image of the bottom of the sample showing the deposition of the sand particles.

the soil to freely move in any direction. Furthermore, it can be seen that the soil is attached to the grooves.

(a) (b)

Figure 4.23: Crack pattern of the soil sample, 85% kaolinite with 15% silica sand at the end of the test: (a) side view; (b) top view

The difference of the amount of curling developed by different mixtures can be explained as a consequence of the sedimentation process. The initial water content of 3×LL induces bigger particles to settle at the bottom and smaller ones at the top of the sample, which leads to a gradual particle size distribution. Therefore, the region near the top surface, composed mainly by clay particles, tends to contract more than the bottom layer that contains a high concentration of silica sand particles. This phenomenon impacts the soil behavior by yielding a differential shrinkage. Thus, when the sample is prepared at higher initial water content (*e.g.*, 3×LL), mixtures with larger concentration of larger particles at the bottom tends to curl more than those samples containing smaller concentration at the bottom.

The formation of the observed upward curling is also governed by the differential shrinkage.

At the beginning of the desiccation test, the evaporation only acts at the top surface of the soil sample since the walls and the bottom of the mold prevent the air to desaturate the sample. As the soil starts to desaturate by allowing water to drain from its voids, the sample shrinks and curls up due to the sedimentation process previously explained. As mentioned before, silicone grease was applied in the interior of the mold to reduce adhesion and allow free shrinkage. As the desaturation process continues, the sample detaches from the mold as a consequence of the shrinkage. At this point, the water also starts to evaporate from the sides and bottom of the soil. This may cause the edges of the sample to move downward and, depending on the soil fabric, to reverse the initial curling. In a skeleton with uniform particle size distribution, the initial curling formed by the differential drying is almost entirely reversed when the bottom is exposed to the environment conditions and water starts to evaporate from it. In this case, the differential drying vanishes because the rates of shrinkage at the top and bottom layers become similar. On the other hand, in a gradual size distribution (*i.e.*, a bottom layer coarser grains), the bigger particles prevent the downward movement, and consequently, the curling does not reverse, even at latest stages when all the external surfaces of the soil are exposed to the evaporation process. In other words, the retraction is hindered by the sand particles settled at the bottom.

4.8 Modeling Soil Shrinkage Behavior

The mesh fragmentation technique (MFT) proposed by Sanchez *et al.* [184] to model the formation of drying cracks in soils was adopted in this work to simulate the desiccation tests. This method was also adopted to model the formation of fractures in concrete (*e.g.*, [125, 178]. In this section a new mechanical constitutive model for capturing the features of soils behavior during curling is proposed and explained.

4.8.1 Damage Model to Simulate the Soil-Plate Interface Behavior

Manzoli *et al.* [125] investigated the orthotropic behavior of soil-plate interfaces by conducting direct shear tests in a modified device that included grooved plates with the different textures. It was observed that the roughness and characteristics of soil-plate interface strongly impact on the directional strength, concluding that isotropic Mohr Coulomb models (*i.e.* same strength in all directions) are not viable to reproduce this type of behavior. Based on these experimental observations, Manzoli *et al.* [125] proposed a generalized Mohr-Coulomb model able to simulate the potential slip between materials with orthotropic characteristics.

The interface damage model proposed in this work is based on the interface orthotropic model proposed by Manzoli *et al.* [125] and extended to simulate the soil-plate detachment typically observe during curling. Hence, in addition to the orthotropic damage model able to represent different directional shear strengths, the model also considers damage in tension (mode I). Figure 4.24 illustrates the main component of this new model. Figures 4.24a and 4.24c correspond to a specimen that experiences shrinkage only (*i.e.*, without curling). In this case the interface model is capable of simulating the relative shear displacements between soil and plate, with the option of capturing different strengths in the s and l directions; feature that is very convenient when dealing with textured interfaces (*e.g.*, grooved plate). Figures 4.24b and 4.24d illustrate the case of a soil that in addition of shearing in the horizontal (interface) plane (*i.e.*, s and l directions) exhibits a curling behavior with the corresponding relative vertical movement in the n direction, associated with the detachment of the soil from the soil plate. To model these features of soil behavior the following three damage criteria are proposed:

$$f_n = \sigma_{nn} - q_n(r_n) \leq 0 \tag{4.24}$$

$$f_s = ||\sigma_{ns}|| + \alpha_s \, \sigma_{nn} - q_n(r_n) \leq 0 \tag{4.25}$$

$$f_l = ||\sigma_{nl}|| + \alpha_l \, \sigma_{nn} - q_l(r_l) \leq 0 \tag{4.26}$$

where q_n, q_s and q_l are stress-like internal variables; r_n, r_s and r_l are strain-like internal variables; α_s and α_l are material parameters that control the influence of the normal component of the stress tensor σ_{nn}.

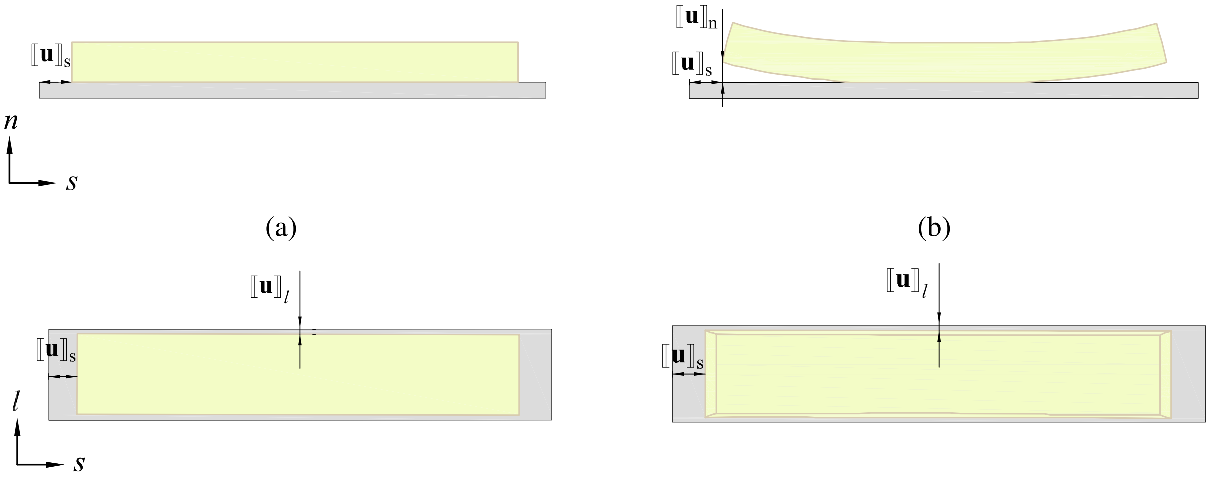

(a) (b)

(c) (d)

Figure 4.24: Scheme representation of new interface damage model: (a) and (c) lateral and top views, respectively, of a soil experiencing shrinkage only, (b) and (d) lateral and top view, respectively, of a specimen exhibiting shear displacement at the soil-plate contact and curling with soil detachment from the plate

The effective stress tensor ($\boldsymbol{\sigma}$) is computed by means of the following constitutive equation:

$$\boldsymbol{\sigma} = (1 - d_n)\bar{\bar{\boldsymbol{\sigma}}} \tag{4.27}$$

where $d_n \in [0, 1]$ is the scalar damage variable associated with damage in tension and $\bar{\bar{\boldsymbol{\sigma}}}$ is

$$\bar{\bar{\boldsymbol{\sigma}}} = \underbrace{\begin{bmatrix} \bar{\boldsymbol{\sigma}}_{nn} & 0 & 0 \\ 0 & \bar{\boldsymbol{\sigma}}_{ss} & \bar{\boldsymbol{\sigma}}_{sl} \\ 0 & \bar{\boldsymbol{\sigma}}_{sl} & \bar{\boldsymbol{\sigma}}_{ll} \end{bmatrix}}_{\bar{\boldsymbol{\sigma}}_{nsl}} + (1 - d_s) \underbrace{\begin{bmatrix} 0 & \bar{\boldsymbol{\sigma}}_{ns} & 0 \\ \bar{\boldsymbol{\sigma}}_{ns} & 0 & 0 \\ 0 & 0 & 0 \end{bmatrix}}_{\bar{\boldsymbol{\tau}}_{s}} + (1 - d_l) \underbrace{\begin{bmatrix} 0 & 0 & \bar{\boldsymbol{\sigma}}_{nl} \\ 0 & 0 & 0 \\ \bar{\boldsymbol{\sigma}}_{nl} & 0 & 0 \end{bmatrix}}_{\bar{\boldsymbol{\tau}}_{l}} \tag{4.28}$$

where $d_s \in [0, 1]$ and $d_n \in [0, 1]$ are damage variables related to damage in shear and $\bar{\boldsymbol{\sigma}}$ is the effective elastic stress tensor expressed by

$$\bar{\boldsymbol{\sigma}} = \mathbb{C} : \boldsymbol{\epsilon} \Rightarrow \begin{bmatrix} \bar{\sigma}_{nn} & \bar{\sigma}_{ns} & \bar{\sigma}_{nl} \\ \bar{\sigma}_{ns} & \bar{\sigma}_{ss} & \bar{\sigma}_{sl} \\ \bar{\sigma}_{nl} & \bar{\sigma}_{sl} & \bar{\sigma}_{ll} \end{bmatrix} \tag{4.29}$$

where $\mathbb{C}$ is the isotropic forth-order elastic tensor and $\boldsymbol{\epsilon}$ is the strain tensor. Note that $\bar{\sigma}_{nn} = \bar{\bar{\sigma}}_{nn}$. The damage criteria can be expressed in terms of elastic stresses by dividing Eqs. (4.24), (4.25) and (4.26) by $(1 - d_n)$, $(1 - d_s)$ and $(1 - d_l)$, respectively. Thus,

$$\bar{f}_n = \bar{\sigma}_{nn} - r_n \leq 0 \tag{4.30}$$

$$\bar{f}_s = ||\bar{\sigma}_{ns}|| + \alpha_s \, \bar{\sigma}_{nn} - r_s \leq 0 \tag{4.31}$$

$$\bar{f}_l = ||\bar{\sigma}_{nl}|| + \alpha_l \, \bar{\sigma}_{nn} - r_l \leq 0 \tag{4.32}$$

Therefore, the damage variable can be written as functions of the strain-like internal variables r as follows:

$$d_n(r_n) = 1 - \frac{q_n}{r_n} \tag{4.33}$$

$$d_s(r_s) = \frac{r_s - q_s}{r_s - \alpha_s \, \bar{\sigma}_{nn}} \tag{4.34}$$

$$d_l(r_l) = \frac{r_l - q_l}{r_l - \alpha_l \, \bar{\sigma}_{nn}} \tag{4.35}$$

An exponential law is assumed for q_n

$$q_n(r_n) = r_{n_o} \exp\left[h \, \mathscr{A} \left(1 - \frac{r_n}{r_{n_o}} \right) \right] \tag{4.36}$$

with $\mathscr{A}$ denoting the softening parameter defined by:

$$\mathscr{A} = \frac{r_o^2}{G_f \, E} \tag{4.37}$$

in which E is the Young's modulus of the material and G_f is the mode I fracture energy, which is the energy dissipated for the complete degradation of the material in opening mode.

The interface damage model is completed with the Kuhn-Tucker relations given by

$$\bar{f}_{n,s,l} < 0, \qquad \dot{r}_{r,s,l} > 0, \qquad \dot{r}_{n,s,l}\, \bar{f}_{n,s,l} = 0 \tag{4.38}$$

and the following consistency condition:

$$\dot{r}_{n,s,l}\, \dot{\bar{f}}_{n,s,l} = 0 \ \text{ if } \ \bar{f}_{n,s,l} = 0 \tag{4.39}$$

The evolution of strain-like internal variables is determined by means of Eqs. (4.30), (4.31), (4.32), (4.38) and (4.39) which yields:

$$r_n = \max_{\tau \in [0,t]} \left[\bar{\sigma}_{nn}(\tau), r_{n_o} \right] \tag{4.40}$$

$$r_s = \max_{\tau \in [0,t]} \left[||\bar{\sigma}_{ns}(\tau)|| + \alpha_s\, \bar{\sigma}_{nn}(\tau), r_{s_o} \right] \tag{4.41}$$

$$r_l = \max_{\tau \in [0,t]} \left[||\bar{\sigma}_{nl}(\tau)|| + \alpha_l\, \bar{\sigma}_{nn}(\tau), r_{l_o} \right] \tag{4.42}$$

The above equations state that the strain-like internal variables reach the maximum value related to the elastic stresses along the loading process, starting from the initial values r_{n_o}, r_{s_o} and r_{l_o}, which are defined as material properties of the soil-plate interface as:

$$r_{n_o} = \sigma_u \tag{4.43}$$

$$r_{s_o} = q_{s_o} = \beta_s \tag{4.44}$$

$$r_{l_o} = q_{l_o} = \beta_l \tag{4.45}$$

where σ_u is the tensile strength of the soil-plate interface; β_s and β_l are the cohesive strengths of the soil-plate interface associated with directions s and l, respectively.

4.9 Computational Aspects

All the analyses were carried out with the aid of the finite element program CODE_BRIGHT (Coupled Deformation, BRIne, Gas and Heat Transport) [149] that is able to solve Thermo- Hydro-Mechanical processes in a fully coupled manner. This code describes the behavior of solids, fluids (liquid and gas) and their interactions based on the following set of governing equations: (i) balance equations (*i.e.*, solid and water mass balance equations and equilibrium equation), constitutive relations (*i.e.*, Darcy's law, Kozeny's law and the cubic law for relative permeability), (iii) initial and boundary conditions, and (iv) equilibrium restrictions (*i.e.*, Henry's law and Kelvin's law). The intrinsic permeability of the HAR elements is governed by the well- known cubic law for crack aperture, while the saturation of such elements is defined following the expression proposed by Olivella and Alonso [147]. In CODE_BRIGHT, the unknowns of a general THM problem are: liquid and gas pressures, displacement and temperature. It is assumed that porosity change occurs at slow rates, and therefore, porosity is not considered as an unknown and it is updated only at the end of each time step. In this work, gas pressure and temperature remain constant through the analysis, and consequently, the primary variables of the hydro-mechanical problem for each node of the mesh are liquid pressure and displacement. The previous assumptions have been adopted because the experimental tests were conducted in the laboratory under constant relative humidity and constant temperature. The program uses the Newton-Raphson iterative algorithm to solve the non-linear system of algebraic equations at each time step.

The constitutive models described in the previous sections were implemented in the FE-program CODE_BRIGHT [149] using the IMPL-EX integration scheme proposed by Oliver *et al.* [153]. This algorithm was developed to tackle problems involving high nonlinearities associated with strong discontinuities, since the purely implicit integration scheme may lead to convergence problems. The IMPL-EX, is a robust method that ensures convergence with only one Newton-Raphson iteration per time-step, which improves computational efficiency when compared with the fully implicit scheme. However, there is an error involved in the use of this alternative scheme, which can be minimized by reducing the time-step, as reported by Oliver *et al.* [153]. This implicit-explicit scheme (IMPL-EX) has been widely used for the integration of constitutive models based on damage mechanics [123, 153] and plasticity theory [153, 170].

Table 4.6 shows the steps of the IMPL-EX integration scheme for the interface damage model. First (step (i)), the strain tensor $\boldsymbol{\epsilon}_{(n+1)}$ at the current time step $t_{(n+1)}$ is rotated according to the coordinate system (n, s, l) and the elastic stress tensor $\boldsymbol{\sigma}_{(n+1)}$ is obtained from $\boldsymbol{\epsilon}_{(n+1)}$ (step (ii)). Afterwards, the loading-unloading conditions are verified for the three-directions and the strain-like internal variables $r_{(n+1)}$ are updated (step (iii)); then, at step (iv) the internal variable increments $\Delta r_{(n+1)}$ are computed by the difference between the internal variable at $t_{(n+1)}$ and the one at $t_{(n)}$ (*i.e.*, previous time step). Note that this increment is only used to approximate the internal variable at next time step. In the implicit-explicit scheme, the variable $\tilde{r}_{(n+1)}$ is approximated to a linear extrapolation of the strain-like internal variable r evaluated at previous time steps (*i.e.*, $\Delta r_{(n)} = r_{(n)} - r_{(n-1)}$) (step (iv in Table 4.6)). Once the damage variable is calculated from $\tilde{r}_{(n+1)}$, the stress tensor $\boldsymbol{\sigma}_{(n+1)}$ is explicitly determined for a given $\boldsymbol{\epsilon_{(n+1)}}$, as shown in step (vi). Finally, the stress tensor is rotated back to the initial configuration.

Although the code has an automatic time step control [196], the maximum time step allowed during the analysis has to be small, otherwise the error associated with the IMPL-EX method may be expressive and affect the results.

4.10 Numerical Modeling of the Soil Surface Curling

The two components of the mixtures studied in this work, *i.e.* the pure-sand (Figures 4.20a and 4.20b) and pure-kaolin (Figure 4.20c and 4.20d) samples do not develop curling when tested alone. However, mixtures of these two materials exhibit curling deformation, as shown in Figure 4.21 for the mixture 85/15 kaolinite/sand. As discussed above, slurries prepared from mixing fine-grained soils and sands tend to develop a non-homogenous distribution of particles sizes, with the larger (sand) particles settled at the bottom, and the fine clay particles at the top of the specimen. The final segregated mixture (with soils with different properties at the bottom and top of the sample), favor soil curling. The region near the top surface, composed mainly by clay particles, tends to contract more than the bottom layer that contains a high concentration of silica sand particles.

Table 4.6: IMPL-EX integration scheme for the interface damage model

```
INPUT: $\boldsymbol{\epsilon}_{(n+1)}$, $\bar{\sigma}_{nn_{(n)}}$, $r_{n_{(n)}}$, $\Delta r_{n_{(n)}}$, $r_{s_{(n)}}$, $\Delta r_{s_{(n)}}$, $r_{l_{(n)}}$, $\Delta r_{l_{(n)}}$
  (i) Transform the current strain tensor obtaining its components according to the local coordinate system $(n, s, l)$
  (ii) Compute the elastic stress tensor
          $\bar{\boldsymbol{\sigma}}_{(n+1)} := \mathbb{C} : \boldsymbol{\epsilon}_{(n+1)}$
  (iii) Check the loading-unloading conditions.
      (a) in direction $n$
          IF $\left(\bar{\sigma}_{nn_{(n+1)}} - r_{n_{(n)}} \leq 0\right)$ THEN
              keep the threshold: $r_{n_{(n+1)}} := r_{n_{(n)}}$
          ELSE
              update the damage threshold: $r_{n_{(n+1)}} := \bar{\sigma}_{nn_{(n+1)}}$
          END IF
      (b) in direction $s$
          IF $\left(||\bar{\sigma}_{ns_{(n+1)}}|| + \alpha_s \, \bar{\sigma}_{nn_{(n+1)}} - r_{s_{(n)}} \leq 0\right)$ THEN
              keep the threshold: $r_{s_{(n+1)}} := r_{s_{(n)}}$
          ELSE
              update the damage threshold: $r_{s_{(n+1)}} := ||\bar{\sigma}_{ns_{(n+1)}}|| + \alpha_s \, \bar{\sigma}_{nn_{(n+1)}}$
          END IF
      (c) in direction $l$
          IF $\left(||\bar{\sigma}_{nl_{(n+1)}}|| + \alpha_l \, \bar{\sigma}_{nn_{(n+1)}} - r_{l_{(n)}} \leq 0\right)$ THEN
              keep the threshold: $r_{l_{(n+1)}} := r_{l_{(n)}}$
          ELSE
              update the damage threshold: $r_{l_{(n+1)}} := ||\bar{\sigma}_{nl_{(n+1)}}|| + \alpha_l \, \bar{\sigma}_{nn_{(n+1)}}$
          END IF
  (iv) Compute the strain-like internal variable increments
          $\Delta r_{n_{(n+1)}} := r_{n_{(n+1)}} - r_{n_{(n)}}; \quad \Delta r_{s_{(n+1)}} := r_{s_{(n+1)}} - r_{s_{(n)}}; \quad \Delta r_{l_{(n+1)}} := r_{l_{(n+1)}} - r_{l_{(n)}}$
  (v) Compute the explicit linear extrapolation of the strain-like internal variable
          $\tilde{r}_{n_{(n+1)}} := r_{n_{(n)}} + \frac{\Delta t_{(n+1)}}{\Delta t_{(n)}} \Delta r_{n_{(n)}}; \; \tilde{r}_{s_{(n+1)}} := r_{s_{(n)}} + \frac{\Delta t_{(n+1)}}{\Delta t_{(n)}} \Delta r_{s_{(n)}}; \; \tilde{r}_{l_{(n+1)}} := r_{l_{(n)}} + \frac{\Delta t_{(n+1)}}{\Delta t_{(n)}} \Delta r_{l_{(n)}}$
```

Table 4.6 Continued: IMPL-EX integration scheme for the interface damage model

(vi) Update the damage variables

$$\tilde{d}_{n_{(n+1)}} := 1 - \frac{\sigma_u}{\tilde{r}_{n_{(n+1)}}} \exp\left[\frac{\sigma_u^2}{G_f\, E}\, h \left(1 - \frac{\tilde{r}_{n_{(n+1)}}}{\sigma_u}\right)\right]$$

$$\tilde{d}_{s_{(n+1)}} := \frac{\tilde{r}_{s_{(n+1)}} - \beta_s}{\tilde{r}_{s_{(n+1)}} - \alpha_s\, \bar{\sigma}_{nn_{(n)}}}$$

$$\tilde{d}_{l_{(n+1)}} := \frac{\tilde{r}_{l_{(n+1)}} - \beta_l}{\tilde{r}_{l_{(n+1)}} - \alpha_l\, \bar{\sigma}_{nn_{(n)}}}$$

(vii) Compute the stress tensor according to Eqs. (4.27) and (4.28)

$$\bar{\bar{\boldsymbol{\sigma}}}_{(n+1)} := \bar{\boldsymbol{\sigma}}_{nsl_{(n+1)}} + \left(1 - \tilde{d}_{s_{(n+1)}}\right) \bar{\boldsymbol{\tau}}_{s_{(n+1)}} + \left(1 - \tilde{d}_{l_{(n+1)}}\right) \bar{\boldsymbol{\tau}}_{l_{(n+1)}}$$

$$\tilde{\boldsymbol{\sigma}}_{(n+1)} := \begin{cases} \left(1 - \tilde{d}_{n_{(n+1)}}\right) \bar{\bar{\boldsymbol{\sigma}}}_{nn_{(n)}} & \text{if} \quad \bar{\boldsymbol{\sigma}}_{nn_{(n)}} > 0 \\ \bar{\bar{\boldsymbol{\sigma}}}_{nn_{(n)}} & \text{if} \quad \bar{\boldsymbol{\sigma}}_{nn_{(n)}} \leq 0 \end{cases}$$

(viii) Rotate the stress tensor obtaining its components according to the global coordinate system (x, y, z)

OUTPUT: $\tilde{\boldsymbol{\sigma}}_{(n+1)}, \bar{\sigma}_{nn_{(n+1)}}, r_{n_{(n+1)}}, \Delta r_{n_{(n+1)}}, r_{s_{(n+1)}}, \Delta r_{s_{(n+1)}}, r_{l_{(n+1)}}, \Delta r_{l_{(n+1)}}$

This phenomenon impacts the soil behavior by yielding a differential shrinkage. To explain this behavior, a 2D finite element mesh with 33819 nodes and 67152 triangular finite elements, in which 27474 are HAR, is used. The dimensions of the sample are the same as the one reported in previous sections (*i.e.*, height of 1.429 cm, width of 2.9 cm and length of 15.9 cm). Figure 4.25 shows the geometry, materials and boundary conditions of the problem. The heights of the bottom material for the mixtures 85/15 and 80/20 are 3 and 5 cm, respectively. The plate at the bottom of the soil sample is only used as a reference for the drying shrinkage and has a high stiffness (210 GPa). Table 4.7 presents the material properties of the upper and lower layers, respectively, while Table 5 contains the mechanical parameters for the HAR finite elements. The suction was imposed only at the top of the soil sample and in all the cases the initial suction was set equal to zero. As for the modeling of the water loss during drying, the time evolution of the suction measured for the mixture 85/15 (*i.e.* Figure 4.19) was assumed. The time history of the differential drying, which is computed by the difference between the suctions at the top and at the bottom of the material divided by the height of the soil, is shown in Figure 4.26. As can be seen, the values of differential drying in the first 80 hours are very small and not expressive. Consequently, the soil does not curl during this period. After 101 hours the differential drying becomes more pronounced and it reaches a peak at 140 hours. The curling process occurs during this stage (*i.e.*, between 101h and 140h). The last part is characterized by a reduction in the differential drying from the maximum value to zero. In other words, at the end of this stage the soil is complete dried.

Table 4.7: Mechanical properties adopted for the 2D model

Elastic parameters of BBM					
Soil sample	κ_{io}	κ_{s_o}	α_{ss}	p_{ref} (MPa)	ν
upper layer	0.025	0.17	0.025	0.10	0.42
lower layer	0.025	0.12	0.023	0.10	0.42

Table 4.8: Mechanical properties of the interface elements

Element	E (MPa)	ν	σ_u (kPa)	β_s (kPa)	β_l (kPa)	G_f (N/m)	Constitutive model
Soil – soil interface	0.4	0.0	10	-	-	4	Tensile damage
Soil – plate interface	0.4	0.0	0.04	0.4	0.4	-	Interface damage
Soil – plate interface (grooves)	0.4	0.0	10	8	2.4	4	Interface damage

Figure 4.27 shows the time history of stress contours for the sample 85% kaolin and 15% sand. The development of this stress state reflects the differential shrinkage between the top and bottom materials. In this case, the top layer shrinks more than the one at the bottom and this phenomenon

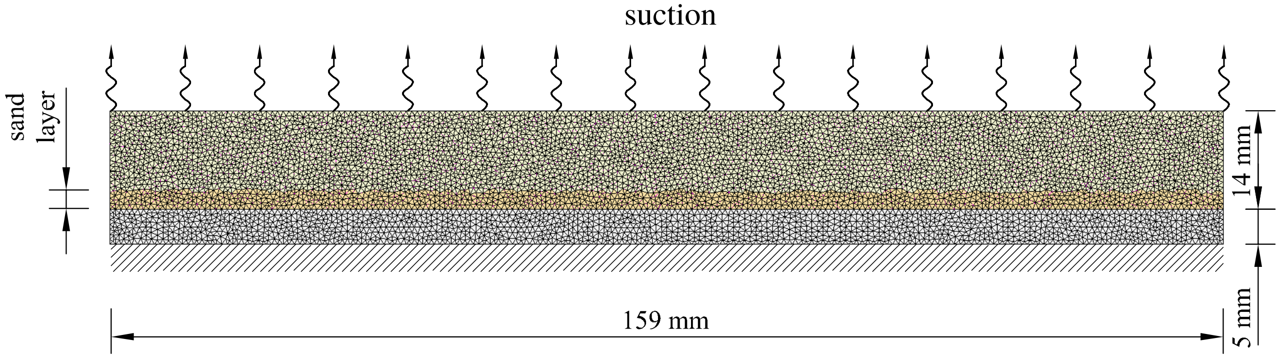

Figure 4.25: Geometry and boundary conditions of the model adopted for the drying test

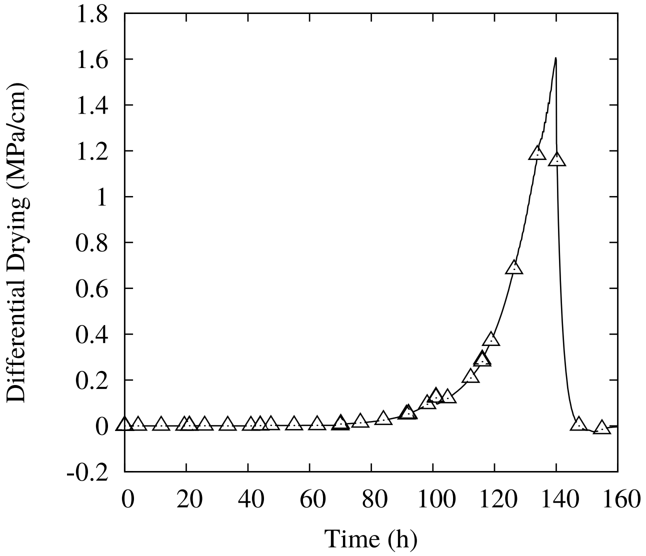

Figure 4.26: Photo of the adopted set-up

induces the extremes of the sample to curl up. The lower region prevents the upper material to shrink as a whole, and consequently, tensile stresses start to concentrate in the middle of the top zone of the sample, while the bottom part of the soil exhibits compressive stresses. The previous process is caused by two phenomena that are different in concept but are correlated to each other: the differential shrinkage and the differential drying. While the former is related to the mechanical shrinkage of the sample (*i.e.*, κ_i and κ_s parameters), the latter is associated to the permeability and retention curve of the soil. For example, a soil with a more uniform texture tends to curl less than a soil with granular particle size distribution. Both cases can have the same differential drying but not the same differential shrinkage.

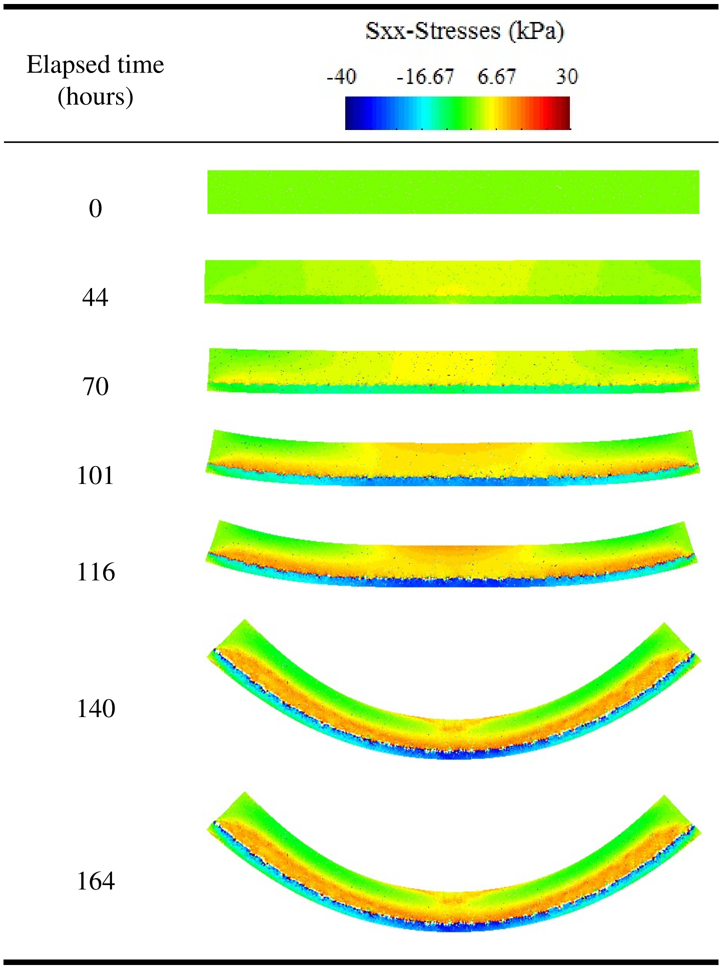

Figure 4.27: Contours of stress field of the model reproducing the behavior of the 85/15 kaolinite/silica sand

In the case of the mixture prepared with 80% of kaolin and 20% of sand (Figure 4.28), the tensile stresses at the central upper part is higher than the one found in the previous case (*i.e.*, 85/15 kaolin/sand) because the increase in the percentage of sand particles, which tends to accumulate at the bottom layer, induces a larger differential shrinkage. This increment is taken into account in the model by increasing the height of the lower layer. Once the tensile stresses overcomes the tensile strenght of the soil (119 h), a crack initiates at the top of the sample and propagates until it breaks into two equal parts (140 h). As expected, there is a stress concentration near the crack tip at 116 hours.

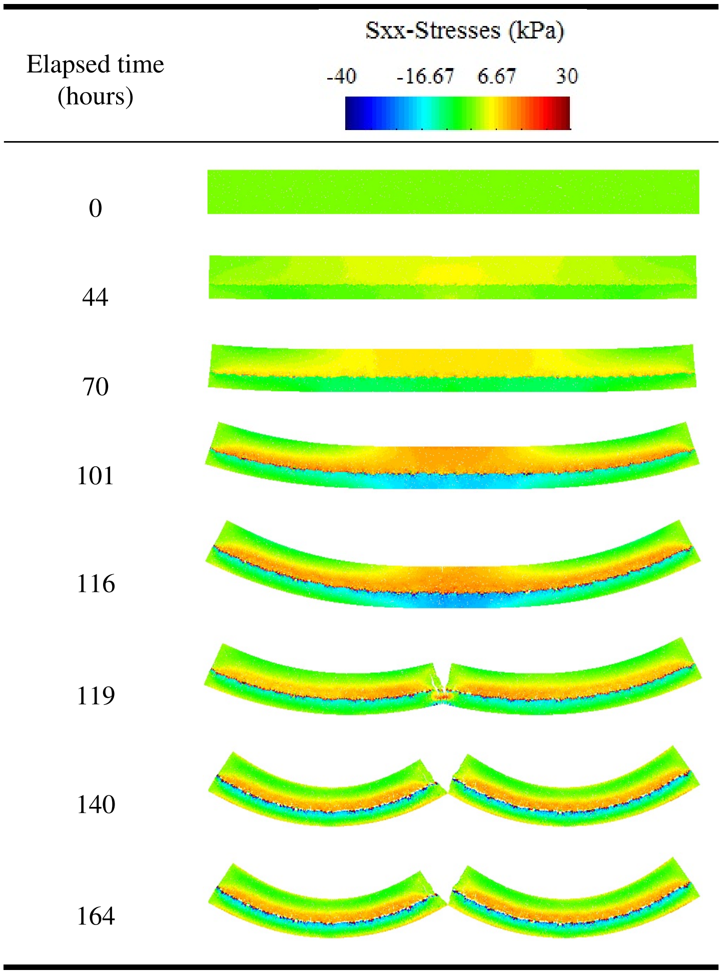

Figure 4.28: Contours of stress field of the model reproducing the behavior of the sample prepared with 80% kaolinite and 20% silica sand

The previous 2D analyses were carried out to investigate the stress distribution over the sample, since finer meshes are possible in such cases. However, in order to realistically model the 3D curling tests reported in Section 4.7, three-dimensional analyses were conducted by considering a mesh consisting of 25634 nodes and 65942 tetrahedral finite elements (33843 of which are HAR), as shown in Figure 4.29. The same initial and the boundary conditions used in the 2D studies are also valid for the present analyses. However, the 85/15 and 80/20 kaolin/sand samples are simulated different from the 2D analyses. In the 3D cases, the height of the bottom material for both mixtures is the same (*i.e.*, 3.5 cm) but the mechanical properties are not, leading to an equivalent differential shrinkage. This approximation is necessary because the 3D fragmented finite element mesh is computational expensive even for a coarse mesh.

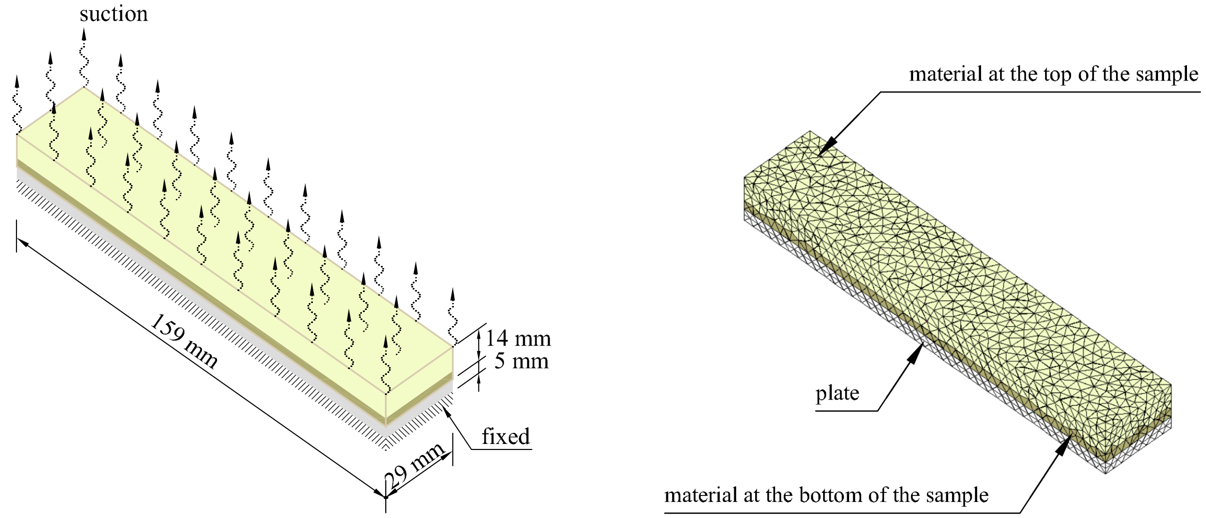

Figure 4.29: (a) Geometry and boundary conditions of the model adopted for the drying test; (b) 3D finite element mesh adopted for the drying test

Figures 4.30a, 4.30b, 4.30c and 4.30d present the lateral, isoparametric, top and front views of the model, respectively, related to the pure kaolin specimen after dying. As expected, this uniform kaolin shrinks without displaying a noticeable curling. Some studies suggest that uniform soils first curl-up (*i.e.* at the initial stages of evaporation); but then (at advanced stages of drying) the deformation reverses and the curled edges start to retreat downward, with no apparent final curling (*e.g.*, [217]). Nevertheless, homogeneous soils subjected to drying generally show a rather uniform shrinkage, without an apparent final curling. All the modeling results correspond to the end of drying. Table 4.9 lists the parameters adopted for modeling the mechanical behavior of the kaolin.

Table 4.9: Mechanical properties adopted for the kaolin and upper layer 3D model

Elastic parameters of BBM				
κ_{io}	κ_{s_o}	α_{ss}	p_{ref} (MPa)	ν
0.025	0.17	0.025	0.10	0.42

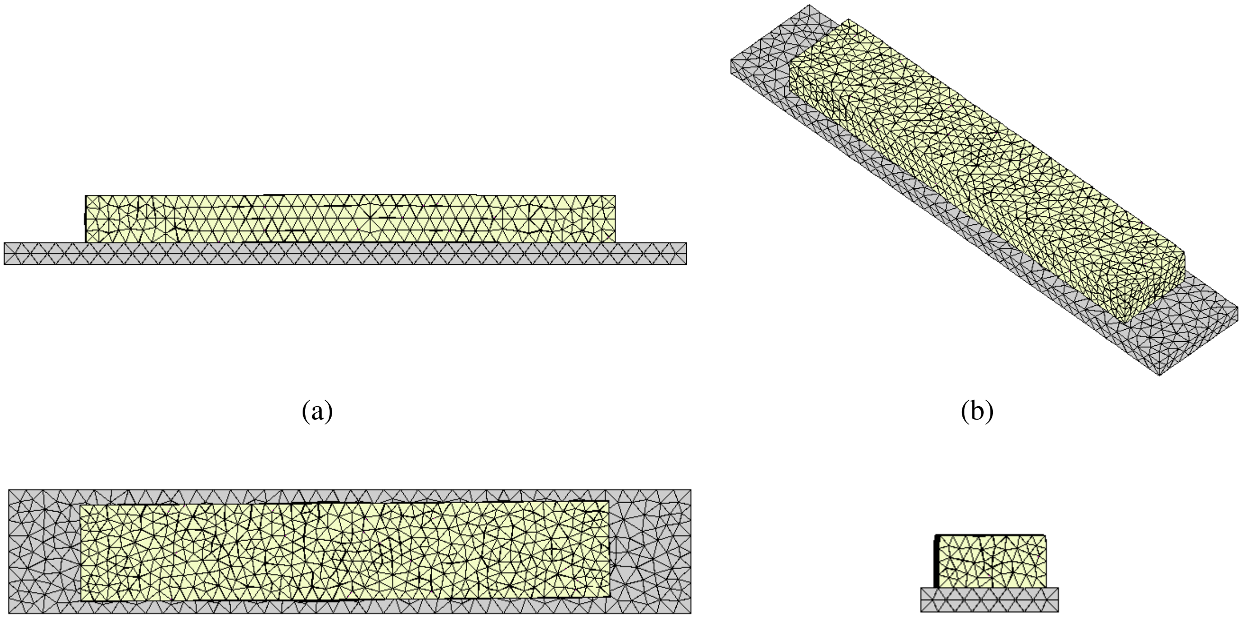

(a) (b)

(c) (d)

Figure 4.30: Deformation of the model reproducing the behavior of pure kaolinite at the end of the analysis: (a) side view; (b) isometric view; (c) top view; (d) front view

In the case of a soil with gradual grain size distribution, the model considered two layers of soils to mimic the sedimentation process that occurred before the drying test initiates. Since two different mixtures of kaolinite and sand have been studied throughout this work, and we have considered the same mesh and layers for both of them, the difference between these two cases was modeled by means of material properties of the bottom layer. Hence, the elastic parameters (*i.e.*, κ_{s_o} and α_{ss}) of the bottom layer were used to represent the concentration of sand settled at the bottom. Tables 4.9 and 4.10 present the mechanical properties assumed for both upper and lower layers. Values closer to those used in the top layer lead to smaller differential shrinkage, which means a smaller concentration of sand particles at the bottom. Thus, the soil with 15% of silica sand was represented by considering a bottom layer with elastic properties smaller than those in top layer and larger than the ones in mixture with 20% of silica sand. Figure 4.31 exhibits the evolution of displacement with elapsed time at the side and top views of the sample prepared with 85% kaolinite and 15% of silica sand and compares the experimental curling development with the numerical one. As can be seen, the model was able to predict the curling progression with time. Such mixture curls up in both directions and it did not reverse at the final drying stages (Figure 4.31), even when the bottom layer is subject to the same drying. As explained by Zielinski *et al.* [217], this takes place because the retraction is hindered by the larger particles settled at the bottom, and therefore, the soil cannot curl back because the downward movement is restricted.

Table 4.10: Mechanical properties adopted for the lower layer 3D model

Elastic parameters of BBM					
Soil sample	κ_{io}	κ_{s_o}	α_{ss}	p_{ref} (MPa)	ν
85/15 – kaolinite/sand	0.025	0.12	0.023	0.10	0.42
80/20 – kaolinite/sand	0.025	0.09	0.018	0.10	0.42

When the sample is made up with 80% of kaolinite and 20% of silica sand, the differential shrinkage is so large that the soil broke in the middle, as shown in Figure 4.32. In the 2D case the lower layer of the 85/15 and 80/20 have the same mechanical properties but different layer thickness. Thus, the larger differential contraction of the mixture with 80% of kaolin is due to the concentration of sand particles at the bottom. For the 3D cases, the previous assumption was approximated by changing the shrinkage parameters of the bottom material, which induces an equivalent retraction. In other words, the assumption of the 3D model was used to mimic the same phenomenon. Figures 4.32a and 4.32c illustrate the top and side views of the model at the end of the analysis, respectively, while Figures 4.32b and 4.32d shows the isoparametric and front views, respectively.

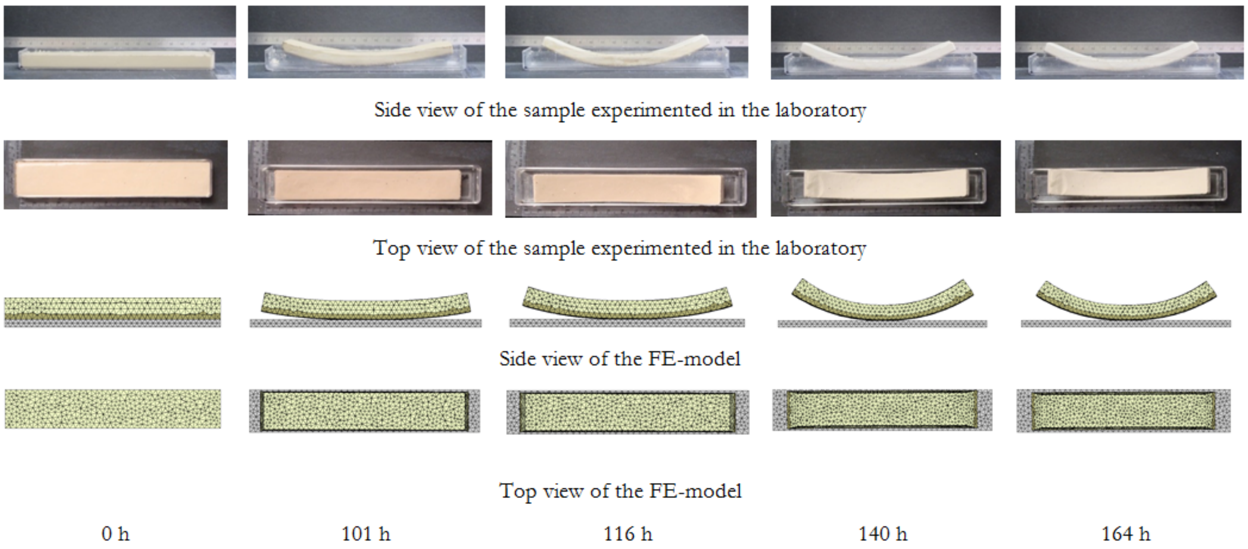

Figure 4.31: Stages of the curling development in a thin soil layer of 85% kaolinite and 15% silica sand

The last analysis simulates the case in which the sample with 85% of kaolinite and 15% of sand is placed upon a support with parallel notches, which means that the sample is restricted in one direction at the bottom. Since the bottom surface was not greased, it is reasonable to assume that the other direction has a small restriction (Table 4.8). Furthermore, the fact that the grooves prevent the soil to deform in the normal direction allows us to consider that the tensile strengths of the soil-plate interface and soil-soil interface are the same. Figure 4.33 presents the crack pattern resulted from the simulation. The next section explains compares and discusses the numerical and experimental results performed in this work.

4.11 Discussion

The main aim of these experiments and numerical analyses was for a better understanding the effect of material type on soil curling deformation. In this work, a total of four series of tests have been performed. It has been observed that particle size distribution has a significant effect on soil curling deformation; although, curling deformation was observed in a mixture of uniform soil particles (*i.e.* pure kaolinite prepared), it was not as significant as the one observed with a mixture of non-uniform soil particles (silica sand with kaolinite). Furthermore, particle size distribution of

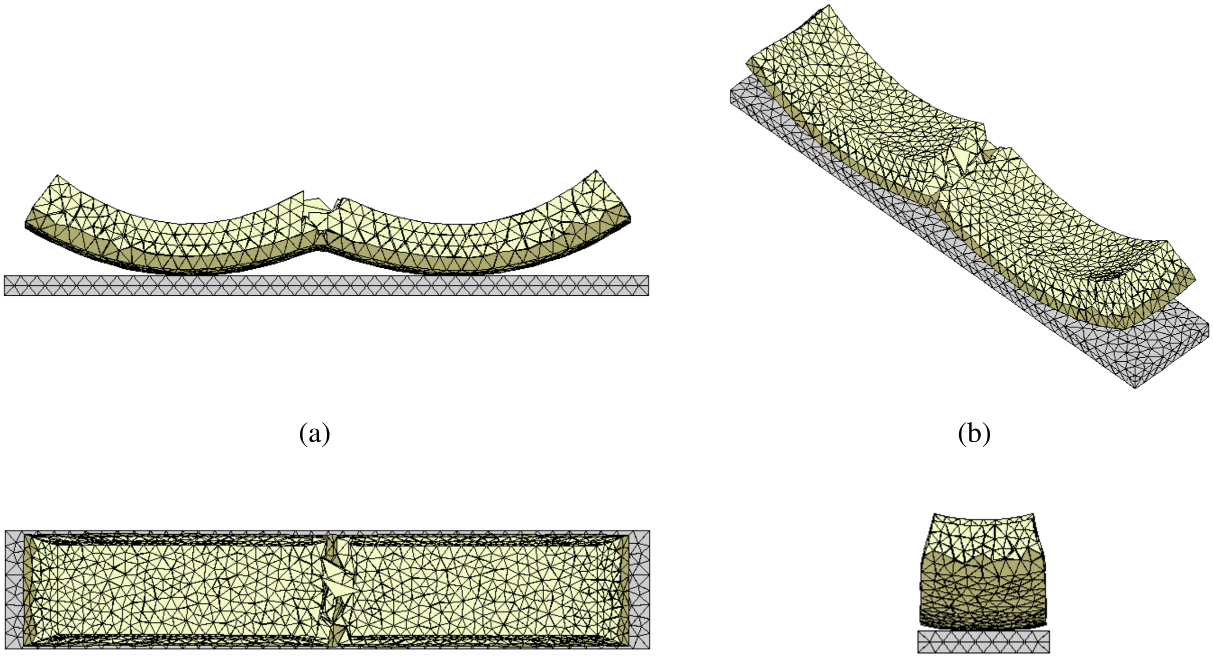

(a) (b)

(c) (d)

Figure 4.32: Curling deformation of the soil sample prepared with 80% kaolinite and 20% silica sand at the end of the simulations: (a) side view; (b) isometric view; (c) top view; (d) front view

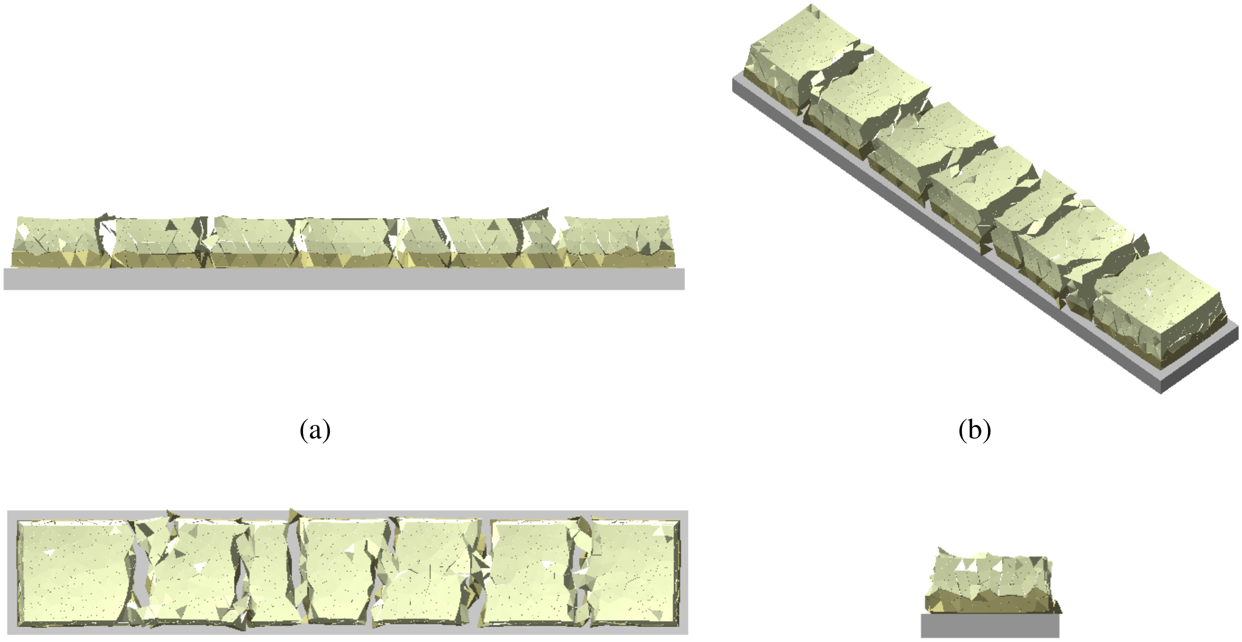

(a) (b)

(c) (d)

Figure 4.33: Crack pattern of the soil sample prepared with 85/15 kaolinite/silica sand at the end of the analysis: (a) side view; (b) isometric view; (c) top view; (d) front view

soil samples is obviously governed by sedimentation phenomenon at early stages of drying.

In the mixture of pure kaolinite (Figures 4.20c and 4.30), small curling (moving up the edges of the sample) was observed at the end of drying path. At the end of drying, the soil sample with 85% kaolinite and 15% sand (Figure 4.31) tried to reach water content equilibrium condition between the upper and the bottom sections; therefore, drying rate at the bottom increased to overcome the one above. Since the sample is already dry and hard in this stage, curling deformation overcomes the shrinkage deformation. This theory was clearly observed with the mixture of 80% kaolinite and 20% silica sand, the soil samples were broken at the end of drying due to curling deformation (moving up the edges of these samples) which led to weakening the middle part of these samples, as shown in Figures 4.22 and 4.32. Furthermore, depending on the type of the soil in this stage, the level of differential shrinkage would be different between the upper and lower parts of the sample; therefore, the resulting curling may be concave-up or convex-up.

4.12 Conclusions

The difference in directional strengths at the contact between materials generally arrives from the presence of textures at the interfaces. The incorporation of these interfaces characteristics between materials is instrumental for a realistic solution of several engineering problems. However, the explicit discretization of these textures in the modeling is generally time consuming (as sometimes relatively small structural details need to be represented), and also the associated meshes are very dense (with the corresponding demand in CPU time).

In this work, an orthotropic mechanical model for soils developed in the framework of the mesh fragmentation technique was proposed. The full mathematical framework alongside the suggested numerical algorithm for its numerical implementation in a FE code were discussed in detail. The capability of the model to reproduce different plausible loading conditions involving orthotropic interfaces was checked by means of tailored synthetic benchmarks. A very good performance of the model was observed in the four cases analyzed. This work also deals with the experimental validation of the suggested model. Direct shear tests involving soil and plates with different textures were conducted to study the dependence of the interface strength properties on orthotropic characteristics. The comparisons between the proposed model and experimental results were very satisfactory, proving the ability of the model to capture the observed response of orthotropic interfaces involving shearing directions perpendicular and parallel to straight grooves, as well as soil shearing respect to a plate grooved following a circular pattern and also a smooth plate. Finally, the model was applied to analyze a boundary value problem related to the drying behavior of a soil subjected to shrinkage with restriction of displacement in one direction. Also in this case the model was able to reproduce very well the developments of drying cracks observed in the experiment.

The influence of the sedimentation process in the soil surface curling was also experimentally and numerically studied in this chapter. Four laboratory tests were conducting by using two digital cameras, which were strategically placed to capture the top and the larger side of the same. Furthermore, a novel interface damage model that is capable of capturing damage in tensile and shearing was also presented.

The tests were carried out by considering three different mixtures: one with 85% kaolinite and 15% silica sand, other with 80% kaolinite and 20% silica sand and the last one with pure kaolinite. All of them were prepared at 3xLL. The samples were subject to the drying process under controlled laboratory conditions. The study has shown differences in the curling surface among different soil mixtures, which is evidence that the sedimentation has a strong impact in the curling phenomenon. While the pure kaolinite sample exhibit only a small presence curling, which curls back at the end of the test, the sample with 15% of sand experienced significant curling at the edges. The effect of the sedimentation is so significant that the sample with 20% of sand broke in the middle due to differential shrinkage. A fourth drying test was performed by placing the soil with 85% kaolinite and 15% silica sand in a container with grooved surface at the bottom. As expected, desiccation cracks were observed in the direction of the grooves.

Therefore, this chapter has also shown that soils with different texture skeletons will develop different surface curling when they are prepared with the same initial water content. In addition, the interface of the soil-container may induce cracks by restraining the movement of the soil.

5. MODELING COUPLED MULTIPHYSICS PHENOMENA IN ROCKS INVOLVING DISCONTINUITIES

5.1 Introduction

In the United States, the volcanic field of Coso, located in California, generates 260 MW of geothermal energy [94], and estimations have shown that this same site will soon be able to produce an additional 20 MW of electricity after the introduction of the technology called Enhanced Geothermal System (EGS). EGS is essential to explore Hot Dry Rock (HDR) reservoirs that are deficient in permeability and water and need to be stimulated for their complete exploration. Thus, two types of wells are drilled, in which one of them cold water is injected and in the other hot water and/or stem is retrieved. The circulation occurs by through a system of artificial and/or natural fractures (pre-existing).

It is noteworthy that the United States is not an exception. Other countries are also involved in similar projects. In 1977 the Camborne School of Mines in the UK conducted a series of studies at the Rosemanowes in Cornwall, which is a HDR. The project was funded mainly by the UK Department of Energy and to a smaller extent by the European Commission [162]. The studies were initially divided in two phases. In the first phase (1977 - 1980), two wells with depth of 300 meters were drilled to improve the permeability of the medium, so that water could circulate through pre-existed fractures by means of hydraulic stimulation. The second phase (1980 - 1988) consisted of studying wells with depths of 2 kilometers. A third phase was started in 1988 and intended to develop a prototype for electrical power production, but the project was terminated in 1991. Note that the first two phases were completed, while the third one was ended before its execution.

Another promising case in Europe is the reservoir in France composed by crystalline rocks. After years of research related to he development of EGS in the Soultz-sous-Forêts reservoirs, which was carried out with French, German and Swiss governmental and European funding, a

French-German industrial consortium built a power plant for electricity generation [70]. The power plant works with three wells of 4.5 km depth and open-hole section of about 500 m. Isobutane is injected into one well and the geothermal fluid, which is a natural brine, is pumped from two production wells. After the isobutane captures the necessary energy, cooled brine solution is injected again. The geothermal plant has produced around 1.5 MW since June 2008.

Japan has also studied the feasibility of energy exploration in HDR through projects in Ogechi and Hiyori. The project at Ogachi in Akita Prefecture (1989 - 2002), which was conducted by the Central Research Institute of Electric Power Industry (CRIEPI), intended to show that large reservoirs could be created and heat energy could be obtained at a depth of 1000 meters [99]. Three wells were drilled, so that river water was injected into one well and hot water and steam were produced from the others. Although the operation was successful, the process resulted in a loss of 70% of water. In the case of the Hiyori project (1986 - 2003), which were conducted by the New Energy and Industrial Development Organization, the reservoir was able to capture 50 KW of energy during the tests [99]. The water recovery from the wells reached a maximum of 70.4%.

The exploration of reservoirs with low permeability occurs by the injection of fluids (water, CO_2, etc.), which induces the formation and propagation of discontinuities and reactivates pre-existing fractures. Both geothermal and shale gas reservoirs have low permeability, and therefore, there are several aspects common to both. For example, both need to be stimulated to create a permeable zone that permits the extraction of energy resources (heat, gas or oil). The stimulation occurs through fluid pressure that alters and disturbs the stress state of the rock mass, resulting in the formation of fractures and reopening pre-existing faults. Thus, in such cases, the permeability of the reservoir is based on its fracture network.

The technique named hydraulic fracturing is one of the main mechanisms applied by the oil industry to activate the permeable zone. The fluid's pressure injected into the well creates and/or reopen fractures. This process is complex and involves distinct engineering fields because, in addition to the stress state and the hydro-mechanical behavior of the rock mass, it also should consider the fracture process and interactions.

The simulation of a low-permeability reservoir should be based on realistic models capable of capturing and reproducing the main phenomena related to the medium, since the design of a reservoir for energy production depends on the interpretation of the analysis [72].

Although nowadays there is a considerable range of work for hydraulic fracturing modeling, studies related to the subject have been conducted since 1950. Perkins and Kern [165] formulated the called PK model, which is considered a pioneer work in this field. Several analytical solutions were developed over the years based on their work [145, 66]. Piggot and Elsworth [169] created a model to study hydraulic fracturing applied to groundwater contamination remediation.

However, the previous solutions suffer from limitations of hypotheses about the opening of cracks or the pressure field. The advances in computers have lead to the development of new techniques capable of mimic the hydraulic fracturing behavior. Li *et al.* [116] adopted a three-dimensional model that considers three coupled processes: (1) the mechanical deformation of the solid medium induced by fluid pressure acting on the fracture surface; (2) fluid flow in the fracture; (3) fracture propagation. They used a parallel code to analyze the reservoir and showed that the fracture initiates in a non-preferred direction and turns and twists during propagation. Discrete element method [84] and Generalized Finite Element Method [81, 82] have also been developed over the years. These approaches are useful to study simple hydro-mechanical problems with a single fracture, but they are not able to reproduce the complex behavior of multiple fractures.

As can be noticed, the works previously mentioned neglected the thermal influence, which strongly affects the reservoir behavior. Perkins *et al.* [164] used empirical equations based on numerical method to calculate the variation of the horizontal stress caused by an increment (or decrement) of temperature (or pressure) in a region of elliptical cross section. The authors showed that the injection of cold water generates fractures under pressures considerable smaller than those observed in the absence of the thermoelastic effect. In addition, depending on the cooled region, secondary fractures perpendicular to the principal one may appear.

Secondary thermal fractures have also been investigated by research groups [142, 19]. These works considered the medium with fractures initially parallel and equally spaced. Tran *et* *al.* [204] used finite elements with discrete cracks to simulate secondary fractures. Thus, fracturing formation occurs when the applied tension stress overcomes the tensile strength of the material (fracture in Mode I). Although they considered the influence and interaction between secondary fractures, the model was not able to reproduce Mode II and mixed fracture propagation. Hofmann *et al.* [89] integrated a hybrid model with discrete and finite elements to study hydraulic fracturing and the development of a complex fracture system. Although 2D analyses assist the investigation of hydraulic fracturing behavior, 3D analyses are usually required, since the three-dimensional stress state may lead to all fracture modes (I, II and III) [72].

The following numerical methods have also been used to model hydraulic fractures: boundary elements with discontinuous displacements [73]; finite element method with cohesive models to reproduce discontinuities [48]; finite volume method to treat the fluid and heat flow in space discretization and finite elements for discretization of the mechanical problem [102]; hybrid finite difference/finite volume method [202]. When the reservoir is represented by two different methods (i.e., finite elements and finite volumes) the problem must be iterated until it converges, since the systems are independently solved (i.e., decoupled analysis). In the case of cohesive models, remeshing algorithms are needed to reproduce the discontinuity, and consequently, it increases the computational cost involved. More information can be found elsewhere [72, 120, 203].

The remainder of this chapter is organized as follows: the mesh fragmentation technique and the kinematics relation is reviewed in the context of small strain hypothesis. Then the governing equations is explained and the approach of treating discontinuity by means of continuum mechanics concepts is shown. Afterwards, the weak form and the finite element formulation are introduced and discussed. Finally, numerical analysis and concluding remarks close out this chapter.

5.2 The Mesh Fragmentation Technique (MFT)

The process in which high aspect ratio finite elements are introduced between the bulk elements of the mesh is called mesh fragmentation technique (MFT). The method can be used to tackle discontinuities in 2D or 3D problems. The main steps associated with this methodology are shown in Figure 5.1 and explained as follows. The first step consists in slightly reducing the original size of the finite elements (Figure 5.1a), which leads to the formation of small gaps between adjacent elements (Figure 5.1b). In this state, the number of nodes is increased because new nodes are needed to separate the elements. The gaps are filled with a pair of HAR finite elements (Figure 5.1c), which increases the number of element in the problem. It is worthwhile to mention that the size of such gaps is very small, typically around 0.1% of the size of the smallest bulk element.

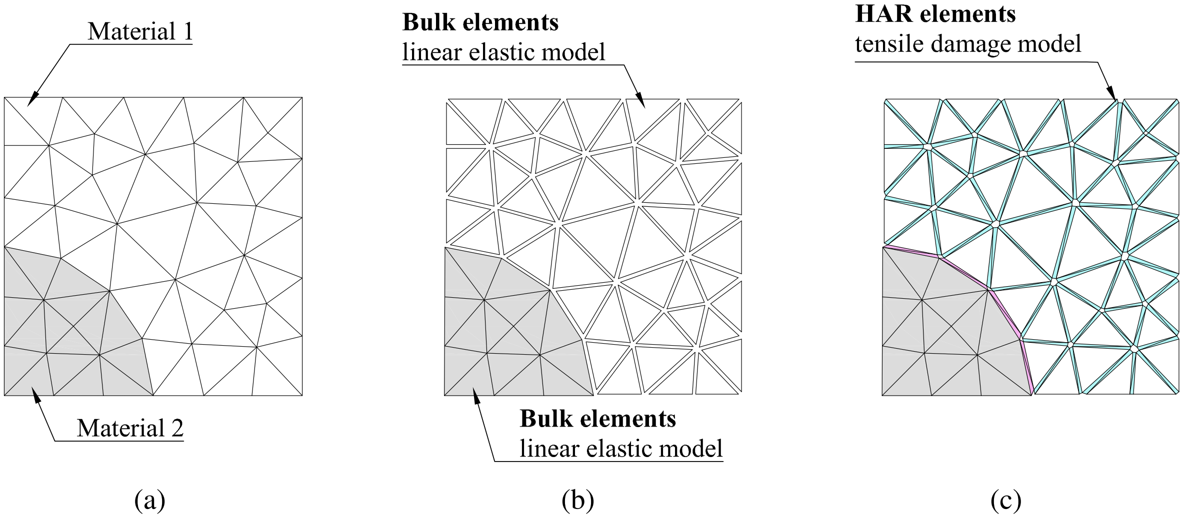

Figure 5.1: Main stages associated with the mesh fragmentation technique: (a) original finite element mesh;(b) size of the bulk elements are reduced, creating gaps between them; (c) such gaps are filled with elements with high aspect ratio, which can reproduce the discontinuity behavior (adapted from [123])

In this work, the bulk elements exhibits a linear elastic behavior while HAR elements are described by the tensile damage model. The degradation process starts when the tensile stress of the HAR element reaches the damage criterion. At this point, a softening behavior dictates the evolution of the damage, which is characterized by stiffness. The damage model incorporates the smallest dimension of the interface element in order to regularize the solution and avoid mesh dependency. Figure 5.2 illustrates a portion of a domain Ω discretized with bulk and HAR finite elements. The subdomain Ω^h consists in a set of HAR elements that have developed damage throughout the loading process and represent the discontinuity surface.

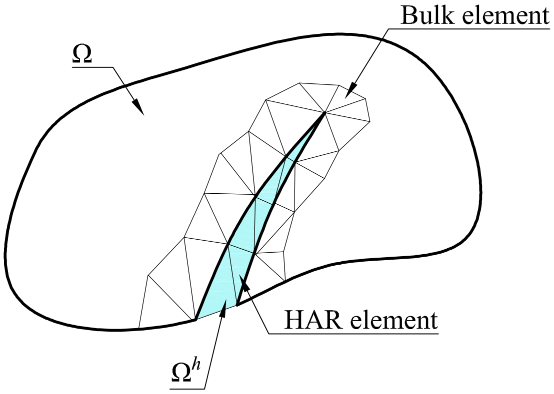

Figure 5.2: Fracture propagation with HAR finite elements

Since the proposed continuous approach of the discontinuity can be represented by linear variation of the associated variables in the subdomain Ω^h, the traditional three-node finite element shown in Figure 5.3 can be used to reproduce the discontinuity behavior. The strain tensor of this triangular element can be written in terms of two tensors, in which the components of the first tensor, $\tilde{\boldsymbol{\epsilon}}$, do not depend on h and the second tensor expresses the discontinuity behavior:

$$\boldsymbol{\epsilon} = \tilde{\boldsymbol{\epsilon}} + \frac{1}{h} (\mathbf{n} \otimes [\![\mathbf{u}]\!]) \tag{5.1}$$

where $(\bullet)^S$ denotes to the symmetric part of $(\bullet)$, $\mathbf{n}$ is the unit vector normal to the base of the finite element, $\otimes$ is the dyadic product and $[\![\mathbf{u}]\!]$ is the vector containing the components of the relative displacement between node 1 and its projection at the element base (1'). When $h \to 0$ the term that depends on h is no longer bounded and the element strains are almost exclusively defined by the relative displacement $[\![\mathbf{u}]\!]$, and therefore, this term becomes the measure of strong discontinuity.

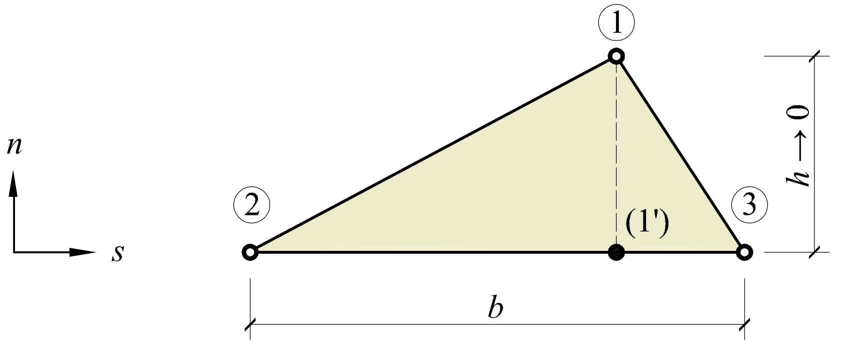

Figure 5.3: Three-node triangular finite element (adapted from [121, 123])

As shown by Manzoli *et al.* [126], the volumetric strain in this case can be written as:

$$\boldsymbol{\nabla} \cdot \mathbf{u} = \boldsymbol{\nabla} \cdot \tilde{\mathbf{u}} + \frac{[\![u]\!]_n}{h} \tag{5.2}$$

In the case of the hydraulic and thermal processes, the liquid pressure and temperature are continuous across the discontinuity surface S, *i.e.*

$$(p_l)_f = (p_l)_{S^+} = (p_l)_{S^-} \tag{5.3}$$

$$T_f = T_{S^+} = T_{S^-} \tag{5.4}$$

with $(p_l)_f$ and T_f denoting the pressure and temperature in S. The water flow and heat flow fields, on the other hand, are characterized by a jump across the discontinuity due to the transport of mass of water and energy along the fracture, such that

$$\dot{M} = \dot{\tilde{M}} + \rho_l \, [\![\, q_l \,]\!] \cdot \mathbf{n} \tag{5.5}$$

$$\dot{E} = \dot{\tilde{E}} + [\![\, \mathbf{j}'_E \,]\!] \cdot \mathbf{n} \tag{5.6}$$

in which $[\![\, \mathbf{q}_l \,]\!] = q_{l_{S+}} - q_{l_{S-}}$ and $[\![\, \mathbf{j}'_E \,]\!] = j'_{E_{S+}} - j'_{E_{S-}}$. The detailed description of the mathematical framework can be found elsewhere [126]. Following the governing equations of thermo-hydro-mechanical problems are introduced.

5.3 Governing Equations

The balance equations, constitutive relations and equilibrium restrictions together with the initial and boundary conditions correspond to the set of governing equations that mathematically describe the physical problem under consideration. The main components of these equations are explained next.

5.3.1 Mechanical Model

The momentum balance equation for the porous material neglecting the inertial term is given by:

$$\boldsymbol{\nabla} \cdot \boldsymbol{\sigma} + \mathbf{b} = \mathbf{0} \tag{5.7}$$

in which $\mathbf{b}$ is the vector of body forces and $\boldsymbol{\sigma}$ is the total stress tensor expressed in terms of effective stress ($\boldsymbol{\sigma}$') and liquid pressure (p_l):

$$\boldsymbol{\sigma}' = \boldsymbol{\sigma} + \mathbf{I}\, b\, p_l \tag{5.8}$$

where $\mathbf{I}$ is the identity tensor and b is the Biot's coefficient defined as:

$$b = 1 - \frac{K}{K_s} \tag{5.9}$$

with K and K_s denoting the bulk moduli of the porous medium and the solid phase, respectively.

The effective stress of the bulk element can be expressed in terms of total strain tensor $\boldsymbol{\epsilon}$ and the temperature variation $\dot{T}$ as follows:

$$\dot{\boldsymbol{\sigma}}' = \mathbb{C} : \underbrace{(\dot{\boldsymbol{\epsilon}} - \dot{\boldsymbol{\epsilon}}^{o})}_{\dot{\boldsymbol{\epsilon}}^{e}} = \mathbb{C} : \left[\dot{\boldsymbol{\epsilon}} - \mathbf{I}\, \alpha_T\, \dot{T}\right] \tag{5.10}$$

where α_T is the linear thermal expansion coefficient.

The HAR finite elements are able to tackle the fracture formation due to following scalar tension damage model, in which the constitutive relationship is given by:

$$\boldsymbol{\sigma}' = (1-d)\mathbb{C} : \boldsymbol{\epsilon} = (1-d)\bar{\boldsymbol{\sigma}} \tag{5.11}$$

where $d \in [0,1]$ is the damage variable, $\mathbb{C}$ is the forth-order elastic tensor, $\boldsymbol{\epsilon}$ is the strain tensor and $\bar{\boldsymbol{\sigma}}$ is the elastic stress tensor.

The failure criterion can be written in terms of the effective stresses as follows:

$$f = \sigma'_{nn} - q(r) \leq 0 \tag{5.12}$$

in which σ'_{nn} is the component of the effect stress tensor normal to the base of the HAR element, r is the strain-like internal variable and q is the stress-like internal variable defined by:

$$q(r) = \sigma_u \, \exp\left[\frac{\sigma_u^2}{E\,G_f}\, h\left(1 - \frac{r}{\sigma_u}\right)\right] \tag{5.13}$$

where σ_u denotes the tensile strength, E is the young modulus and G_f stands for the fracture energy of the rock.

The criterion given by Eq. (5.12) can also be expressed in terms of the elastic stresses by dividing both terms by $(1-d)$:

$$\bar{f} = \bar{\sigma}_{nn} - r \leq 0 \tag{5.14}$$

Therefore, since $r = q/(1-d)$, one can write the following damage law:

$$d(r) = 1 - \frac{q(r)}{r} \tag{5.15}$$

The last ingredient of the damage model corresponds to the Kuhn-Tucker relations:

$$\bar{f} \leq 0, \; \dot{r} \geq 0, \; \dot{r}\bar{f} = 0 \tag{5.16}$$

and the consistency condition:

$$\dot{r}\,\dot{\bar{f}} = 0 \text{ if } \dot{\imath}\bar{f} = 0 \tag{5.17}$$

Based on these equations (*i.e.*, Eq. (5.15), (5.16) and (5.17)) the evolution of the strain-like internal variable can be defined as:

$$r(t) = r = \max_{s \in [0,t]} [\bar{\tau}(s), r_0] \tag{5.18}$$

The constitutive model explained in this section was implemented in CODE_BRIGHT using the IMPL-EX stress integration scheme proposed by Oliver *et al.* [153].

5.3.2 Hydraulic Model

The water mass balance equation for a fully saturated porous medium can be written as:

$$\phi \frac{D\rho_l}{Dt} + \left[\frac{(1-\phi)}{\rho_s} \frac{D\rho_s}{Dt} + \boldsymbol{\nabla} \cdot \dot{\mathbf{u}} \right] \rho_l + \boldsymbol{\nabla} \cdot (\rho_l \, \mathbf{q}_l) = 0 \tag{5.19}$$

where ϕ denotes the porosity, ρ_l is the liquid density, ρ_s is the solid density, $\dot{\mathbf{u}}$ is the velocity vector and $\mathbf{q}_l$ is the fluid Darcy's velocity vector expressed as:

$$\mathbf{q}_l = -\frac{\mathbf{k}}{\mu_l} \cdot (\boldsymbol{\nabla} p_l - \rho_l \, \mathbf{g}) \tag{5.20}$$

where $\mathbf{k}$ is the intrinsic permeability tensor of the porous medium and μ_l is the dynamic viscosity of the liquid. The previous equation is valid for both types of elements (*i.e.*, bulk and interface elements). In the case of the fracture with domain Ω^h, the water mass balance equation is:

$$(\mathbf{q}_l)_{\Omega^h} = -\frac{\mathbf{k}_{\Omega^h}}{\mu_l} \boldsymbol{\nabla} p_l = -\frac{1}{\mu_l} \left(\mathbf{k} + \frac{[\![u]\!]_n^3}{R\,12\,h} \mathbf{t} \otimes \mathbf{t} \right) \boldsymbol{\nabla} p_l \tag{5.21}$$

in which the first term on the right hand side of Eq. (5.21) corresponds to the continuous part of the liquid flux and the second term is the discontinuous counterpart associated with the enhancement in the s-direction due to the displacement discontinuity and modeled by mean of the well-known cubic law [197]. In Eq. (5.21), $R \geq 1$ is a parameter that accounts for deviation from the ideal parallel surface conditions [212]. In this work $R = 1$ is assumed for all analyses.

The porosity is also affected by the fracture opening as follows [126]:

$$\phi_{\Omega^h} = \phi + \frac{[\![u]\!]_n}{h} \tag{5.22}$$

The second term in Eq. (5.22) is the enhancement due to an increase in void ratios during the loading process.

Finally, the solid density for the continuous medium is given by:

$$\rho_s = \rho_{s0} \exp\left[\frac{(b-\phi)}{K_s}(p_l - p_{lo}) - (b-\phi)\,\alpha_T\,(T - T_o) - (1-b)\,\epsilon_v\right] \tag{5.23}$$

with ϵ_v denoting the volumetric deformation. Note that this last equation is not valid for the discontinuity, since it is assumed that the fracture is filled with fluids and does not contain any solid particle.

5.3.3 Thermal Model

The internal energy balance equation for the fully saturated porous material is given by:

$$\begin{aligned} \phi\frac{D}{Dt}\left(E_l\,\rho_l\right) + \left(E_l\,\rho_l\right)\left[\frac{(1-\phi)}{\rho_s}\frac{D\rho_s}{Dt} + \boldsymbol{\nabla}\cdot\dot{\mathbf{u}}\right] \\ + (1-\phi)\rho_s\frac{DE_s}{Dt} + \boldsymbol{\nabla}\cdot\underbrace{\left(\mathbf{i}_c + E_l\,\rho_l\,\mathbf{q}_l\right)}_{\mathbf{j}'_E} = f^E \end{aligned} \tag{5.24}$$

where E_s and E_l are the specific internal energies of solid and liquid phases, respectively; $\mathbf{j}'_E$ is the total heat flux and $\mathbf{i}_c$ is the thermal conductivity flux expressed as:

$$\mathbf{i}_c = \mathbf{I}\,\lambda\,\boldsymbol{\nabla}T = \mathbf{I}\,\left[\lambda_s\,(1-\phi) + \lambda_l\,\phi\right]\,\boldsymbol{\nabla}T \tag{5.25}$$

in which λ_s and λ_l represent the thermal conductivity of the solid and liquid phases, respectively, and T denotes the temperature field.

Once the damage process is initiated, the domain Ω^h is assumed to be filled with fluid, and consequently, $(1-\phi)_{\Omega^h}$ vanishes since the fracture phenomenon is characterized by the absence of solid particles. In this sense, the thermal conductivity of the domain Ω^h is:

$$(\mathbf{i}_c)_{\Omega^h} = \mathbf{I}\,\left[\lambda_l\,\phi_{\Omega^h}\right]\,\boldsymbol{\nabla} T \tag{5.26}$$

The specific internal energies of the solid (E_s) and liquid (E_l) phases are computed based on the specific heat at constant pressure as follows:

$$E_s = c_s\,T \tag{5.27a}$$

$$E_l = c_l\,T \tag{5.27b}$$

with c_s and c_l denoting the specific heats of the solid and liquid phases, respectively.

The next sections covers the weak form and corresponding finite element equations associated with the proposed methodology.

5.4 Finite Element Equations

5.4.1 Weak Form of the Governing Equations

By multiplying both sides of the governing equations by the corresponding weight functions and integrating in the domain, one can obtain:

$$\int_\Omega \delta\mathbf{u} : \left[\boldsymbol{\Sigma}_*(\boldsymbol{\epsilon}) + \mathbf{m}\,b\,p_l\right]\mathrm{d}\Omega = \int_{\Gamma_\sigma} \delta\mathbf{u}\cdot\bar{\mathbf{t}}\,\mathrm{d}\Gamma + \int_\Omega \delta\mathbf{u}\cdot\mathbf{b}\,\mathrm{d}\Omega \qquad \forall\delta\mathbf{u}\in\mathbf{U}_0, \tag{5.28}$$

$$\begin{aligned}\int_\Omega \delta p_l \cdot \left(\phi_*\frac{D\rho_l}{Dt}\right)\mathrm{d}\Omega + \int_\Omega \delta p_l \cdot \left\{\left[\frac{(1-\phi)_*}{\rho_s}\frac{D\rho_s}{Dt} + \boldsymbol{\nabla}\cdot\dot{\mathbf{u}}\right]\rho_l\right\}\mathrm{d}\Omega \\ + \int_\Omega \boldsymbol{\nabla}\delta p_l \cdot \left[\rho_l\,(\mathbf{q}_l)_*\right]\mathrm{d}\Omega = \int_{\Gamma_q} \delta p_l\,\rho_l\,\bar{q}_l\,\mathrm{d}\Gamma\end{aligned} \qquad \forall\delta p_l\in\mathbf{P}_0 \tag{5.29}$$

and

$$\begin{aligned}
&\int_{\Omega} \delta T \left\{ \phi_* \frac{D}{Dt}(E_l\,\rho_l) + (1-\phi)_* \rho_s \frac{DE_s}{Dt} \right\} \mathrm{d}\Omega \\
&\quad + \int_{\Omega} \delta T \left\{ E_l\,\rho_l \left[\frac{(1-\phi)_*}{\rho_s} \frac{D\rho_s}{Dt} + \boldsymbol{\nabla} \cdot \dot{\mathbf{u}} \right] \right\} \mathrm{d}\Omega \\
&\quad + \int_{\Omega} \boldsymbol{\nabla} \delta T \cdot (\mathbf{i}_c)_* \,\mathrm{d}\Omega + \int_{\Omega} \boldsymbol{\nabla} \delta T \cdot [E_l\,\rho_l\,(\mathbf{q}_l)_*] \,\mathrm{d}\Omega \\
&\quad = \int_{\Gamma_{j_E}} \delta T\; \bar{j}'_E \,\mathrm{d}\Gamma
\end{aligned} \qquad \forall \delta T \in \mathbf{T}_0 \tag{5.30}$$

where $\mathbf{U}_0$, $\mathbf{P}_0$, and $\mathbf{T}_0$ are the space of admissible displacement, pressure and temperature fields, respectively. Eqs. (5.28), (5.29) and (5.30) are the weak form of the mechanical, hydraulic and thermal governing equations, respectively. Finally, the set of material parameters can be defined as follows:

$$[\boldsymbol{\Sigma}_*(\bullet), \mathbf{k}_*, \phi_*, (1-\phi)_*, \lambda_*] = \begin{cases} [\boldsymbol{\Sigma}_{\Omega^h}(\bullet), \mathbf{k}_{\Omega^h}, \phi_{\Omega^h}, 0, \lambda_{\Omega^h}] \text{ in } \Omega^h \\ [\boldsymbol{\Sigma}(\bullet), \mathbf{k}, \phi, (1-\phi), \lambda] \text{ in } \Omega \backslash \Omega^h \end{cases} \tag{5.31}$$

5.4.2 Fluid Mass Balance Equation in the Fracture

The weak form of the fluid mass balance equation in the fracture is given by:

$$\begin{aligned}
&\int_{\Omega} \delta p_l \cdot \left(\phi_{\Omega^h} \frac{D\rho_l}{Dt} \right) \mathrm{d}\Omega + \int_{\Omega} \delta p_l \cdot [(\boldsymbol{\nabla} \cdot \dot{\mathbf{u}})\,\rho_l] \,\mathrm{d}\Omega \\
&\quad + \int_{\Omega} \boldsymbol{\nabla} \delta p_l \cdot [\rho_l\,(\mathbf{q}_l)_{\Omega^h}] \,\mathrm{d}\Omega = - \left[\int_{S^+} \delta p_l\,\rho_l\,q_{l_{S^+}} \mathrm{d}S - \int_{S^-} \delta p_l\,\rho_l\,q_{l_{S^-}} \mathrm{d}S \right]
\end{aligned} \tag{5.32}$$

where $q_{l_{S^+}} = \mathbf{q}_{l_{S^+}} \cdot \mathbf{n}$ and $q_{l_{S^-}} = \mathbf{q}_{l_{S^-}} \cdot (-\mathbf{n})$ are the fluid flow from the subdomain Ω^h towards the surrounding medium.

Neglecting the gravitational terms and substituting Eqs. (5.2), (5.21) and (5.22) into (5.32) yields:

$$\begin{aligned}
&\int_S \int_{-h/2}^{h/2} \delta p_l \cdot \left[\left(\phi + \frac{\llbracket u \rrbracket_n}{h} \right) \frac{D\rho_l}{Dt} \right] \mathrm{d}\eta \, \mathrm{d}\xi + \int_S \int_{-h/2}^{h/2} \delta p_l \cdot \left(\boldsymbol{\nabla} \cdot \dot{\tilde{\mathbf{u}}} + \frac{\llbracket \dot{u} \rrbracket_n}{h} \right) \rho_l \, \mathrm{d}\eta \, \mathrm{d}\xi \\
&\qquad + \int_S \int_{-h/2}^{h/2} \boldsymbol{\nabla} \delta p_l \cdot \left[\frac{\rho_l}{\mu_l} \left(\mathbf{k} + \frac{\llbracket u \rrbracket_n^3}{R12h} \right) \boldsymbol{\nabla} p_l \right] \mathrm{d}\eta \, \mathrm{d}\xi \\
&\qquad = - \left[\int_{S^+} \delta p_l \, \rho_l \, q_{l_{S^+}} \mathrm{d}S - \int_{S^-} \delta p_l \, \rho_l \, q_{l_{S^-}} \mathrm{d}S \right]
\end{aligned} \tag{5.33}$$

The final form is obtained by integrating the previous equation over the width h and taking the limit as $h \to 0$:

$$\int_S \delta p_l \llbracket u \rrbracket_n \frac{D\rho_l}{Dt} \mathrm{d}\xi + \int_S \delta p_l \llbracket \dot{u} \rrbracket \, \rho_l \, \mathrm{d}\xi + \int_S \frac{\partial \delta p_l}{\partial \xi} \frac{\rho_l}{\mu_l} \frac{\llbracket u \rrbracket_n^3}{R12} \frac{\partial p_l}{\partial \xi} \, \mathrm{d}\xi = - \int_S \delta p_l \, \rho_l \, \llbracket q_l \rrbracket \, \mathrm{d}S \tag{5.34}$$

where $\llbracket q_l \rrbracket$ is the jump in the water flow caused by the discontinuity. The previous expression is the weak form of the following differential equation:

$$\llbracket u \rrbracket_n \frac{D\rho_l}{Dt} + \llbracket \dot{u} \rrbracket \, \rho_l + \frac{\partial}{\partial \xi} \left(\frac{\rho_l}{\mu_l} \frac{\llbracket u \rrbracket_n^3}{R12} \frac{\partial p_l}{\partial \xi} \right) + \llbracket q_l \rrbracket = 0 \tag{5.35}$$

which is the strong form of the fluid mass balance equation in the discontinuity.

5.4.3 Internal Energy Balance Equation in the Fracture

Similarly, the internal energy balance equation in the fracture is expressed as

$$\begin{aligned}
&\int_\Omega \delta T \left[\phi_{\Omega^h} \frac{D}{Dt} \left(E_l \, \rho_l \right) \right] \mathrm{d}\Omega + \int_\Omega \delta T \left[\boldsymbol{\nabla} \cdot \dot{\mathbf{u}} \left(E_l \, \rho_l \right) \right] \mathrm{d}\Omega + \int_\Omega \boldsymbol{\nabla} \delta T \cdot \left(\mathbf{i}_c \right)_{\Omega^h} \, \mathrm{d}\Omega \\
&\qquad + \int_\Omega \boldsymbol{\nabla} \delta T \cdot \left[E_l \, \rho_l \left(\mathbf{q}_l \right)_{\Omega^h} \right] \mathrm{d}\Omega = - \left[\int_{S^+} \delta T \, (j'_E)_{S^+} \mathrm{d}S - \int_{S^-} \delta T \, (j'_E)_{S^-} \mathrm{d}S \right]
\end{aligned} \tag{5.36}$$

where $(j'_E)_{S^+} = (\mathbf{j}'_E)_{S^+} \cdot \mathbf{n}$ and $(j'_E)_{S^-} = (\mathbf{j}'_E)_{S^-} \cdot (-\mathbf{n})$ are the heat flow from the subdomain towards the surrounding medium.

Inserting Eqs. (5.2), (5.21) and (5.22) into (5.30) gives

$$
\begin{aligned}
&\int_S \int_{-h/2}^{h/2} \delta T \left\{ \left(\phi + \frac{[\![u]\!]_n}{h} \right) \frac{D}{Dt}(E_l\,\rho_l) \right\} \mathrm{d}\eta\,\mathrm{d}\xi \\
&\quad + \int_S \int_{-h/2}^{h/2} \delta T \cdot \left[\left(\boldsymbol{\nabla} \cdot \dot{\bar{\mathbf{u}}} + \frac{[\![\dot{u}]\!]_n}{h} \right) E_l\,\rho_l \right] \mathrm{d}\eta\,\mathrm{d}\xi \\
&\quad + \int_S \int_{-h/2}^{h/2} \boldsymbol{\nabla} \delta T \cdot \left[\lambda_l\,\mathbf{I} \left(\phi + \frac{[\![u]\!]_n}{h} \right) \right] \cdot \boldsymbol{\nabla} T \,\mathrm{d}\eta\,\mathrm{d}\xi \\
&\quad + \int_S \int_{-h/2}^{h/2} \boldsymbol{\nabla} \delta T \cdot \left[\frac{E_l\,\rho_l}{\mu_l} \left(\mathbf{k} + \frac{[\![u]\!]_n^3}{R12h} \right) (\boldsymbol{\nabla} p_l - \rho_l \mathbf{g}) \right] \mathrm{d}\eta\,\mathrm{d}\xi \\
&\quad = -\left[\int_{S^+} \delta T\,(j'_E)_{S^+} \mathrm{d}S - \int_{S^-} \delta T\,(j'_E)_{S^-} \mathrm{d}S \right]
\end{aligned}
\tag{5.37}
$$

Integrating the above equation over $[-h/2, h/2]$, taking the limit $h \to 0$ yields and ignoring the gravitational terms,

$$
\begin{aligned}
&\int_S \delta T\,[\![u]\!]_n \frac{D}{Dt}(E_l\,\rho_l)\,\mathrm{d}\xi + \int_S \delta T\,[\![\dot{u}]\!]_n\,(E_l\,\rho_l)\,\mathrm{d}\xi + \int_S \frac{\partial \delta T}{\partial \xi} \left(\lambda_l\,[\![u]\!]_n \frac{\partial T}{\partial \xi} \right) \mathrm{d}\xi \\
&\qquad + \int_S \frac{\partial \delta T}{\partial \xi} \left(\frac{E_l\,\rho_l}{\mu_l} \frac{[\![u]\!]_n^3}{R12} \frac{\partial p_l}{\partial \xi} \right) \mathrm{d}\xi = \int_S \delta T\,[\![j'_E]\!]\,\mathrm{d}S
\end{aligned}
\tag{5.38}
$$

Analogous to the fluid mass balance equation, Eq. (5.38) is the weak form of the internal energy balance equation in the fracture:

$$
[\![u]\!]_n \frac{D}{Dt}(E_l\,\rho_l) + [\![\dot{u}]\!]_n\,(E_l\,\rho_l) + \frac{\partial}{\partial \xi} \left(\lambda_l\,[\![u]\!]_n \frac{\partial T}{\partial \xi} \right) + \frac{\partial}{\partial \xi} \left(E_l\,\rho_l \frac{[\![u]\!]_n^3}{R12} \frac{k_{rl}}{\mu_l} \frac{\partial p_l}{\partial \xi} \right) = [\![j'_E]\!]
\tag{5.39}
$$

Therefore, Eq. (5.30) describes the internal energy balance equation in the fracture and the interaction with its surrounding medium.

5.4.4 FEM Approximations

The finite element approximation of the displacement, liquid pressure and temperature fields are, respectively:

$$
\mathbf{u}(\mathbf{X}, t) \approx \mathbf{N}_u(\mathbf{X})\,\mathbf{U}(t)
\tag{5.40}
$$

$$p_l(\mathbf{X},t) \approx \mathbf{N}_p(\mathbf{X})\,\mathbf{P}_l(t) \tag{5.41}$$

$$T(\mathbf{X},t) \approx \mathbf{N}_p(\mathbf{X})\,\mathbf{T}(t) \tag{5.42}$$

where $\mathbf{N}_u$ and $\mathbf{N}_p$ are matrices of the standard FE shape function matrices for vector and scalar field problems [63], respectively; $\mathbf{U}$, $\mathbf{P}_l$ and $\mathbf{T}$ are the nodal displacement, nodal liquid pressure and nodal temperature vectors, respectively. The strains, liquid pressure and temperature gradients are obtained evaluating the derivatives of the shape functions, *i.e.*:

$$\boldsymbol{\epsilon}(\mathbf{X},t) \approx \mathbf{B}(\mathbf{X})\,\mathbf{U}(t) \tag{5.43}$$

$$\boldsymbol{\nabla} p_l(\mathbf{X},t) \approx \boldsymbol{\nabla}\mathbf{N}_p(\mathbf{X})\,\mathbf{P}_l(t) \tag{5.44}$$

$$\boldsymbol{\nabla} T(\mathbf{X},t) \approx \boldsymbol{\nabla}\mathbf{N}_p(\mathbf{X})\,\mathbf{T}(t) \tag{5.45}$$

in which $\mathbf{B}$ and $\boldsymbol{\nabla}\mathbf{N}_p$ are the shape function derivative matrices.

The discrete Galerkin approximations of the governing equations (5.28), (5.29) and (5.30)) are expressed as:

$$\begin{aligned}
\int_\Omega (\mathbf{B})^{\mathrm{T}}\,\boldsymbol{\Sigma}_*(\boldsymbol{\epsilon})\,\mathrm{d}\Omega + \mathbf{Q}_{(u\,p_l)}\dot{\mathbf{P}}_l + \mathbf{Q}_{(u\,T)}\dot{\mathbf{T}} + \dot{\mathbf{F}}_{(u)} &= \mathbf{R}_{(u)} \approx \mathbf{0}\\
\mathbf{C}_{(p_l\,u)}\dot{\mathbf{U}} + \dot{\mathbf{S}}_{(p_l)} + \mathbf{A}_{(p_l\,p_l)}\mathbf{P}_l + \mathbf{F}_{(p_l)} &= \mathbf{R}_{(p_l)} \approx \mathbf{0}\\
\mathbf{C}_{(T\,u)}\dot{\mathbf{U}} + \dot{\mathbf{S}}_{(T)} + \mathbf{A}_{(T\,p_l)}\mathbf{P}_l + \mathbf{A}_{(T\,T)}\mathbf{T} + \mathbf{F}_{(T)} &= \mathbf{R}_{(T)} \approx \mathbf{0}
\end{aligned} \tag{5.46}$$

where the mechanical, hydraulic and thermal matrices are:

$$\mathbf{Q}_{(u\,p_l)} = \int_\Omega (\mathbf{B})^{\mathrm{T}}\,\mathbf{m}\,b\,\mathbf{N}_p\,\mathrm{d}\Omega$$

$$\mathbf{Q}_{(u\,T)} = \int_\Omega (\mathbf{B})^{\mathrm{T}}\,\mathbb{C}\,\alpha_T\,\mathbf{m}\,\mathbf{N}_p\,\mathrm{d}\Omega$$

$$\dot{\mathbf{F}}_u = \int_{\Gamma_\sigma} (\mathbf{N}_u)^{\mathrm{T}}\,\bar{\mathbf{t}}\,\mathrm{d}\Gamma + \int_\Omega (\mathbf{N}_u)^{\mathrm{T}}\,\mathbf{b}\,\mathrm{d}\Omega$$

$$\mathbf{C}_{(p_l\,u)} = \rho_l \int_\Omega (\mathbf{N}_p)^{\mathrm{T}}\, \mathbf{m}\, \mathbf{B}\, \mathrm{d}\Omega$$

$$\mathbf{C}_{(T\,u)} = E_l\, \rho_l \int_\Omega (\mathbf{N}_p)^{\mathrm{T}}\, \mathbf{m}\, \mathbf{B}\, \mathrm{d}\Omega$$

$$\dot{\mathbf{S}}_{(p_l\,p_l)} = \left[\phi_* \, \frac{\partial \rho_l}{\partial t} + \frac{(1-\phi)_*}{\rho_s} \frac{\partial \rho_s}{\partial t}\, \rho_l\right] \int_\Omega (\mathbf{N}_p)^{\mathrm{T}}\, \mathrm{d}\Omega$$

$$\dot{\mathbf{S}}_{(T\,T)} = \left[\phi_* \, \frac{\partial}{\partial t}\,(E_l\, \rho_l) + \frac{(1-\phi)_*}{\rho_s} \frac{\partial \rho_s}{\partial t}\,(E_l\, \rho_l) + (1-\phi)_* \rho_s \frac{\partial E_s}{\partial t}\right] \int_\Omega (\mathbf{N}_p)^{\mathrm{T}}\, \mathrm{d}\Omega$$

$$\mathbf{A}_{(p_l\,p_l)} = \frac{\rho_l}{\mu_l} \int_\Omega (\boldsymbol{\nabla}\mathbf{N}_p)^{\mathrm{T}}\, \mathbf{k}_*\, \boldsymbol{\nabla}\mathbf{N}_p\, \mathrm{d}\Omega$$

$$\mathbf{A}_{(T\,T)} = \int_\Omega (\boldsymbol{\nabla}\mathbf{N}_p)^{\mathrm{T}}\, \boldsymbol{\lambda}_*\, \boldsymbol{\nabla}\mathbf{N}_p\, \mathrm{d}\Omega$$

$$\mathbf{A}_{(T\,p_l)} = \frac{E_l\, \rho_l}{\mu_l} \int_\Omega (\boldsymbol{\nabla}\mathbf{N}_p)^{\mathrm{T}}\, \mathbf{k}_*\, \boldsymbol{\nabla}\mathbf{N}_p\, \mathrm{d}\Omega$$

$$\mathbf{F}_{p_l} = \int_{\Gamma_{q_l}} (\mathbf{N}_p)^{\mathrm{T}}\, \rho_l\, \bar{q}_l\, \mathrm{d}\Gamma + \frac{\rho_l^2}{\mu_l} \int_\Omega (\boldsymbol{\nabla}\mathbf{N}_p)^{\mathrm{T}}\, \mathbf{k}_*\, \mathbf{g}\, \mathrm{d}\Omega$$

$$\mathbf{F}_{T} = \int_{\Gamma_{j'_E}} (\mathbf{N}_p)^{\mathrm{T}}\, \bar{j}'_E\, \mathrm{d}\Gamma + E_l\, \frac{\rho_l^2}{\mu_l} \int_\Omega (\boldsymbol{\nabla}\mathbf{N}_p)^{\mathrm{T}}\, \mathbf{k}_*\, \mathbf{g}\, \mathrm{d}\Omega$$

Finally, an explicit finite difference method is used for time discretization, which leads to the following time derivatives of the primary variables:

$$\begin{aligned} \dot{\mathbf{U}} &= \frac{\mathbf{U}_{(n+1)} - \mathbf{U}_{(n)}}{t_{(n+1)} - t_{(n)}} \\ \dot{\mathbf{P}}_l &= \frac{\mathbf{P}_{l\,(n+1)} - \mathbf{P}_{l\,(n)}}{t_{(n+1)} - t_{(n)}} \\ \dot{\mathbf{T}} &= \frac{\mathbf{T}_{(n+1)} - \mathbf{T}_{(n)}}{t_{(n+1)} - t_{(n)}} \end{aligned} \tag{5.47}$$

Considering the small strain rate assumption, the material time derivatives can be approximated as local derivatives:

$$\frac{D\rho_l}{Dt} \approx \frac{\partial \rho_l}{\partial t} = \frac{\rho_{l\,(n+1)} - \rho_{l\,(n)}}{t_{(n+1)} - t_{(n)}} \tag{5.48}$$

with $(\bullet)_{(n+1)}$ and $(\bullet)_{(n)}$ denoting the values of the variable $(\bullet)$ at the current time step $t_{(n+1)}$

and previous time-step $t_{(n)}$, respectively. Finally, the Newton-Raphson iteration method is used to iteratively solve the fully-coupled non-linear system given by Eq. (5.46).

5.5 Applications

To demonstrate that the technique can tackle THM processes in porous media with discontinuities, three different cases are analyzed. In the first case, two hydro-mechanical benchmarks are simulated to validate the proposed method against published numerical results. The second case corresponds to the study of hydraulic fracturing process and the last one corresponds to the investigation of the crack pattern induced by thermal gradients. All the simulations are conducted with the aid of the finite element program CODE_BRIGHT, so that the discontinuity behavior is treated by HAR elements that are inserted between the bulk elements of the mesh (MFT).

5.5.1 Benchmarks

5.5.1.1 2D Hot Dry Rock Benchmark

In this section and in the next one we present two cases based on the benchmarks of Watanabe *et al.* [210]. In the original work, the authors used linear elements to represent the fractures, while we used finite elements with high aspect ratio to model fractures. In this first case, a reservoir located at a depth of 4 km and with temperatures of 200^{o}C was analyzed. The energy production system consists of two wells separated by a distance of 150 m. Although the name "2D hot dry rock benchmark", the reservoir was considered fully saturated in [210] and in the present work.

The reservoir was modeled with a finite element mesh of 500 m×500 m (Figs 5.4a and 5.4b). The initials conditions of the reservoir are $T_o = 200^o$C and $P_o = 10$ MPa. In addition, water circulates at a rate of $1/300$ kg/s, so that the injection temperature is 70^{o}C. The parameters of the rock are: $k_r = 10^{-17}$ m^2, $\phi_r = 0.01$, $\rho_s = 2600$ kg/m^3 and $\lambda_T = 3$ W/m/K. In the case of fracture, we have admitted $k_f = 8.3333 \times 10^{-10}$ m^2, $\phi_f = 1.0$, $\rho_l = 1000$ kg/m^3, $\lambda_T = 0.65$ W/m/K and thickness of $100\,\mu$m. Finally, the density of water was kept constant, while the water viscosity was expressed by:

$$\mu_w = A \exp\left(\frac{B}{T + 273.15}\right) \tag{5.49}$$

where $A = 2.12 \cdot 10^{-12}$ MPa·s is the reference viscosity and $B = 1808.5$ K is a parameter that establishes how the viscosity changes with temperature.

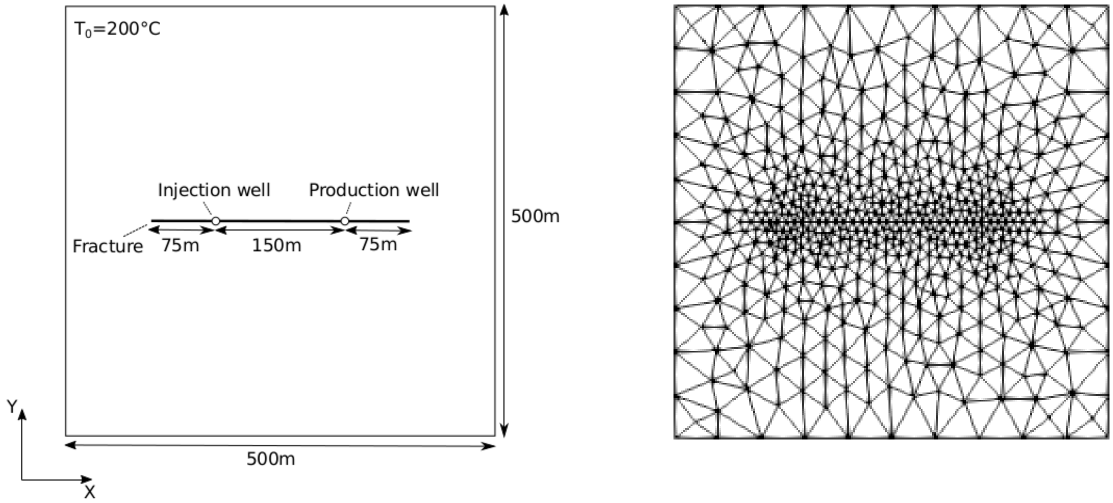

(a) (b)

Figure 5.4: Hot dry rock benchmark: (a) geometry and boundary conditions;(b) finite element mesh (reprinted from [210])

Figures 5.5a and 5.5b display the distributions of temperature and pore-pressure after 30 years of operation. The low permeability of the rock limit the penetration of water, and therefore, the heat exchange concentrates in the fracture. The pressure field shows that the system is in equilibrium at the end of the analyzed period. Figure 5.6 shows the temporal evolution of production temperature, comparing the numerical results with those reported by Watanabe *et al.* [210].

5.5.1.2 2D Hot Sedimentary Aquifer Benchmark

The sedimentary aquifer is a permeable medium. Thus, the fracture does not need to connect the two well to extract hot water. In this case, two parallel fractures separated by a distance of 150 m are created to enhance the permeability of the medium and the energy production (Figure 5.7).

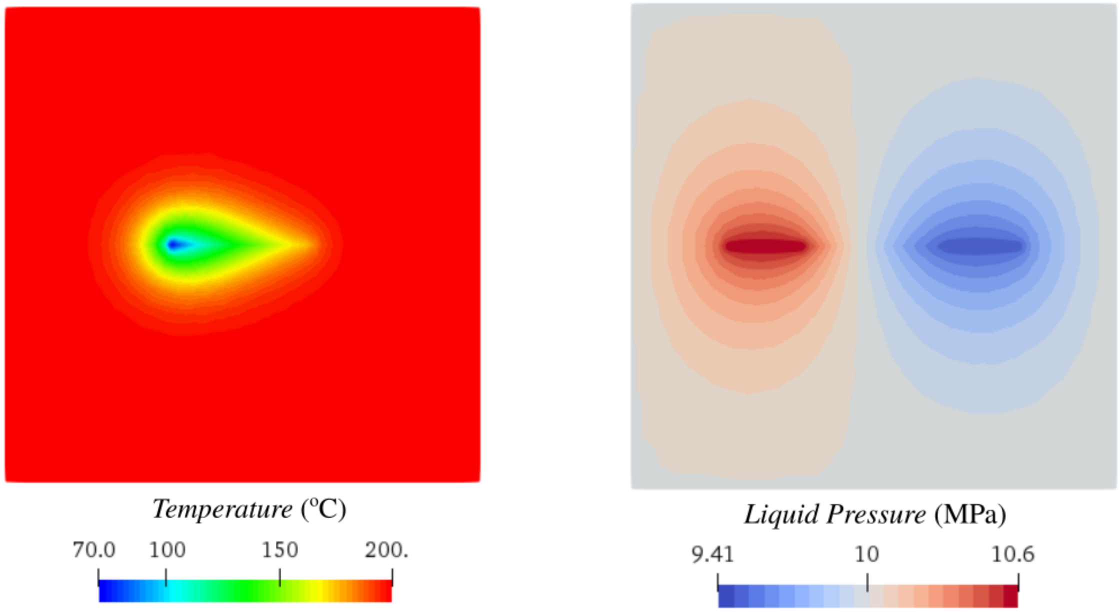

(a) (b)

Figure 5.5: Results from the numerical modeling of the 2D hot dry rock reservoir: (a) temperature distribution after 30 years; (b) steady-state pressure distribution after 30 years

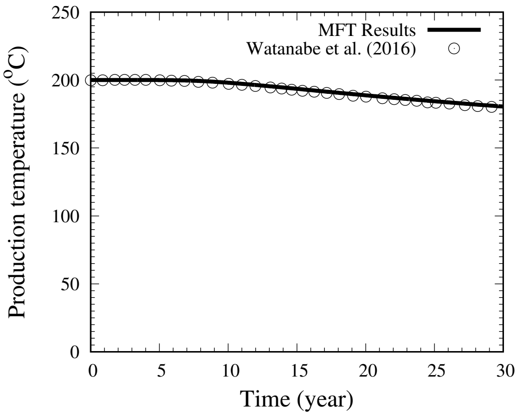

Figure 5.6: Temporal evolution of production temperature of the 2D hot dry rock reservoir

This is a sandstone aquifer with permeability and porosity of 10^{-15} m^2 and 0.1, respectively. The initial temperature of the rock mass is 150^{o}C, and the water is injected and extracted at a rate of 0.03 kg/s. As in the previous study, the injection temperature is 70^oC. Furthermore, the present analysis considers the same data of the hot dry reservoir, with the exception of those previously mentioned.

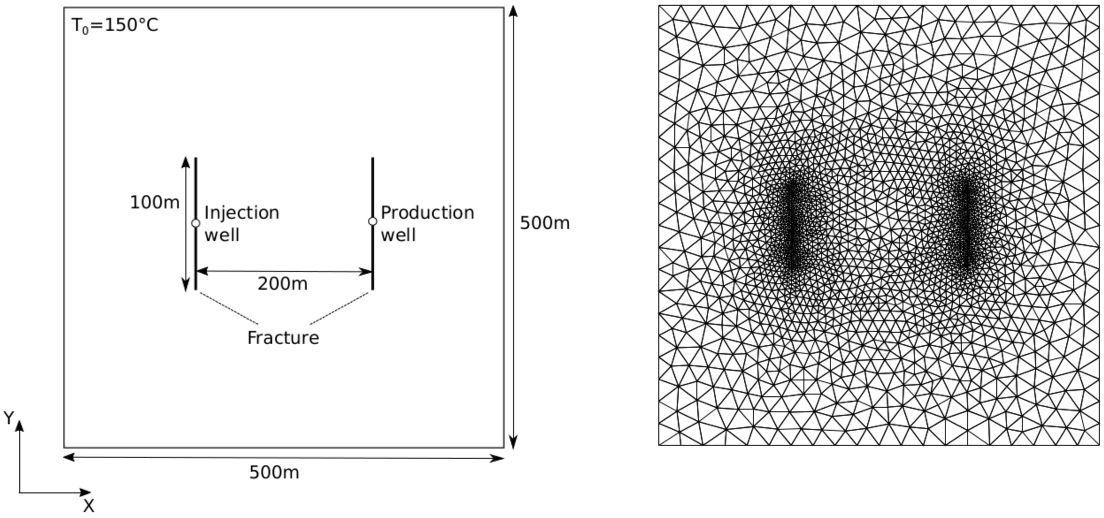

(a) (b)

Figure 5.7: Hot dry rock benchmark: (a) geometry and boundary conditions;(b) finite element mesh (reprinted from [210])

Figures 5.8a, 5.8b and 5.8c illustrate the distributions of temperature, pore-pressure and flux after 30 years of injection, respectively. The fractures enhance the permeability of the medium, as well as the extraction of hot water. Finally, Figure 5.8d exhibits the temporal evolution of temperature along 60 years. Note that the numerical results agree with those obtained by Watanabe *et al.* [210]. The production temperature declines from 150^{o}C to 128^{o}C after 60 years of operations, which corresponds to a reduction of 15%.

5.5.2 Hydraulic Fracturing Propagation

The storage-toughness and storage-viscosity dominated regime of the hydraulic fracturing process reported by Carrier and Granet [39] are investigated by using the proposed technique. The fracture is induced by the injection of an incompressible Newtonian viscous fluid at a constant rate $\bar{q} = 0.5$ kg/s. The initial liquid pressure of the entire porous medium was set to zero. The domain

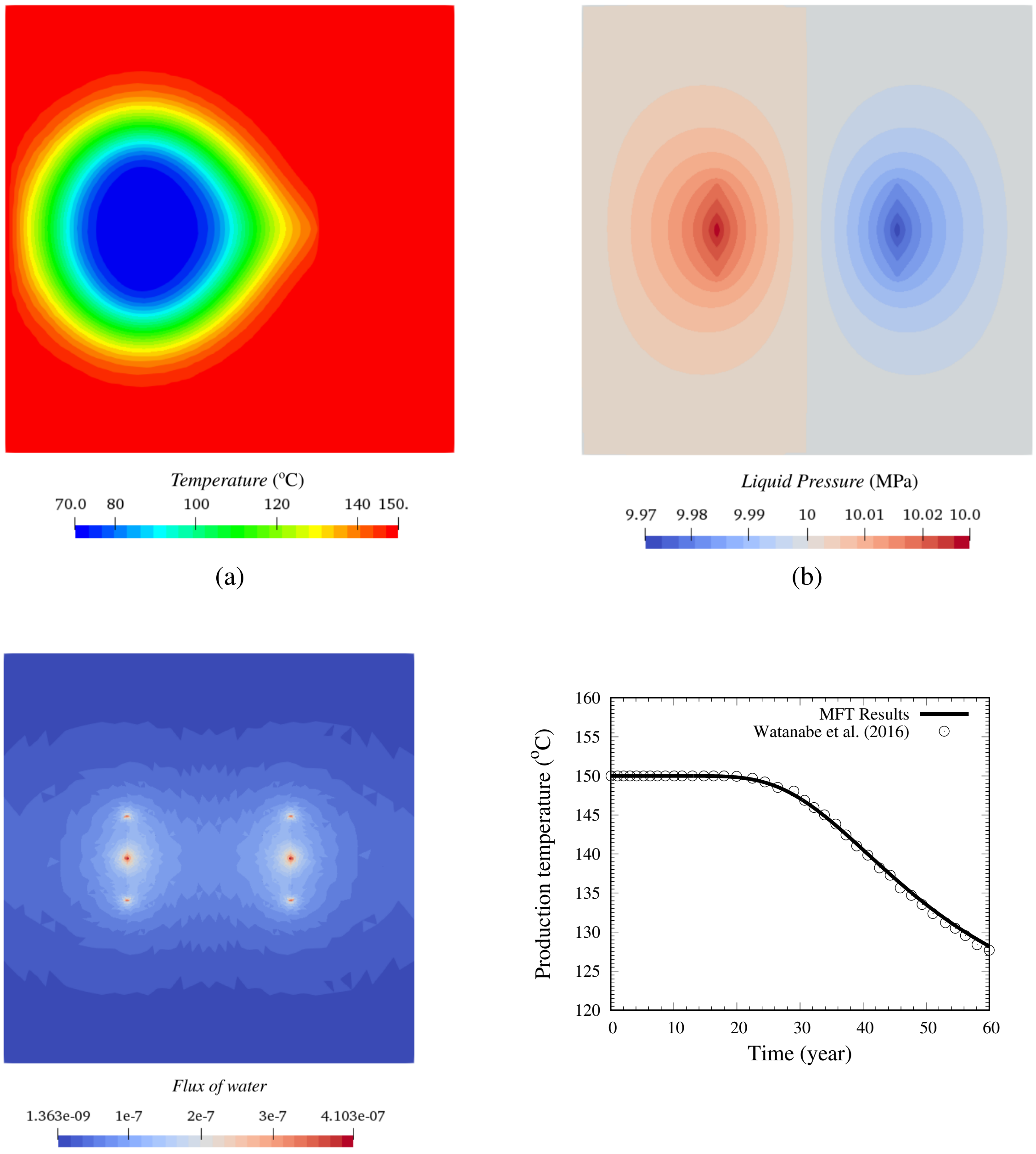

(a) (b)

(c) (d)

Figure 5.8: Results from the numerical modeling of the 2D hot sedimentary aquifer: (a) temperature distribution after 30 years; (b) pressure distribution after 30 years; (c) fluid velocity distribution; (d) temporal evolution of the production temperature

of the problem is 45x60m, in which an in situ vertical stress of $\sigma_o = 3.7$ MPa is considered. Figure 5.9 presents the geometry, boundary conditions and the finite element mesh of the problem, which contains 4666 nodes and 9264 elements. HAR finite elements were introduced at the center of the domain in the horizontal direction, so that the fracture is only able to propagate in the x-direction. In addition, the couple of HAR elements near the injection point were broken to obtain the initial configuration of the KGD fracture problem [39]. As explained by Bao *et al.* [15], the storage regimes are given by the near-K and M solutions which are determined by considering small time solutions.

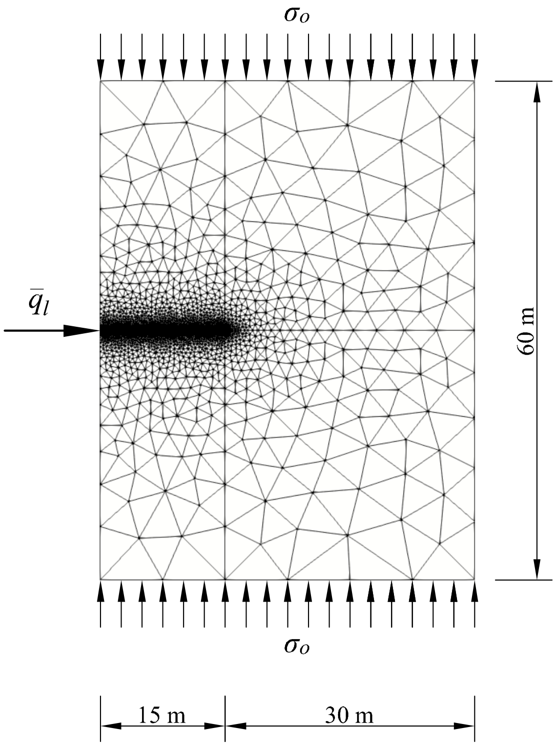

Figure 5.9: Mesh, geometry and boundary conditions of the hydraulic fracturing

The material properties of the porous medium that are common to both studies are given in Table 5.1. The fluid dynamic viscosity and intrinsic permeability depends on the dominated regime and are described in each case, accordingly.

Table 5.1: Main rock properties

Young's modulus	E	17 GPa
Poisson's ratio	ν	0.2
Fracture energy	G_f	120 N/m
Tensile strength	σ_u	1.25 MPa
Biot's coefficient	b	0.75 GPa
Biot's modulus	M	68.7 GPa
Porosity	ϕ	0.2

For the analytical solutions, the parameters are conveniently reduced as follows:

$$E' = \frac{E}{1-\nu^2}, \qquad \nu' = 12\nu, \qquad K' = 4K_{Ic}\sqrt{\frac{2}{\pi}}, \qquad C' = 2C_L \tag{5.50}$$

in which C_l is the leak-off parameter and K_{Ic} is the fracture toughness in mode-I defined as:

$$K_{Ic} = \sqrt{G_f\,\frac{E}{1-\nu^2}} \tag{5.51}$$

5.5.2.1 Storage-Toughness Dominated Regime

Two intrinsic permeability values (*i.e.*, $k = 1\times10^{-16}$ m^2 and $k = 1\times10^{-15}$ m^2) were considered in order to study the effect of permeability on fracture aperture, length and pressure. Assuming $\mu = 1\times10^{-4}$ Pa.s, the fracture propagates in the storage-toughness dominated regime and the analytical results are obtained via the Near-K solutions.

Hence, the analytical solutions of the injection pressure, fracture aperture and length proposed by Bunger *et al.* [33] are:

$$p = \varepsilon\,E'\,(2^{-5/2}\gamma^{-1/2}), \qquad w = \varepsilon\,L\sqrt{\gamma\frac{1-\xi^2}{2}}, \qquad l = \gamma\,L \tag{5.52}$$

where

$$\tau = \frac{t}{t_*}, \qquad \xi = x/l(t), \qquad \gamma = \tau^{2/3}\sum_{i=0}^{n}\gamma_{k_i}\,\tau^{i/6} \tag{5.53}$$

The values of γ_{k_i} were determined by Bunger *et al.* [33] and are shown in Table 5.2. In Eq. (5.52), the small parameter ε, lengthscale L and the timescale t_* for the KGD model are expressed as:

$$\varepsilon = \frac{C'^2}{Q_o}, \qquad L = \left(\frac{K'\,Q_o}{E'\,C'^2}\right)^2, \qquad t_* = \frac{K'^4\,Q_o^2}{E'^4\,C'^6} \tag{5.54}$$

Table 5.2: First five terms of the asymptotic solution [33]

i	γ_{k_i}
0	0.9324
1	-1.714
2	2.196
3	-1.863
4	0.7093

Figures 5.10a and 5.10b show that the analytical and numerical responses agree very well in terms of both lisp displacement and fracture aperture for both permeabilities. As expected, the fracture aperture of the medium with lower permeability leads to a wider fracture mouth and higher aperture, since the fluid is forced to propagate in the fracture because the lower permeability reduces the capability of the fluid from entering the surrounding medium.

As shown in Figure 5.11a, the numerical solution of the fluid injection pressure (*i.e.*, $p_f + \sigma_o$) for $k = 1 \times 10^{-16}$ m^2 presents a small departure from the analytical ones due to the so-called back-stress effect. A large fluid pressure is required at the beginning to break the rock and initiate the fracture propagation, then the injection pressure exhibits an asymptotic behavior because both aperture and length evolve with time, decreasing the pressure needed it. Figure 5.11b illustrates the fracture length time history for both permeabilities. The FE results reproduces very satisfactory the near K-solution.

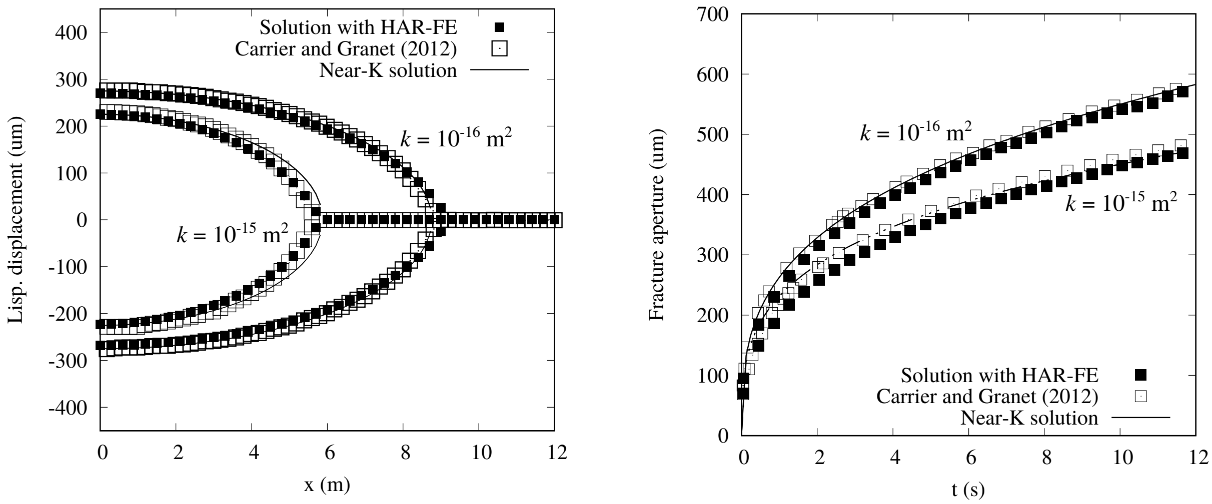

(a) (b)

Figure 5.10: HAR finite element solution of the fracture aperture for the storage-toughness dominated regime with the analytical and the numerical results [39] found in the literature: (a) fracture profile at $t = 10$ s; (b) time history of fracture aperture

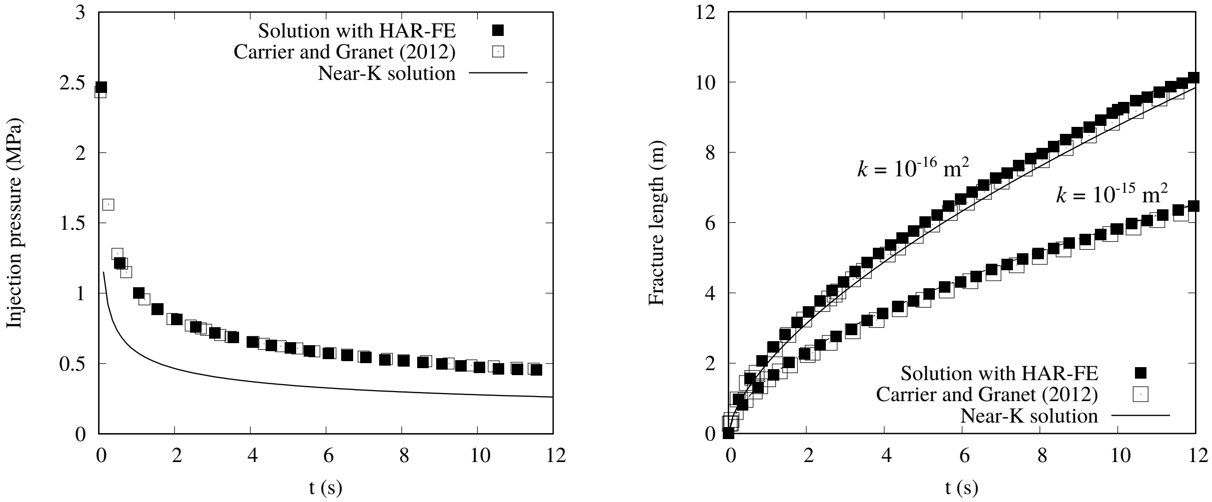

(a) (b)

Figure 5.11: Comparison of the storage-toughness dominated regime results obtained via HAR elements with the numerical ones reported by Carrier and Granet [39] in terms of: (a) injection pressure or $k = 1 \times 10^{-16}$ m^2; (b) fracture length

5.5.2.2 Storage-Viscosity Dominated Regime

The storage-viscosity dominated regime can be studied by assuming $k = 1 \times 10^{-16}$ m^2 and $\mu = 0.1$ Pa s. In this case, the liquid has a very high viscosity which strongly affects the behavior of the medium. The M-analytical solution developed by Adachi *et al.* [3] is used to describe the fracture aperture, injection pressure and fracture length for the storage-viscosity dominated regime as follows:

$$w_m = 1126\, \varepsilon_m\, L_m, \qquad p_m = 0.54495\, \varepsilon_m\, E' \qquad l_m = 0.61524\, L_m \tag{5.55}$$

respectively, in which

$$\varepsilon_m = \left(\frac{\mu}{E'\, t}\right)^{1/3}, \qquad L_m = \left(\frac{E'\, Q_o^3\, t^4}{\mu'}\right)^{1/6} \tag{5.56}$$

The time history of the fracture aperture, injection pressure and fracture length are shown in Figures 5.12a, 5.12b and 5.12c, respectively. The HAR finite element results show good agreement with the ones provided by Carrier and Granet [39]. As previously mentioned, the difference between the numerical and analytical responses is due to the back-stress effect, which induces higher fluid pressure and lower fracture aperture.

5.5.3 Thermal Fracking in Transparent Sample

The experimental tests conducted by Cha *et al.* [41] are also simulated to show that the MFT is able to reproduce cracks due to thermal shock. The sample consists of an acrylic cylinder submitted to a temperature gradient. Acrylic is chosen because it is transparent material and relatively brittle, so as rocks. The dimensions of the specimen are as follows: 10 cm diameter × 23 cm height, with a borehole 1.3 cm in diameter and 18cm in height positioned at the center of the sample. A steel tube is introduced and attached to the wall of the borehole with epoxy. The authors carried out two experiments to investigate how the injection point position affects the crack pattern.

With respect to the numerical modeling, both analyses were performed by assuming

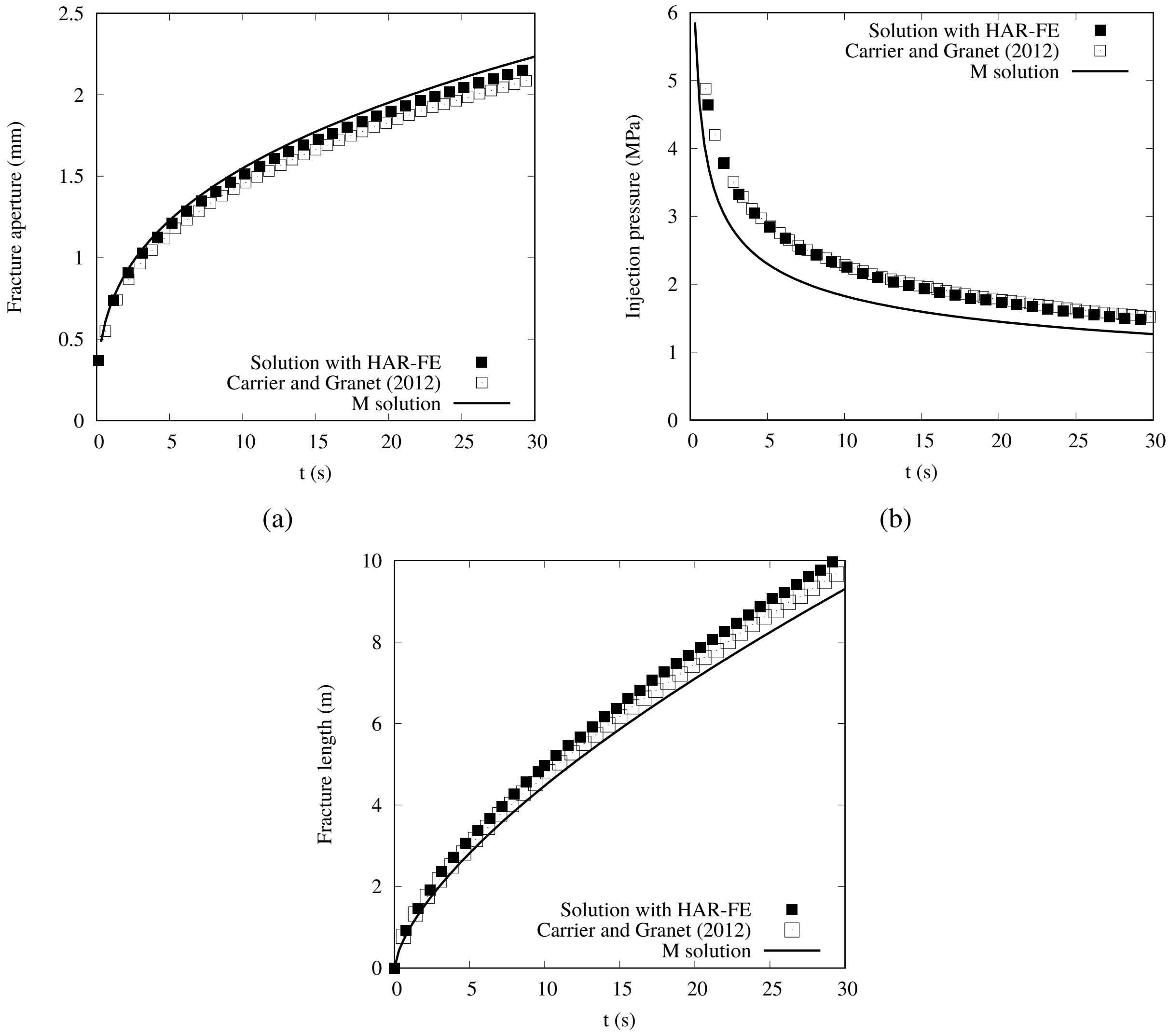

(a) (b)

(c)

Figure 5.12: Numerical and analytical curves for the storage-viscosity dominated regime: (a) fracture aperture; (b) injection pressure; (c) fracture length

axisymmetric conditions to reduce computational effort. Tables 5.3 and 5.4 contain the adopted parameters of the bulk and HAR elements, respectively. The thermal conductivity and specific heat of the fluid are $\lambda_l = 0.14\,\mathrm{W/(m\,K)}$ and $c_l = 64\,\mathrm{J/(kg\,K)}$. To emulate the temperature distribution in the void, the thermal conductivity of the liquid in this region is assumed to be $100\,\mathrm{W/(m^K)}$. The following two sections explain the main assumption adopted to model these laboratory experiments.

Table 5.3: Mechanical properties adopted for the thermal shock test

Element	E (GPa)	ν	α_T (^{o}C^{-1})	σ_u (MPa)	G_f (N/m)	Constitutive model
Acrylic	3.2	0.35	35×10^{-5}	-	-	Linear elastic
Steel	210	0.30	0	-	-	Linear elastic
Epoxy	210	0.30	0	-	-	Linear elastic
Void	0.001	0.00	0	-	-	Linear elastic
Acrylic – acrylic interface	3.2	0.00	-	69	100	Tensile damage
Acrylic – void interface	0.001	0.00	-	0.1	100	Tensile damage
Acrylic – epoxy interface	0.001	0.00	-	0.1	100	Tensile damage

Table 5.4: Thermal properties adopted for the thermal shock test

Element	ϕ_o	λ_s (W/m/K)	c_s (W/m/K)
Acrylic	0.01	0.20	1466
Steel	0.01	40.0	502
Epoxy	0.01	0.17	1100
Void	1.0	0.0	65
Acrylic – acrylic interface	0.01	0.20	1466
Acrylic – void interface	1.0	0.20	65
Acrylic – epoxy interface	0.01	0.20	1100

5.5.3.1 Specimen 1

In this case, a steel tube is inserted to the depth of 12cm and epoxy is placed at the first 6 cm to attach the tube to the borehole walls. Figure 5.13 shows the mesh, geometry and boundary conditions of the problem at steak. The mesh contains 35604 elements and 17964 nodes. The void is filled with liquid nitrogen and it is modeled by considering a very flexible material with porosity of 1 and large thermal conductivity ($\lambda_l = 100$ W/m/K). The whole domain is at 20^{o}C at the beginning of the analysis. The circulation of LN$_2$ is simulated by imposing temperature variation at the nodes located at the end of the tube. The time history of the temperature in different positions (left, bottom and right edges) is shown in Figure 5.14.

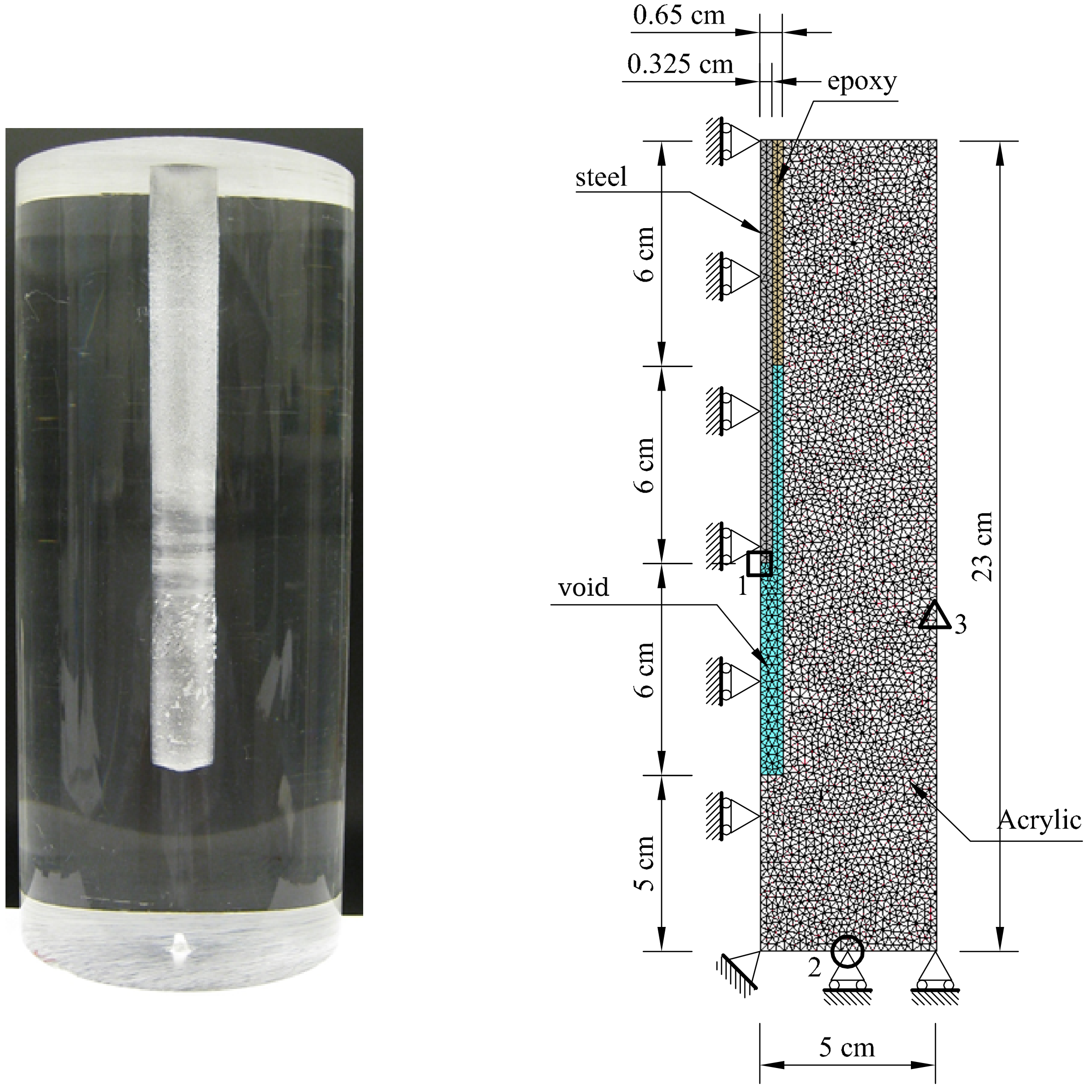

(a) (b)

Figure 5.13: Acrylic specimen 1: (a) experimental sample (reprinted from [41]); (b) mesh, geometry and boundary conditions

The evolution of crack pattern and temperature are shown in Figure 5.15. The crack morphology is characterized by the formation of three horizontal radial cracks that emerges in the borehole in contact with the fluid. An addition crack at the top of the sample, between the acrylic and the epoxy, was also observed in experimental results but the numerical results did not capture it because the thermal conductivity of the epoxy material is very small. The agreement between

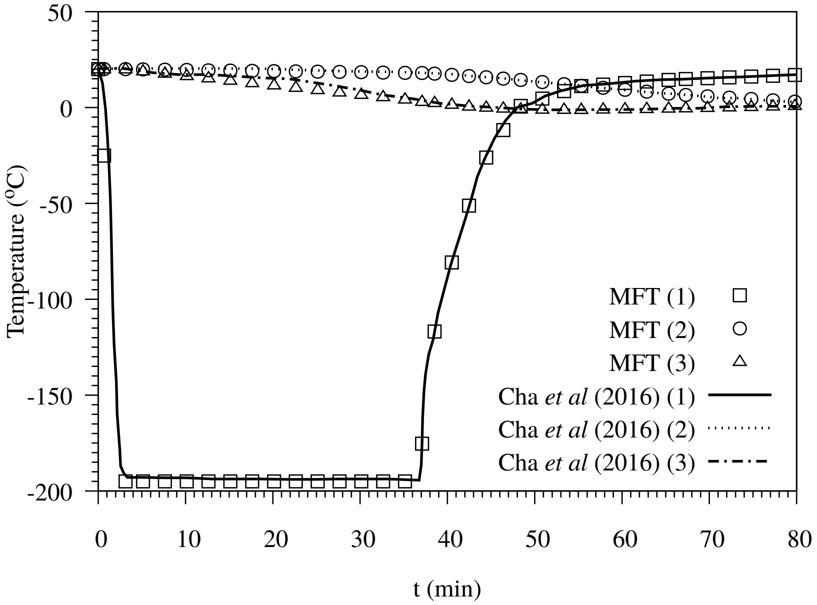

Figure 5.14: Temperature evolution of the numerical model and thermal shock experiment

the experimental and numerical results is reasonable. The fracture process is explained as follows. The bulk elements contract due to the thermal gradient, which disturb the stress state of the domain and leads to a concentration of tensile stresses at the wall of the borehole. HAR elements starts to degrade once such tensile stresses reach the strength of the acrylic material and then the thermal conductivity is enhanced based on the previous proposed law. As shown in Figures 5.15(i-l), the lower temperature in the fractures is an evidence that the model emulates the penetration of fluid in the fracture.

5.5.3.2 Specimen 2

A second laboratory experiment was conducted by Cha *et al.* [41] to study the influence of the injection point position. In this case, both steel tube and epoxy are 3.8 cm in depth. Figure 5.16a is a photo of the acrylic specimen, while Figure 5.16b illustrates the mesh, materials and boundary conditions considered in the analysis. The mesh consists of 20190 nodes, 3095 bulk elements and 8599 HAR elements. Analogous to the previous case, the initial temperature o the domain is set to 20^oC and temperature change is imposed at the end of the inlet tube.

Two cracks were observed in the experiments, one next to the inlet point and a second one around the epoxy material. However, the simulation is only able to capture the crack that is close to the inlet point. This is probably because the thermal conductivity of the epoxy is small compared with the one in the void. As previously studied, the temperature change induces volumetric strains, which trigger fracture formation when the resultant tensile stress reaches the tensile strength of the material. The contour of temperature indicates that the proposed technique can properly model the penetration of the fluid in the fracture.

5.6 Conclusions

In this chapter, a mathematical framework capable of modeling thermo-hydro-mechanical processes in rocks with discontinuities (fractures) is proposed. In this context, elements with high aspect ratio enhanced with appropriate constitutive laws are used to reproduce the behavior of the fracture. The mesh fragmentation technique, which consists of inserting the high aspect ratio elements between the regular (bulk) elements of the mesh, is used to deal with discontinuities. Thus, the fracture evolves by contouring the boundaries of the bulk elements, which behavior is described by a linear elastic model.

The proposed approach considers continuous concepts to treat the discontinuity, so that its implementation only requires the enrichment of some material properties, such as porosity, thermal conductivity and hydraulic conductivity. With respect to the mechanical model representing the discontinuity, a tensile damage model with the IMPL-EX scheme is used to capture the main phenomena related to the formation and propagation of fracture. Therefore, the MFT does not require the use of re-meshing techniques, tracking algorithms or enriched shape functions to incorporate the discontinuity effects in the finite element formulation.

The chapter closes out by studying the following cases: (i) benchmarks involving thermo-hydraulic analysis, (ii) hydraulic fractures triggered by the injection of a fluid at high pressure, and (iii) fractures induced by thermal shock. The results obtained with the proposed methodology are validated against other numerical methods. The agreement between the results is satisfactory, showing that the model is able to replicate the main trends and results related to THM processes.

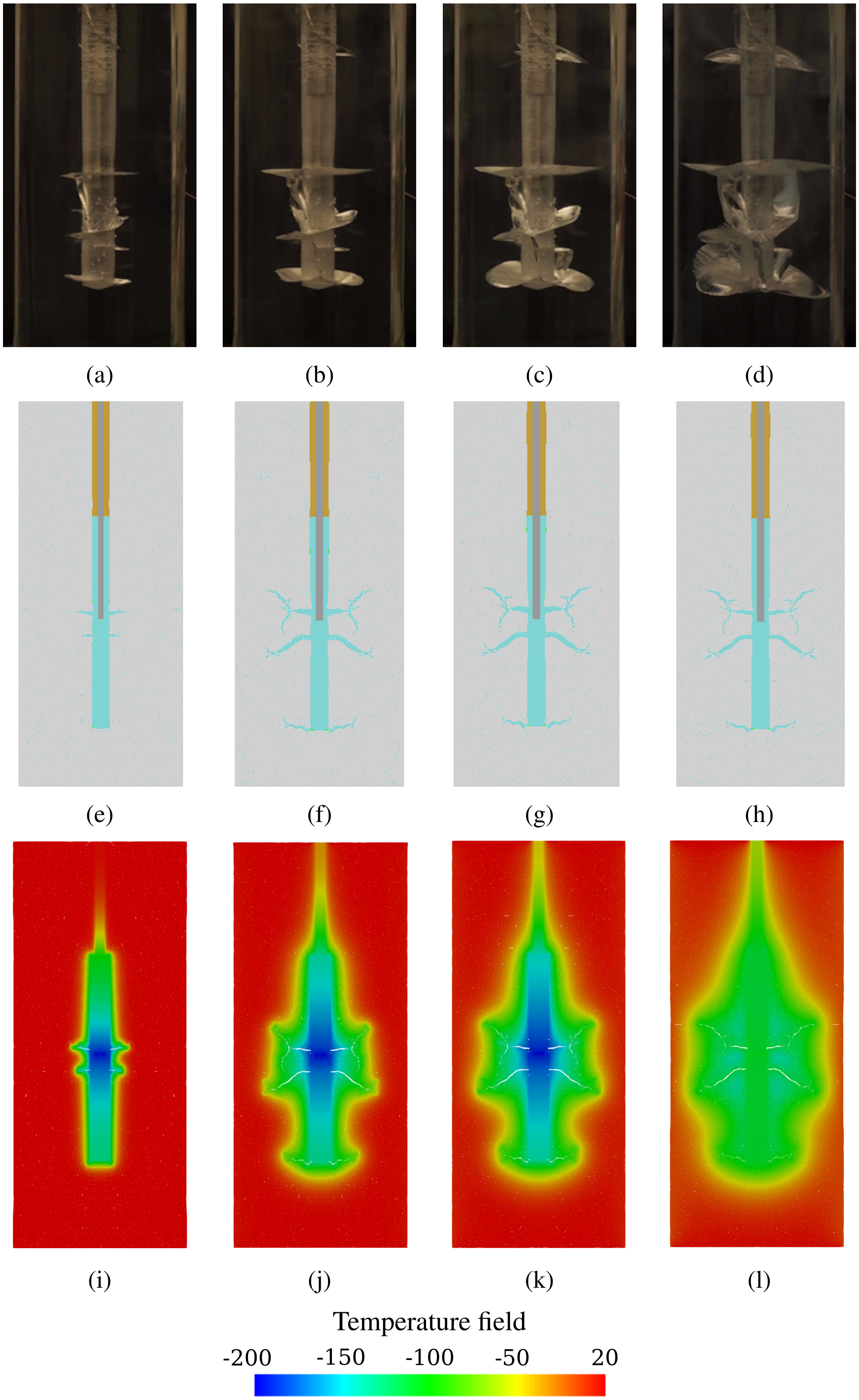
(a) (b) (c) (d)

(e) (f) (g) (h)

(i) (j) (k) (l)

Figure 5.15: Acrylic specimen 1: (a-d) experimental crack pattern (reprinted from [41]); (e-h) numerical cracks; (i-l) contours of temperature versus time

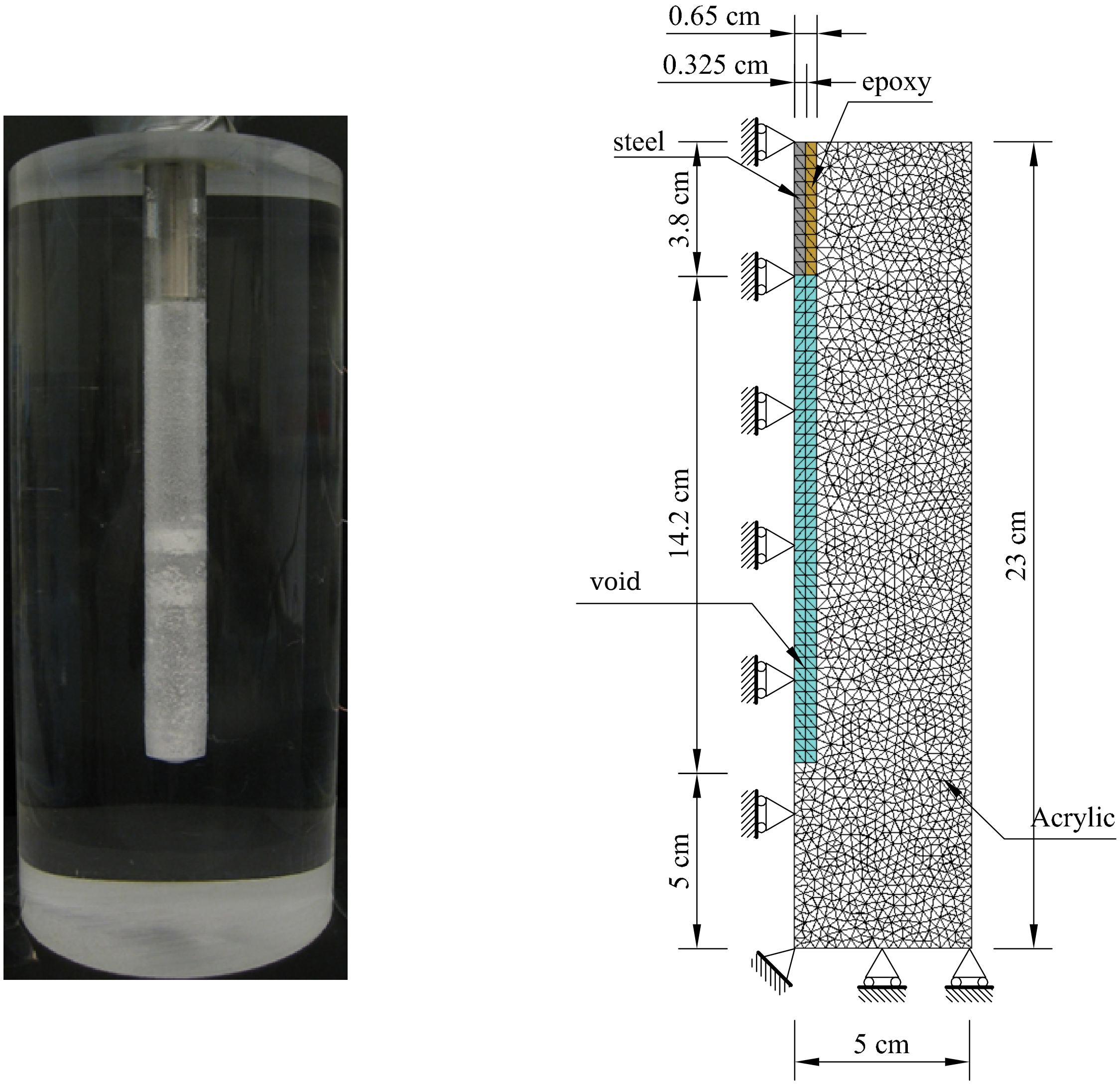

(a) (b)

Figure 5.16: Acrylic specimen 2: (a) experimental sample (reprinted from [41]); (b) mesh, geometry and boundary conditions

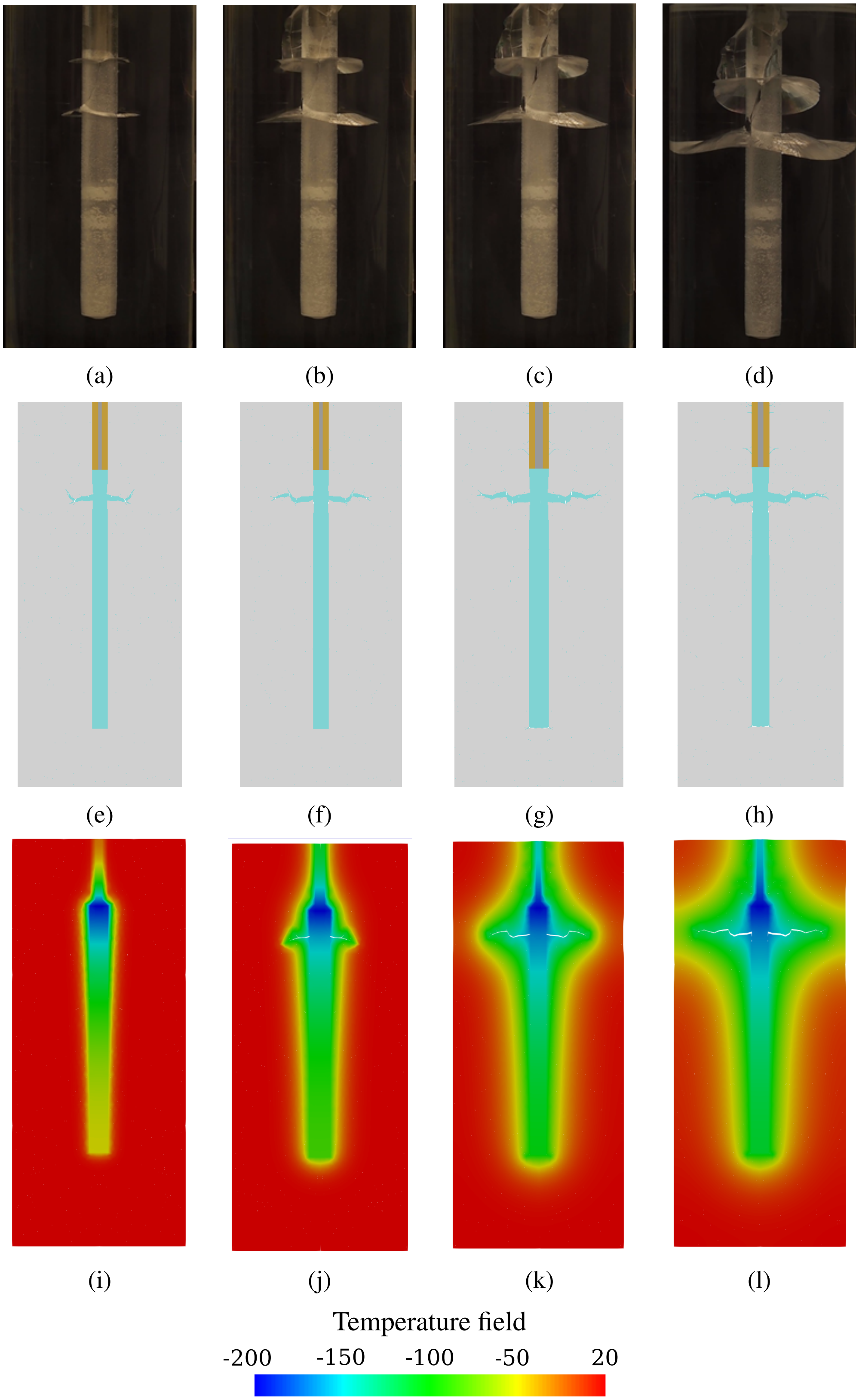

Figure 5.17: Acrylic specimen 2: (a-d) experimental crack pattern (reprinted from [41]); (e-h) numerical cracks; (i-l) contours of temperature versus time

6. CONCLUSIONS AND FUTURE WORK

6.1 Conclusions

A fully coupled thermo-hydro-mechanical approach is proposed in this work to tackle discontinuities (in the form of fissures, cracks or fractures) in porous media. The discontinuity behavior is described in the context of continuous mechanics with the aid of high aspect ratio (HAR) finite elements that are introduced in-between the regular (bulk) elements of the mesh during the pre-process. In addition, the technique does not need adaptive re-meshing techniques or enrichment schemes to take into account the presence of the discontinuity in the interpolation functions (like the Elements with embedded discontinuity or X-FEM). In addition, HAR element does not need the use of large dummy values of stiffness for the undamaged material (like the zero thickness interface elements). Thus, the implementation of the proposed technique only requires the enhancement of THM constitutive laws and standard finite elements available in any commercial finite element program can be used to reproduce the discontinuity behavior.

Therefore, this work describes in detail the theoretical framework proposed to model the coupled THM problem in geo-materials (*i.e.*, soils and rocks) with discontinuities, which effects are taken into account by enhancing the intrinsic permeability, porosity, pore air entry value and thermal conductivity. The mechanical behavior of the fracture is defined by a continuum tensile damage model and the contact between distinct materials are represented by special interface damage models proposed in this work. The stress-strain relationship is integrated by using the implicit-explicit integration scheme (IMPL-EX), which is a very robust method, but requires a convergence study to ensure reliable results. The main phenomena related to the problem, the weak form and the finite element equations are also presented.

The numerical results are validated against other numerical techniques and experimental tests found in the literature. The agreement between the numerical results and the experimental ones shows that the proposed technique is able to replicate the desiccation crack phenomenon associated with unsaturated soils. It can also be used to study the hydraulic fractures induced by the injection of viscous fluid at high pressure in geo-reservoirs, which is a common process used in Petroleum Engineering to retrieve oil and gas. In addition, the technique is also able to deal with the thermal-fracking due to the thermal shock, which it has been widely investigated in the development of Enhanced Geothermal Systems (EGS). Hence, the proposed technique is very attractive to model the formation and propagation of multiple cracks in geo-materials (*i.e.*, soils and rocks).

6.2 Future Work

The contributions provided by the development of this work are fundamental for new lines of investigations involving coupled THM problems in porous materials with discontinuities, since a detailed evaluation of the methodology was carried out in this work. In this sense, the following topics are suggested as future work:

- Several laboratory and field experimental works have been conducted over the years to study the crack pattern of soils subjected to drying-wetting cycles, but few efforts have been made to model such behavior. The proposed methodology can be extended to account for the effects of drying-wetting cycles in soils and to study the crack process.

- Laboratory experiments have shown that osmotic suction can also lead to the formation and propagation of cracks in soils, even when they are fully saturated. In this case, the soil experiences shrinkage due to the presence of a saline solution (chemical solution) that induces osmotic suctions. Thus, HAR elements can also be used to model discontinuities in soils subjected to osmotic suction.

- The extending of the theoretical framework to treat cases involving finite deformations, *i.e.*, when the small strain hypothesis is no longer valid. Re-meshing algorithms are usually required in such cases to avoid distorted meshes. In this context, it is necessary to develop techniques that take into account the presence of HAR elements during the re-meshing process.

- Chemical processes also strongly affect the geo-material behavior and coupled Thermo-Hydro-Mechanical-Chemical analyses are essential to properly model and understand the main phenomena associated with geo-reservoirs and engineered barriers for radioactive waste disposal. In this sense, the technique can also be extended to incorporate the chemical effects in rocks and soils with discontinuities.

- Finally, since the insertion of HAR elements during the preprocess increases significantly the number of degrees of freedom of the problem, it is necessary to optimize the processing time by using the element-by-element data structure, iterative solvers (*e.g.*, Biorthogonal Conjugate Gradient method) and a parallel code. CODE_BRIGHT can be enhanced by implementing the previous computational tool in the code. In addition, a complete numerical study comparing the proposed technique with other methods, such as the smeared crack model, zero-thickness interface elements, elements with embedded discontinuity and X-FEM, can also be performed to verify the computational efficiency.

REFERENCES

[1] Abdelaziz, Y. and Hamouine, A. (2008). A survey of the extended finite element.

[2] Abu Al-Rub, R. K. (2007). Prediction of micro and nanoindentation size effect from conical or pyramidal indentation. *Mechanics of Materials*, 39(8):787–802.

[3] Adachi, J. I. and Detournay, E. (2002). Self-similar solution of a plane-strain fracture driven by a power-law fluid. *International Journal for Numerical and Analytical Methods in Geomechanics*.

[4] Ahrens, J., Geveci, B., and Law, C. (2005). ParaView: An end-user tool for large-data visualization. In *Visualization Handbook*.

[5] Allen, J. R. L. (1986). On the curl of desiccation polygons. *Sedimentary Geology*, 46(1-2):23–31.

[6] Alonso, E. E., Gens, A., and Josa, A. (1990). A constitutive model for partially saturated soils. *Géotechnique*, 40(3):405–430.

[7] Amarasiri, A. L. and Kodikara, J. K. (2013). Numerical Modeling of Desiccation Cracking Using the Cohesive Crack Method. *International Journal of Geomechanics*, 13(3):213–221.

[8] Amarasiri, A. L., Kodikara, J. K., and Costa, S. (2011). Numerical modelling of desiccation cracking. *International Journal for Numerical and Analytical Methods in Geomechanics*, 35(1):82–96.

[9] Armero, F. and Callari, C. (1999). An analysis of strong discontinuities in a saturated poro-plastic solid. *International Journal for Numerical Methods in Engineering*.

[10] Armero, F. and Garikipati, K. (1996). An analysis of strong discontinuities in multiplicative finite strain plasticity and their relation with the numerical simulation of strain localization in solids. *International Journal of Solids and Structures*.

[11] Asahina, D., Houseworth, J. E., Birkholzer, J. T., Rutqvist, J., and Bolander, J. E. (2014). Hydro-mechanical model for wetting/drying and fracture development in geomaterials. *Computers and Geosciences*, 65:13–23.

[12] ASTM C778 - 17 (2017). Standard Specification for Standard Sand. *ASTM International*.

[13] ASTM D3080 (2011). American Society for Testing and Materials. *Standard Test Method for Direct Shear Test of Soils Under Consolidated Drained Conditions*.

[14] Ayachit, U. (2015). *The ParaView Guide: A Parallel Visualization Application*.

[15] Bao, J. Q., Fathi, E., and Ameri, S. (2015). Uniform investigation of hydraulic fracturing propagation regimes in the plane strain model. *International Journal for Numerical and Analytical Methods in Geomechanics*.

[16] Barenblatt, G. I. (1959). The formation of equilibrium cracks during brittle fracture. General ideas and hypotheses. Axially-symmetric cracks. *Journal of Applied Mathematics and Mechanics*.

[17] Barenblatt, G. I. (1962). The mathematical theory of equilibrium cracks in brittle fracture. *Advances in applied mechanics*, 7(1):55–129.

[18] Bažant, Z. P. and Oh, B. H. (1983). Crack band theory for fracture of concrete. *Matériaux et Constructions*.

[19] Bažant, Z. P., Ohtsubo, H., and Aoh, K. (1979). Stability and post-critical growth of a system of cooling or shrinkage cracks. *International Journal of Fracture*.

[20] Bazant, Z. P. and Planas, J. (1997). *Fracture and Size Effect in Concrete and Other Quasibrittle Materials*.

[21] Bear, J. (2013). *Dynamics of fluids in porous media*. Courier Corporation.

[22] Belytschko, T. and Black, T. (1999). Elastic crack growth in finite elements with minimal remeshing. *International Journal for Numerical Methods in Engineering*.

[23] Belytschko, T., Fish, J., and Engelmann, B. E. (1988). A finite element with embedded localization zones. *Computer Methods in Applied Mechanics and Engineering*.

[24] Belytschko, T., Gracie, R., and Ventura, G. (2009). A review of extended/generalized finite element methods for material modeling.

[25] Belytschko, T., Krongauz, Y., Organ, D., Fleming, M., and Krysl, P. (1996). Meshless methods: An overview and recent developments. *Computer Methods in Applied Mechanics*

and Engineering.

[26] Bhandari, A. R., Powrie, W., and Harkness, R. M. (2012). A digital image-based deformation measurement system for triaxial tests. *Geotechnical Testing Journal*, 35(2).

[27] Biot, M. A. and Willis, D. G. (1957). The Elastic Coefficients of the Theory of Consolidation. *Journal of Applied Mechanics*.

[28] Bishop, A. (1959). The principle of effective stress.

[29] Bower, A. F. (2018). *Applied Mechanics of Solids*.

[30] Bradley, W. H. (1933). Factors that determine the curvature of mud-cracked layers. *American Journal Science*, pages 55–71.

[31] Budyn, É., Zi, G., Moës, N., and Belytschko, T. (2004). A method for multiple crack growth in brittle materials without remeshing. *International Journal for Numerical Methods in Engineering*.

[32] Bui, H. H., Nguyen, G. D., Kodikara, J. K., and Sanchez, M. (2015). Soil cracking modelling using the mesh-free SPH method. In *12th Australia New Zealand Conference on Geomechanics*, pages 122–129.

[33] Bunger, A. P., Detournay, E., and Garagash, D. I. (2005). Toughness-dominated hydraulic fracture with leak-off. *International Journal of Fracture*.

[34] Caballero, A., Carol, I., and López, C. M. (2006). A meso-level approach to the 3D numerical analysis of cracking and fracture of concrete materials. *Fracture of Engineering Materials & Structures*, 29(12):979–991.

[35] Caggiano, A., Etse, G., and Martinelli, E. (2012). Zero-thickness interface model formulation for failure behavior of fiber-reinforced cementitious composites. *Computers and Structures*, 98-99:23–32.

[36] Callari, C., Armero, F., and Abati, A. (2010). Strong discontinuities in partially saturated poroplastic solids. *Computer Methods in Applied Mechanics and Engineering*.

[37] Camacho, G. T. and Ortiz, M. (1996). Computational modelling of impact damage in brittle materials. *International Journal of solids and structures*, 33(20):2899–2938.

[38] Carol, I., Prat, P. C., and López, C. M. (1997). Normal/Shear Cracking Model: Application to Discrete Crack Analysis. *Journal of Engineering Mechanics*, 123(8):765–773.

[39] Carrier, B. and Granet, S. (2012). Numerical modeling of hydraulic fracture problem in permeable medium using cohesive zone model. *Engineering Fracture Mechanics*.

[40] Cervera, M. and Chiumenti, M. (2006). Smeared crack approach: Back to the original track.

[41] Cha, M., Alqahtani, N., Yao, B., Wang, L., Yin, X., Wu, Y., and Kneafsey, T. (2016). Studying cryogenic fracturing process using transparent specimens. In *Energy Geotechnics*.

[42] Chaduvula, U., Viswanadham, B. V., and Kodikara, J. (2017). A study on desiccation cracking behavior of polyester fiber-reinforced expansive clay. *Applied Clay Science*.

[43] Chen, Q., Andrade, J. E., and Samaniego, E. (2011). AES for multiscale localization modeling in granular media. *Computer Methods in Applied Mechanics and Engineering*, 200(33-36):2473–2482.

[44] Chen, Z., Bunger, A. P., Zhang, X., and Jeffrey, R. G. (2009). Cohesive zone finite element-based modeling of hydraulic fractures. *Acta Mechanica Solida Sinica*.

[45] Cleto, P. R. (2016). *Simulação de fraturamento hidráulico usando elementos finitos de elevada razão de aspecto com acoplamento hidromecânico*. Thesis, Universidade Estadual Paulista Júlio de Mesquita Filho (UNESP).

[46] Corte, A, E. and Higashi, A. (1964). Experimental research on desiccation cracks in soils.

[47] Coussy, O. (2005). *Poromechanics*.

[48] Dahi Taleghani, A., Ahmadi, M., Wang, W., and Olson, J. E. (2014). Thermal Reactivation of Microfractures and its Potential Impact on Hydraulic-Fracture Efficiency. *SPE Journal*.

[49] Daux, C., Moës, N., Dolbow, J., Sukumar, N., and Belytschko, T. (2000). Arbitrary branched and intersecting cracks with the extended finite element method. *International Journal for Numerical Methods in Engineering*.

[50] De Borst, R. (2001). Fracture in quasi-brittle materials: A review of continuum damage-based approaches. *Engineering Fracture Mechanics*.

[51] Dolbow, J., Moës, N., and Belytschko, T. (2000). Discontinuous enrichment in finite elements

with a partition of unity method. *Finite elements in analysis and design*, 36(3):235–260.

[52] Dow, D. B. (1964). The effect of salinity on the formation of mudcracks. *The Compass of Sigma Gamma Epsilon*, 41:162–166.

[53] Duarte, C. A., Babuška, I., and Oden, J. T. (2000). Generalized finite element methods for three-dimensional structural mechanics problems. *Computers and Structures*.

[54] Duarte, C. A., Hamzeh, O. N., Liszka, T. J., and Tworzydlo, W. W. (2001). A generalized finite element method for the simulation of three-dimensional dynamic crack propagation. *Computer Methods in Applied Mechanics and Engineering*.

[55] Duarte, C. A. and Kim, D. J. (2008). Analysis and applications of a generalized finite element method with global-local enrichment functions. *Computer Methods in Applied Mechanics and Engineering*.

[56] Duarte, C. A. and Oden., J. T. (1995). Hp clouds a meshless method to solve boundary-value problems.

[57] Duarte, C. A. and Oden, J. T. (1996). An h-p adaptive method using clouds. *Computer Methods in Applied Mechanics and Engineering*.

[58] Dugdale, D. S. (1960). Yielding of steel sheets containing slits. *Journal of the Mechanics and Physics of Solids*, 8(2):100–104.

[59] Dvorkin, E. N., Cuitiño, A. M., and Gioia, G. (1990). Finite elements with displacement interpolated embedded localization lines insensitive to mesh size and distortions. *International Journal for Numerical Methods in Engineering*.

[60] Dyer, M., Utili, S., and Zielinski, M. (2009). Field survey of desiccation fissuring of flood embankments. *Proceedings of the Institution of Civil Engineers - Water Management*.

[61] Etse, G., Caggiano, A., and Vrech, S. (2012). Multiscale failure analysis of fiber reinforced concrete based on a discrete crack model. *International Journal of Fracture*, 178(1-2):131–146.

[62] Ferrara, A. and Pandolfi, A. (2008). Numerical modelling of fracture in human arteries. *Computer Methods in Biomechanics and Biomedical Engineering*, 11(5):553–567.

[63] Fish, J. and Belytschko, T. (2007). *A First Course in Finite Elements*.

[64] Foster, C. D., Borja, R. I., and Regueiro, R. A. (2007). Embedded strong discontinuity finite elements for fractured geomaterials with variable friction. *International Journal for Numerical Methods in Engineering*.

[65] Fredlund, D. G. and Morgenstern, N. R. (1977). Stress state variables for Unsaturated Soils. *Journal of Geotechnical Division*, 103(GT5):447–466.

[66] Geertsma, J. and De Klerk, F. (1969). A Rapid Method of Predicting Width and Extent of Hydraulically Induced Fractures. *Journal of Petroleum Technology*.

[67] Geißler, G., Netzker, C., and Kaliske, M. (2010). Discrete crack path prediction by an adaptive cohesive crack model. *Engineering Fracture Mechanics*, 77(18):3541–3557.

[68] GENS, A. (2009). Soil–environment interactions in geotechnical engineering. *Géotechnique*.

[69] Gens, A., Carol, I., and Alonso, E. E. (1989). An interface element formulation for the analysis of soil-reinforcement interaction. *Computers and Geotechnics*, 7(1-2):133–151.

[70] Genter, A., Goerke, X., Graff, J.-J., Cuenot, N., Krall, G., Schindler, M., and Ravier, G. (2010). Current status of the EGS Soultz Geothermal Project (France). In *World Geothermal Congress*.

[71] Geuzaine, C. and Remacle, J. F. (2009). Gmsh: A 3-D finite element mesh generator with built-in pre- and post-processing facilities. *International Journal for Numerical Methods in Engineering*.

[72] Ghassemi, A. (2012). A review of some rock mechanics issues in geothermal reservoir development.

[73] Ghassemi, A., Tarasovs, S., and Cheng, A. H. (2007). A 3-D study of the effects of thermomechanical loads on fracture slip in enhanced geothermal reservoirs. *International Journal of Rock Mechanics and Mining Sciences*.

[74] Ghataora, G. S., Burns, B., Hassan, B., and Morris, M. (2007). Soil piping tests on Thorngumbald flood embankment. Technical report.

[75] Gilliot, J. M., Vaudour, E., and Michelin, J. (2017). Soil surface roughness measurement: A new fully automatic photogrammetric approach applied to agricultural bare fields. *Computers*

and Electronics in Agriculture, 134:63–78.

[76] Gray, W. G. and Schrefler, B. A. (2001). Thermodynamic approach to effective stress in partially saturated porous media. *European Journal of Mechanics, A/Solids*, 20(4):521–538.

[77] Griffith, A. A. (1921). The Phenomena of Rupture and Flow in Solids.

[78] Gui, Y. and Zhao, G. F. (2015). Modelling of laboratory soil desiccation cracking using DLSM with a two-phase bond model. *Computers and Geotechnics*.

[79] Gui, Y. L., Hu, W., Zhao, Z. Y., and Zhu, X. (2018). Numerical modelling of a field soil desiccation test using a cohesive fracture model with Voronoi tessellations. *Acta Geotechnica*.

[80] Gui, Y. L., Zhao, Z. Y., Kodikara, J., Bui, H. H., and Yang, S. Q. (2016). Numerical modelling of laboratory soil desiccation cracking using UDEC with a mix-mode cohesive fracture model. *Engineering Geology*, 202:14–23.

[81] Gupta, P. and Duarte, C. A. (2014). Simulation of non-planar three-dimensional hydraulic fracture propagation. *International Journal for Numerical and Analytical Methods in Geomechanics*.

[82] Gupta, P. and Duarte, C. A. (2016). Coupled formulation and algorithms for the simulation of non-planar three-dimensional hydraulic fractures using the generalized finite element method. *International Journal for Numerical and Analytical Methods in Geomechanics*.

[83] Hamid, T. B. and Miller, G. a. (2009). Shear strength of unsaturated soil interfaces. *Canadian Geotechnical Journal*, 46(5):595–606.

[84] Hamidi, F. and Mortazavi, A. (2014). A new three dimensional approach to numerically model hydraulic fracturing process. *Journal of Petroleum Science and Engineering*.

[85] Hauseux, P., Roubin, E., Seyedi, D. M., and Colliat, J. B. (2016). FE modelling with strong discontinuities for 3D tensile and shear fractures: Application to underground excavation. *Computer Methods in Applied Mechanics and Engineering*, 309:269–287.

[86] He, J., Wang, Y., Li, Y., and Ruan, X. C. (2015). Effects of leachate infiltration and desiccation cracks on hydraulic conductivity of compacted clay. *Water Science and Engineering*.

[87] Hillerborg, A., Modéer, M., and Petersson, P.-E. (1976). Analysis of crack formation and

crack growth in concrete by means of fracture mechanics and finite elements. *Cement and concrete research*, 6(6):773–781.

[88] Hirobe, S. and Oguni, K. (2016). Coupling analysis of pattern formation in desiccation cracks. *Computer Methods in Applied Mechanics and Engineering*, 307:470–488.

[89] Hofmann, H., Babadagli, T., Yoon, J. S., Blöcher, G., and Zimmermann, G. (2016). A hybrid discrete/finite element modeling study of complex hydraulic fracture development for enhanced geothermal systems (EGS) in granitic basements. *Geothermics*.

[90] Inglis, C. E. (1913). Stresses in a plate due to the presence of cracks and sharp corners. *Transactions of the Institute of Naval Architects*, 55(219 - 241):193 – 198.

[91] Ingraffea, A. R. and Saouma, V. (1985). Numerical modeling of discrete crack propagation in reinforced and plain concrete. In *Fracture mechanics of concrete: Structural application and numerical calculation*, pages 171–225.

[92] Irwin, G. R. (1957). Analysis of Stresses and Strains Near the End of a Crack Traversing a Plate. In *Applied Mechanics Division Summer Conference, ASME.*

[93] Irwin, G. R. (1958). Fracture. *Handbuch der Physik*, 6:551 – 590.

[94] Jelacic, A., Fortuna, R., LaSala, R., Nathwani, J., Nix, G., Visser, C., Green, B., Renner, J., Blankenship, D., Kennedy, M., and Bruton, C. (2008). An evaluation of enhanced geothermal systems technology. Technical report.

[95] Jirásek, M. (2000). Comparative study on finite elements with embedded discontinuities. *Computer Methods in Applied Mechanics and Engineering*.

[96] Jirásek, M. and Belytschko, T. (2002). Computational resolution of strong discontinuities. In *Proceedings of Fifth World Congress on Computational Mechanics, WCCM V, Vienna University of Technology, Austria*.

[97] Jirásek, M. and Zimmermann, T. (1998). Rotating crack model with transition to scalar damage. *Journal of Engineering Mechanics*, 124:277 – 284.

[98] Julina, M. and Thyagaraj, T. (2018). Quantification of desiccation cracks using X-ray tomography for tracing shrinkage path of compacted expansive soil.

[99] Kaieda, H. (2015). Multiple Reservoir Creation and Evaluation in the Ogachi and Hijiori HDR Projects, Japan. *World Geothermal Congress 2015*.

[100] Karihaloo, B. L. and Xiao, Q. Z. (2003). Modelling of stationary and growing cracks in FE framework without remeshing: A state-of-the-art review.

[101] Khoei, A. R., Moslemi, H., Majd Ardakany, K., Barani, O. R., and Azadi, H. (2009). Modeling of cohesive crack growth using an adaptive mesh refinement via the modified-SPR technique. *International Journal of Fracture*, 159(1):21–41.

[102] Kim, J., Sonnenthal, E. L., and Rutqvist, J. (2012). Formulation and sequential numerical algorithms of coupled fluid/heat flow and geomechanics for multiple porosity materials. *International Journal for Numerical Methods in Engineering*.

[103] Kindle, E. (1917). Some factors affecting the development of mud-cracks. *The Journal of Geology*, 25(2):135–144.

[104] Kindle, E. M. (1926). Contrasted types of mud-cracks. *Transactions of the Royal Society of Canada*, 20:71–75.

[105] Kindle, E. M. and Cole, L. H. (1938). Some mud cracks experiments. *Geologie der Meere und Binnergewasser*, pages 278–283.

[106] Klisinski, M., Runesson, K., and Sture, S. (2007). Finite Element with Inner Softening Band. *Journal of Engineering Mechanics*.

[107] Kodikara, J. K., Nahlawi, H., and Bouazza, A. (2004). Modelling of curling in desiccating clay. *Canadian Geotechnical Journal*, 41(3):560–566.

[108] Konrad, J. M. and Ayad, R. (1997a). A idealized framework for the analysis of cohesive soils undergoing desiccation. *Canadian Geotechnical Journal*.

[109] Konrad, J.-M. and Ayad, R. (1997b). Desiccation of a sensitive clay: field experimental observations. *Canadian Geotechnical Journal*.

[110] Lakshmikantha, M. R., Prat, P. C., and Ledesma, A. (2009). Image analysis for the quantification of a developing crack network on a drying soil. *Geotechnical Testing Journal*, 32(6).

[111] Laloui, L., Klubertanz, G., and Vulliet, L. (2003). Solid-liquid-air coupling in multiphase porous media. *International Journal for Numerical and Analytical Methods in Geomechanics*, 27(3):183–206.

[112] Lecampion, B. (2009). An extended finite element method for hydraulic fracture problems. *Communications in Numerical Methods in Engineering*.

[113] Levatti, H. U., Prat, P. C., Ledesma, A., Cuadrado, A., and Cordero, J. A. (2017). Experimental analysis of 3D cracking in drying soils using ground-penetrating radar. *Geotechnical Testing Journal*.

[114] Lewis, R. W. and Schrefler, B. A. (1998). *Finite Element Method in the Deformation and Consolidation of Porous Media*.

[115] Li, B., Jiang, Y., Mizokami, T., Ikusada, K., and Mitani, Y. (2014). Anisotropic shear behavior of closely jointed rock masses. *International Journal of Rock Mechanics and Mining Sciences*, 71:258–271.

[116] Li, L. C., Tang, C. A., Wang, S. Y., Liang, Z. Z., and Zhang, Y. B. (2012). Numerical simulation of 3d hydraulic fracturing based on an improved flow-stress-damage model and a parallel fem technique. *Rock Mech Rock Eng*.

[117] Liu, C., Tang, C. S., Shi, B., and Suo, W. B. (2013). Automatic quantification of crack patterns by image processing. *Computers and Geosciences*, 57:77–80.

[118] López, C. M., Carol, I., and Aguado, A. (2008a). Meso-structural study of concrete fracture using interface elements. I: numerical model and tensile behavior. *Materials and Structures*, 41(3):583–599.

[119] López, C. M., Carol, I., and Aguado, A. (2008b). Meso-structural study of concrete fracture using interface elements. II: Compression, biaxial brazilian test. *Materials and Structures*, 41(3):601–620.

[120] Lu, S. M. (2018). A global review of enhanced geothermal system (EGS).

[121] Maedo, M. A. (2015). *Simulação computacional por elementos finitos de múltiplas fissuras em sólidos usando técnica de fragmentação da malha*. PhD thesis, Universidade Estadual

Paulista Júlio de Mesquita Filho (UNESP).

[122] Malvern, L. E. (1969). *Introduction to the Mechanics of a Continuous Medium*. Number Monograph.

[123] Manzoli, O., Maedo, M., Bitencourt, L., and Rodrigues, E. (2016). On the use of finite elements with a high aspect ratio for modeling cracks in quasi-brittle materials. *Engineering Fracture Mechanics*, 153.

[124] Manzoli, O., Maedo, M., Rodrigues, E., and Bittencourt, T. (2014). Modeling of multiple cracks in reinforced concrete members using solid finite elements with high aspect ratio. In *Computational Modelling of Concrete Structures - Proceedings of EURO-C 2014*, volume 1.

[125] Manzoli, O., Sánchez, M., Maedo, M., Hajjat, J., and Guimararães, L. J. N. (2017). An orthotropic interface damage model for simulating drying processes in soils. *Acta Geotechnica*, pages 1–16.

[126] Manzoli, O. L., Cleto, P. R., Sánchez, M., Guimarães, L. J., and Maedo, M. A. (2019). On the use of high aspect ratio finite elements to model hydraulic fracturing in deformable porous media. *Computer Methods in Applied Mechanics and Engineering*.

[127] Manzoli, O. L., Gamino, A. L., Rodrigues, E. A., and Claro, G. K. S. (2012). Modeling of interfaces in two-dimensional problems using solid finite elements with high aspect ratio. *Computers and Structures*, 94-95:70–82.

[128] Melenk, J. M. and Babuška, I. (1996). The partition of unity finite element method: Basic theory and applications. *Computer Methods in Applied Mechanics and Engineering*.

[129] Miller, C. J., Mi, H., and Yesiller, N. (1998). Experimental analysis of desiccation crack propagation in clay liners. *Journal of the American Water Resources Association*.

[130] Miller, G. and Hamid, T. (2007). Direct shear apparatus for unsaturated soil interface testing. *ASTM Geotechnical Testing Journal*, 30(3):182–191.

[131] Minter, W. E. L. (1970). Origin of mud polygons that are concave downward. *Journal of Sedimentary Petrology*, pages 755–764.

[132] Misra, A. (1999). Micromechanical model for anisotropic rock joints. *Journal of*

Geophysical Research, 104:23–175.

[133] Moës, N. and Belytschko, T. (2002). Extended finite element method for cohesive crack growth. *Engineering Fracture Mechanics*, 69(7):813–833.

[134] Moës, N., Dolbow, J., and Belytschko, T. (1999). A finite element method for crack growth without remeshing. *International Journal for Numerical Methods in Engineering*.

[135] Mohammadnejad, T. and Khoei, A. R. (2013). An extended finite element method for hydraulic fracture propagation in deformable porous media with the cohesive crack model. *Finite Elements in Analysis and Design*.

[136] Molinari, J. F., Gazonas, G., Raghupathy, R., Rusinek, A., and Zhou, F. (2007). The cohesive element approach to dynamic fragmentation: The question of energy convergence. *International Journal for Numerical Methods in Engineering*, 69(3):484–503.

[137] Morris, P. H., Graham, J., and Williams, D. J. (1992). Cracking in drying soils. *Canadian Geotechnical Journal*, 29(2):263–277.

[138] Mosler, J. and Meschke, G. (2004). Embedded crack vs. smeared crack models: A comparison of elementwise discontinuous crack path approaches with emphasis on mesh bias. *Computer Methods in Applied Mechanics and Engineering*.

[139] Mota, A., Knap, J., and Ortiz, M. (2008). Fracture and fragmentation of simplicial finite element meshes using graphs. *International Journal for Numerical Methods in Engineering*, 73(11):1547–1570.

[140] Nahlawi, H. and Kodikara, J. K. (2006). Laboratory experiments on desiccation cracking of thin soil layers. *Geotechnical and Geological Engineering*, 24(6):1641–1664.

[141] Needleman, A. (2013). Some issues in cohesive surface modeling. In *Procedia IUTAM*.

[142] Nemat-Nasser, S., Keer, L. M., and Parihar, K. S. (1978). Unstable growth of thermally induced interacting cracks in brittle solids. *International Journal of Solids and Structures*.

[143] Ngo, D. and Scordelis, A. C. (1967). Finite element analysis of reinforced concrete beams. *Journal Proceedings*, 64(3):152 – 163.

[144] Nilson, A. (1968). Nonlinear analysis of reinforced concrete by the finite element method.

ACI Journal, 65(9):757 – 776.

[145] Nordgren, R. (1972). Propagation of a Vertical Hydraulic Fracture. *Society of Petroleum Engineers Journal*.

[146] Nouwakpo, S. K. and Huang, C. H. (2012). A simplified close-range photogrammetric technique for soil erosion assessment. *Soil Science Society of America Journal*, 76(1):70–84.

[147] Olivella, S. and Alonso, E. E. (2008). Gas flow through clay barriers. *Géotechnique*, 58(3):157–176.

[148] Olivella, S., Carrera, J., Gens, A., and Alonso, E. E. (1994). Nonisothermal multiphase flow of brine and gas through saline media. *Transport in porous media*, 15(3):271–293.

[149] Olivella, S., Gens, A., Carrera, J., and Alonso, E. (1996). Numerical formulation for a simulator (CODE_BRIGHT) for the coupled analysis of saline media. *Engineering Computations*, 13(7):87–112.

[150] Oliver, J. (1996). Modelling strong discontinuities in solid mechanics via strain softening constitutive equations. Part 1: Fundamentals. *International Journal for Numerical Methods in Engineering*, 39(21):3575–3600.

[151] Oliver, J., Cervera, M., and Manzoli, O. (1999). Strong discontinuities and continuum plasticity models: The strong discontinuity approach. *International journal of plasticity*, 15(3):319–351.

[152] Oliver, J. and Huespe, A. E. (2004). Continuum approach to material failure in strong discontinuity settings. *Computer Methods in Applied Mechanics and Engineering*, 193(30):3195–3220.

[153] Oliver, J., Huespe, A. E., and Cante, J. C. (2008). An implicit/explicit integration scheme to increase computability of non-linear material and contact/friction problems. *Computer Methods in Applied Mechanics and Engineering*, 197(21-24):1865–1889.

[154] Oliver, J., Huespe, A. E., and Sánchez, P. J. (2006). A comparative study on finite elements for capturing strong discontinuities: E-FEM vs X-FEM. *Computer Methods in Applied Mechanics and Engineering*.

[155] Ortiz, M., Leroy, Y., and Needleman, A. (1987). A finite element method for localized failure analysis. *Computer Methods in Applied Mechanics and Engineering*.

[156] Ortiz, M. and Pandolfi, A. (1999). Finite-deformation irreversible cohesive elements for three-dimensional crack-propagation analysis. *International Journal for Numerical Methods in Engineering*.

[157] Pan, P. Z., Rutqvist, J., Feng, X. T., and Yan, F. (2014). TOUGH-RDCA modeling of multiple fracture interactions in caprock during CO2 injection into a deep brine aquifer. *Computers and Geosciences*, 65:24–36.

[158] Panday, S. and Corapcioglu, M. Y. (1989). Reservoir transport equations by compositional approach. *Transport in Porous Media*.

[159] Pandolfi, A. and Ortiz, M. (2002). An efficient adaptive procedure for three-dimensional fragmentation simulations. *Engineering with Computers*, 18(2):148–159.

[160] Pandolfi, A. and Weinberg, K. (2011). A numerical approach to the analysis of failure modes in anisotropic plates. *Engineering Fracture Mechanics*, 78(9):2052–2069.

[161] Papanastasiou, P. (1999). An efficient algorithm for propagating fluid-driven fractures. *Computational Mechanics*.

[162] Parker, R. (1999). The Rosemanowes HDR project 1983-1991. *Geothermics*.

[163] Pereira, L. C., Guimarães, L. J. N., Horowitz, B., and Sánchez, M. (2014). Coupled hydro-mechanical fault reactivation analysis incorporating evidence theory for uncertainty quantification. *Computers and Geotechnics*, 56:202–215.

[164] Perkins, T. and Gonzalez, J. (1985). The Effect of Thermoelastic Stresses on Injection Well Fracturing. *Society of Petroleum Engineers Journal*.

[165] Perkins, T. and Kern, L. (1961). Widths of Hydraulic Fractures. *Journal of Petroleum Technology*.

[166] Peron, H., Hueckel, T., Laloui, L., and Hu, L. B. (2009). Fundamentals of desiccation cracking of fine-grained soils: experimental characterisation and mechanisms identification. *Canadian Geotechnical Journal*, 46(10):1177–1201.

[167] Peron, H., Laloui, L., Hu, L. B., and Hueckel, T. (2013). Formation of drying crack patterns in soils: A deterministic approach. *Acta Geotechnica*, 8(2):215–221.

[168] Phongthanapanich, S. and Dechaumphai, P. (2004). Adaptive Delaunay triangulation with object-oriented programming for crack propagation analysis. *Finite Elements in Analysis and Design*, 40(13-14):1753–1771.

[169] Piggott, A. R. and Elsworth, D. (1996). Displacement of formation fluids by hydraulic fracturing. *Géotechnique*.

[170] Prazeres, P. G., Bitencourt, L. A., Bittencourt, T. N., and Manzoli, O. L. (2016). A modified implicit–explicit integration scheme: an application to elastoplasticity problems.

[171] Rabczuk, T., Bordas, S., and Zi, G. (2010). On three-dimensional modelling of crack growth using partition of unity methods. In *Computers and Structures*.

[172] Ramezani, M., de Las Casas, E. B., Mattos, C. M. d. A., Manzoli, O. L., and Rodrigues, E. (2018). Finite element simulation of fracture in a restored premolar tooth. *Research on Biomedical Engineering*, 34(1):54–64.

[173] Rashid, Y. R. (1968). Ultimate strength analysis of prestressed concrete pressure vessels. *Nuclear engineering and design*, 7(4):334–344.

[174] Regueiro, R. A. and Borja, R. I. (1999). A finite element model of localized deformation in frictional materials taking a strong discontinuity approach. *Finite Elements in Analysis and Design*, 33(4):283–315.

[175] Remij, E. W., Remmers, J. J., Huyghe, J. M., and Smeulders, D. M. (2018). On the numerical simulation of crack interaction in hydraulic fracturing. *Computational Geosciences*.

[176] Rice, J. R. (1968). Mathematical analysis in the mechanics of fracture. *Fracture: an advanced treatise 2*, 2:191–311.

[177] Rice, J.R. (Brown University, Providence, R. (1968). A path Independent Integral and the Approximate Analysis of Strain concentration by Notches and Cracks. *HJournal of Applied Mechanics*.

[178] Rodrigues, E. A., Manzoli, O. L., Bitencourt Jr., L. A., Bittencourt, T. N., and Sánchez, M.

(2017). An adaptive concurrent multiscale model for concrete based on coupling finite elements. *Comput. Methods Appl. Mech. Engrg.*

[179] Rodríguez, R., Sánchez, M., Ledesma, A., and Lloret, A. (2007). Experimental and numerical analysis of desiccation of a mining waste. *Canadian Geotechnical Journal*, 44(6):644–658.

[180] Safari, E., Jalili Ghazizade, M., Abduli, M. A., and Gatmiri, B. (2014). Variation of crack intensity factor in three compacted clay liners exposed to annual cycle of atmospheric conditions with and without geotextile cover. *Waste Management*.

[181] Sanchez, M., Atique, A., Kim, S., Romero, E., and Zielinski, M. (2013). Exploring desiccation cracks in soils using a 2D profile laser device. *Acta Geotechnica*, 8(6):583–596.

[182] Sánchez, M., Gens, A., do Nascimento Guimarães, L., and Olivella, S. (2005). A double structure generalized plasticity model for expansive materials. *International Journal for Numerical and Analytical Methods in Geomechanics*.

[183] Sánchez, M., Gens, A., and Olivella, S. (2012). THM analysis of a large-scale heating test incorporating material fabric changes. *International journal for numerical and analytical methods in geomechanics*, 36(4):391–421.

[184] Sánchez, M., Manzoli, O. L., and Guimarães, L. J. N. (2014). Modeling 3-D desiccation soil crack networks using a mesh fragmentation technique. *Computers and Geotechnics*, 62:27–39.

[185] Sarris, E. and Papanastasiou, P. (2011). The influence of the cohesive process zone in hydraulic fracturing modelling. *International Journal of Fracture*.

[186] Schrefler, B. A., Secchi, S., and Simoni, L. (2006). On adaptive refinement techniques in multi-field problems including cohesive fracture. *Computer Methods in Applied Mechanics and Engineering*.

[187] Secchi, S. and Schrefler, B. A. (2012). A method for 3-D hydraulic fracturing simulation. In *International Journal of Fracture*.

[188] Segura, J. M. and Carol, I. (2008a). Coupled HM analysis using zero-thickness interface elements with double nodes. Part I: Theoretical model. *International Journal for Numerical*

and Analytical Methods in Geomechanics.

[189] Segura, J. M. and Carol, I. (2008b). Coupled HM analysis using zero-thickness interface elements with double nodes-Part II: Verification and application. *International Journal for Numerical and Analytical Methods in Geomechanics*.

[190] Shit, P. K., Bhunia, G. S., and Maiti, R. (2015). Soil crack morphology analysis using image processing techniques. *Modeling Earth Systems and Environment*, 1(4):35.

[191] Shokri, N., Zhou, P., and Keshmiri, A. (2015). Patterns of Desiccation Cracks in Saline Bentonite Layers. *Transport in Porous Media*.

[192] Sima, J., Jiang, M., and Zhou, C. (2014). Numerical simulation of desiccation cracking in a thin clay layer using 3D discrete element modeling. *Computers and Geotechnics*.

[193] Simo, J. C., Oliver, J., and Armero, F. (1993). An analysis of strong discontinuities induced by strain-softening in rate-independent inelastic solids. *Computational Mechanics*, 12(5):277–296.

[194] Simoni, L. and Secchi, S. (2003). Cohesive fracture mechanics for a multi-phase porous medium. *Engineering Computations (Swansea, Wales)*.

[195] Simoni, L., Secchi, S., and Schrefler, B. A. (2008). Numerical difficulties and computational procedures for thermo-hydro-mechanical coupled problems of saturated porous media. *Computational Mechanics*.

[196] Sloan, S. W. (1987). Substepping schemes for the numerical integration of elastoplastic stress–strain relations. *International Journal for Numerical Methods in Engineering*.

[197] Snow, D. T. (1965). *A parallel plate model of fractured permeable media*. PhD thesis, University of California, Berkeley.

[198] Song, W.-K., Cui, Y.-J., Tang, A. M., Ding, W.-Q., and Wang, Q. (2016). Experimental study on water evaporation from compacted clay using environmental chamber. *Canadian Geotechnical Journal*.

[199] Stirling, R. A., Glendinning, S., and Davie, C. T. (2017). Modelling the deterioration of the near surface caused by drying induced cracking. *Applied Clay Science*, 146:176–185.

[200] Sukumar, N., Moës, N., Moran, B., and Belytschko, T. (2000). Extended finite element method for three-dimensional crack modelling. *International Journal for Numerical Methods in Engineering*.

[201] Tang, C. S., Wang, D. Y., Zhu, C., Zhou, Q. Y., Xu, S. K., and Shi, B. (2018). Characterizing drying-induced clayey soil desiccation cracking process using electrical resistivity method. *Applied Clay Science*.

[202] Taron, J., Elsworth, D., and Min, K. B. (2009). Numerical simulation of thermal-hydrologic-mechanical-chemical processes in deformable, fractured porous media. *International Journal of Rock Mechanics and Mining Sciences*.

[203] Tomac, I. and Sauter, M. (2018). A review on challenges in the assessment of geomechanical rock performance for deep geothermal reservoir development.

[204] Tran, D., Settari, A., and Nghiem, L. (2012). Initiation and propagation of secondary cracks in thermo-poroelastic media. *46th US Rock Mechanics / Geomechanics Symposium 2012*.

[205] van Genuchten, M. T. (1980). A Closed-form Equation for Predicting the Hydraulic Conductivity of Unsaturated Soils1. *Soil Science Society of America Journal*, 44(5):892.

[206] Varsei, M., Miller, G. A., and Hassanikhah, A. (2016). Novel Approach to Measuring Tensile Strength of Compacted Clayey Soil during Desiccation. *International Journal of Geomechanics*.

[207] Vo, T. D., Pouya, A., Hemmati, S., and Tang, A. M. (2017). Numerical modelling of desiccation cracking of clayey soil using a cohesive fracture method. *Computers and Geotechnics*.

[208] Wang, H. Y. (2016). Numerical investigation of fracture spacing and sequencing effects on multiple hydraulic fracture interference and coalescence in brittle and ductile reservoir rocks. *Engineering Fracture Mechanics*.

[209] Ward, F. (1923). Note on mud cracks. *American Journal of Science*, pages 308–309.

[210] Watanabe, N., Blocher, G., Cacace, M., Held, S., and Kohl, T. (2017). *Geoenergy Modeling III Enhanced Geothermal Systems*.

[211] Wen, L. and Tian, R. (2016). Improved XFEM: Accurate and robust dynamic crack growth simulation. *Computer Methods in Applied Mechanics and Engineering*, 308:256–285.

[212] Witherspoon, P. A., Wang, J. S., Iwai, K., and Gale, J. E. (1980). Validity of Cubic Law for fluid flow in a deformable rock fracture. *Water Resources Research*.

[213] Xu, X. P. and Needleman, A. (1994). Numerical simulations of fast crack growth in brittle solids. *Journal of the Mechanics and Physics of Solids*, 42(9):1397–1434.

[214] Xu, X. P. and Needleman, A. (1995). Numerical simulations of dynamic interfacial crack growth allowing for crack growth away from the bond line. *International Journal of Fracture*.

[215] Xu, X. P. and Needleman, A. (1996). Numerical simulations of dynamic crack growth along an interface. *International Journal of Fracture*.

[216] Zhang, X., Li, L., Chen, G., and Lytton, R. (2014). A photogrammetry-based method to measure total and local volume changes of unsaturated soils during triaxial testing. *Acta Geotechnica*, 10(1):55–82.

[217] Zielinski, M., Sánchez, M., Romero, E., and Atique, A. (2014). Precise observation of soil surface curling. *Geoderma*, 226-227(1):85–93.

[218] Zielinski, M., Sánchez, M., Romero, E., and Sentenac, P. (2011). Water Retention Behaviour of an Embankment Model. In *Geo-Frontier*, pages 3566–3575.